**The Dissertation Committee for Julia Dianne Cushen Certifies that this is the approved version of the following dissertation:**

# High Interaction Parameter Block Copolymers for Advanced Lithography

**Committee:**

Christopher J. Ellison, Supervisor

C. Grant Willson

Benny Freeman

S.V. Sreenivasan

Ricardo Ruiz

# High Interaction Parameter Block Copolymers for Advanced Lithography

**by**

**Julia Dianne Cushen, B.S.C.E.**

**Dissertation**

Presented to the Faculty of the Graduate School of

The University of Texas at Austin

in Partial Fulfillment

of the Requirements

for the Degree of

**Doctor of Philosophy**

**The University of Texas at Austin**

**December, 2013**

# Dedication

To Mom, Dad, and Rob, who were behind me every step of the way. And to Mr. Copenhaver, who introduced me to Chemistry.

# Acknowledgements

There are many people who have helped me throughout the course of my doctoral journey and without them the work detailed in the following chapters couldn't have been possible. Through the ups and downs, my advisor, Dr. Christopher Ellison has been there to offer his expertise and guidance through the process. It is through working for him that I have found my passion for polymers and have developed the skills necessary to conduct both independent and team-focused research that is invaluable in my career ahead.

Secondly, I couldn't have made it through my Ph.D. without the support I received from several colleagues. My labmate and close friend Josh Katzenstein was there to offer support, without fail, through any crisis imaginable. Chris Bates consistently offered fresh insight into my work and I am grateful for his willingness to edit countless documents for me with his phenomenal editing and writing skills. I am also very grateful for my undergrad, Erica Rausch, who performed much of the tedious work during the first three years when the project was getting started. I am happy to pass this project along to Sunshine Zhou, a good friend and colleague and wish her the best of luck in her research endeavors.

The research findings described in the following chapters came about largely due to the collaborative efforts of many contributors. The advisors on this project, Drs. Christopher J. Ellison and C. Grant Willson led our team and helped us all focus on the direction of the project. Graduate students Christopher Bates, Michael Maher, William Durand, and Gregory Blachut, visiting scientist Takehiro Seshimo, and their undergraduate students, Morgan Schulze, Leon Dean, Jeffrey Ting, Anthony Thio, Litan Li, and Brennen Mueller pioneered the top coat work that made orientation of the BCPs

in Chapters 2 and 4 possible. Graduate student Jeffrey Easley, visiting scientist Issei Otsuka, and my undergraduate student Erica Rausch helped develop the synthesis protocols that will be described in Chapter 3.

Most of the results presented in Chapter 4 were obtained during an internship/collaboration our group at the University of Texas had with HGST-WD. I did not acknowledge many individuals specifically in this chapter because I performed most of the experiments myself. However, this work would not have been possible without helpful discussions with other members of the HGST-WD DSA team. Ricardo Ruiz provided valuable insight into solvent annealing BCPs, island/hole behavior, and ALD. Yves-Andres Chapuis also provided valuable suggestions for ALD experiments. K.C. Patel was instrumental in enhancing my understanding of etch protocols for pattern transfer. Lei Wan created the chemical contrast patterns that enabled DSA of the PTMSS-*b*-PLA and Tom Albrecht, the team manager, provided valuable insight during group meetings that helped guide my work. Gila Stein and Indranil Mitra from the University of Houston provided some insightful GISAXS measurements that appear in Chapter 5 and Gunja Pandav and Venkat Ganesan from a collaborating group at the University of Texas performed the simulations studies.

Along the way, LaShanda Korley and Tiffani Burt from Case Western University helped with some synchrotron scattering experiments at Brookhaven National Laboratory. Richard Register from Princeton University provided advice and a valuable calibration standard necessary to perform the absolute intensity SAXS experiments detailed in Chapter 6. Joe Lott at the University of Minnesota helped with some cryogenic TEM experiments that were unfortunately unsuccessful in Chapter 7. Several entities also generously provided funding for my graduate work. The Nissan Chemical Company provided funding for part of my stipend and equipment and material costs for

the project. I am also grateful to have received a Graduate Research Fellowship from the National Science Foundation, which supported my tuition and stipend for three years of my graduate study.

While I will direct credit where it is due to the individuals who performed specific work in this document, this research in its entirety would be incomplete at best if not for the collective contributions from the aforementioned individuals. I am very grateful to have had the opportunity to work with all of these talented people and a significant amount of credit for the successful results presented in this document goes to them for their contributions.

# High Interaction Parameter Block Copolymers for Advanced Lithography

Julia Dianne Cushen, Ph.D.

The University of Texas at Austin, 2013

Supervisor: Christopher J. Ellison

Block copolymers demonstrate potential in next-generation lithography as a solution for overcoming the limitations of conventional lithographic techniques. Ideal block copolymer materials for this application can be synthesized on a commercial scale, have high $\chi$-parameters promoting self-assembly into sub-20 nm pitch domains, have controllable alignment and orientation, and have high etch contrast between the domains for facilitating pattern transfer into the underlying substrate. Block copolymers that contain silicon in one domain are attractive for nanopatterning since they often fulfill at least three of these requirements. However, silicon-containing materials are notoriously difficult to orient in thin films due to the low surface energy of the silicon-containing block, which typically wets the free surface interface.

In this work, the methodology behind material choice and the synthesis of new silicon-containing block copolymers by a variety of polymerization techniques will be described. Thin film self-assembly of the block copolymers with domains oriented perpendicular to the plane of the substrate is achieved using different solvent annealing and neutral surface treatments with thermal annealing conditions. Block copolymer patterns are transferred to the underlying substrate by reactive ion etching and directed

self-assembly of the polymers is demonstrated using chemical contrast patterns. Interesting thermodynamics governing the self-assembly of block copolymers with solvent annealing will also be discussed. Finally, new amphiphilic block copolymers will be described that were created with lithographic applications in mind but that are most useful for biological applications in drug delivery.

# Table of Contents

# List of Tables

# List of Figures

# List of Schemes

# Chapter 1: Block Copolymer Nanolithography

## 1.1 Introduction – The Lithography Challenge

In modern times, it is difficult to imagine life without a computer, cellular telephone, or many of the countless other electronic devices whose convenience we take for granted on a daily basis. However, many of these devices were nonexistent or in the early stages of development at the time I was born. Growing up in the '90s and '00s, I have been in a position to observe the vast improvement of many electronics from their bulky, first generation models to the sleek, multifunctional versions we enjoy today. The early cellular telephones of the 1980s (**Figure 1.1a**),[1] which only had the ability to make phone calls, have improved drastically to the familiar iPhone 5 (**Figure 1.1b**)[2] which was released in 2012 and has the ability to function much like a modern computer.


**Figure 1.1:** a) A Motorola DynaTAC 8000X from 1984. The phone weighed 790g and only had the ability to make phone calls. b) The iPhone 5, released in 2012. The phone weighs 112 g, and in addition to making phone calls, has the ability to perform a variety of complex functions such as surfing the web and running various programs. Images are public domain from [1] and [2].

Personal computers have also come a long way since the IBM computers of the early 1980s (**Figure 1.2a**).[3] The modern Macbook Air, released in 2008, has both higher processing speed and larger storage capacity than early computers for a fraction of the price (**Figure 1.2b**).[4]

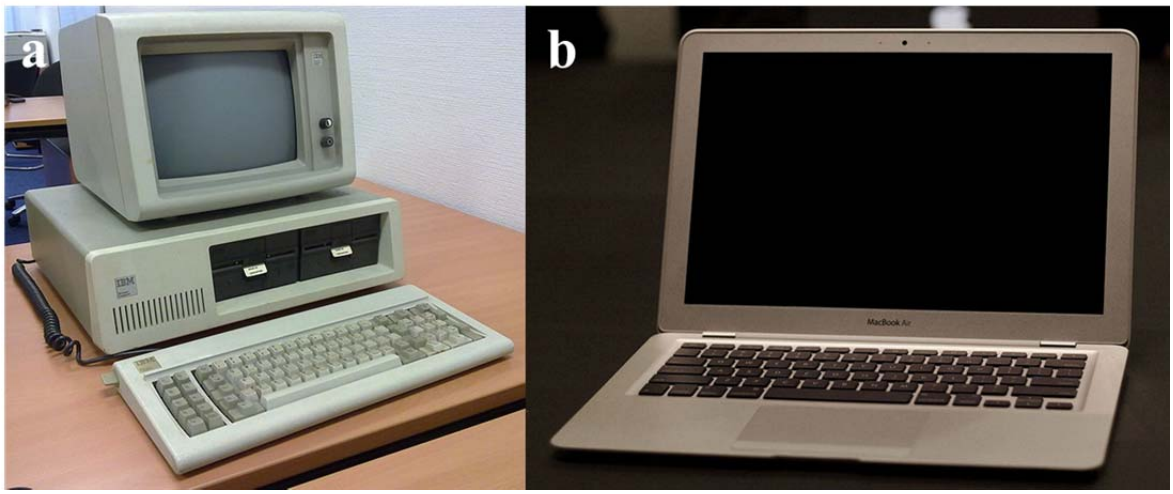


**Figure 1.2:** a) IBM Personal Computer model 5150 with a 5151 monitor from 1981. The maximum memory was 256 kB and sold for approximately $7500 (adjusting for inflation). b) The original MacBook Air, released in 2008 with 80 GB of memory, a 1.8 GHz processor, and cost approximately $1000. Both images are public domain from [3] and [4].

The decrease in size and increase in functionality of electronic devices over the past few decades are attributed to an increase in the density of their micro and nanoscale components. Over the past few decades, the rate of this densification has followed an exponential scaling trend depicted in **Figure 1.3** called Moore's law,[5] which is an observation that the number of transistors on a chip approximately doubles every two years.[6] This exponential scaling trend is similarly observed in other sectors of the microelectronics industry, such as hard disk storage capacity (Kryder's law),[7] network

capacity (Butters' law),[8] and number of pixels per dollar in digital cameras (Hendy's law).[9]

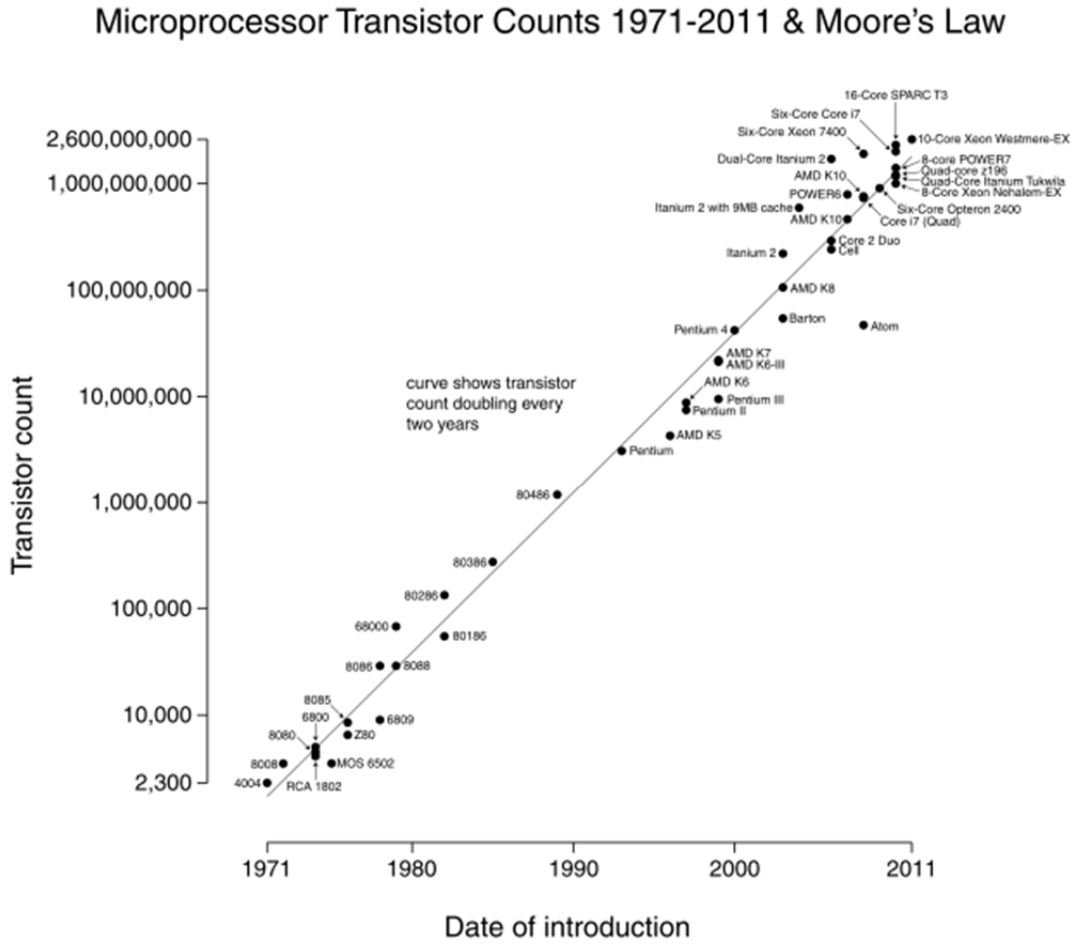


**Figure 1.3:** Transistor count vs. date of introduction for various technologies.[5] The transistor count is on a logarithmic axis; this plot depicts an approximate doubling of transistor count every two years. Image is public domain from [5].

Since the 1980s, the trend of feature density increase has largely been attributed to advances in photolithography. In photolithography, light of a specific wavelength is directed through a patterned mask that blocks a portion of the light. The mask features are

typically larger than the features that are ultimately patterned due to lenses and other optical components. The light not blocked by the mask reaches and changes the solubility characteristics of a polymeric coating (photoresist) on the substrate. A subsequent processing step selectively removes either the exposed or unexposed portions of the photoresist and results in a positive or negative tone pattern of the mask, respectively. The pattern is then transferred to the substrate using an etch protocol.[10] This process is described visually in **Figure 1.4**.[11]

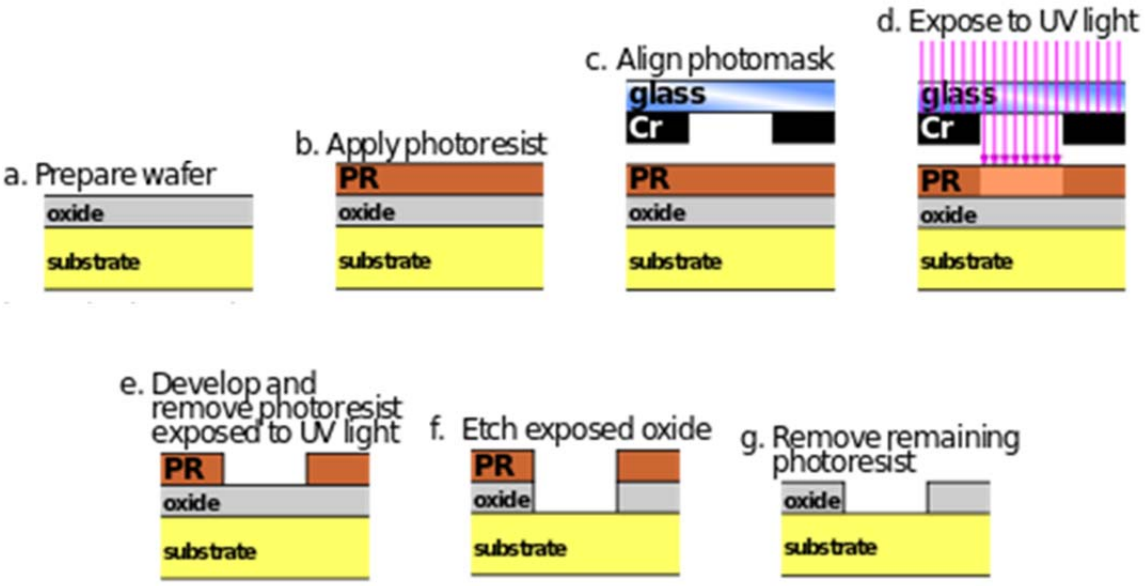


**Figure 1.4:** Schematic diagram of the photolithography process with a positive tone resist. Image is public domain from [11].

The resolution of the features created by photolithographic patterning is defined by Rayleigh's equation, shown in **Equation 1.1**, where $W$ represents the feature resolution, $k_1$ is a process-related constant, $\lambda$ is the wavelength of light, and $nsin\theta$ is the numerical aperture.[12]

$$W = k_1 \frac{\lambda}{n \sin \theta} \qquad \textbf{Eq. 1.1}$$

Advances in photolithography have been realized through optimization of the process constant, the wavelength of the light source, and the numerical aperture. The wavelength of light used in the process has been reduced through technologies such as i-line technology (385 nm) and the excimer laser (KrF – 248 nm and ArF – 193 nm). Further developments have included the invention of immersion lithography, in which the air between the lens and the wafer surface is replaced with water, thereby increasing the refractive index and thus the numerical aperture.[13]

Unfortunately, patterning by photolithography has reached a ceiling due to physical limitations of current 193 nm optical immersion lithography, which has resolution limits at approximately 36 nm.[12] Alternative patterning technologies must be developed to enable manufacturing of next-generation integrated circuits, flash memory and hard disk drives with increased speed and storage capabilities. Extreme ultraviolet lithography[14] and electron beam lithography[15] are potential candidates for achieving sub-36 nm feature dimensions, but both are currently prohibitively expensive and have a low throughput. For example, creating a bit-patterned magnetic storage media template with a 1 Tbit/in$^2$ dot array by electron beam lithography is estimated to require more than a month of continuous writing time at a cost exceeding 1 million dollars.[16] Nanoimprint technology is another candidate for replicating sub-36 nm features which, unlike photolithography, creates an exact 1:1 replica of the template and has demonstrated successful pattern transfer down to <3 nm.[17] However, economical creation of an imprint template remains a considerable challenge.

Block copolymers (BCPs) present a promising route for fabricating nanoscale patterns that could be used to economically produce nanoimprint templates with features smaller than those achievable using conventional photolithographic techniques due to their ability to self-assemble into well-ordered periodic arrays with feature sizes well

below 36 nm.[18-20] These self-assembled materials can be converted into lithographic templates upon removal of one block using processing steps that are compatible with current semiconductor fabrication such as spin coating, annealing, and etching.[21, 22] The work described in this dissertation presents new BCP materials with properties that are attractive for this application and the processing steps that must be considered for their implementation as a solution to next-generation lithography.

### 1.2 Block Copolymer Self-Assembly

Diblock copolymers (**Figure 1.5a**) are a two-component subset of multiblock copolymers (**Figure 1.5b**), a special class of polymers composed of chemically distinct segments of a particular repeat unit that are covalently bound together. Random copolymers (**Figure 1.5c**) are another type of copolymer, described in more detail in subsequent sections, that are composed of two or more chemically distinct repeat units arranged within the polymer chain in a random fashion.

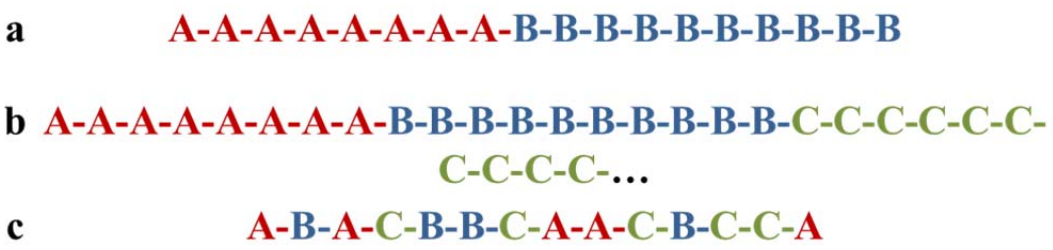


**Figure 1.5:** a) Diblock copolymer composed of block segments A and B, b) multiblock copolymer that could be composed of any number of segments, and c) random copolymer composed of segments A, B, and C arranged in a random fashion.

Due to the chemical incompatibility of the segments in a block copolymer and their inability to macrophase separate because of the covalent linkage, blocks of a

sufficiently high molecular weight will phase separate into periodic nanostructures such as body- or face-centered cubic spheres, hexagonally-packed cylinders, and lamellae. The morphology of the block copolymer is dependent on the volume fraction of each block (*f*) and the degree of polymerization (N) times the segregation strength ($\chi$).[18-20] The phase separation characteristics and morphologies of block copolymers based on these parameters has been mapped out based on self-consistent field theory simulations (**Figure 1.6a**)[20] and experimental work (**Figure 1.6b**).[20]

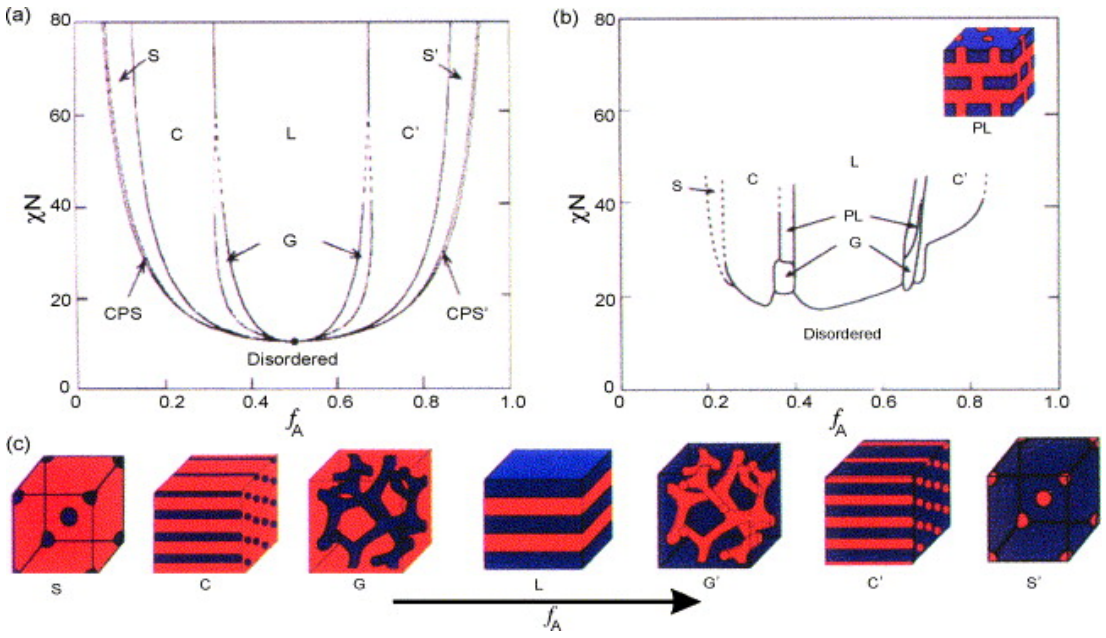


**Figure 1.6:** a) Phase diagram of a diblock copolymer based on self-consistent mean field theory, b) phase diagram of poly(styrene-*block*-isoprene) created from experimental work, c) morphologies accessible from self-assembled diblock copolymers include spheres (S), cylinders (C), bicontinuous gyroid (G), and lamellae (L). Reprinted with permission from [20]. Copyright 1999, American Institute of Physics.

The phase separation of BCPs into periodic thin film structures can be useful as a means for substrate patterning for nanoimprint template fabrication.[21] Since BCPs phase

separate on the ca. 1-100 nm length scale,[18, 23, 24] they provide a potential solution to sub-36 nm patterning. **Figure 1.7** describes the process for patterning a substrate using a block copolymer, from deposition of the material by spin coating to pattern transfer through a reactive ion etch process. Since diblock copolymers produce line and dot patterns, they are most useful for applications in bit patterned media[25] and some limited applications in integrated circuit components such as FinFETs and contact hole shrink.[26] More complex multiblock copolymer structures have potential for producing other desirable feature geometries for lithography,[27-29] although they have been less thoroughly studied than diblock copolymers due to their morphological complexity.

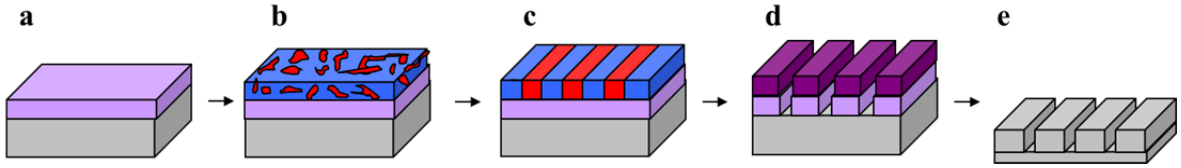


**Figure 1.7:** Process used to create patterns in a substrate using a lamellae-forming block copolymer mask. a) A surface treatment is deposited onto the substrate, b) a block copolymer is spin-coated on top of the surface treatment, c) a block copolymer annealing process promotes self-assembly and orientation perpendicular to the plane of the substrate, d) an etch process selectively removes one block and underlying surface treatment (potentially changes the chemistry of the remaining block), e) a dry etch process removes remaining polymer and transfers pattern into the substrate.

While a wide variety of block copolymer systems have been considered for use in substrate patterning, three requirements for a successful material emerge: the BCP should be spin-coatable, one block should be easily removable, there should be a strong driving force for microphase separation for the creation of small features, and feature orientation must be controllable. Pattern transfer requires the selective removal of one block first before transferring the pattern into a substrate. However, most BCP systems, such as the

heavily studied poly(styrene-*b*-methyl methacrylate) (PS-*b*-PMMA), have poor reactive ion etch selectivity between the blocks which limits patterns to low aspect-ratio features.[30] Furthermore, wet etching techniques are generally limited to relatively low aspect ratio features due to feature collapse.[31] Details on the etching process and a brief literature review on the subject will be discussed in Section 1.4.

The ability to create small features is linked to the interaction parameter, $\chi$, which is a measure of the chemical incompatibility between the A and B segments. Self-assembled domains are present when $\chi N$ (where $N$ is the degree of polymerization) is larger than a critical value (10.5 for symmetric diblocks).[19] Furthermore, the domain periodicity of microphase separation ($d$) scales as $d \sim aN^{2/3}\chi^{1/6}$ in the strong-segregation limit.[19] Since $d$ is more strongly a function of $N$ than $\chi$, reducing $N$ is the most favorable approach to decrease $d$, subject to the constraint that $\chi N$ must be larger than a critical value for producing self-assembled structures. Thus, it is crucial to pursue block copolymers that have small $N$ and high $\chi$ values to minimize self-assembled feature sizes while simultaneously maximizing feature densities for next-generation lithography. Finally, feature orientation is critical for successful implementation of block copolymer nanolithography and is addressed in Section 1.3.

### 1.3 Thin Film Orientation of Diblock Copolymers

Nanoscale thin films of BCPs are usually spin-coated from a homogeneous polymer-solvent solution that produces smooth films with relatively low surface roughness. As-cast, the BCP is often poorly ordered within the film due to kinetic trapping of non-equilibrium structures during rapid solvent evaporation, although this can be improved by selecting appropriate casting solvents and spin-coating conditions.[32, 33] Highly ordered, equilibrium thin film BCP structures can be subsequently formed by

either heating the film above the glass transition temperatures of the blocks or by solvent annealing the film. During annealing, top-down line patterns can be formed from either lamellae oriented perpendicular to the plane of the substrate or a monolayer of cylinders oriented parallel to the substrate. Likewise, hexagonally-packed dots are created from either cylinders oriented perpendicular to the substrate or a monolayer of spheres (**Figure 1.8)**. For successful substrate pattern transfer of line and dot patterns, the perpendicularly oriented structures are usually preferable since the curvature of parallel structures can result in feature collapse when attempting to etch the pattern into the substrate. Pattern transfer of parallel structures also imposes thickness limitations of one domain periodicity, which can result in low aspect ratio lines or pillars after transfer.

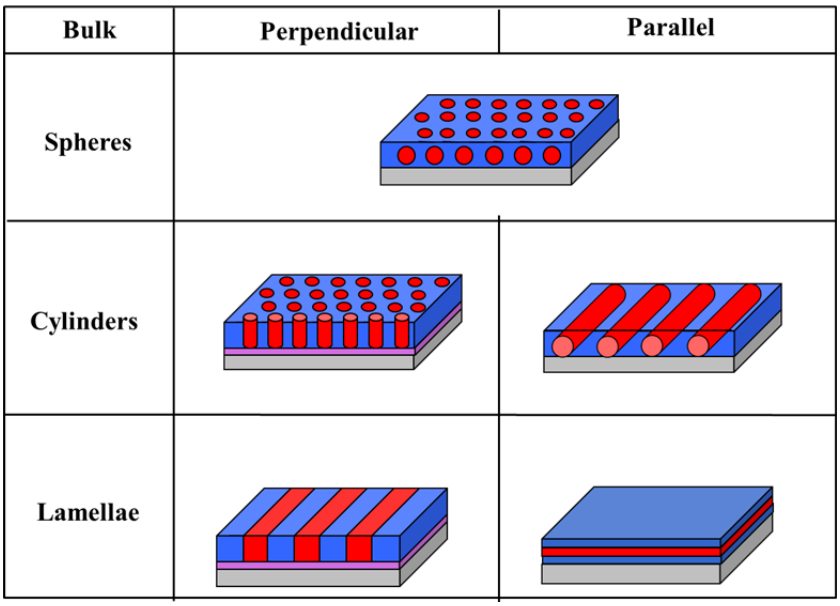


**Figure 1.8:** Thin films of spherical, cylindrical, and lamellae morphologies oriented perpendicular and parallel to the plane of the substrate.

Unfortunately, perpendicular orientations of block copolymers are almost always more difficult to attain in thin films than parallel orientations. In the absence of interface

modification, one block of the copolymer will usually preferentially wet the substrate and/or the free surface interface if the interactions between that block and the interface are more preferential than those of the other block.[34] However, if the interfaces can be modified such that neither block preferentially wets them (i.e. a "neutral" interface), the domains orient perpendicular to the substrate. This can be visualized in terms of the behavior of individual polymer chains of a lamellae-forming block copolymer in **Figure 1.9** for a gradient of wetting conditions. The color gradients in the figure represent possible block wetting preferences for the substrate and free surface interface. This figure shows that there are ranges of substrate and free interface surface chemistries that promote wetting and a window of non-wetting surface chemistry that enables perpendicular orientation of the domains. This figure is representative of a film thickness that is a 1.5 multiple of the domain periodicity of the BCP; the consequences of non-integer multiple thicknesses will be discussed in a later chapter.

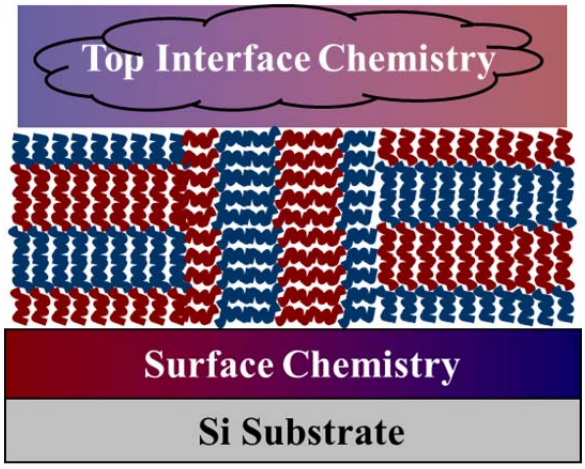


**Figure 1.9:** Orientation of polymer chains of a lamellae-forming block copolymer for possible wetting conditions where the color gradients at the surface and air interfaces represent block preference. Blue surface chemistry prefers to contact the blue block and red surface chemistry prefers to wet the red block.

Unlike most BCP systems, PS-*b*-PMMA can be oriented perpendicular to the substrate during thermal annealing without modifying the free surface interface. PS and PMMA have nearly equivalent surface energies at the free surface at 190°C under vacuum,[35] resulting in neither block preferentially wetting the free surface interface, and will therefore orient perpendicular to the substrate at that temperature as long as a neutral substrate is present. However, since this is not the case with most BCP systems, much work has been devoted to development of a nearly universal method to alter the chemistry of the thin film interfaces to induce perpendicular orientation of BCP domains. While many strategies have been explored, the following sections will discuss interface modification using surface treatments, polymeric top coats, and solvent annealing due to their versatility and success with the block copolymers that are the focus of this dissertation.

### 1.3.1 Surface Treatments

Surface treatments modify the interface between the substrate and the BCP, often through the use of a polymeric coating that does not significantly intermix with the block copolymer layer deposited on top of it. The polymeric coatings can be homopolymers or random copolymers, and generally fall into one of two categories: cross-linked surface treatments or polymer brushes (substrate-grafted polymers).

Cross-linked polymeric surface treatments contain a component within the polymer that causes it to cross-link upon heating.[36, 37] The cross-linkable polymer is spin-coated directly on the substrate and then heated to promote cross-linking (**Figure 1.10a**). A rinsing step is used to remove any unreacted material and may result in a slight decrease in film thickness of the surface treatment. The BCP is subsequently spin-coated on top of the surface treatment but does not significantly intermix with it during

annealing since it is cross-linked. For BCPs in which neither block wets the air interface, such as PS-*b*-PMMA, this can be sufficient to orient the domains perpendicular to the plane of the substrate upon thermal annealing.[37]

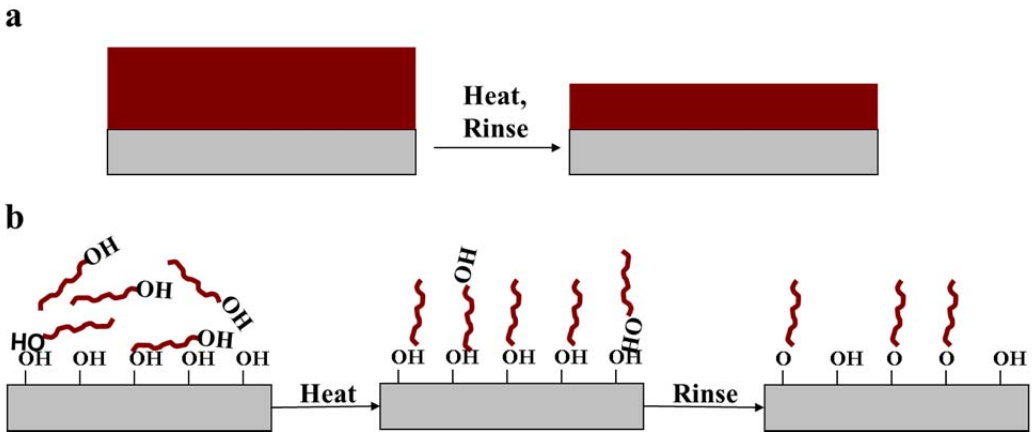


**Figure 1.10:** a) Cross-linked surface treatment deposition steps and b) grafted polymeric surface treatment deposition steps.

Graftable polymeric surface treatments have an end group that reacts with the substrate upon heating. In the case of a substrate with free hydroxyls on the surface, such as silicon with a native oxide layer, a hydroxyl-terminated polymer will graft to the substrate at elevated temperatures.[38] These polymers are spin-coated on a substrate, heated to react the end group with the substrate, and then rinsed to remove excess polymer (**Figure 1.10b**). The grafting density of the polymer (and thus the degree to which the surface treatment alters the chemistry of the substrate) is dependent on the molecular weight of the polymer and time and temperature of the annealing.[39]

### 1.3.2 Thermal Annealing with a Top Coat

The chemistry at the free surface interface is much more difficult to control than the substrate interface because it is not as easily modified. It is difficult to control the

chemistry of the atmosphere directly without the addition of a small molecule, which usually penetrates the BCP and changes the surface energies of the blocks and/or the morphology. Neutral top coats could be used to alter the top interface, but are often difficult to apply to the block copolymer because of solubility challenges. To apply a polymer with a surface energy intermediate to that of the two blocks of the BCP, it will typically only dissolve in a solvent that also dissolves the BCP. This would make it impossible to spin-coat on top of the BCP without destroying or removing the BCP.

In previous work, neutral surface energy polymeric coatings that have a glass transition temperature above that of the BCP have been spin coated on a substrate, floated onto a fluid surface, deposited on top of the BCP layer, and annealed to promote orientation.[40] However, the film floating process often does not allow the top coat to develop good contact with the BCP film, making perpendicular orientation non-uniform across the entire surface. The floating process is also cumbersome and not particularly compatible with current semiconductor fabrication processes.

Another process was recently developed by my colleagues that allowed direct spin coating of a polarity-switching polymeric top coat on a BCP film and has demonstrated the ability to promote orientation in several BCP systems. This process uses a random copolymer top coat that has a component which switches solubility and polarity under different conditions.[41] The polymer contains a maleic anhydride moiety that is soluble as a ring-opened salt form in aqueous base. The maleic anhydride moiety is present in a high enough concentration within the random copolymer that the entire polymer dissolves in the aqueous spin coating solution. The top coat is spin coated out of aqueous base on top of the BCP (that is coated on a neutral substrate layer) but does not destroy it since the BCP is insoluble in aqueous solution. The entire film stack is then heated above the glass transition temperature of the BCP, which also causes the maleic

anhydride salt to ring-close, bringing the surface energy of the top coat in between that of the two blocks of the BCP, i.e. a "neutral" top coat (**Figure 1.11**). The mechanism of this ring-closing is still under investigation in our group and recent results lead us to believe the ring-closed product may actually be a maleimide. During this thermal annealing process, the BCP also reorganizes and orients perpendicular to the substrate since it is confined by energetically neutral interfaces.

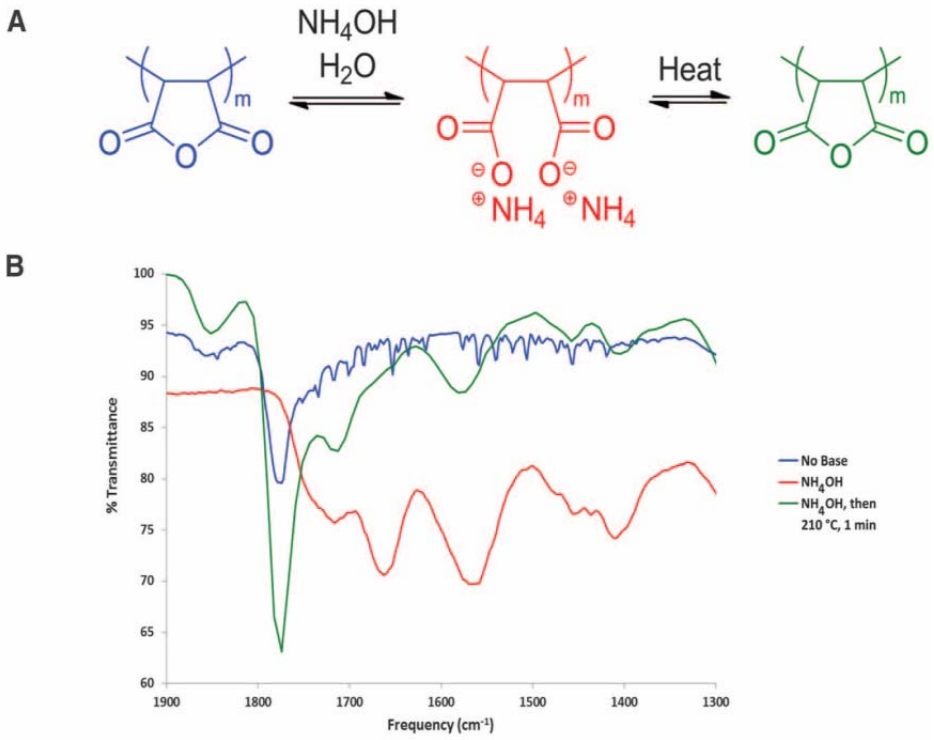


**Figure 1.11:** a) Ring-opening and -closing reactions that modulate the polarity of the top coats. b) IR data from a model top coat that demonstrate the ring-opening and -closing reactions of the poly(maleic anhydride) component. Blue curve, cast from 2-butanone; red curve, cast from 30 weight % (wt %) aqueous (aq.) $NH_4OH$; green curve, aqueous $NH_4OH$-cast sample subsequently annealed at 210°C for 1 min. From [41]. Reprinted with permission from AAAS.

### 1.3.3 Solvent Annealing

Among the different strategies, solvent annealing has proven to be a versatile process that uses a solvent vapor environment to promote reorganization of a polymer film. Solvent vapor is introduced to a chamber or other controlled environment that contains the thin film on a substrate. The solvent vapor swells the film, giving the polymer chains mobility to reassemble and simultaneously changes the chemistry of the top interface through the addition of the small molecules to the atmosphere and the substrate interface by altering block interactions. Under optimized conditions, this enables perpendicular orientation of BCP domains due to neutralization of the surface energy of the top interface.

Many variables such as solvent selectivity,[42, 43] composition of solvent/polymer system,[43-45] and annealing time,[46] among others, have been investigated and play an important role in inducing the desired block copolymer domain orientation. Early solvent annealing experiments were carried out in a simple jar with an open vial of solvent providing the solvent vapor (**Figure 1.12a**). The degree of swelling of the BCP was often not understood in these experiments since it could not be easily monitored, and process conditions that affected orientation usually included the volume of the jar, amount of solvent, and annealing time. Most solvent annealing experiments are now performed in more complex but controllable environments where pressure and vapor composition can be controlled by the flow rates of nitrogen through different streams into the chamber and degree of swelling can be monitored in-situ (**Figure 1.12b**).

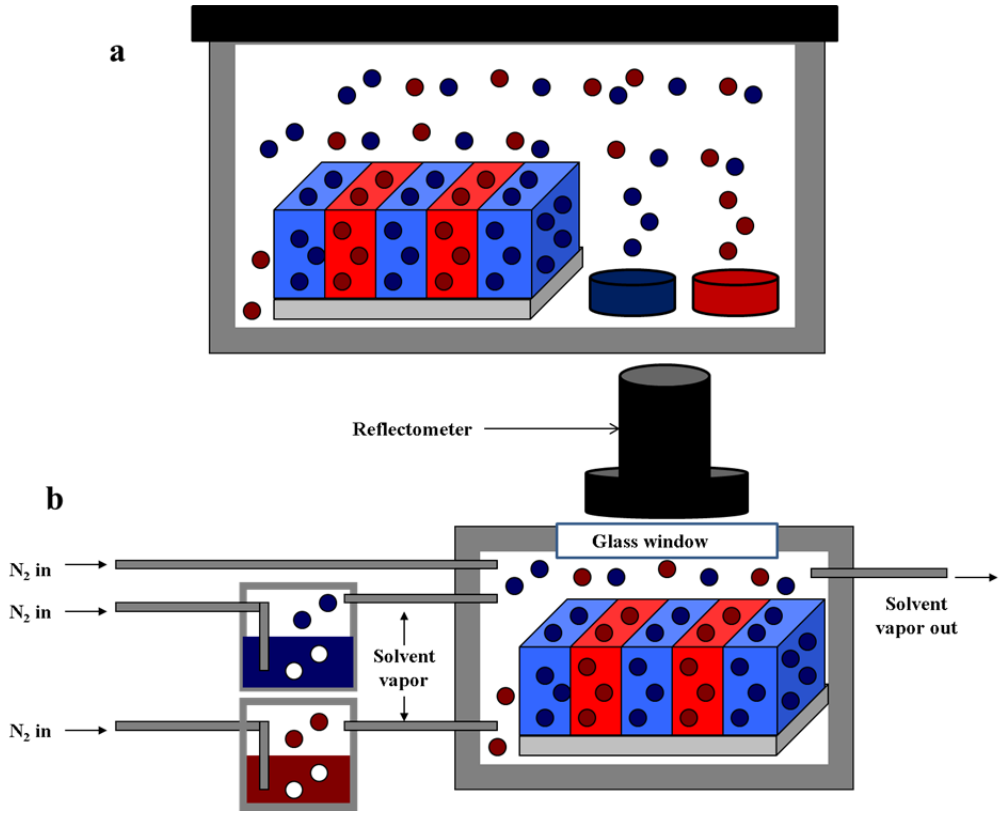


**Figure 1.12:** Different solvent annealing chambers used for annealing experiments. a) Early experiments were typically performed in a tightly-sealed jar or other closed container with the thin film and open vials of solvent. b) Now, experiments are usually performed in an environment where the pressure of the chamber and vapor composition are controlled by the flow rate of nitrogen into the chamber and the film thickness is monitored through a window in the chamber. Figures not drawn to scale. Figure adapted with permission.[47]

### 1.4 Directed Self-Assembly

For proper device function, there is low tolerance with regard to size, roughness, and placement defects of the features in lithographically defined patterns.[48] Unfortunately, BCP line and dot patterns in thin films exhibit placement defects without implementing alignment techniques during the annealing process. Line patterns tend to adopt a "fingerprint" in-plane orientation with significant curvature among the BCP

domains and dot patterns typically have good short-range but poor long-range hexagonal order. Long-range order and specified domain placement can be improved by directed self-assembly (DSA), most often with sparse lithographically pre-defined patterns. These prepatterns either induce alignment of the BCP within a confined topographic relief structure (graphoepitaxy) or are designed to have sparse chemically distinct surface regions that induce alignment of the BCP on top of them from the chemical contrast. Several other methods such as application of an electric field,[49] salt complexation with solvent annealing,[50] substrate roughening,[51] and application of thermal gradients[52] have also been explored as alignment strategies.

### 1.4.1 Graphoepitaxy

When confined within a topographical relief structure, the lateral alignment of BCP domains is influenced by effectively adding interfaces perpendicular to the plane of the BCP film. By controlling the surface chemistry of these new interfaces, the in-plane alignment and vertical orientation of a BCP line pattern can be controlled.[53] An example of this type of prepattern and the consequences of different trench and substrate surface chemistries for a lamellae-forming BCP is shown in **Figure 1.13**. The long-range order of a hexagonally-packed dot pattern, in the case of spheres, can be improved similarly by patterning posts and appropriately altering their surface chemistry.[54] Some topographic directing patterns can be generated by the relatively inexpensive photolithographic process since the trenches are typically patterned on the tens of nm to micron scale, which could limit application of graphoepitaxy in large-area, high feature density patterning. This is because the lateral area outside the trench does not direct the BCP pattern.

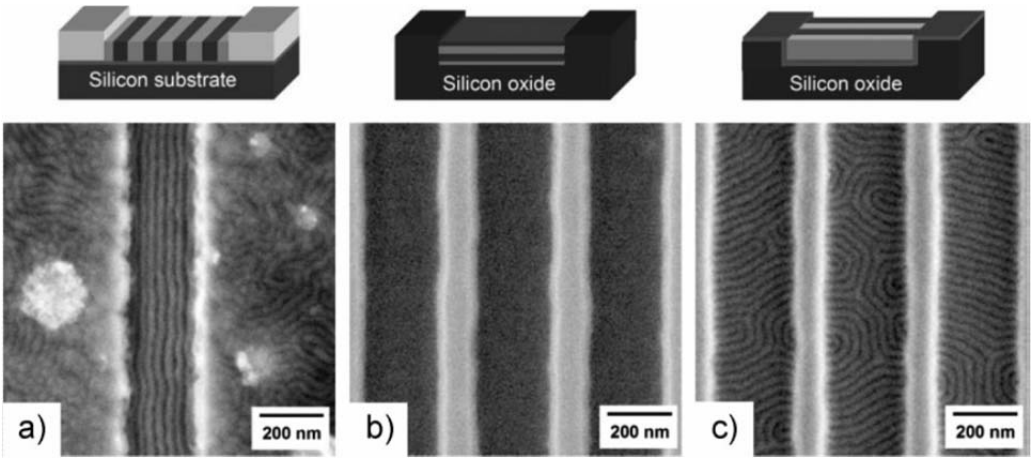


**Figure 1.13:** Examples of different alignments of a lamellae-forming BCP confined within a trench with different side wall chemistries. a) Nonpreferential (neutral) substrate and preferential trench walls. b) Preferential substrate and nonpreferential trench walls. c) Nonpreferential substrate and nonpreferential trench walls. From [52] Copyright © 2007 WILEY-VCH Verlag GmbH & Co. KGaA, Weinheim. Reprinted with permission.

### 1.4.2 Chemical Contrast Patterns

Chemical contrast patterns are another type of guiding pattern that are often used to direct the self-assembly of BCPs. Unlike topographical relief structures, these guiding patterns are topographically homogeneous and do not greatly reduce the lateral area available on the substrate for device structures. However, they require a prepattern created by electron beam, nanoimproint, or photolithography. The expense of making the prepattern can be reduced by using a sparse array of guiding structures that rectify the BCP domain defectivity, decreasing the time required to create the e-beam pattern and thus the cost of the prepattern.[16, 55] Sparse lines of a cross-linked polymer are created by e-beam patterning of a photoresist and removing sections of the exposed resist and the underlying cross-linked polymer to expose the substrate. The exposed substrate is then filled with a polymer brush with a slightly different chemistry than the cross-linked

polymer and any remaining photoresist is removed.[56] A diagram of this process is shown in **Figure 1.14**.

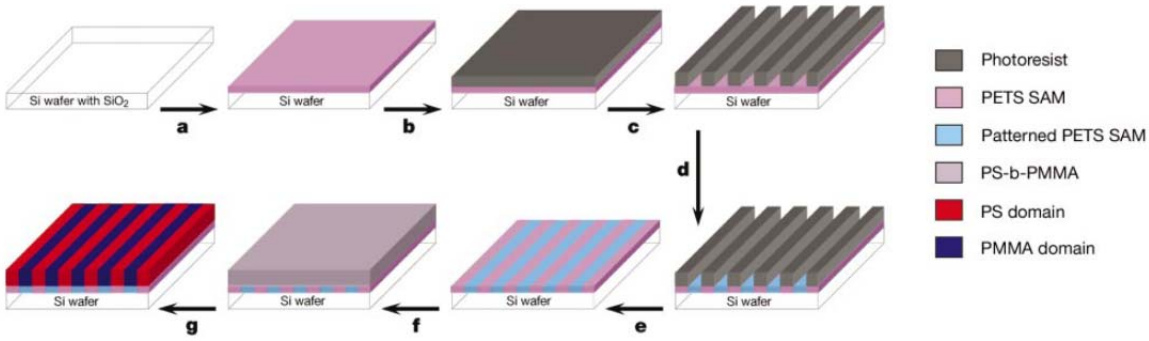


**Figure 1.14:** Schematic representation of the strategy used to create chemically nanopatterned surfaces and investigate the epitaxial assembly of block-copolymer domains. a) A self-assembled monolayer (SAM) of phenylethyltrichlorosilane (PETS) was deposited on a silicon wafer. b) Photoresist was spin-coated on the SAM-covered substrate, and c) patterned by EUV-IL with alternating lines and spaces of period $L_s$. d) The topographic pattern in the photoresist was converted to a chemical pattern on the surface of the SAM by irradiating the sample with soft X-rays in the presence of oxygen. e) The photoresist was then removed with repeated solvent washes. f) A symmetric, lamella-forming PS-*b*-PMMA copolymer of period $L_o$ was spin-coated onto the patterned SAM surface and g) annealed, resulting in surface-directed block-copolymer morphologies. Reprinted by permission from Macmillan Publishers Ltd: Nature [55] copyright 2003.

A BCP will align on top of the sparse prepattern when the appropriate chemical contrast of the pattern is present, the areal ratio of the different surface chemistries is correct, and the pitch of the prepattern exactly matches an integer multiple of the BCP (**Figure 1.15**). Chemical contrast patterns are generally preferred over graphoepitaxy since lateral area is not compromised and they typically reduce issues with the translational order of the domains that arise with graphoepitaxy.

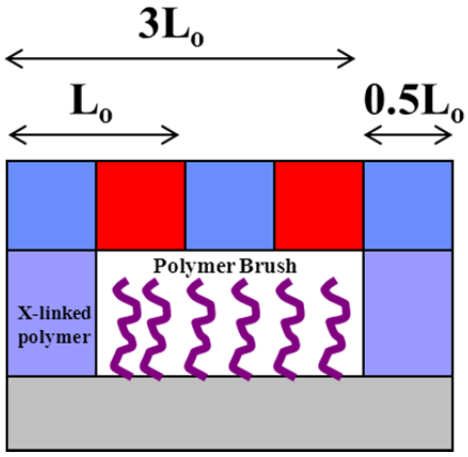


**Figure 1.15:** Example of the ideal dimensions of a chemical contrast prepattern used to induce alignment of a BCP on top of it. The prepattern should have a pitch that is an integer multiple of the BCP $L_o$ and the width of the line should be commensurate with 0.5 $L_o$ for optimal alignment.

### 1.5 PATTERN TRANSFER

BCPs have several similarities to photoresists that have been selectively exposed to light through a mask in that the individual domains can have different degradation characteristics and/or dry etch rates, making the transfer of their periodic structures possible by dry or wet etching techniques. Many examples of wet and dry etching processes used to transfer block copolymer patterns into substrates or hard masks exist in the literature. However dry etching is often the preferred method since wet etching techniques can lead to pattern collapse due to capillary forces in patterns with small features.[25]

The first demonstration of BCP pattern transfer used self-assembled poly(styrene-*block*-butadiene) spheres to pattern hexagonally-packed dot structures into silicon nitride.[22] Since this first demonstration, lines, posts, and holes have also been transferred into substrates. In recent work, a second patterning step was used to cut BCP lines into

rectangular structures desirable for magnetic media patterning that were subsequently transferred into the substrate.[25]

A typical dry reactive ion etch process first uses etch contrast between the domains to selectively remove one domain that is either inherent to the BCP system or added by a domain-selective modification step. A second etch step is then used to etch the substrate exposed by the removed polymer. The etch steps rely on either oxygen- or fluorine-based reactive gases to selectively remove materials. With fully organic materials, this inherent etch contrast is usually low and additional processing steps are required to modify one domain to generate high aspect ratio features. Several examples of these modification processes include selectively staining, i.e. embedding a slowly etching component into one domain,[22, 51, 57] and atomic layer deposition.[58, 59] Ideally, a high inherent etch contrast between the two domains should exist to facilitate the creation of high aspect ratio features in as few processing steps as possible. This has been one of the primary motivations for the synthesis of the new silicon-containing BCPs described in this work.

### 1.6 Inorganic-Containing Block Copolymers

Previous research has shown that incorporating a sufficient amount of silicon[60] or metal into one block creates an inorganic oxide etch mask when exposed to oxygen plasma. Materials such as poly(lactide-*b*-dimethylsiloxane-*b*-lactide) (PLA-*b*-PDMS-*b*-PLA),[61] poly(styrene-*b*-dimethylsiloxane) (PS-*b*-PDMS),[62] poly(styrene-*b*-ferrocenylsilane) (PS-*b*-PFS),[63] and polyhedral oligomeric silsesquioxane-containing polymers (PS-*b*-PMAPOSS)[64] demonstrate high etch contrast due to their inorganic components, which form inorganic oxides during an oxygen dry etch step, while the organic block is simultaneously removed.

An additional advantage of materials with inorganic components is that they often have higher interaction parameters than fully organic materials. This allows them to self-assemble into remarkably small structures,[64, 65] which is an important criterion for selection of an ideal BCP for lithography in the pursuit of Moore's law. However, due to the low surface energy of inorganic-containing polymers, they are very difficult to orient perpendicular to the substrate because the inorganic-containing block preferentially wets the air interface.[66] Until now, the inability to orient these polymers perpendicular to the plane of the substrate has limited their utility in lithography.

The increased etch contrast and interaction parameter of inorganic-containing materials served as the primary motivations for the work in the following chapters. Because of its prevalence and compatibility with current semiconductor manufacturing processes, silicon was chosen as the inorganic component for these new materials. Before this work, only a few silicon-containing materials had been synthesized and explored for lithographic applications with limited success in orientation control.

## 1.7 REFERENCES


1. DynaTAC8000X. Wikimedia Commons. (2008)
2. Z. Vega. IPhone 5. Wikimedia Commons. (2012)
3. R. de Rijcke. IBM PC 5150. Wikimedia Commons. (2010)
4. T. Malabuyo. MacBook Air black. Wikimedia Commons. (2008)
5. Transistor Count and Moore's Law. Wikimedia Commons. (2011)
6. G. E. Moore, *Solid-State Circuits Society Newsletter, IEEE* **2006,** *11*, 33-35.
7. C. Walter, *Scientific American* **2005**, 32-33.
8. G. Robinson, *EE Times* **2000,** *26*.
9. R. A. Athale; G. W. Euliss; J. N. Mait, *Proceedings of SPIE* **2008,** *6978*, H1-H5.
10. R. Jaeger, *Introduction to Microelectronic Fabrication*. 2nd ed.; Prentice Hall: 2002.
11. Photolithography etching process. Wikimedia Commons.
12. B. J. Lin, *Journal of Microlithography Microfabrication and Microsystems* **2004,** *3*, 377-395.
13. B. l. Fontaine, *SPIE Professional* **2010**, 20.

14. C. W. Gwyn; R. Stulen; D. Sweeney; D. Attwood, *Journal of Vacuum Science & Technology B* **1998,** *16*, 3142-3149.
15. M. M. Greve; B. Holst, *Journal of Vacuum Science & Technology B: Microelectronics and Nanometer Structures* **2013,** *31*, 043202-043208.
16. R. Ruiz; H. M. Kang; F. A. Detcheverry; E. Dobisz; D. S. Kercher; T. R. Albrecht; J. J. de Pablo; P. F. Nealey, *Science* **2008,** *321*, 936-939.
17. F. Hua; Y. G. Sun; A. Gaur; M. A. Meitl; L. Bilhaut; L. Rotkina; J. F. Wang; P. Geil; M. Shim; J. A. Rogers; A. Shim, *Nano Letters* **2004,** *4*, 2467-2471.
18. H.-C. Kim; S.-M. Park; W. D. Hinsberg, *Chemical Reviews* **2010,** *110*, 146-177.
19. F. S. Bates; G. H. Fredrickson, *Annual Review of Physical Chemistry* **1990,** *41*, 525-557.
20. F. S. Bates; G. H. Fredrickson, *Physics Today* **1999,** *52*, 32-38.
21. R. A. Segalman, *Materials Science and Engineering: R: Reports* **2005,** *48*, 191-226.
22. M. Park; C. Harrison; P. M. Chaikin; R. A. Register; D. H. Adamson, *Science* **1997,** *276*, 1401-1404.
23. M. A. Hillmyer, Nanoporous materials from block copolymer precursors. In *Block Copolymers II*, Abetz, V., Ed. 2005; Vol. 190, pp 137-181.
24. G. J. Liu; J. F. Ding; T. Hashimoto; K. Kimishima; F. M. Winnik; S. Nigam, *Chemistry of Materials* **1999,** *11*, 2233-2240.
25. R. Ruiz; E. Dobisz; T. R. Albrecht, *ACS Nano* **2011,** *5*, 79-84.
26. W. K. Li; S. Yang, *Journal of Vacuum Science & Technology B* **2007,** *25*, 1982-1984.
27. W. Zheng; Z.-G. Wang, *Macromolecules* **1995,** *28*, 7215-7223.
28. V. P. Chuang; J. Gwyther; R. A. Mickiewicz; I. Manners; C. A. Ross, *Nano Letters* **2009,** *9*, 4364-4369.
29. J. G. Son; J. Gwyther; J.-B. Chang; K. K. Berggren; I. Manners; C. A. Ross, *Nano Letters* **2011,** *11*, 2849-2855.
30. K. Asakawa; T. Hiraoka; H. Hieda; M. Sakurai; Y. Kamata, *Journal of Photopolymer Science and Technology* **2002,** *15*, 465-470.
31. S. P. Delcambre; R. A. Riggleman; J. J. de Pablo; P. F. Nealey, *Soft Matter* **2010,** *6*, 2475-2483.
32. S. Park; J.-Y. Wang; B. Kim; J. Xu; T. P. Russell, *ACS Nano* **2008,** *2*, 766-772.
33. G. Kim; M. Libera, *Macromolecules* **1998,** *31*, 2569-2577.
34. J. N. L. Albert; T. H. Epps III, *Materials Today* **2010,** *13*, 24-33.
35. E. W. Edwards; M. P. Stoykovich; H. H. Solak; P. F. Nealey, *Macromolecules* **2006,** *39*, 3598-3607.
36. D. Y. Ryu; K. Shin; E. Drockenmuller; C. J. Hawker; T. P. Russell, *Science* **2005,** *308*, 236-239.
37. C. M. Bates; J. R. Strahan; L. J. Santos; B. K. Mueller; B. O. Bamgbade; J. A. Lee; J. M. Katzenstein; C. J. Ellison; C. G. Willson, *Langmuir* **2011,** *27*, 2000-2006.
38. P. Mansky; Y. Liu; E. Huang; T. P. Russell; C. J. Hawker, *Science* **1997,** *275*, 1458-1460.

39. R. Guo; E. Kim; J. Gong; S. Choi; S. Ham; D. Y. Ryu, *Soft Matter* **2011,** *7*, 6920-6925.
40. E. Huang; T. P. Russell; C. Harrison; P. M. Chaikin; R. A. Register; C. J. Hawker; J. Mays, *Macromolecules* **1998,** *31*, 7641-7650.
41. C. M. Bates; T. Seshimo; M. J. Maher; W. J. Durand; J. D. Cushen; L. M. Dean; G. Blachut; C. J. Ellison; C. G. Willson, *Science* **2012,** *338*, 775-779.
42. T. P. Lodge; B. Pudil; K. J. Hanley, *Macromolecules* **2002,** *35*, 4707-4717.
43. M. Y. Paik; J. K. Bosworth; D. M. Smilges; E. L. Schwartz; X. Andre; C. K. Ober, *Macromolecules* **2010,** *43*, 4253-4260.
44. J. N. L. Albert; T. D. Bogart; R. L. Lewis; K. L. Beers; M. J. Fasolka; J. B. Hutchison; B. D. Vogt; T. H. Epps, *Nano Letters* **2011,** *11*, 1351-1357.
45. Y. S. Jung; C. A. Ross, *Advanced Materials* **2009,** *21*, 2540-2545.
46. M. Vayer; M. A. Hillmyer; M. Dirany; G. Thevenin; R. Erre; C. Sinturel, *Thin Solid Films* **2010,** *518*, 3710-3715.
47. J. Cushen; L. Wan; G. Pandav; I. Mitra; G. Stein; V. Ganesan; R. Ruiz; C. G. Willson; C. J. Ellison, *Journal of Polymer Science Part b* **2013,** *in press*.
48. I. Koren; Z. Koren, *Proceedings of the IEEE* **1998,** *86*, 1819-1838.
49. T. Thurn-Albrecht; J. Schotter; G. A. Kästle; N. Emley; T. Shibauchi; L. Krusin-Elbaum; K. Guarini; C. T. Black; M. T. Tuominen; T. P. Russell, *Science* **2000,** *290*, 2126-2129.
50. S. H. Kim; M. J. Misner; L. Yang; O. Gang; B. M. Ocko; T. P. Russell, *Macromolecules* **2006,** *39*, 8473-8479.
51. S. Park; D. H. Lee; J. Xu; B. Kim; S. W. Hong; U. Jeong; T. Xu; T. P. Russell, *Science* **2009,** *323*, 1030-1033.
52. B. C. Berry; A. W. Bosse; J. F. Douglas; R. L. Jones; A. Karim, *Nano Letters* **2007,** *7*, 2789-2794.
53. S. M. Park; M. P. Stoykovich; R. Ruiz; Y. Zhang; C. T. Black; P. E. Nealey, *Advanced Materials* **2007,** *19*, 607-611.
54. I. Bita; J. K. W. Yang; Y. S. Jung; C. A. Ross; E. L. Thomas; K. K. Berggren, *Science* **2008,** *321*, 939-943.
55. J. Y. Cheng; C. T. Rettner; D. P. Sanders; H.-C. Kim; W. D. Hinsberg, *Advanced Materials* **2008,** *20*, 3155-3158.
56. S. O. Kim; H. H. Solak; M. P. Stoykovich; N. J. Ferrier; J. J. de Pablo; P. F. Nealey, *Nature* **2003,** *424*, 411-414.
57. D. Zschech; D. H. Kim; A. P. Milenin; R. Scholz; R. Hillebrand; C. J. Hawker; T. P. Russell; M. Steinhart; U. Gosele, *Nano Letters* **2007,** *7*, 1516-1520.
58. S. J. Jeong; G. D. Xia; B. H. Kim; D. O. Shin; S. H. Kwon; S. W. Kang; S. O. Kim, *Advanced Materials* **2008,** *20*, 1898-1904.
59. S. J. Ku; G. C. Jo; C. H. Bak; S. M. Kim; Y. R. Shin; K. H. Kim; S. H. Kwon; J.-B. Kim, *Nanotechnology* **2013,** *24*, 085301.
60. M. Colburn; A. Grot; M. Amistoso; B. J. Choi; T. Bailey; J. Ekerdt; S. V. Sreenivasan; S. Hollenhorst; C. G. Willson, Step and flash imprint lithography for sub-

100nm patterning. In *Emerging Lithographic Technologies IV*, Dobisz, E. A., Ed. Spie-Int Soc Optical Engineering: Bellingham, 2000; Vol. 3997, pp 453-457.
61. M. D. Rodwogin; C. S. Spanjers; C. Leighton; M. A. Hillmyer, *ACS Nano* **2010,** *4*, 725-732.
62. Y. S. Jung; C. A. Ross, *Nano Letters* **2007,** *7*, 2046-2050.
63. V. P. Chuang; C. A. Ross; J. Gwyther; I. Manners, *Advanced Materials* **2009,** *21*, 3789-3793.
64. T. Hirai; M. Leolukman; C. C. Liu; E. Han; Y. J. Kim; Y. Ishida; T. Hayakawa; M.-a. Kakimoto; P. F. Nealey; P. Gopalan, *Advanced Materials* **2009,** *21*, 4334-4338.
65. E. W. Cochran; D. C. Morse; F. S. Bates, *Macromolecules* **2003,** *36*, 782-792.
66. C. A. Ross; Y. S. Jung; V. P. Chuang; F. Ilievski; J. K. W. Yang; I. Bita; E. L. Thomas; H. I. Smith; K. K. Berggren; G. J. Vancso; J. Y. Cheng In *Si-containing block copolymers for self-assembled nanolithography*, AVS: 2008; pp 2489-2494.

# Chapter 2: Poly(Styrene-*block*-Methyltrimethylsilylmethacrylate) and Poly(Styrene-*block*-Trimethylsilylstyrene-*block*-Styrene)

As discussed in Chapter 1, in the pursuit of lithographic patterns with small features, there is a need to design new BCP systems that have high interaction parameters so they self-assemble into small structures. Good inherent etch contrast in these materials is also desirable so the BCP pattern can be easily transferred to a substrate using as few processing steps as possible. For reasons discussed in Section 1.8, the focus of this dissertation is on the design and synthesis of new silicon-containing materials and subsequent protocols to align and process them in thin films. Since orientation control is often the most challenging step in processing BCPs for lithography, I first chose to study materials that I had reason to believe would be less challenging to orient in thin films.

PS-*b*-PMMA remains the most heavily studied BCP for patterning applications. Since there is a wealth of literature addressing strategies for controlling the orientation of this material in thin films,[1, 2] it was a reasonable starting point to design a material that overcomes PS-*b*-PMMA's low $\chi$ and etch contrast disadvantages but that is structurally similar in hopes that the same orientation control strategies would work with the new material. Since it has been shown that silicon-containing polymers often have high $\chi$-parameters[3, 4] as well as good etch contrast,[5] I investigated whether a silicon-containing analogue to PS-*b*-PMMA would self-assemble into sub-21 nm pitch structures, the relatively large minimum achievable pitch of PS-*b*-PMMA due to its low $\chi$-parameter.[6] Based on these criteria, I synthesized a modified poly(styrene-*block*-methyltrimethylsilylmethacrylate), PS-*b*-PMTMSMA, which has a trimethylsilyl group on the PMMA repeat unit but is otherwise identical in structure to PS-*b*-PMMA. Christopher Bates and Morgan Schulze played key roles in development of the anionic polymerization techniques and synthesis protocols for this material and my colleagues

performed the thin film orientation studies presented in Section 2.2.1. Details on the synthesis and characterization of PS-*b*-PMTMSMA are presented here since the synthesis and characterization I performed was a large part of the work that went into the $\chi$-parameter analysis detailed in Chapter 6.

It has also been shown that perpendicular orientation of symmetric ABA triblock copolymers (which self-assemble into the same morphologies as diblock copolymers), is easier to achieve when the low surface energy block is the middle block for reasons detailed in **Figure 2.1**.[7-9] Orientation control is a formidable challenge with silicon-containing materials since the very low surface-energy silicon-containing block strongly wets the air interface during thermal annealing. This motivated the synthesis of a silicon-containing symmetric triblock copolymer, poly(styrene-*block*-trimethylsilylstyrene-*block*-styrene), or PS-*b*-PTMSS-*b*-PS, which has the low surface energy PTMSS block in the middle in hopes that perpendicular orientation would be more easy to implement. A second motivation behind the selection of this material was that PTMSS is not chemically or structurally much different from PS, which I believed could decrease the challenges with orientation control. I developed the synthesis protocols for this material from methods based on previous work[10, 11] and conducted the interaction parameter studies described in Chapter 6. My colleagues pioneered the thin film self-assembly and orientation control discussed in Section 2.2.2.

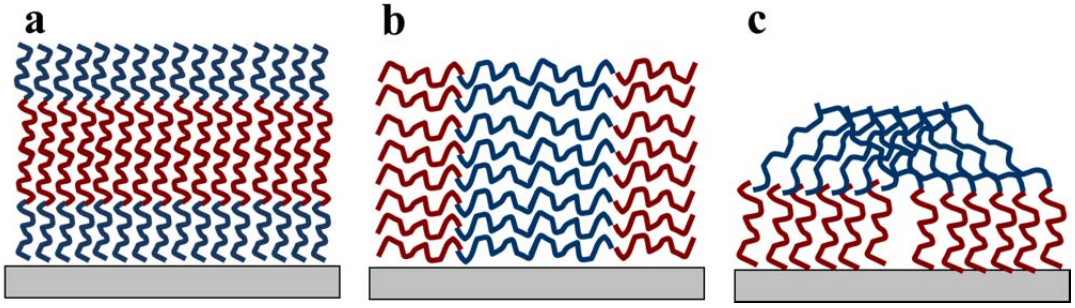


**Figure 2.1:** Possible orientations of ABA triblock copolymer chains in a thin film where the blue block is the low surface energy block that prefers to wet the air interface. Substrate effects are neglected. a) Most likely orientation of the ABA triblock copolymer when the low surface energy block is the A block, resulting in parallel orientation of the domains. b) Most likely orientation of an ABA triblock copolymer when the low surface energy block is the middle block, resulting in perpendicular orientation. c) Unlikely parallel orientation of an ABA triblock copolymer when the low surface energy block is the B block due to energetic penalties from chain stretching.

## 2.1 Synthesis by Anionic Polymerization

Anionic polymerization is a living polymerization technique, whereby one initiator molecule initiates one living chain and monomer units add without termination or reinitiating events. For this reason, conversion goes nearly to completion and targeted molecular weights and compositions are generally easy to attain. Anionic polymerization is often used to synthesize block copolymers since monomers of different types can be sequentially added to form the blocks without intermediate isolation and reinitiation steps between each block polymerization. It is versatile with styrene and acrylate monomers and can produce polymers with a low chain length distribution or polydispersity index (PDI). The living anions are extremely sensitive to termination or coupling events in the presence of water, oxygen, or other impurities, and therefore the technique requires special glassware and purification techniques. Great care must be taken to remove these

impurities from monomers, solvents, and reaction vessels before proceeding with the reaction.[12]

The components of an anionic polymerization include an anionic initiator, a solvent, the monomer being polymerized, and a terminating agent.[13] While several initiators exist for various monomer types, *sec*-butyllithium (a monofunctional initiator) and potassium naphthelanide (a difunctional initiator) are common initiators for diblock and symmetric triblock styrene BCP polymerizations, respectively. The solvent chosen must be miscible with any monomers added to the reaction mixture, the polymers produced from the polymerization, and the initiator. Common anionic polymerization solvents include cyclohexane and tetrahydrofuran (THF). Methanol is a common hydrogen-donating terminating agent.

Any dissolved water, oxygen, or other impurities in the monomer and solvent must be removed before polymerization. This is accomplished by high vacuum distillation of the monomer and solvent over a purification agent, which is typically an organometallic compound, before polymerization. An appropriate purification agent for a given monomer or solvent is reactive enough to react with water, oxygen, and impurities from the monomer synthesis process, but is not reactive enough to initiate polymerization. Dibutyl magnesium is a common purification agent for styrene derivatives and calcium hydride is a common purification agent for acrylates. Calcium hydride does not react with acrylate impurities, which must be further titrated with trioctylaluminum. Glassware is subjected to several cycles of pumping and purging with an inert gas to remove oxygen. Water adsorbed to the surface of reaction glassware is removed by flame drying the glassware and pulling vacuum to remove the water vapor that desorbs.[12]

Purified solvent is added to the purged and flame-dried reaction vessel and the initiator is added to the vessel dropwise. A few drops of monomer are added to the initiator solution to "seed" the reaction, converting each initiator to a living anion version of the monomer unit. The rest of the monomer is then slowly added to the vessel and polymerizes. A second chemically distinct monomer can be added upon complete polymerization of the first block to form another block. Once polymerization is complete, the reaction is terminated and end-group functionality can be introduced. Anionic polymers can be functionalized with a hydrogen end group by quenching the reaction with an alcohol such as methanol, however the alcohol must be sparged with an inert gas first to remove oxygen, which would cause chain coupling to occur. In the presence of ethylene oxide, one repeat unit of ethylene oxide will add to styrenic anions with lithium counterions and can be subsequently quenched with methanol to produce a hydroxyl-functionalized styrene polymer.[14] The steps in this process are summarized in **Figure 2.2**.

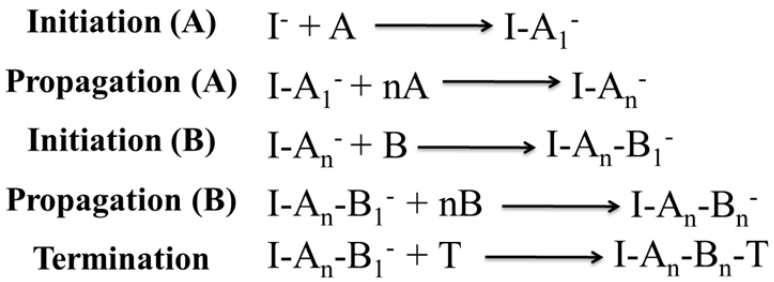


**Figure 2.2:** Steps in synthesizing a block copolymer by anionic polymerization where $I^-$ represents the anionic initiator, A is the A block monomer repeat unit, B is the B block monomer repeat unit, and T is the terminating agent. The associated cations that are paired with the anion are not shown.

The polymers synthesized by anionic polymerization in this work were PS-*b*-PMTMSMA, PS-*b*-PTMSS-*b*-PS, and PTMSSOH homopolymer. The utility of

PTMSSOH as a macroinitiator for other BCP synthesis will be discussed in Chapter 4. The structures of the initiators, solvents, monomers, and terminating agents for the synthesis of these polymers are summarized in **Table 2.1**.

| Polymer | PS-*b*-PMTMSMA | PS-*b*-PTMSS-*b*-PS | PTMSSOH |
|---|---|---|---|
| Initiator |  Sec-butyllithium | 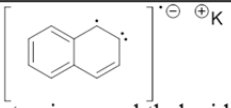 Potassium naphthelanide |  Sec-butyllithium |
| Solvent |  Tetrahydrofuran |  Tetrahydrofuran |  Cyclohexane |
| First Monomer | 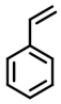 Styrene | 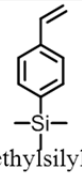 Trimethylsilylstyrene | 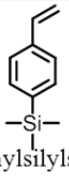 Trimethylsilylstyrene |
| Second Monomer | 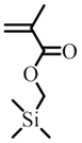 Methyltrimethylsilyl methacrylate | 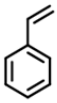 Styrene | N/A |
| Terminating Agent |  Methanol |  Methanol |  Ethylene oxide |

**Table 2.1**: Structures of the reagents used in anionic polymerization of the materials described in this dissertation.

### 2.1.1 PS-*b*-PMTMSMA

MTMSMA monomer is available commercially, making it attractive for polymer synthesis for commercial applications. PS-*b*-PMTMSMA was synthesized by sequential anionic polymerization using similar conditions to PS-*b*-PMMA synthesis.[13] The PS-*b*-PMTMSMA synthesis is shown in **Scheme 2.1**. Ten drops of styrene were added to *sec*-

butyllithium at -78 °C in approximately 250 mL of THF. The reaction was performed at this temperature to prevent the living anions from reacting with the solvent. A 10-fold excess of LiCl was present to maximize control of the MTMSMA block polymerization.[15] The rest of the styrene was added drop-wise and after 4 h, a 5 mL aliquot of PS in solution was carefully extracted from the reactor and terminated with degassed methanol so the molecular weight and PDI of this block could be analyzed. Diphenyl ethylene was added in 5-fold molar excess and reacted for 3 h to endcap each chain with one unit and allow control over the MTMSMA polymerization.[13] Ten drops of MTMSMA were then added to the reactor to seed polymerization of the second block, and after 10 minutes the rest was added and reacted for 3 h, followed by addition of degassed methanol to quench the living anions. The block copolymer was precipitated in methanol, filtered, and dried *in vacuo*.

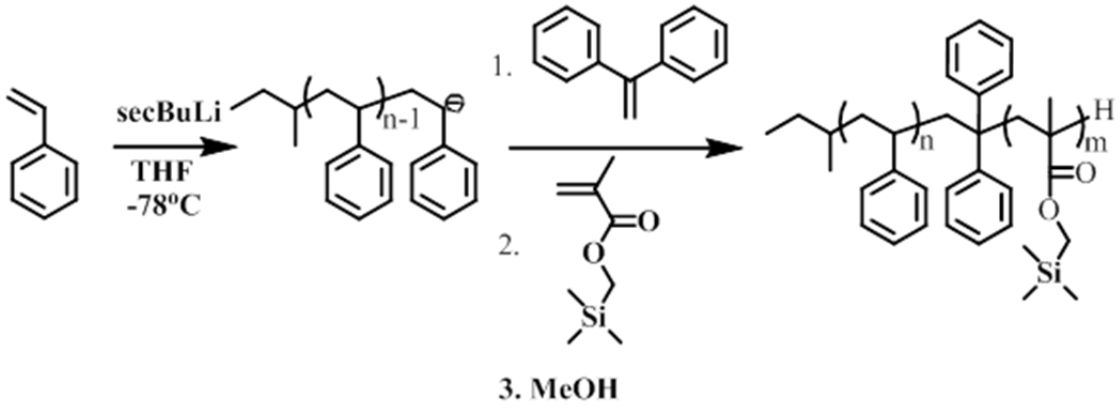


**Scheme 2.1:** Synthesis PS-*b*-PMTMSMA by sequential anionic polymerization

PS-*b*-PMTMSMA block copolymer samples were characterized by a variety of common polymer characterization techniques. The following molecular weight, volume fraction, and morphology data is from $PS_{10.2}$-*b*-$PMTMSMA_{11.5}$, a sample which will be

discussed in Chapter 6, where the subscripts represent the molecular weight of the respective block in kDa. The characterization data that follow are representative of the characterization data analyzed for all the PS-*b*-PMTMSMA samples reported.

The molecular weight and PDI of the PS block and PDI of the PS-*b*-PMTMSMA polymers were characterized by gel permeation chromatography (GPC). Briefly, in GPC, a polymer sample is separated into its different chain lengths by a column of porous material. Larger molecular weight chains elute first and smaller molecular weight chains elute later since they penetrate the smaller pores in the column.[16] This allows a distribution of molecular weights to be established for a given polymer sample, giving rise to a measure of the sample's dispersity. By calibrating the instrument with standards of known molecular weight and dn/dc (change in refractive index with change in concentration), the molecular weight of a polymer can also be determined.[16]

All polymer samples in this dissertation were run on a Viscotek VE 2001 triple-detector GPC. THF was used as the eluent, with a flow rate of 1.0 mL/min. Samples were dissolved in THF (5 mg/mL) before analysis. GPC traces were obtained from the refractive index detector for the PS first block from the aliquot drawn from the reactor after complete styrene polymerization and the block copolymer after the MTMSMA block was added (**Figure 2.3**). **Figure 2.3** shows that the curves are approximately Gaussian and unimodal, indicating that the polydispersity index is low and that there is little if any homopolymer of the first block, from untimely chain termination, or coupling events in the BCP.[16] A large peak shift to the left (to higher molecular weight) indicates that a significant amount of PMTMSMA grew from the living first block after addition of the MTMSMA monomer. Molecular weight data for the PS block and the PDIs of the PS block and BCP were determined using the GPC software.

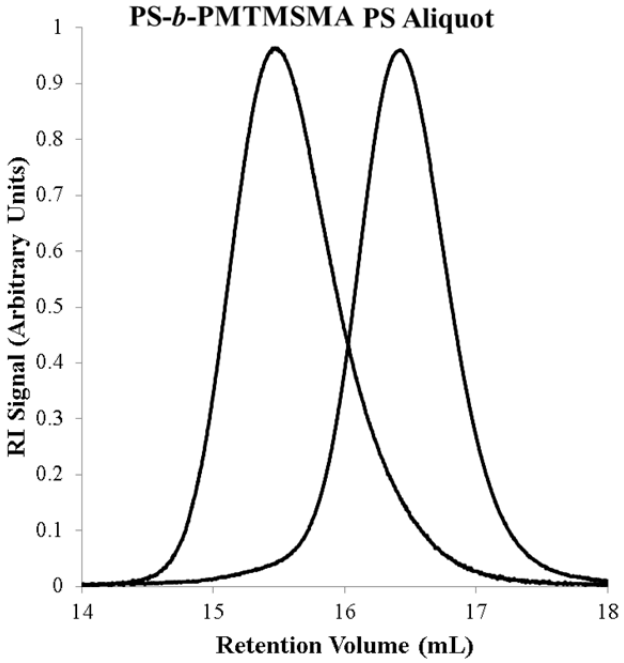


**Figure 2.3:** GPC traces of $PS_{10.2}$-*b*-$PMTMSMA_{11.5}$ and its PS aliquot. Both peaks have low PDIs and a peak shift that indicates the growth of the second block.

Since NMR gives information about the relative numbers of a certain type of hydrogen on a molecule, the block compositions of $PS_{10.2}$-*b*-$PMTMSMA_{11.5}$ were determined by comparing the integrated areas under certain peaks in the representative NMR trace (**Figure 2.4**). Because of their low molecular weight and negligible contribution to the composition, diphenylethylene and the end groups were neglected in this analysis. The mole percentage of the PMTMSMA block was calculated from the ratio of the area under the aromatic peaks (found only in the PS block) to the area under the TMS peak (found only in the PMTMSMA block). Each peak integration was normalized by the number of hydrogen atoms in each group of interest, i.e. 5 aromatic hydrogen atoms in PS and 9 in TMS. Given the molecular weight of the repeat units, the molecular weight of the PS block from the GPC analysis of the aliquot, and the homopolymer densities of each block, this mole percentage was used to calculate the

molecular weight of the PMTMSMA block and the volume fraction in the copolymer. Since the density of PMTMSMA is not reported in the literature, a homopolymer sample was sent for testing. Cambridge Polymer reported that the density of PMTMSMA is 1.02 g/mL.

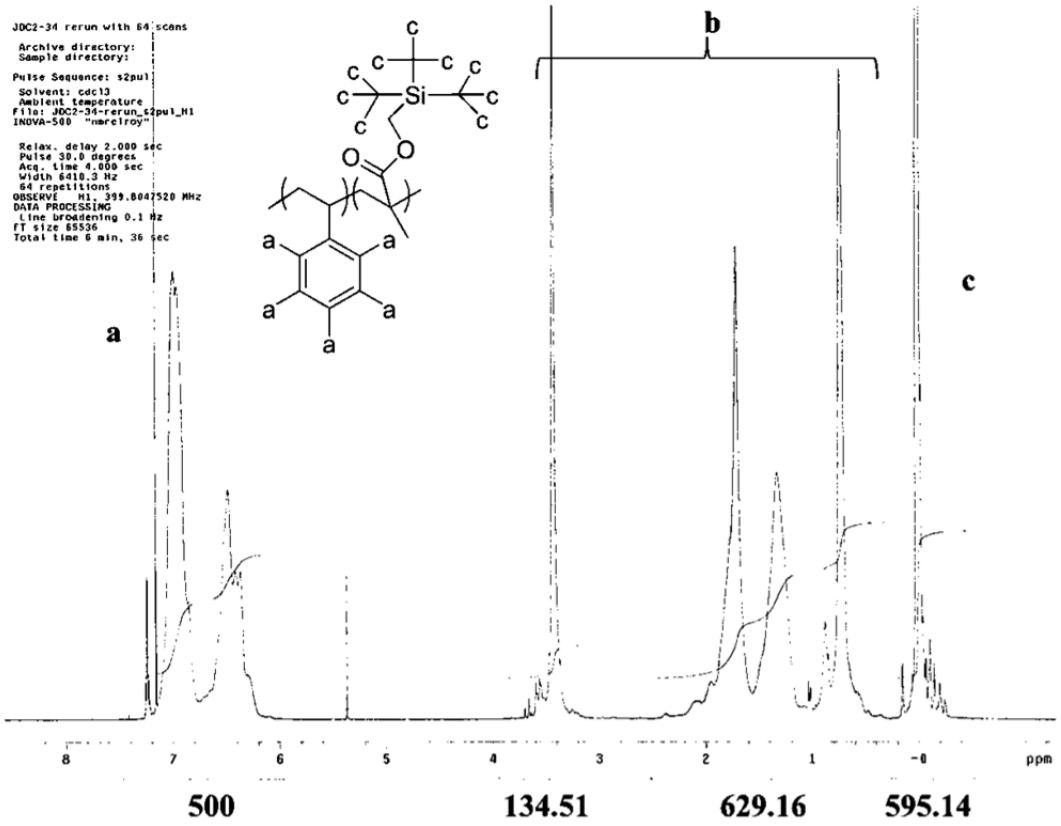


**Figure 2.4:** NMR spectrum used to determine the composition of $PS_{10.2}$-*b*-$PMTMSMA_{11.5}$. By comparing the integration of the TMS peak (c) and the aromatic peak (a) the mole fraction of each block could be determined. Backbone (b) hydrogens are left off on the structure for figure clarity. Diphenylethylene and end groups are neglected.

The thermal properties of a BCP must be known to characterize or process the material in the melt state. The glass transition temperature ($T_g$) of each block must be

known since polymer chains must be heated above this temperature to be in the liquid state and to have enough mobility to reassemble. Bulk characterization is typically performed above the $T_g$s of both blocks so that thermal history of the material is erased and data is collected in an equilibrium state. The degradation temperature ($T_d$) of the polymer should also be characterized so samples are not heated above a temperature that causes thermal decomposition.

The block $T_g$s of the BCP can be identified by differential scanning calorimetry (DSC). DSC experiments were performed for $PS_{60.0}$-*b*-$PMTMSMA_{15.2}$, a sample synthesized by Christopher Bates, on a Mettler Toledo DSC-1 under a nitrogen purge at a heating rate of 10 °C per minute. Data is reported from second heat. A $T_g$ is evidenced by a drop in the heat flow during a temperature scan. From analysis within the software of the DSC trace for $PS_{60.0}$-*b*-$PMTMSMA_{15.2}$ (**Figure 2.5**), only one $T_g$ is observed for the material at around 100 °C. This is likely due to overlap of the $T_g$s of PS and PMTMSMA that the DSC trace cannot distinguish. The DSC data for this specific sample was collected by Christopher Bates.

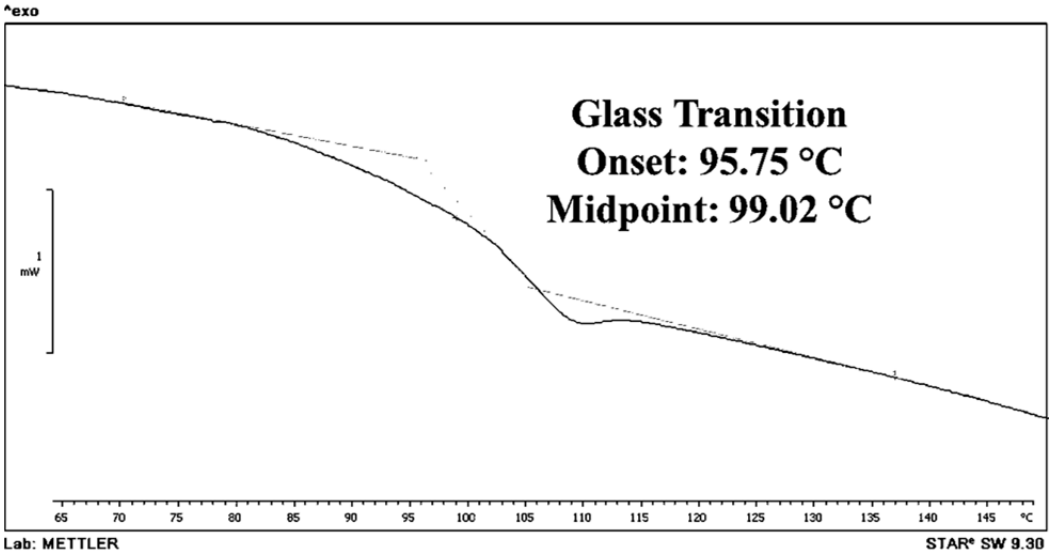


**Figure 2.5:** DSC trace of $PS_{60.0}$-*b*-$PMTMSMA_{15.2}$

The $T_d$ of a polymer can be determined by thermogravimetric analysis (TGA). In TGA experiments, a sample is heated at a specified rate either in an air or inert gas atmosphere and the mass of the sample is monitored. When the polymer begins to degrade, the mass decreases as gaseous degradation products are formed and leave the sample pan. The onset of this mass decrease is typically identified as the $T_d$. TGA experiments were conducted on a Mettler-Toledo TGA/DSC 1 using a ramp rate of 10 °C per minute up to 1000 °C under nitrogen gas. The TGA trace for $PS_{16.8}$-*b*-$PMTMSMA_{20.2}$ is shown in **Figure 2.6**, indicating a $T_d$ of about 300°C, where a rapid increase in weight loss of the sample is observed. This degradation temperature is consistent with what is observed for anionically-synthesized PS[17] and PMMA[18] homopolymers. This particular sample was used for the extensive TGA analysis that follows because it was being annealed at high temperatures for χ-parameter investigations discussed in Chapter 6 during which interesting degradation behavior was observed as described in the following paragraphs.

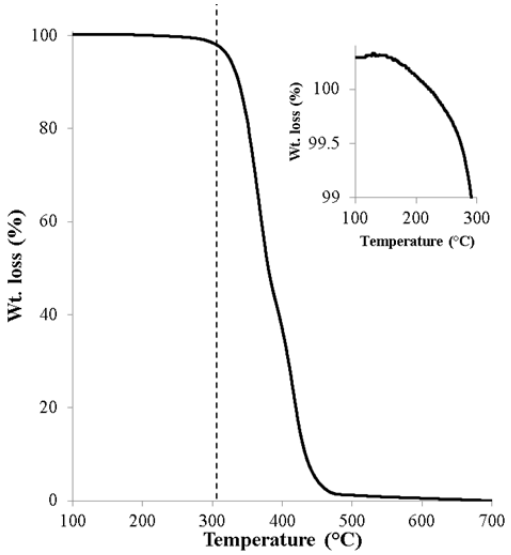


**Figure 2.6:** TGA trace of $PS_{16.8}$-*b*-$PMTMSMA_{20.2}$. The vertical line is present to guide the eye to the rapid weight loss around 300 °C. The inset is an enlarged plot of the weight loss over a temperature range of 100-300 °C.

While a $T_d$ slightly higher than 300 °C was observed by TGA, during rheology experiments (which will be described in Chapter 6), $PS_{16.8}$-*b*-$PMTMSMA_{20.2}$ began bubbling from between the rheometer plates when heated to 300 °C (**Figure 2.7**). It was also observed that the bubbling increased with time at elevated temperature. In the inset of **Figure 2.6**, only a small decrease in mass is observed upon reaching 300 °C, so initially it was not considered that significant degradation events were taking place below this temperature. However, upon NMR analysis of the sample after 5 minutes at 300 °C, a 10% decrease in the TMS peak was observed. I hypothesized that the bubbles could be gaseous TMS degradation product that may contribute too insignificantly to a weight change to observe in TGA. It is also possible that the TMS degradation is a relatively slow process that is not observed in TGA with a high temperature ramp rate. Based on an approximation of 1000 bubbles with a 1-2 mm diameter, I estimated that a total of 5 x $10^{19}$ units of TMS gas would be present in this many bubbles. For a typical 0.5 g rheometer sample of a known molecular weight and volume fraction, 8 x $10^{19}$ TMS units are present in 10% of the polymer. Since these calculations are relatively consistent, it is likely that the bubbles are a result of TMS degradation.

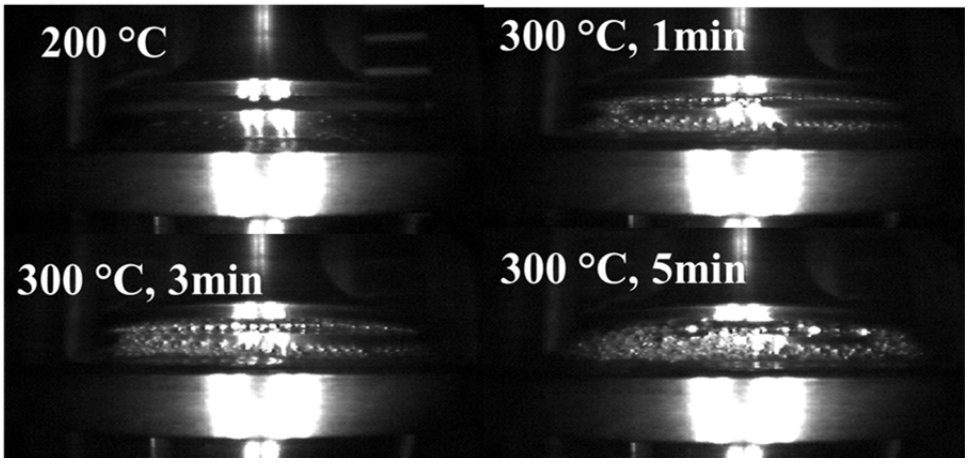


**Figure 2.7:** Pictures obtained from a rheology experiment of $PS_{16.8}$-*b*-$PMTMSMA_{20.2}$ at 200 °C and 300 °C for various times.

To support this hypothesis, additional TGA analysis was performed. An additional temperature ramp from 200-300 °C with a slower ramp rate of 1 °C/min was performed on the sample (**Figure 2.8a**). At this slower rate, although still not very significant, a larger degree of mass loss was observed than in the inset of **Figure 2.6**, supporting the possibility of a slow degradation event. Since very little mass loss was observed below 250 °C in **Figure 2.8a**, a second TGA experiment was performed to investigate the thermal stability of the material at that temperature. The data in **Figure 2.8b** shows the weight loss of the sample when held at 250 °C for 25 minutes, which was less than 0.8% over this time period. Based on this observation, samples were determined to be thermally stable at 250 °C and were subsequently annealed at or below this temperature to avoid degradation.

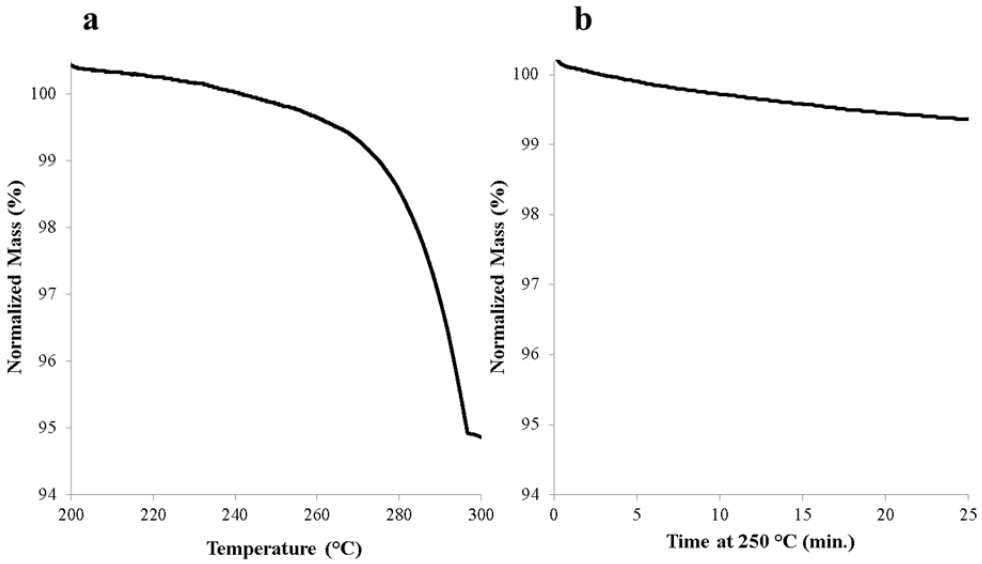


**Figure 2.8:** a) TGA trace of $PS_{16.8}$-*b*-$PMTMSMA_{20.2}$ at a slow (1 °C/min) ramp rate from 200-300 °C. b) TGA trace of $PS_{16.8}$-*b*-$PMTMSMA_{20.2}$ when held at 250 °C for 25 minutes.

Once the thermal properties of the polymer were determined, the bulk morphology could be investigated in the melt state. The bulk morphologies of block copolymers can be determined by small angle x-ray scattering (SAXS). In SAXS, x-rays pass through a material and scatter at very small angles into a diffraction pattern collected by a 2-D detector (**Figure 2.9**). Samples are typically annealed above the $T_g$s of both blocks to remove kinetically-trapped structures from sample preparation and promote self-assembly into the BCP's equilibrium structure. The SAXS pattern from the 2-D detector is then integrated azimuthally and the radial direction indicates the "q" or inverse domain space. Since the scattering properties of a structured material are constant at a given angle, q-space is dependent on the distance the sample is placed from the detector, i.e. at larger sample to detector distances, the same q will be farther from the center of the detector for a given scattering angle. Therefore, the sample to detector distance is calibrated by running a sample with a known domain spacing, often silver behenate, from the same sample to detector distance as the sample of interest. It should also be noted that the sample to detector distance should be optimized for a given domain size of the structured material. If the sample to detector distance is too small, q* (the first-order peak) may end up within the beam stop q-space of the detector (a small lead circle in the center of the detector used to prevent detector saturation from x-rays that are transmitted directly through the sample and not scattered). If the sample to detector distance is too large, q* will be very large and will be outside the detector range. Therefore, some information about the size of the BCP structure should be used to supplement SAXS measurements such as domain spacing from imaging.

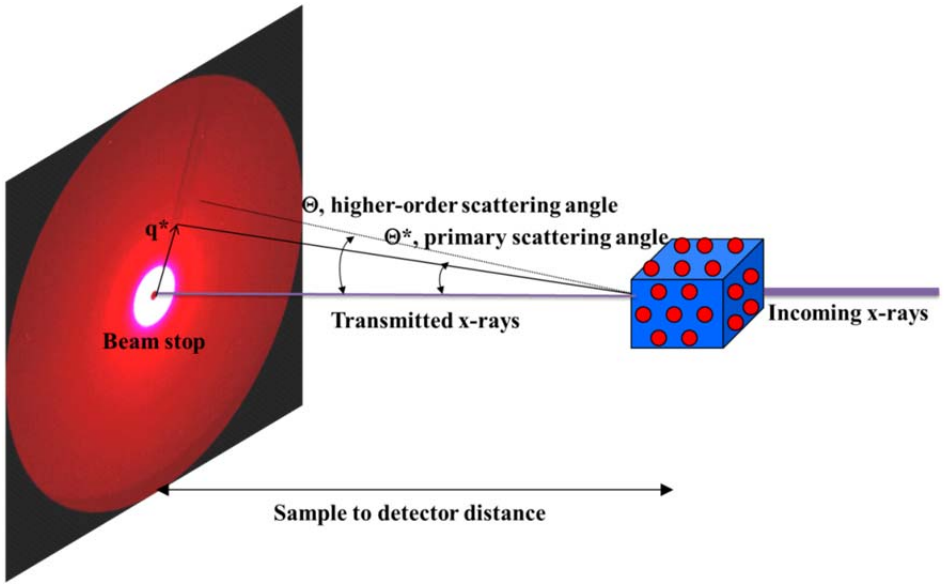


**Figure 2.9:** Scattering of a self-assembled BCP with primary and higher-order scattering intensity.

If the BCP is self-assembled, there will usually be a strong first-order q* peak and one or more higher-order peaks. The distance between the peaks indicates the morphology of the BCP and the location of q* with respect to the origin indicates the domain spacing of the copolymer; the domain spacing is inversely related to q by the relationship $d = 2\pi/q^*$. d is defined as the row spacing for cylindrical BCPs and the spacing of both domains for lamellar BCPs. The $L_o$, the period or pitch, is defined the same as the domain spacing for a lamellar BCP but differently for cylinder BCPs where it is the center-to-center cylinder spacing. (**Figure 2.10**).

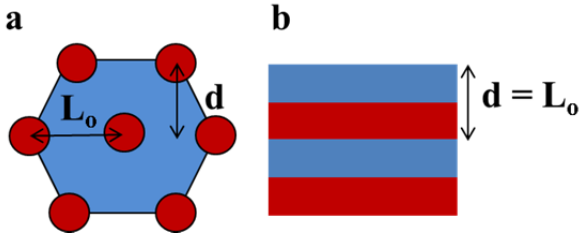


**Figure 2.10:** Domain spacing (d) and pitch ($L_o$) definitions for a) hexagonally packed cylindrical and b) lamellar BCP self-assembly

Different BCP morphologies will scatter x-rays into different distinct peak scattering ratios. The peak scattering ratios of the five common BCP morphologies are summarized in **Table 2.2**.[19]

| Morphology | q/q* |
|---|---|
| **Lamellar** | 1, 2, 3, 4, 5, 6… |
| **Cylindrical** | 1, √3, 2, √7, 3, √12, … |
| **Gyroid** | 1, √4/3, √7/3, √8/3, √10/3, √11/3… |
| **Body-Centered Cubic** | 1, √2, √3, √4, √5, √6… |
| **Face-Centered Cubic** | 1, √4/3, √8/3, √11/3, √12/3√16/3… |

**Table 2.2**: Peak scattering ratios of the common BCP morphologies.

SAXS measurements in this work were collected using Cu-$K_\alpha$ radiation ($\lambda$ = 1.5418 Å) from a Molecular Metrology instrument using a high brilliance rotating copper anode source and a two-dimensional 120 mm gas filled multiwire detector. Vertical focus was achieved with a single crystal Ge mirror and horizontal focus and wavelength selection were controlled with an asymmetric cut Si(111) monochromator. The beam center was calibrated using silver behenate with the primary reflection peak at 1.076 $nm^{-1}$. Scattering data were collected for one hour unless otherwise noted. In the diffraction pattern from the detector and the azimuthally integrated plot of a $PS_{10.2}$-*b*-$PMTMSMA_{11.5}$ (**Figure 2.11**), there was only one scattering peak due to the low resolution of the scattering patterns. Therefore, while we believe this sample is lamellar based on the composition, confirming this would require additional characterization techniques. The

resolution of the SAXS pattern is determined by the x-ray scattering contrast between the two blocks of the copolymer, which is not very high for PS-*b*-PMTMSMA.

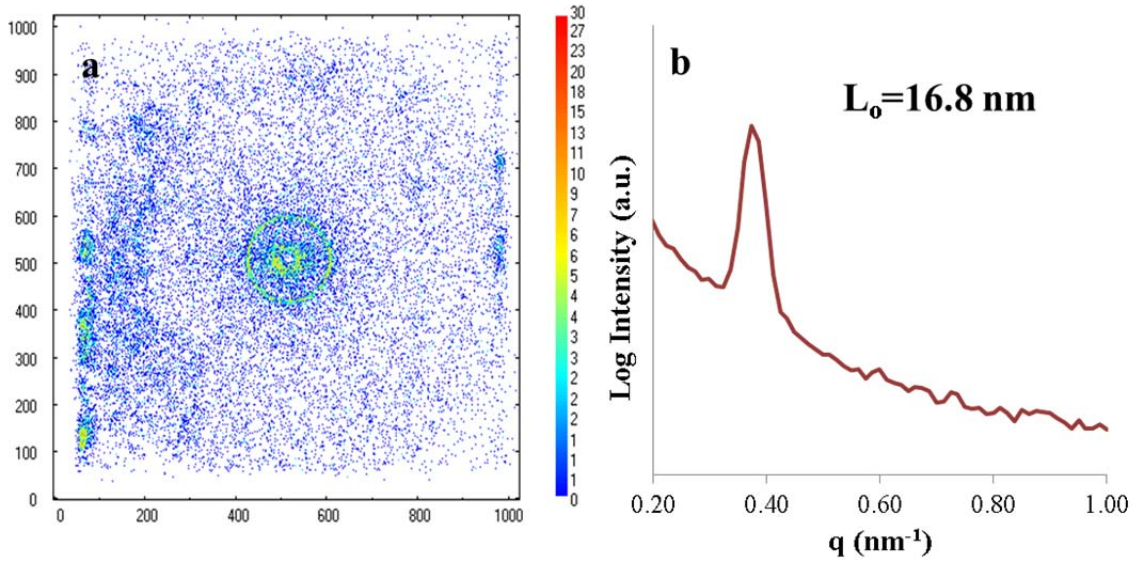


**Figure 2.11:** a) X-ray diffraction pattern obtained for lamellae-forming $PS_{10.2}$-*b*-$PMTMSMA_{11.5}$ from the SAXS detector. b) Two-dimensional pattern obtained after azimuthally integrating the pattern in a).

While many more PS-*b*-PMTMSMA polymer samples will be investigated in Chapter 6, the thin film orientation work in Section 2.2 was performed on a sample whose characterization data is summarized in **Table 2.3**. This cylinder-forming sample, $PS_{60.0}$-*b*-$PMTMSMA_{15.2}$, was synthesized and characterized by Christopher Bates. The subscripts represent the molecular weight of the respective blocks in kDa.

| Sample | PS $M_n$ (kDa) | PS PDI | PMTMSMA $M_n$ (kDa) | BCP PDI | Vol. % PMTMSMA | Morphology (SAXS) | Pitch |
|---|---|---|---|---|---|---|---|
| $PS_{60.0}$-*b*-$PMTMSMA_{15.2}$ | 60.0 | 1.17 | 15.2 | 1.17 | 34.0 | Cylindrical | 60.5 nm |

**Table 2.3**: Characterization data for the $PS_{60.0}$-*b*-$PMTMSMA_{15.2}$ sample used in thin film orientation studies.

### 2.1.2 TMSS Monomer Synthesis

*p*-trimethylsilyl styrene (TMSS) is not available commercially and was therefore synthesized similarly to a literature procedure by a Grignard reaction.[10] Briefly, magnesium shavings (52.6 g, 216.4 mol) were added to a 500 mL flame dried 3-neck round bottom flask. Dry THF (65 mL) was added to the flask. 3 drops of dibromoethane were added to the flask, and then chlorotrimethylsilane (27.37mL, 216.4 mol) was added dropwise. Chlorostyrene (13.0 mL, 108.2 mol) was filtered through alumina to remove inhibitor and then added dropwise to the flask through an addition funnel. The contents of the flask were allowed to react for 12 h and then the reaction was quenched with water. The TMSS product was then isolated and purified by extraction with ether and fractional distillation. The monomer synthesis reaction is shown in **Scheme 2.2**.

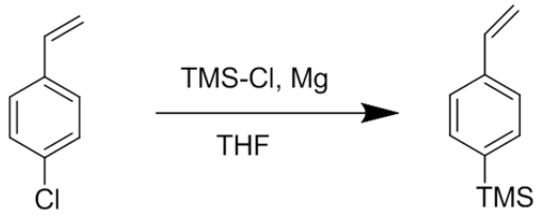


**Scheme 2.2:** Synthesis of TMSS monomer by a Grignard reaction

The purity and reaction success was confirmed by hydrogen nuclear magnetic resonance ($^1$H NMR). NMR experiments were run on a Unity Plus 400 MHz instrument using deuterated chloroform as the solvent. Chemical shifts are reported in ppm downfield from TMS using the residual protonated solvent as an internal standard ($CDCl_3$, $^1$H 7.24 ppm). The areas under the peaks of a $^1$H NMR trace are proportional to the number of hydrogen atoms in a specific location on the molecule, and from this the composition can be determined. The hydrogen peak ratios indicated on the TMSS

monomer closely match the integrated peak ratios obtained from the NMR experiment (**Figure 2.12**), indicating good purity of the monomer.

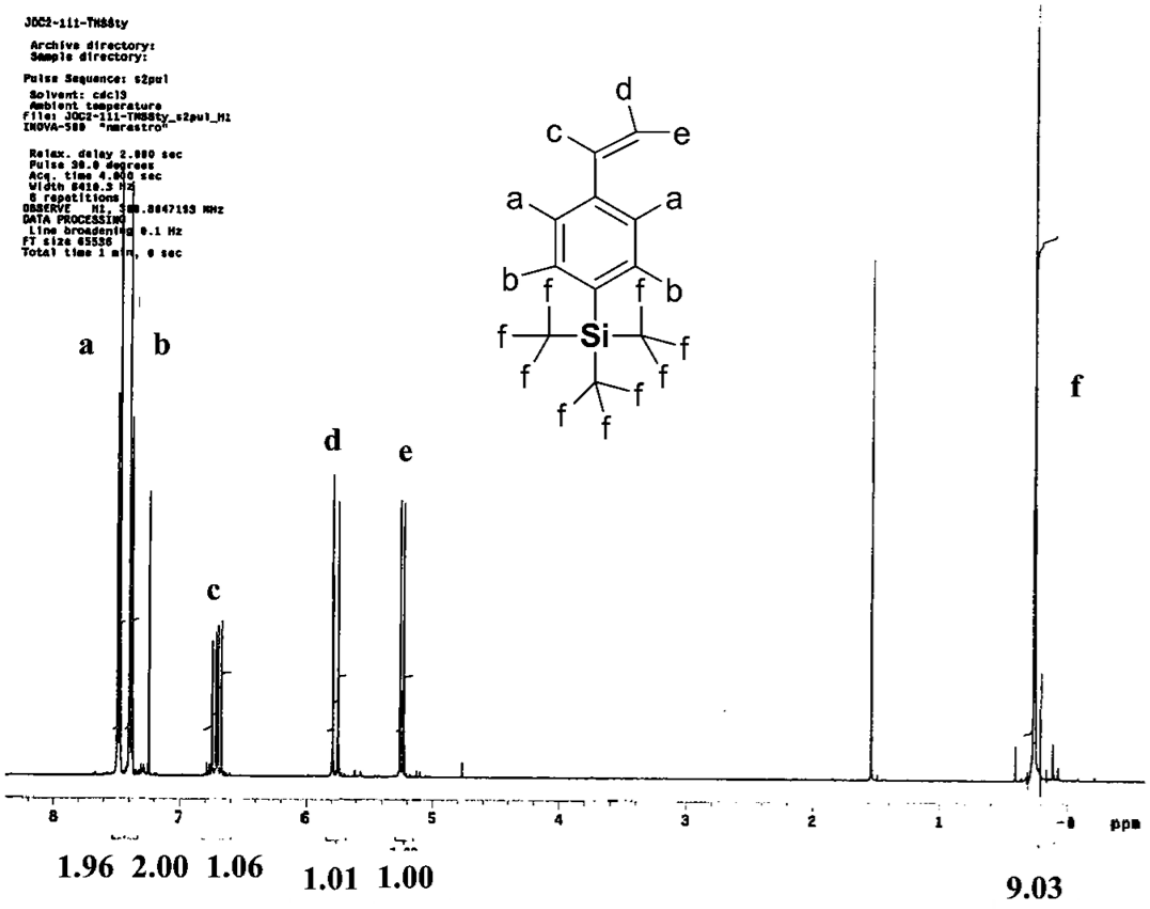


**Figure 2.12:** NMR trace of TMSS monomer showing peak integration agreement with ratios of distinct hydrogens on the TMSS molecule. The peak at approximately 1.5 ppm represents water contamination.

### 2.1.3 PS-*b*-PTMSS-*b*-PS

PS-*b*-PTMSS-*b*-PS was also synthesized by anionic polymerization and characterized similarly to PS-*b*-PMTMSMA. Potassium naphthalenide and an appropriate amount of α-methylstyrene to react 4 monomer units per chain were stirred in THF at -78

°C for ca. 2 hours. TMSS was then added into the reactor while ensuring the reactor internal temperature remained less than -65 °C. After 4 hours, styrene was added dropwise to the reactor. After 4 more hours, methanol was rapidly added into the reaction mixture. The resulting triblock copolymer was precipitated in methanol and filtered to yield a white powder that was dried *in vacuo*. The block copolymer synthesis is shown in **Scheme 2.3**.

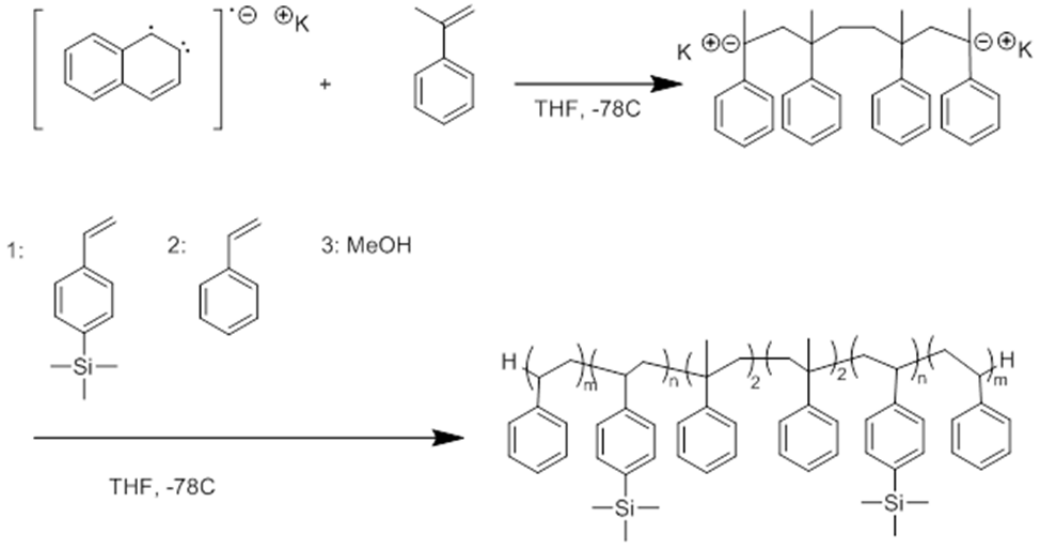


**Scheme 2.3**: Synthesis of PS-*b*-PTMSS-*b*-PS by anionic polymerization.

Representative GPC traces from $PS_{19}$-*b*-$PTMSS_{41}$-*b*-$PS_{19}$ were used to determine the molecular weight and PDI of the PTMSS aliquot and the PDI of the BCP (**Figure 2.13**). From these traces, a peak shift to higher molecular weight was observed, confirming addition of the PS block, and the PDIs of both blocks were low. A dn/dc of 0.138 was used for molecular weight analysis of the PTMSS block based on literature[20] and was confirmed experimentally by plotting the integrated refractive index signal for

the PTMSS homopolymer peak for various sample concentrations and extracting the slope as the dn/dc.

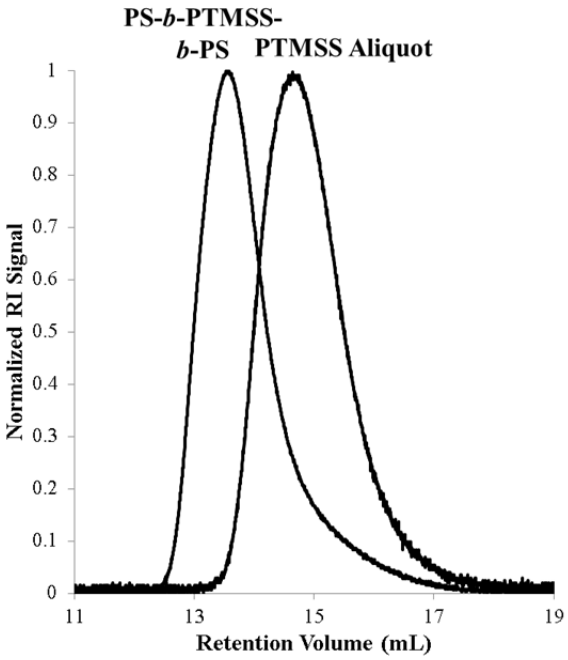


**Figure 2.13:** GPC traces of a $PS_{19}$-*b*-$PTMSS_{41}$-*b*-$PS_{19}$ BCP sample and its PTMSS aliquot. Both peaks have low PDIs and a peak shift that indicates the growth of the second block.

Volume percentages of PTMSS and PS were determined by NMR (**Figure 2.14**). Calculating the mole fractions of the blocks is slightly more complicated for this polymer since both blocks have peaks in the aromatic region of the NMR trace. The peaks were first normalized to a TMS peak value of 9 and then 4 was subtracted (to encapsulate the 4 aromatic hydrogens in the TMSS monomer) from the aromatic peak. The subsequent ratio of aromatic to TMS peaks after subtraction was used to determine the mole ratio of PS to PTMSS. Mass and volume percentages were calculated as reported previously and a PTMSS homopolymer density of 0.963 was used.[21] Due to their low molecular weights

and negligible contribution to the composition, α-methylstyrene and end groups were neglected in the block composition analysis.

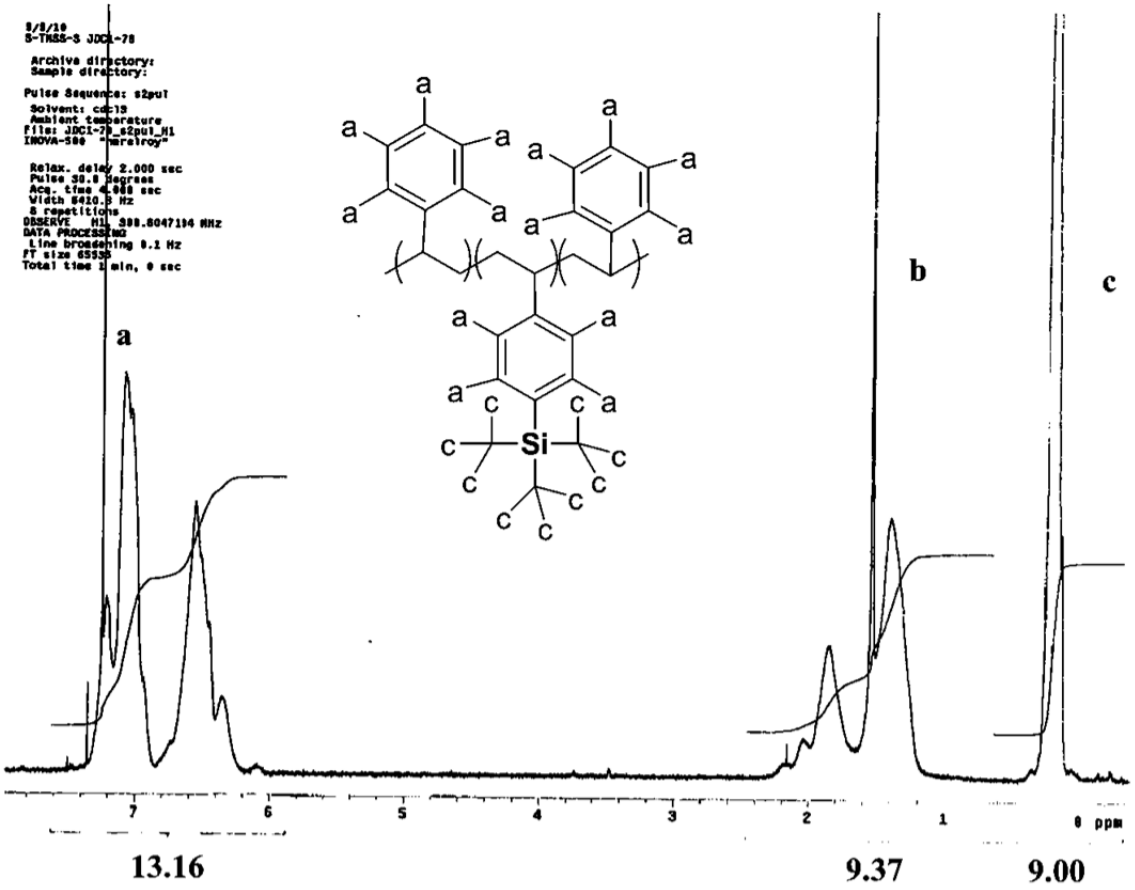


**Figure 2.14:** NMR spectrum used to determine the composition of $PS_{19}$-*b*-$PTMSS_{41}$-*b*-$PS_{19}$. By comparing the integration of the TMS peak (c) and the aromatic peak (a) the mole fraction of each block could be determined. The backbone hydrogens (b) are left off the structure for figure clarity.

The thermal properties of $PS_{19}$-*b*-$PTMSS_{41}$-*b*-$PS_{19}$ were investigated to determine appropriate annealing conditions for the material. The software analysis of the DSC trace of this material (**Figure 2.15**) indicated one $T_g$ at around 100 °C. Only one $T_g$ is observed for the material since the $T_g$s of PS and PTMSS are likely similar and overlap since the PTMSS homopolymer $T_g$ is ~100 °C (shown in Chapter 3).

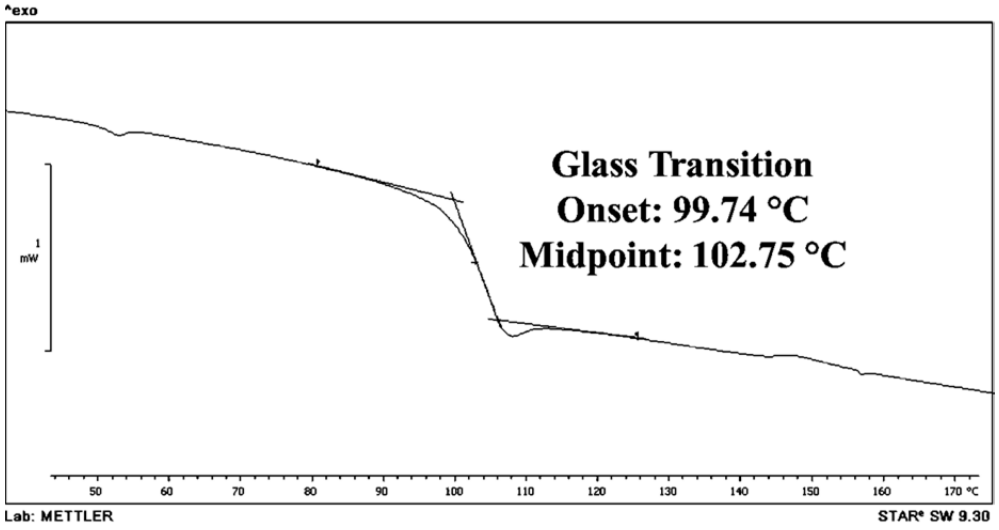


**Figure 2.15:** DSC trace of $PS_{19}$-*b*-$PTMSS_{41}$-*b*-$PS_{19}$.

The TGA trace of $PS_{19}$-*b*-$PTMSS_{41}$-*b*-$PS_{19}$ (**Figure 2.16**) indicated a $T_d$ of approximately 350 °C for the material. The TGA data in this figure was collected by Christopher Bates.

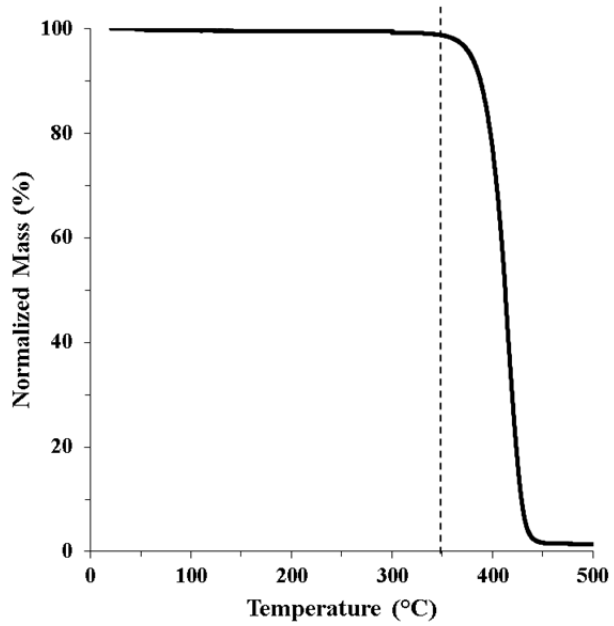


**Figure 2.16:** TGA trace of $PS_{19}$-*b*-$PTMSS_{41}$-*b*-$PS_{19}$. The vertical line is present to guide the eye to the rapid weight loss around 350 °C.

The morphology of $PS_{19}$-*b*-$PTMSS_{41}$-*b*-$PS_{19}$ was determined from its azimuthally integrated SAXS diffraction pattern (**Figure 2.17**). Based on the composition, the peak scattering ratios, and the location of the primary peak, we believe this material is lamellae-forming with a pitch of 30.0 nm. The 2q* peak is not observed here since it is commonly excluded with nearly symmetric lamellar materials due to destructive x-ray scattering interference.[22]

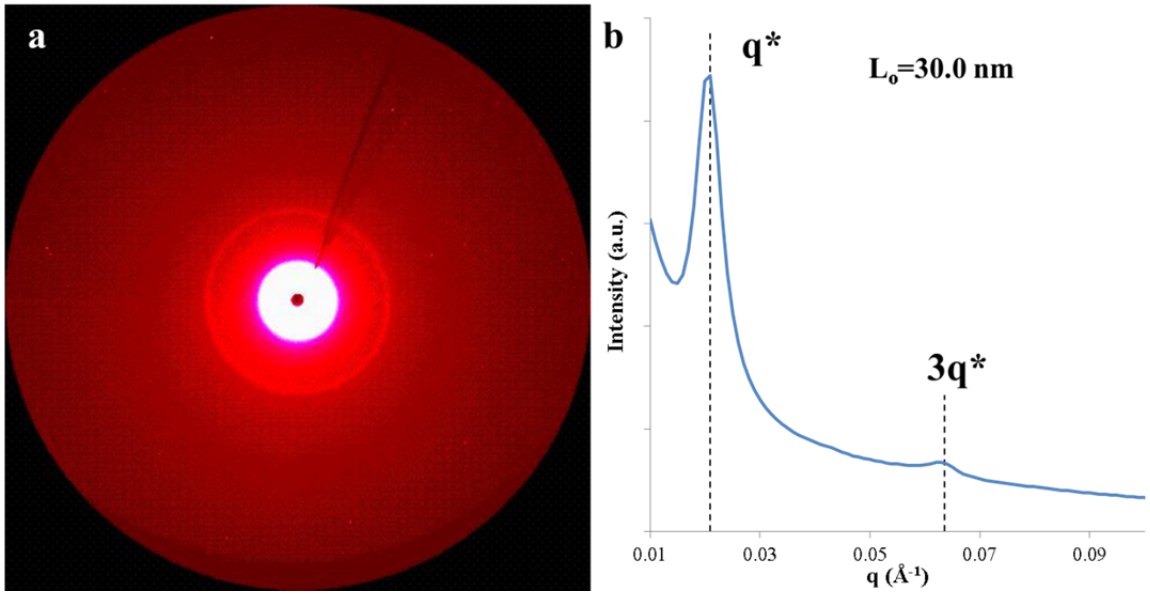


**Figure 2.17:** a) X-ray diffraction pattern obtained for $PS_{19}$-*b*-$PTMSS_{41}$-*b*-$PS_{19}$ from the SAXS detector. b) Two-dimensional pattern obtained after azimuthally integrating the pattern in **Figure 2.17a**.

The characterization data for the specific sample used in the thin film studies that follow in Section 2.2 are summarized in **Table 2.4**. Many more PS-*b*-PTMSS-*b*-PS samples were synthesized in addition to this one and will be discussed in Chapter 6.

| Sample | PTMSS $M_n$ (kDa) | PS PDI | PS $M_n$ (kDa) | BCP PDI | Vol. % PTMSS | Morphology | Pitch |
|---|---|---|---|---|---|---|---|
| $PS_{19}$-*b*-$PTMSS_{41}$-*b*-$PS_{19}$ | 38.0 | 1.08 | 41.1 | 1.20 | 48.0 | Lamellar | 30.0 nm |

**Table 2.4**: Characterization data for the PS-*b*-PTMSS-*b*-PS sample used in thin film orientation studies.

## 2.2 THIN FILM ORIENTATION CONTROL

The thin film orientation of $PS_{60.0}$-*b*-$PMTMSMA_{15.2}$ was accomplished by Christopher Bates using dimethylformamide (DMF). The orientation of $PS_{19}$-*b*-$PTMSS_{41}$-*b*-$PS_{19}$ using polymeric top coats was investigated by Christopher Bates, Michael Maher, William Durand, Gregory Blachut, Takehiro Seshimo, Leon Dean, Jeffrey Ting, Anthony Thio, Litan Li, and Brennen Mueller. While I did not contribute to this work, a brief summary of the results is presented here to provide a complete description of all the processing conditions developed for these polymers.

### 2.2.1 Solvent Annealing PS-*b*-PMTMSMA

Although PS-*b*-PMTMSMA is structurally similar to PS-*b*-PMMA, it proved to be very difficult to self-assemble. The only annealing technique that yielded self-assembly of the polymer intially was solvent annealing in DMF using a jar annealing setup, and this produced cylinders oriented parallel to the substrate. Since these initial solvent annealing experiments, the polymer has also been oriented using a polymeric top coat and thermal annealing. The polymer also self-assembles into smaller domains than PS-*b*-PMMA as evidenced by the calculated $\chi$-parameter in Chapter 6, showing potential for lithographic applications. The orientation and pattern transfer of this material is the subject of ongoing work in our group.

Graphoepitaxy was successfully used to align the parallel cylinder domains of $PS_{60.0}$-*b*-$PMTMSMA_{15.2}$ within a trench after solvent annealing. The results of this experiment are shown in **Figure 2.18** and experimental details are reported in Christopher Bates' dissertation.

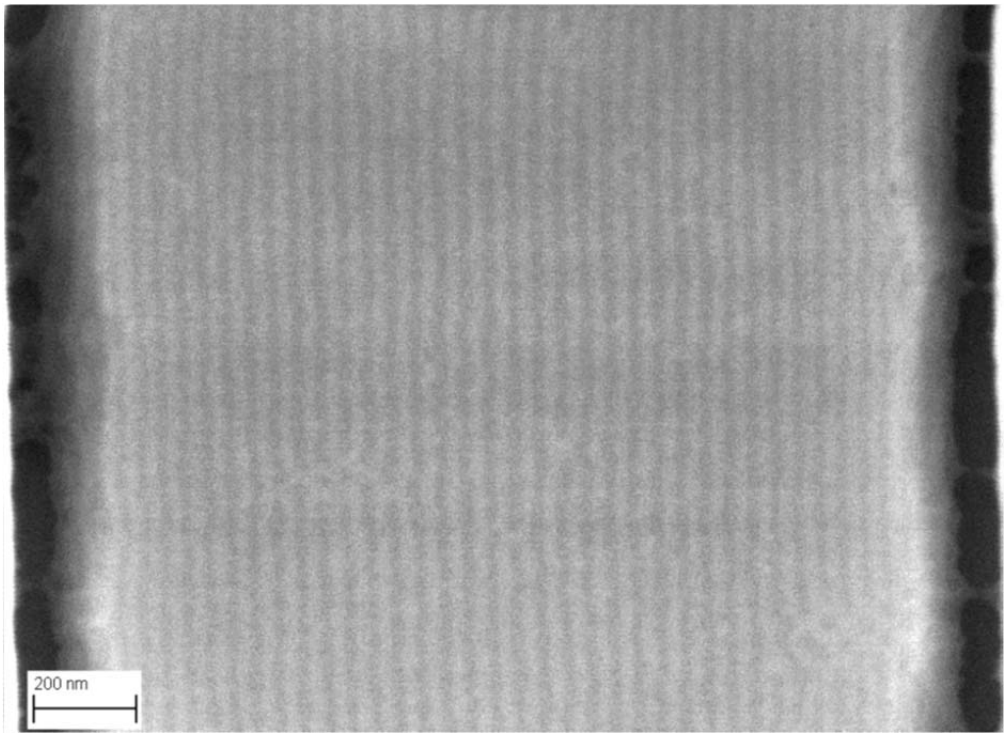


**Figure 2.18:** Directed self-assembly of 60.5 nm pitch $PS_{60.0}$-*b*-$PMTMSMA_{15.2}$ using graphoepitaxy.

### 2.2.2 Thermally Annealing PS-*b*-PTMSS-b-PS with a Top Coat

Lamellae-forming $PS_{19}$-*b*-$PTMSS_{41}$-*b*-$PS_{19}$ was oriented perpendicular to the substrate by thermally annealing a thin film sample on a neutral surface treatment with a top coat. This polymer also self-assembles into smaller domains than PS-*b*-PMMA, although not quite as small as the minimum achievable sizes of PS-*b*-PMTMSMA as described in Chapter 6. Orienting this material with a top coat was the first demonstration

of using polarity-switching top coats to orient a BCP.[23] A BCP with larger domains than the minimum achievable with this polymer was used since there were some initial difficulties with orienting smaller domains. The orientation of smaller domains of this BCP is the subject of ongoing work in our group.

There are four main requirements for a spin-coatable top coat: (1) it must be spin-coatable out of a solvent that will not dissolve the BCP beneath it (typically must be soluble in a polar solvent since most BCPs are soluble in organic solvents), (2) the $T_g$ of the top coat must be higher than that of the two blocks of the BCP to prevent intermixing during thermal annealing, (3) the surface energy of the top coat must be in between that of the blocks of the BCP such that it "neutralizes" the top interface, enabling perpendicular orientation of the BCP, and (4) the top coat must be easily removable after annealing. **Figure 2.19** shows the structure of the polarity-switching random copolymer top coat used to orient $PS_{19}$-*b*-$PTMSS_{41}$-*b*-$PS_{19}$ and highlights the monomer components of the random copolymer that were used to satisfy these three conditions. As described in Chapter 1, polarity-switching top coats are designed to overcome the solubility and related surface energy matching challenges associated with spin-coatable top coats. The maleic anhydride moiety is nonpolar enough in its ring-closed form to make the top coat neutral for a nonpolar BCP, but is polar enough in its ring-opened salt form to make the copolymer soluble in aqueous base. The norbornene moiety in the random copolymer increases the $T_g$ above that of the BCP. Finally, the amount of the 4-trifluoromethyl styrene component (which has a very low surface energy) was used to tune the surface energy of the random copolymer.

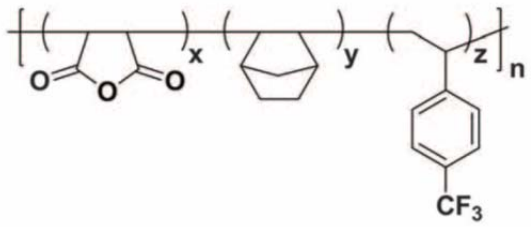


**Figure 2.19:** Structure of the random copolymer top coat used to orient $PS_{19}$-*b*-$PTMSS_{41}$-*b*-$PS_{19}$ in thin films where for this set of conditions, the successful top coat had x = 56, y = 18, and z = 26. From [23]. Reprinted with permission from AAAS.

Details related to the synthesis of the top coat and the process used to find the optimal surface treatment, top coat, and thermal annealing conditions will not be described here but can be found elsewhere.[23] $PS_{19}$-*b*-$PTMSS_{41}$-*b*-$PS_{19}$ was annealed at 210 °C for one minute in air with a neutral substrate surface treatment and top coat to produce the self-assembly in **Figure 2.20**.

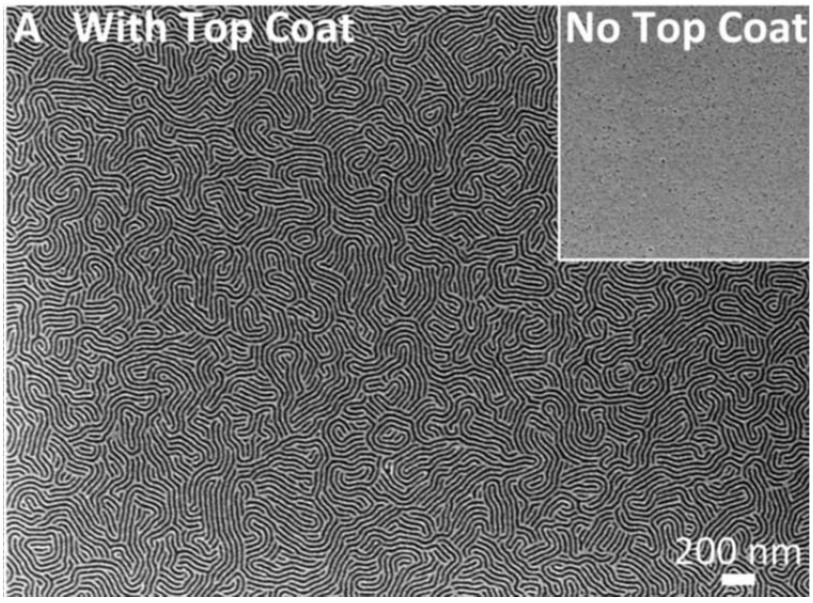


**Figure 2.20:** Thin film orientation of $PS_{19}$-*b*-$PTMSS_{41}$-*b*-$PS_{19}$ with and without a top coat (inset). From [23]. Reprinted with permission from AAAS.

### 2.3 PS-*b*-PTMSS-*b*-PS PATTERN TRANSFER

After orienting $PS_{19}$-*b*-$PTMSS_{41}$-*b*-$PS_{19}$ with the top coat described in Section 2.2.2, the pattern was etched with $O_2$ to reveal the through film structure (**Figure 2.21a**) and transferred into the substrate by reactive ion etching with a fluorinated and $O_2$ etch. (**Figure 2.21a**). The details of these etch protocols are described elsewhere.[23] It can be seen from these images that the perpendicular orientation propagates through the film and high aspect ratio features were transferred into the underlying silicon.

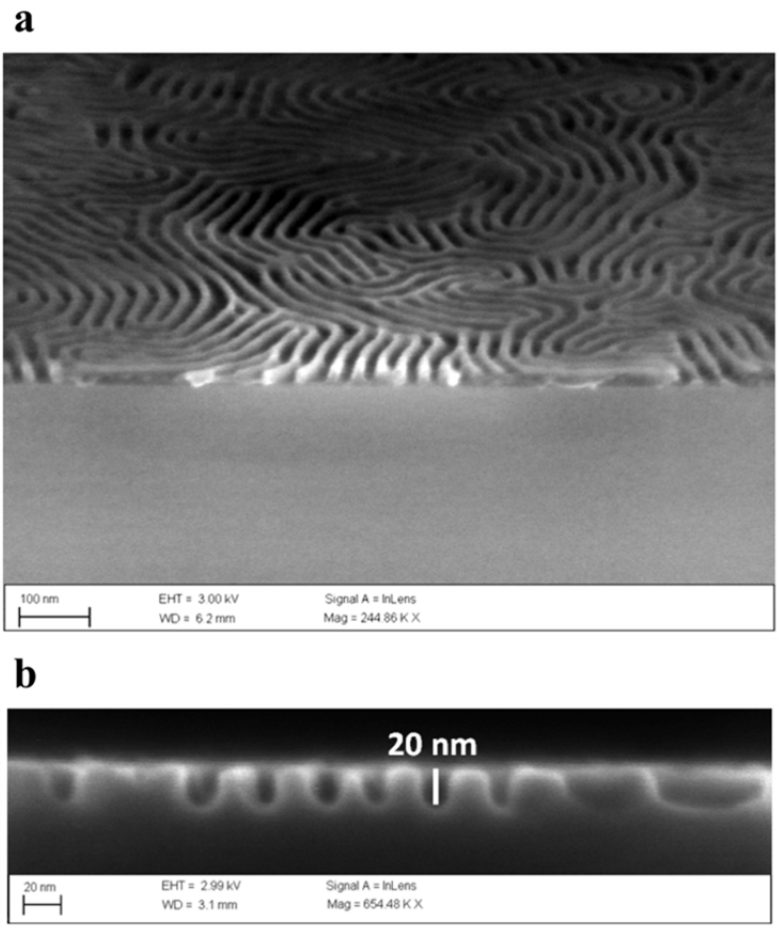


**Figure 2.21:** a) Through-film structure revealed by $O_2$ reactive ion etching and b) pattern transfer of $PS_{19}$-*b*-$PTMSS_{41}$-*b*-$PS_{19}$ by fluorinated and $O_2$ etch protocols. From [23]. Reprinted with permission from AAAS.

## 2.4 CONCLUSIONS

The synthesis of PS-*b*-PMTMSMA and PS-*b*-PTMSS-*b*-PS and my colleagues' work on the self-assembly of these two new silicon-containing BCPs in thin films was presented in this chapter. Successful controlled synthesis and alignment control using graphoepitaxy/solvent annealing for PS-*b*-PMTMSMA and orientation control of PS-*b*-PTMSS-*b*-PS using a polarity-switching top coat was demonstrated. These block copolymers self-assemble into smaller domains than the heavily-studied PS-*b*-PMMA, showing promise in the pursuit of Moore's law and the study of their thin film orientation is the subject of future work in our group. However, I wanted to push the boundaries of minimum attainable feature sizes with BCPs even further by careful material design. The next chapter of this dissertation will explore the synthesis and self-assembly of other new silicon-containing BCPs that have more unfavorable block interactions and promote self-assembly into even smaller structures than those presented in this chapter.

## 2.5 REFERENCES


1. R. D. Peters; X. M. Yang; T. K. Kim; B. H. Sohn; P. F. Nealey, *Langmuir* **2000,** *16*, 4625-4631.
2. Y. Xuan; J. Peng; L. Cui; H. Wang; B. Li; Y. Han, *Macromolecules* **2004,** *37*, 7301-7307.
3. E. W. Cochran; D. C. Morse; F. S. Bates, *Macromolecules* **2003,** *36*, 782-792.
4. T. Hirai; M. Leolukman; C. C. Liu; E. Han; Y. J. Kim; Y. Ishida; T. Hayakawa; M.-a. Kakimoto; P. F. Nealey; P. Gopalan, *Advanced Materials* **2009,** *21*, 4334-4338.
5. M. Colburn; A. Grot; M. Amistoso; B. J. Choi; T. Bailey; J. Ekerdt; S. V. Sreenivasan; S. Hollenhorst; C. G. Willson, Step and flash imprint lithography for sub-100nm patterning. In *Emerging Lithographic Technologies IV*, Dobisz, E. A., Ed. Spie-Int Soc Optical Engineering: Bellingham, 2000; Vol. 3997, pp 453-457.
6. T. P. Russell; R. P. Hjelm; P. A. Seeger, *Macromolecules* **1990,** *23*, 890-893.
7. V. Khanna; E. W. Cochran; A. Hexemer; G. E. Stein; G. H. Fredrickson; E. J. Kramer; X. Li; J. Wang; S. F. Hahn, *Macromolecules* **2006,** *39*, 9346-9356.
8. T. Vu; N. Mahadevapuram; G. M. Perera; G. E. Stein, *Macromolecules* **2011,** *44*, 6121-6127.
9. M. W. Matsen, *Macromolecules* **2009,** *43*, 1671-1674.

10. M. Harada; T. Suzuki; M. Ohya; A. Takano; Y. Matsushita, *Polymer Journal* **2004,** *36*, 538-541.
11. P. Chaumont; G. Beinert; J. E. Herz; P. Rempp, *Makromolekulare Chemie-Macromolecular Chemistry and Physics* **1982,** *183*, 1181-1190.
12. D. Uhrig; J. W. Mays, *Journal of Polymer Science Part a-Polymer Chemistry* **2005,** *43*, 6179-6222.
13. H. Hsieh; R. Quirk, *Anionic Polymerization* 1996.
14. T. S. Bailey; H. D. Pham; F. S. Bates, *Macromolecules* **2001,** *34*, 6994-7008.
15. S. K. Varshney; Z. S. Gao; X. F. Zhong; A. Eisenberg, *Macromolecules* **1994,** *27*, 1076-1082.
16. P. Hiemenz; T. Lodge, *Polymer Chemistry*. 2 ed.; 2007.
17. L. A. Wall; S. Straus; R. E. Florin; L. J. Fetters, *Journal of Research of the National Bureau of Standards Section a-Physics and Chemistry* **1973,** *A 77*, 157-170.
18. T. Kashiwagi; A. Inaba; J. E. Brown; K. Hatada; T. Kitayama; E. Masuda, *Macromolecules* **1986,** *19*, 2160-2168.
19. I. W. Hamley; V. Castelletto, *Progress in Polymer Science* **2004,** *29*, 909-948.
20. M. Harada; T. Suzuki; M. Ohya; D. Kawaguchi; A. Takano; Y. Matsushita; N. Torikai, *Journal of Polymer Science Part B: Polymer Physics* **2005,** *43*, 1486-1494.
21. M. Harada; T. Suzuki; M. Ohya; D. Kawaguchi; A. Takano; Y. Matsushita, *Macromolecules* **2005,** *38*, 1868-1873.
22. Hashimot.T; Nagatosh.K; A. Todo; H. Hasegawa; H. Kawai, *Macromolecules* **1974,** *7*, 364-373.
23. C. M. Bates; T. Seshimo; M. J. Maher; W. J. Durand; J. D. Cushen; L. M. Dean; G. Blachut; C. J. Ellison; C. G. Willson, *Science* **2012,** *338*, 775-779.

# Chapter 3: Polytrimethylsilylstyrene-*block*-Oligosaccharide

In Chapter 2, the synthesis and thin film self-assembly of PS-*b*-PMTMSMA and PS-*b*-PTMSS-*b*-PS were investigated. We chose to work with these materials initially because I believed that, due to their relative chemical similarity to previously studied BCPs, established techniques could work in controlling their orientation in thin films. I also investigated how adding a silicon-containing group to polymers, otherwise similar to those previously studied, impacts the interaction parameter (details in Chapter 6). Unfortunately, orientation control was challenging with these materials due to the low surface energy of the silicon-containing block. While my colleagues pioneered some very interesting work on new methods of controlling the orientation of these challenging materials in thin films, their interaction parameters are only slightly better than others currently being examined for BCP lithography. The work in Chapter 6 concludes that the minimum feature sizes of PTMSS-*b*-PMMA and PS-*b*-PTMSS-*b*-PS are better than the minimum accessible feature size of PS-*b*-PMMA, but only by several nanometers.

While many factors contribute to the interaction parameter of a BCP, in very general terms, strong segregation will be present when the blocks of the copolymer are very chemically dissimilar. Therefore, we decided to next design a material that focused on a polarity difference between blocks as the critical design criterion. After working with PS-*b*-PMTMSMA and PS-*b*-PTMSS-*b*-PS, my colleagues and we believed that adding silicon to a domain makes it generally more nonpolar based on the drastic decrease in surface energy that is observed in surface energy measurements of the silicon-containing block homopolymers.[1] We therefore chose to design BCPs that leverage the chemical incompatibility of an amphiphilic BCP with silicon incorporated in the *nonpolar* domain (to increase its hydrophobicity and introduce etch resistance) and a

very polar component comprising the other domain. For this reason, PTMSS was chosen as the silicon-containing nonpolar domain as opposed to PMTMSMA since styrene is more nonpolar than PMMA and PTMSS is more thermally stabe. Three different oligosaccharides with different structures were chosen for the hydrophilic block since they are extremely polar. The choice of the oligosaccharides as the polar domain was motivated by a collaboration with CERMAV CNRS, where functionalization and BCP synthesis from oligosaccharide materials had been previously investigated. Visiting scientist Dr. Issei Otsuka brought this expertise to the University of Texas during a three-month visit to help facilitate the synthesis of the new polymers and investigate their thin film characteristics. The work that follows in this chapter resulted from a collaborative effort between our two research groups.[2]

### 3.1 SYNTHESIS

Since oligosaccharides technically exist naturally as large molecules instead of polymerized monomer repeat units, forming a BCP from them requires a different synthetic approach to conventional polymerization techniques. As an alternative to sequential monomer polymerization, two materials can be coupled by a copper catalyzed reaction that forms a triazole linkage between azide and alkyne functionalized materials. This coupling technique, called azide-alkyne cycloaddition, is a subset of "click" coupling reactions that was chosen to synthesize these materials due to its high conversion and known ability to produce similar BCP materials.[3] The synthesis of the amphiphilic PTMSS-*b*-Oligosaccharide BCPs was carried out in a series of three major steps. First, PTMSS was synthesized by activators regenerated by electron transfer atom transfer polymerization (ARGET ATRP). This bromine-terminated polymer was subsequently functionalized with an azide group. Second, the oligosaccharides were

functionalized with an alkyne moiety at a single location using techniques established by the scientists at CERMAV. Finally, the two blocks were coupled by azide-alkyne cycloaddition.

### 3.1.1 PTMSS Synthesis by ARGET ATRP and Azide Functionalization

As reported in Chapter 2, PTMSS can be synthesized by anionic polymerization. However, to couple it to an alkyne-functionalized oligosaccharide by azide-alkyne cycloaddition, the PTMSS must contain an azide functional group. This can be accomplished by tosylation, and azidification[4] of a hydroxyl-functionalized anionically-polymerized polymer. However, this is cumbersome due to the potentially hazardous hydroxyl functionalization step,[5] and labor intensive isolation and purification processes after each functionalization step. For this reason, a different approach was taken to synthesize PTMSSAz. Halogen-terminated polymers can be synthesized by ATRP and then can undergo a single functionalization step to replace the halogen end group with an azide. ATRP is a more attractive synthetic approach for this polymer since it is a much less labor-intensive synthesis technique than anionic polymerization and subsequent functionalization to reach an azide end group requires fewer purification and isolation steps.

Unlike anionic polymerization, controlled radical polymerizations are not living polymerizations since less than 100% of the polymer chains have a reactive radical at the end of the propagating chain at any given time. Instead, the reaction mechanism consists of a series of reversible radical activating and deactivating events which are catalyzed by a copper halide catalyst. ATRP is a type of controlled radical polymerization that enables some control of the dispersity of the polymer chains produced due to a low concentration of the propagating radical, which is the result of the radical activating rate constant being

much smaller than the radical deactivating rate constant (**Figure 3.1**).[6, 7] However, in conventional ATRP reactions, it can be difficult to achieve very low polydispersity due to termination and chain coupling events[8] and side reactions with the catalyst.[9] Also, large concentrations of copper catalyst are required for the polymerization due to irreversible copper oxidation side reactions with impurities. The large amount of catalyst leads to a need for a high deactivation rate to keep the concentration of propagating chains low for low polydispersity. So much catalyst is required that the polymer may even be blue in color from the copper, even after extensive purification.[10] Since the semiconductor industry typically has low tolerance levels for metal contaminants in manufacturing processes,[11, 12] including the presence of large concentrations of copper that could also have an unpredictable influence on the self-assembly and etch processes in BCP pattern transfer, we investigated an alternative to conventional ATRP.

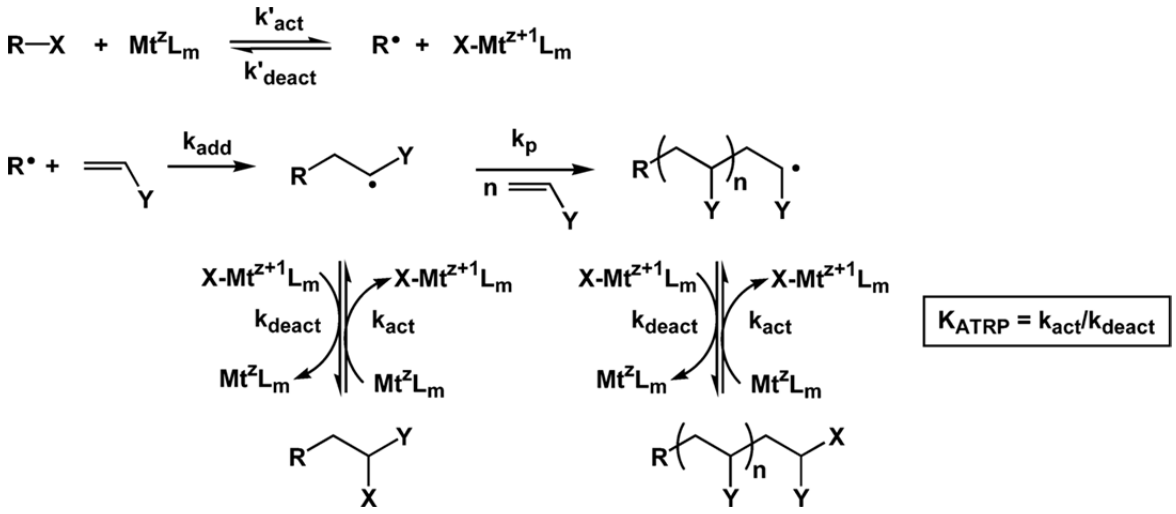


**Figure 3.1:** Mechanism of conventional ATRP where R-X is an alkyl halide initiator, $M_t$ is the catalyst with an oxidation state of z, $L_m$ is the ligand, and k is the rate constant where act is activating, deact is deactivating, add is addition, p is propagation.[10] Reprinted with permission from [10]. Copyright 2007 American Chemical Society.

My colleague Jeffrey Easley adapted ARGET ATRP,[13] a modified form of conventional ATRP, from literature for use in his research and, as a general technique, has since been widely used in our laboratory. ARGET ATRP allows more control over polydispersity than conventional ATRP due to impurity scavenging from the addition of a reducing agent and requires several orders of magnitude lower copper concentration. In ARGET ATRP, a lower catalyst concentration can be used since activation is increased with the use of a tridentate ligand. To avoid irreversible deactivation of such a small amount of catalyst over time, a reducing agent is added to reduce the Cu (II) to the active Cu (I) catalyst (**Figure 3.2**). The complete reaction mechanism of ATRP is complex so a simplified mechanism of ARGET ATRP is shown in **Figure 3.2** to highlight the function of the reducing agent. A more detailed discussion of the conventional and ARGET ATRP reaction mechanisms will not be described here but can be found in the references cited.

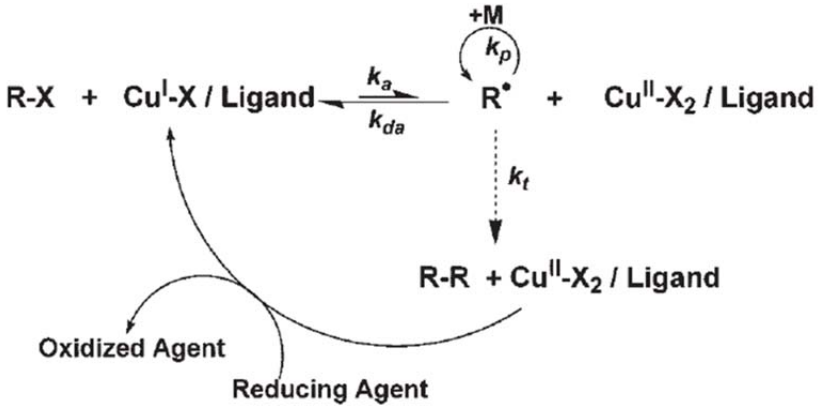


**Figure 3.2:** Simplified mechanism of ARGET ATRP[13] including Cu (I) catalyst regeneration with the addition of a reducing agent where $k_a$, $k_{da}$, $k_p$, and $k_t$ are the activating, deactivating, propagation, and termination rate constants, respectively. Copyright © 2006 WILEY-VCH Verlag GmbH & Co. KGaA, Weinheim from [13].

The components of an ARGET ATRP reaction include a bromine-functionalized initiator with an activating substituent on the α-carbon,[7] an oxidatively stable copper (II)

halide catalyst, a ligand to complex with the catalyst and solubilize it in the solvent, the solvent, and a reducing agent.[13] The components of the PTMSSBr synthesis were chosen based on optimized reaction conditions reported for synthesizing bromine-terminated PS (PSBr) with low polydispersity reported in the literature[14, 15] and experiments further optimized for PSBr by Jeffrey Easley. Through helpful discussions with Jeff and with the help of undergraduate Erica Rausch, the conditions necessary to polymerize PTMSSBr at low molecular weights using this technique were developed. In general, the conditions that produced the desired polymers were very similar to those for successful PSBr synthesis with only some issues controllably synthesizing molecular weights less than 8 kDa. The components used to synthesize PTMSSBr and their structures are summarized in **Table 3.1** and all reagents were used as received, except tris[2-(dimethylamino) ethyl]amine ($Me_6$TREN) which was synthesized following a previously reported procedure.[16]

| | |
|---|---|
| **Initiator** | 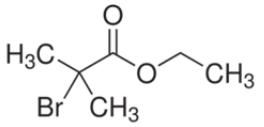 Ethylbromoisobutyrate (EBIB) |
| **Solvent** | 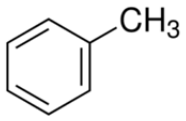 Toluene |
| **Catalyst** | $CuBr_2$ Copper (II) Bromide |
| **Ligand** | 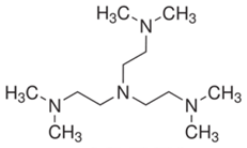 $ME_6TREN$ |
| **Reducing Agent** | 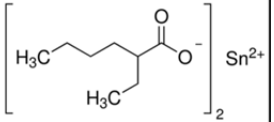 Tin(II) 2-ethylhexanoate $Sn(EH)_2$ |

**Table 3.1:** Reagents used in the ARGET ATRP synthesis of PTMSS.

The general procedure is as follows. TMSS and toluene were stirred over calcium hydride (to remove dissolved water) and basic alumina (to remove inhibitor) for 1 h and filtered through filter paper. Dry TMSS (23.05 g, 130.7 mmol), EBIB (554 mg, 2.8 mmol), $CuBr_2$ (6.3 mg, 0.028 mmol), $Me_6TREN$ (65 mg, 0.284 mmol), and dry toluene (27.5 mL) were added to a round bottom flask. The solution was sparged with high-purity argon for 10 min to remove air from the head space of the flask and then $Sn(EH)_2$ (115 mg, 0.284 mmol) was added via syringe. The solution was submerged in an oil bath at 90 °C and polymerized for three hours and twenty minutes at which point it reached approximately 40% conversion. Unfortunately, PTMSS would not polymerize

controllably to high conversion at molecular weights lower than 8000 g/mol, so low molecular weights were obtained by using the same reaction conditions described above (which target an 8000 g/mol molecular weight at 100% conversion) and changing the reaction time, thus limiting the conversion and molecular weight. The polymer was precipitated in methanol and dried under vacuum. The molecular weight and PDI was analyzed by GPC.

PTMSSBr was functionalized with an azide group using a previously reported procedure as shown in **Scheme 3.1**.[17] PTMSSBr (6000 mg, 1.7 mmol), sodium azide (325 mg, 5.0 mmol), and 80 mL DMF were added to a round bottom flask. The reaction was stirred overnight at room temperature. The polymer was precipitated in methanol, dried, dissolved in THF, and reprecipitated in methanol three times to remove excess sodium azide salt. Care was taken to keep sodium azide waste separate from other laboratory waste and the chemical was handled with a plastic spatula since sodium azide can react with acids and heavy metals (in metal spatulas) to form toxic $HN_3$ and heavy metal azides.

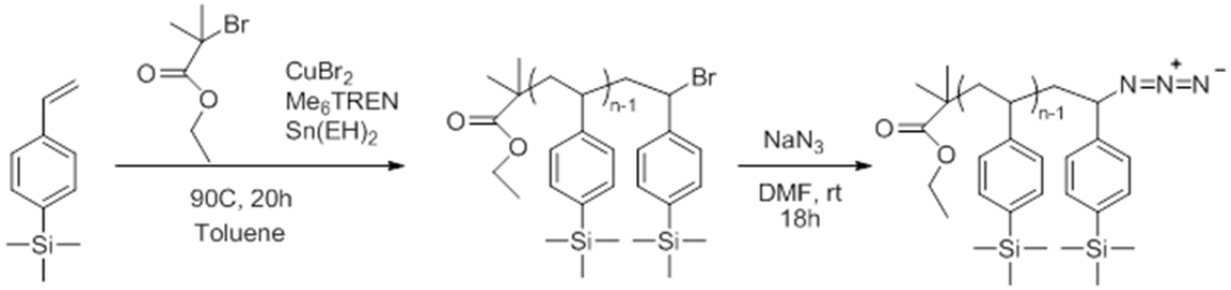


**Scheme 3.1:** Synthesis of PTMSSBr by ARGET ATRP and azide functionalization.

The success of the azide substitution was confirmed by the complete end group shift observed in NMR (**Figure 3.3**). Due to the very low molecular weights synthesized,

end group mole fractions by NMR were high enough to be used as a characterization technique. Successful functionalization was also characterized by infrared spectroscopy (IR) as described in Section 3.1.3.

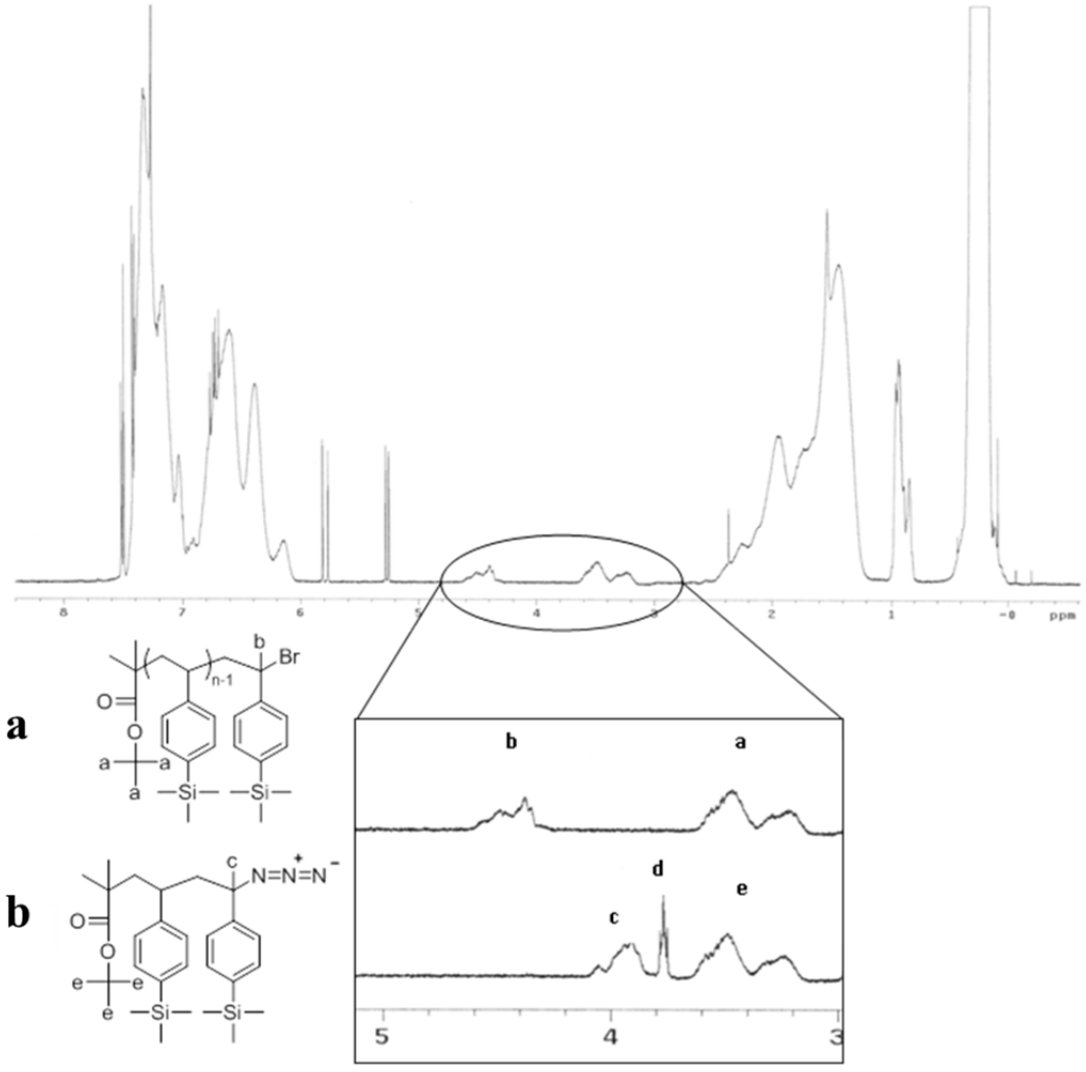


**Figure 3.3:** NMR spectra showing the complete transformation from a) PTMSSBr to b) PTMSSAz. In the magnified image, there is no evidence of a Br end group (peak b) in the PTMSSAz $^{1}$H NMR after functionalization indicating complete end group transformation. In Figure 3.1b, peak d is residual THF. Reprinted with permission from [2]. Copyright 2012 American Chemical Society.

### 3.1.2 Oligosaccharide Functionalization

The oligosaccharides used in this work were *N*-maltoheptaosyl-3-acetamido-1-propyne (ethynyl-MH), a linear oligosaccharide, *N*-xyloglucooligosaccharide-3-acetamido-1-propyne (ethynyl-XGO), a branched oligosaccharide, and mono-$6^A$-*N*-propargylamino-$6^A$-deoxy-β-cyclodextrin (ethynyl-βCyD), a cyclic oligosaccharide. The structures of these materials are shown in **Figure 3.4**.

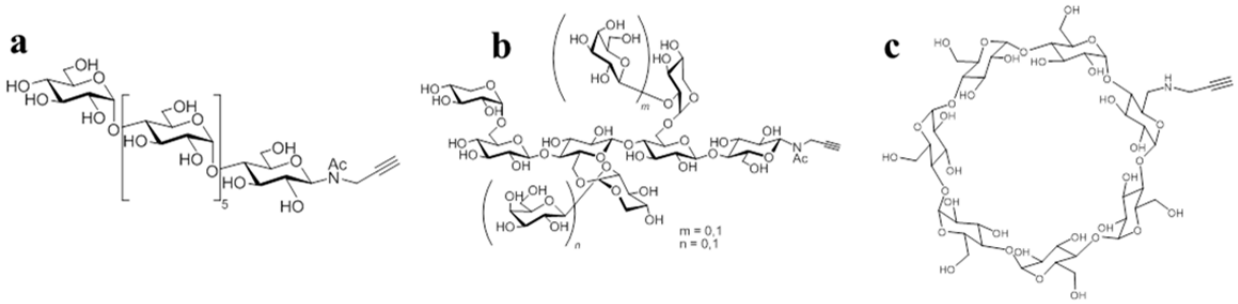


**Figure 3.4:** Structures of the alkyne-functionalized oligosaccharides coupled to PTMSS: a) ethynyl-MH, b) ethynyl-XGO, and c) ethynyl-βCyD. Reprinted with permission from [2]. Copyright 2012 American Chemical Society.

The oligosaccharides were functionalized with a single alkyne group using procedures reported previously.[18-20] The materials were prepared and characterized by scientists at CERMAV CNRS.

### 3.1.3 Coupling of PTMSS and Oligosaccharide by "Click" Chemistry

The ethynyl-oligosaccharides and PTMSSAz were coupled by azide-alkyne cycloaddition as reported previously and as shown in **Scheme 3.2**.[21] The general procedure is as follows: ethynyl-oligosaccharide (0.23 g, 0.18 mmol) and PTMSSAz (0.36 g, 0.14 mmol) were dissolved in 20 mL DMF in separate flasks. The catalyst ligand N, N, N', N', N" pentamethyltriethylenediamine (PMDETA) (0.045 mL) was added to the oligosaccharide flask. The flasks were sparged with high-purity argon for 10 minutes

and then cannulated to a third flask containing Cu(I)Br under argon atmosphere (40.2 mg, 0.28 mmol), which had been dispensed in a glove box due to the oxygen sensitivity of CuBr. The solution turned green and was stirred for 72 h at 40 °C. The solution was passed through basic alumina to remove the copper, concentrated under vacuum, and precipitated in methanol.

The success of the coupling reaction (**Scheme 3.2**) was confirmed by GPC (**Figure 3.5**). A shift to higher molecular weight in the normalized RI signal for all block copolymers and the absence of a peak or shoulder overlaying the PTMSSAz precursor indicates that the coupling reaction went to completion. Oligosaccharide precursors could not be analyzed by GPC since they were not soluble in THF. Attempts to run the samples with DMF as the carrier solvent were unsuccessful due to interaction of the oligosaccharides and oligosaccharide-containing BCPs with the columns.

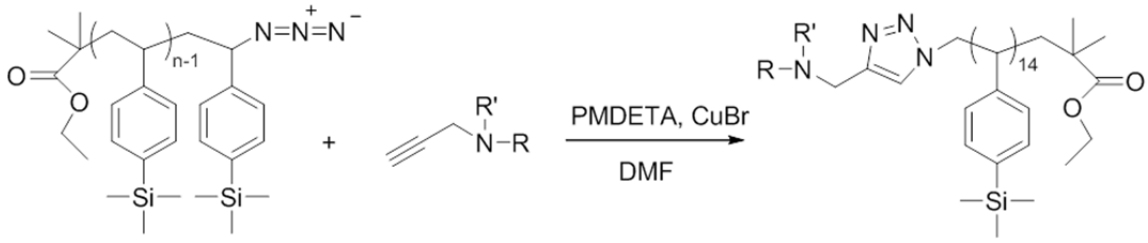


**Scheme 3.2:** Coupling of PTMSSAz and ethynyl-oligosaccharides. Here, R represents MH, XGO, or β-CyD and R' represents Ac for MH and XGO and H for βCyD. Reprinted with permission from [2]. Copyright 2012 American Chemical Society.

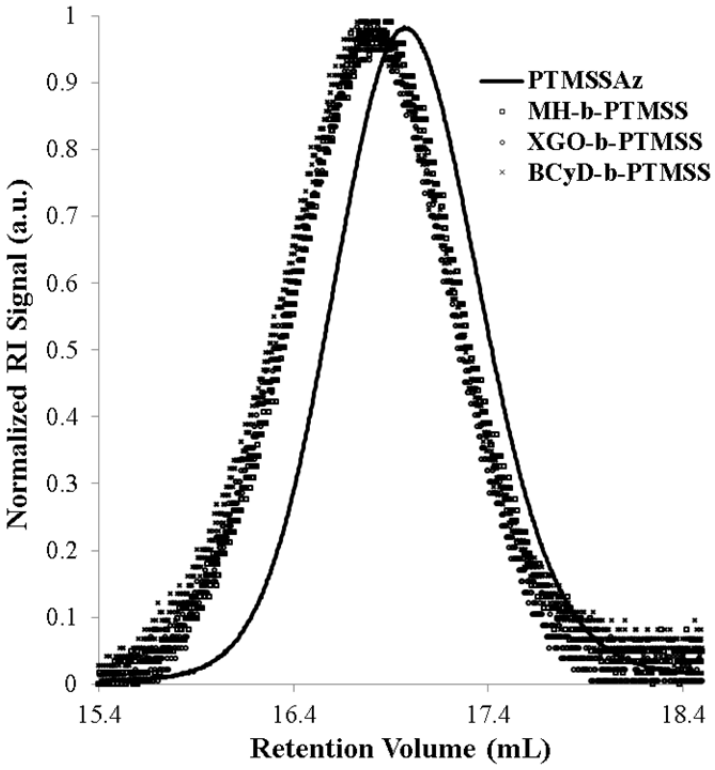


**Figure 3.5:** Normalized GPC traces from the refractive index detector showing peak shifts to higher molecular weight polymer from the $PTMSSAz_{4.6}$ precursor (-) to the block copolymers (MH-*b*-$PTMSS_{4.6}$ ( □ ), XGO-*b*-$PTMSS_{4.6}$ ( ○ ), and βCyD-*b*-$PTMSS_{4.6}$ ( x )). Reprinted with permission from [2]. Copyright 2012 American Chemical Society.

Reaction success was also confirmed by IR. IR data was recorded on a Nicolet 550 infrared spectrometer. A peak around 2100 $cm^{-1}$ (which is a typical location of an $N_3$ group in IR) appears after PTMSSBr (**Figure 3.6a**) is functionalized with azide (**Figure 3.6b**). This peak fully disappears after the coupling reaction (**Figure 3.6c**) in addition to the appearance of a hydroxyl peak from the oligosaccharides. A complete disappearance of the azide peak indicates complete coupling of the blocks. Additionally, after precipitating the BCP in methanol, a solvent that completely solubilizes free

oligosaccharides, a hydroxyl peak would not be observed in IR unless the oligosaccharide was chemically bound to the PTMSS.

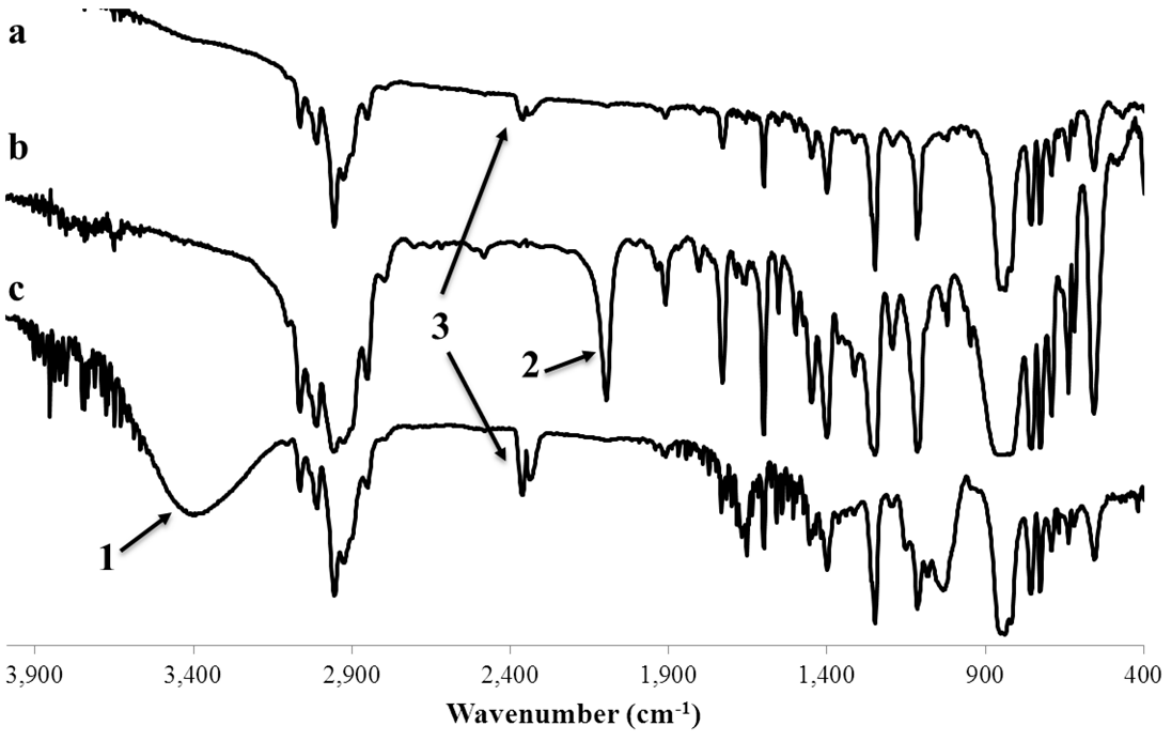


**Figure 3.6:** Representative normalized transmission IR spectra of a) PTMSSBr, b) PTMSSAz, and c) PTMSS-*b*-Oligosaccharide after coupling. Peak 1 indicates the presence of OH groups in the block copolymer, peak 2 indicates the presence of azide in the PTMSSAz homopolymer, and the peaks indicated by the number 3 are representative of $CO_2$ contamination. Reprinted with permission from [2]. Copyright 2012 American Chemical Society.

The properties of the polymers synthesized for further examination are summarized in **Table 3.2**. The numerical subscripts after PTMSS indicate the molecular weight in kDa. The molecular weight of PTMSSBr was determined by GPC using a dn/dc of 0.138.[22] The volume percentages of the block copolymers were calculated using

the known molecular weights of the two blocks and the known densities of PTMSS (0.963 g/mL)[23] and amylose (1.36 g/mL),[24] for the oligosaccharides.

| Sample | $M_n$ PMTSS (g/mol) | PDI PTMSS | $M_n$ Sugar (g/mol) | Volume % PTMSS |
|---|---|---|---|---|
| **MH-PTMSS$_{4.6}$** | 4600 | 1.09 | 1232 | 84.1 |
| **XGO-PTMSS$_{4.6}$** | 4600 | 1.09 | 1360 | 82.7 |
| **βCyD-PTMSS$_{4.6}$** | 4600 | 1.09 | 1072 | 85.8 |
| **MH-PTMSS$_{2.7}$** | 2700 | 1.30 | 1232 | 70.1 |

**Table 3.2:** Properties and compositions of the PTMSS-*b*-Oligosaccharide polymers synthesized for further study. Reprinted with permission from [2]. Copyright 2012 American Chemical Society.

### 3.2 Bulk Self-Assembly by Solvent Annealing

As discussed previously, BCPs need to be given mobility for nanoscale self-assembly to occur. Typically, thermally annealing the sample between the $T_g$s and $T_d$s of the blocks can provide such mobility. Although the PTMSS has an accessible $T_g$ of ~105 °C, the PTMSS-*b*-Oligosaccharides could not be thermally annealed because there was no accessible annealing temperature that gave the oligosaccharide block mobility to reassemble. As observed by TGA (**Figure 3.7**), the degradation temperatures of the oligosaccharides range from approximately 170-190°C. However, in DSC experiments (**Figure 3.8**), the oligosaccharides show no glass transition or melting temperature below this temperature range. This is likely because the oligosaccharides are hydrogen bonded and highly crystalline, giving rise to high melting temperatures.

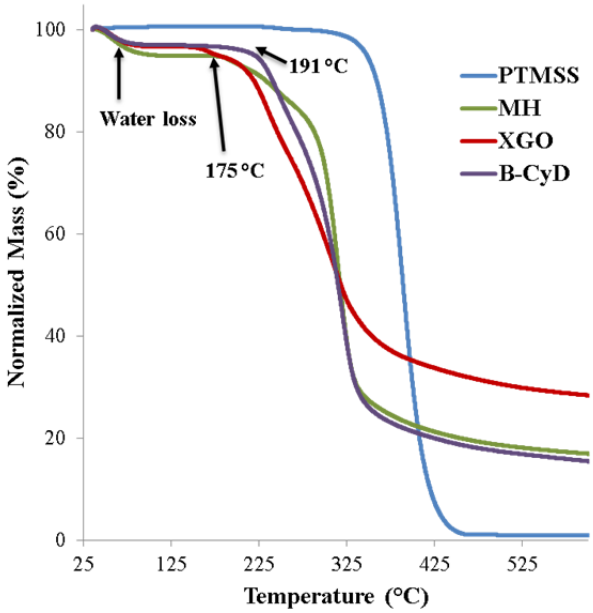


**Figure 3.7:** TGA data indicating the degradation of PTMSS, MH, XGO, and βCyD. There is significant water loss around 100 °C in the TGA experiments with the oligosaccharides since these materials are relatively hygroscopic. Reprinted with permission from [2]. Copyright 2012 American Chemical Society.

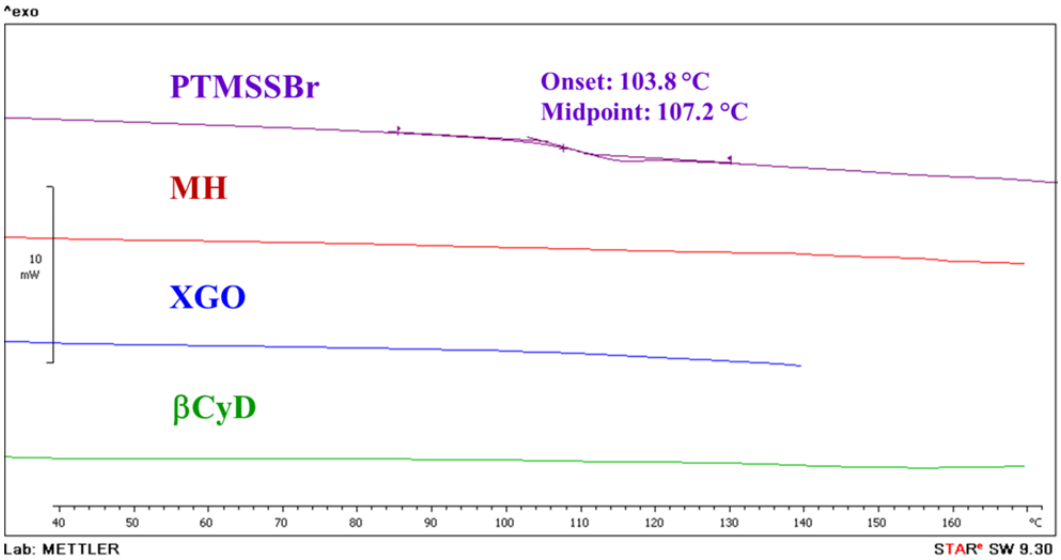


**Figure 3.8:** DSC traces of PTMSS ($T_g$ ~ 105°C), MH, XGO, and βCyD, which do not exhibit glass transitions or melt transitions below their $T_d$s. Reprinted with permission from [2]. Copyright 2012 American Chemical Society.

Thermal annealing experiments were performed on the bulk materials below the $T_d$s of the oligosaccharides to validate concerns about the inability to promote reorganization without oligosaccharide mobility. SAXS was performed on bulk samples that were annealed for various times and temperatures below the oligosaccharide $T_d$s. The SAXS data for all thermal annealing conditions (not shown) were nearly identical to the data for samples that were not treated with an annealing step. Without an accessible $T_g$ in the oligosaccharides, the polymer does not have mobility to reassemble at elevated temperature and will remain trapped in its as-precipitated nanostructure. As-precipitated, all samples exhibited broad shoulders of intensity typical of poorly-ordered spherical structures (likely kinetically-trapped micelles from precipitation) instead of the distinct peaks at specific q/q* ratios observed for self-assembled block copolymers (**Figure 3.9**). The form factor of spherical nanostructures with poor long-range order is also plotted in **Figure 3.9** for a sphere radius of 5 nm, which lines up well with the peak intensity shoulders on the block copolymer samples. Dashed vertical lines are included in the figure at the form factor peaks to guide the eye. The equation used to calculate the form factor for a sphere is reported previously (**Equation 3.1**) where *P(q)* is the form factor and *R* is the spherical particle radius.[25] It is possible that the shoulders of intensity observed in the micelle SAXS patterns are from the form factor contribution but could also be contributions from the structure factor and coincidentally in the same place since the form factor contribution to a scattering pattern is typically small compared to the structure factor contribution. Further evidence for the presence of a micelle structure will be presented in Section 3.3 where the thin film self-assembly of these materials is described.

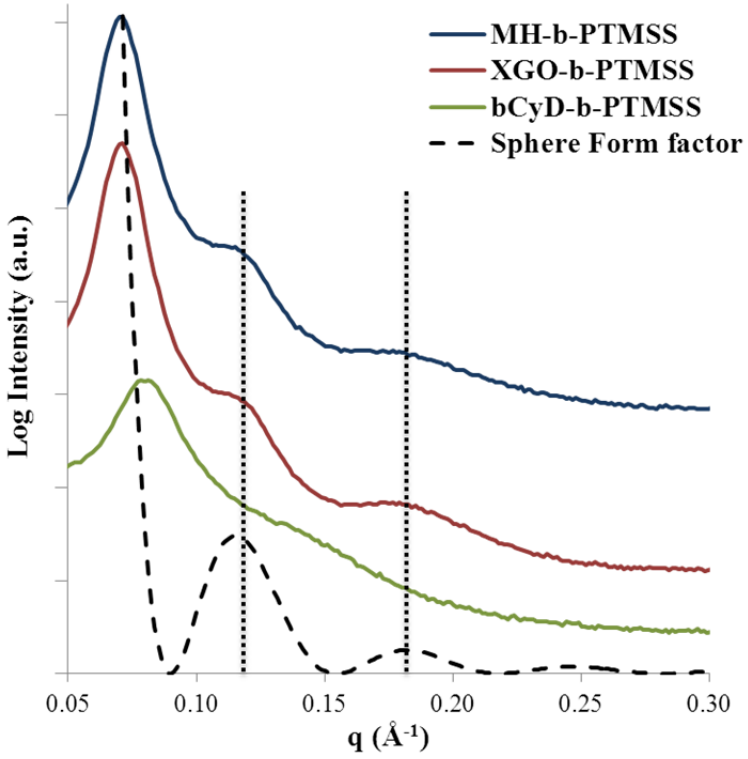


**Figure 3.9:** SAXS patterns of the as-precipitated PTMSS-*b*-Oligosaccharide materials and the sphere form factor calculated for diameter of 5 nm.

$$P(q) = \left[ \frac{3*[\sin(qR) - qR\cos(qR)]}{(qR)^3} \right]^2 \qquad \textbf{Eq. 3.1}$$

Although most commonly used in thin films, solvent annealing was used to give the PTMSS-*b*-Oligosaccharide materials mobility to reassemble into nanostructures in the bulk since thermal annealing could not be used. Bulk samples were solvent annealed in a tightly-capped 125 mL jar (Fisher, catalog number 02-911-455) at room temperature for 24 hours initially at atmospheric pressure. Within the jar was an uncapped 20 mL vial (Fisher, catalog number 03-337-15) filled with a mixture of 2.5 g THF and 2.5 g water.

Solvent annealing the silicon-containing oligosaccharide bulk samples led to well-ordered morphologies as evidenced by the evolution of bulk SAXS patterns. A THF/water mixture was chosen as the solvent system for these experiments because the

PTMSS block is soluble in THF but has low solubility in water and the oligosaccharide block is soluble in water but has low solubility in THF. This approach imparts mobility to both blocks of the copolymer that is necessary to enable rearrangement and enhanced ordering of the self-assembled structure. Solvent annealing experiments performed in only a hydrophilic solvent (water) or only a hydrophobic solvent (benzene) resulted in no improvement in the order of the system, likely because in these cases mobility was only introduced into one domain. It is possible that annealing with a mixture of selective solvents alters the equilibrium morphology and domain spacing of the materials from the bulk equilibrium state. A discussion of these effects with another BCP system will take place in Chapter 5 but was not studied for the PTMSS-*b*-Oligosaccharides.

From SAXS profiles of bulk samples after solvent annealing with a 50/50 (by volume) mixture of THF/water for 24 h, hexagonally packed cylindrical morphologies were observed in MH-*b*-PTMSS$_{4.6}$ as indicated by 1, √3, and √4 peak scattering ratios, $q/q^*$ (**Figure 3.10a**) and XGO-*b*-PTMSS$_{4.6}$ as indicated by 1, √3, √4, √9 and √12 peak scattering ratios (**Figure 3.10b**). Given that the major component is PTMSS, it is likely that PTMSS is the continuous (or matrix) domain and the oligosaccharide is the cylinder domain. In contrast, the SAXS pattern of βCyD-*b*-PTMSS$_{4.6}$ (**Figure 3.10c**) appears disordered. From the relationship $d = 2\pi/q^*$ block copolymer domain spacings are 10.7 nm for MH-*b*-PTMSS$_{4.6}$ and 10.1 nm for XGO-*b*-PTMSS$_{4.6}$. Cylindrical feature diameters were calculated to be 5.2 nm for MH-*b*-PTMSS$_{4.6}$ and 5.1 nm for XGO-*b*-PTMSS$_{4.6}$ based on the volume fractions of the blocks and geometrical considerations for hexagonally packed cylinders. In MH-*b*-PTMSS$_{2.7}$, a bulk cylinder-forming morphology was also observed as indicated by the 1, √3, √4, √7, and √9 peak scattering ratios (**Figure 3.10d**). The calculated domain spacing for this sample is 8.3 nm, which corresponds with feature diameters of 5.5 nm. Since the MH domain is unchanged, the cylinder diameter is

roughly the same but the domain spacing, as defined by the primary scattering peak, is smaller. These features are remarkably small and represent some of the smallest self-assembled BCP structures reported to date.

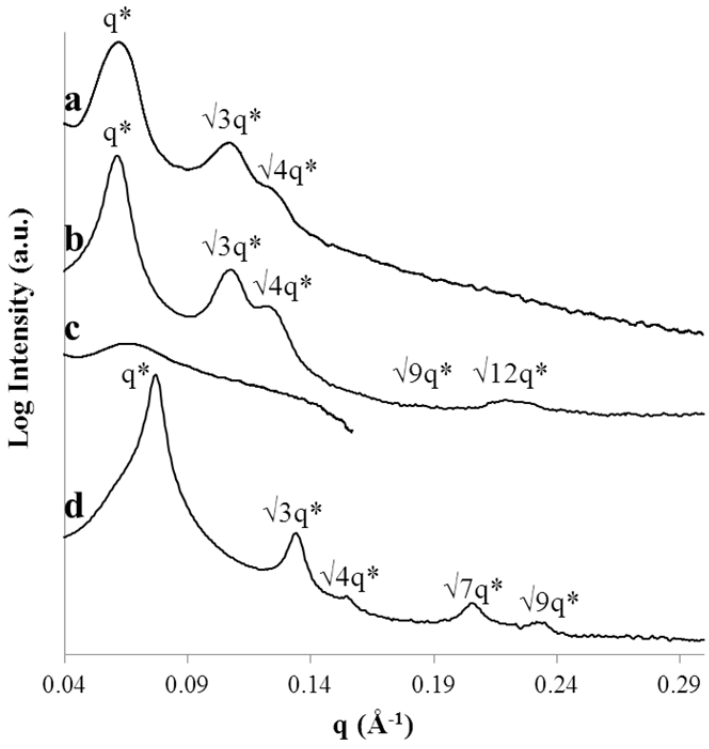


**Figure 3.10:** SAXS profiles after solvent annealing for (a) MH-*b*-PTMSS$_{4.6}$, (b) XGO-*b*-PTMSS$_{4.6}$, (c) βCyD-*b*-PTMSS$_{4.6}$, and (d) MH-*b*-PTMSS$_{2.7}$. Profiles are shifted vertically for clarity. Reprinted with permission from [2]. Copyright 2012 American Chemical Society.

### 3.3 THIN FILM ORIENTATION CONTROL

To explore the thin film self-assembly of the PTMSS-*b*-Oligosaccharides, films were spin coated out of toluene. This solvent reproducibly produced smooth films without defects or film thickness variations. Thin films were prepared by spin coating 1 wt % polymer solutions in toluene at various spin speeds for 60s onto a silicon wafer with

a native oxide layer. No attempt was made to alter the surface energy of the substrate with a surface treatment in this work. Films were spin coated on a Brewer CEE 100CB Spincoater. Film thicknesses were determined with a J.A. Woollam Co, Inc. VB 400 VASE Ellipsometer using wavelengths from 382 to 984 nm with a 65° angle of incidence.

The as-cast, non-annealed films are shown in **Figure 3.11** for a variety of film thicknesses of MH-*b*-PTMSS$_{4.6}$. Atomic force microscopy (AFM) images were obtained using an Agilent 5500 AFM in tapping mode. All AFM images shown are phase images unless otherwise specified and were obtained using 300 series tapping mode AFM tips from Ted Pella with a resonant frequency of 300 kHz and a force constant of 40 N/m. The AFM phase images in **Figure 3.11** exhibit poorly ordered circular features that we believe are kinetically trapped micelles from the spin coating solution in the absence of any subsequent annealing steps and are present regardless of film thickness.

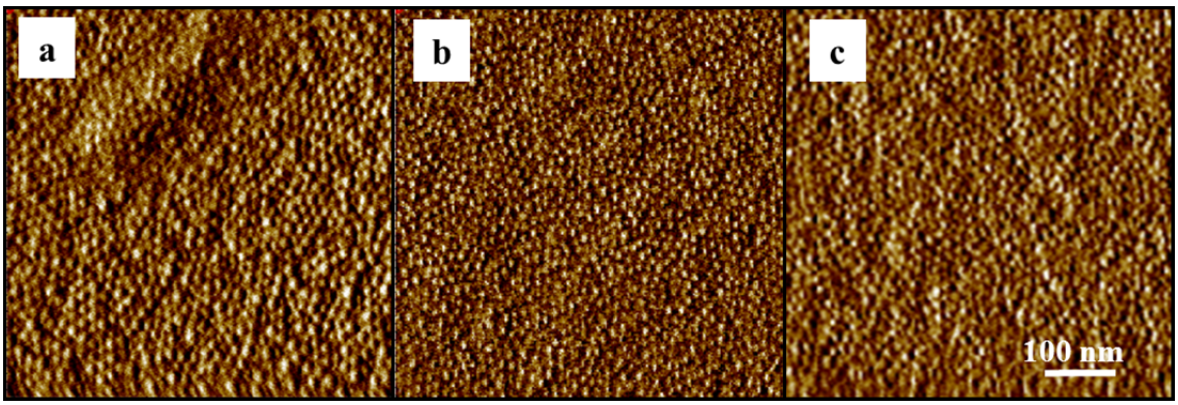


**Figure 3.11:** AFM phase images of as-cast MH-*b*-PTMSS$_{4.6}$ with film thicknesses of a) 6.8 nm, b) 30.1 nm, and c) 124 nm. Reprinted with permission from [2]. Copyright 2012 American Chemical Society.

Toluene is a good solvent for the PTMSS block and a poor solvent for the oligosaccharide block, promoting micelle formation in solution. To support this, the

casting solutions were examined by dynamic light scattering (DLS), which was performed on a Zetasizer nano ZS instrument. These measurements confirmed the presence of micelles presumably consisting of a hydrophobic PTMSS corona around the hydrophilic oligosaccharide core. DLS results show peak particle diameters ranging from 12 to 22 nm for the different block copolymer samples (**Figure 3.12**). This explanation is also consistent with bulk scattering patterns collected from as-precipitated bulk samples which indicated poorly ordered spheres.

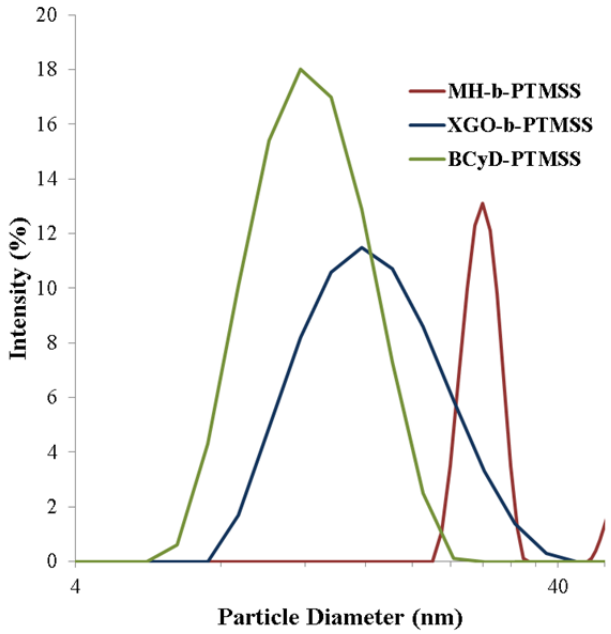


**Figure 3.12:** Dynamic light scattering on 0.5 wt% solutions in toluene of MH-*b*-PTMSS$_{4.6}$, XGO-*b*-PTMSS$_{4.6}$, βCyD-*b*-PTMSS$_{4.6}$ showing peak particle diameters of 22.2 nm, 17.2 nm, and 12.6 nm, respectively.

Approximately 30 nm thick films of MH-*b*-PTMSS$_{4.6}$, XGO-*b*-PTMSS$_{4.6}$, βCyD-*b*-PTMSS$_{4.6}$, and MH-*b*-PTMSS$_{2.7}$ were examined before and after solvent vapor annealing. Before any annealing steps, AFM phase images of MH-*b*-PTMSS$_{4.6}$ (**Figure 3.13a**) and XGO-*b*-PTMSS$_{4.6}$, (**Figure 3.13c**) were collected. The disordered circular

features of as-cast XGO-*b*-PTMSS$_{4.6}$ are consistent with the micelles observed for the as-cast MH-*b*-PTMSS$_{4.6}$ shown in **Figure 3.11**. This result is in perfect agreement with the single broad shoulder observed in the SAXS profiles of non-annealed bulk MH-*b*-PTMSS$_{4.6}$ and XGO-*b*-PTMSS$_{4.6}$ systems.

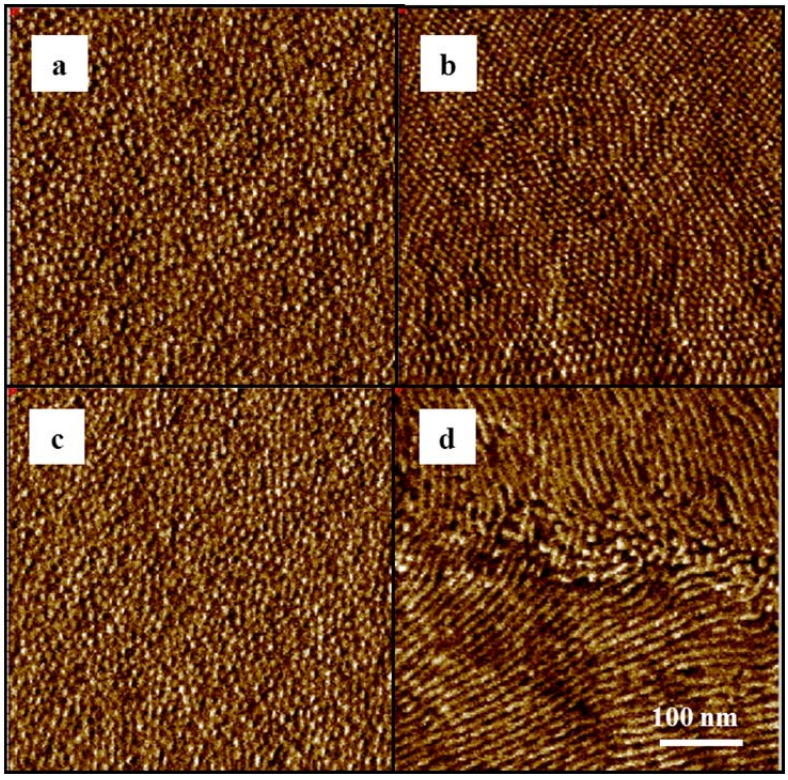


**Figure 3.13:** (a) MH-*b*-PTMSS$_{4.6}$ without annealing. (b) MH-*b*-PTMSS$_{4.6}$ after a 50/50 (by volume) THF/water jar solvent anneal. c) XGO-*b*-PTMSS$_{4.6}$ without annealing. d) XGO-*b*-PTMSS$_{4.6}$ after a 50/50 THF/water jar solvent anneal. Reprinted with permission from [2]. Copyright 2012 American Chemical Society.

AFM phase images of MH-*b*-PTMSS$_{4.6}$ (**Figure 3.13b**) and XGO-*b*-PTMSS$_{4.6}$ (**Figure 3.13d**) films exposed to 50/50 (by volume) THF/water condition for 24 h exhibited regions of circular features (like those dominating **Figure 3.13b**), that could be interpreted as either ordered body-centered cubic spheres (BCC) or hexagonally packed

cylinders oriented perpendicular to the substrate, together with regions of cylindrical domains oriented parallel to the substrate (like those dominating **Figure 3.13d**). Recall that the SAXS patterns in **Figure 3.12** for the bulk samples under the same annealing conditions are consistent with hexagonally packed cylindrical morphology.

While as presented in **Figure 3.13** it appears that the MH-*b*-PTMSS$_{4.6}$ and XGO-*b*-PTMSS$_{4.6}$ have different morphologies and/or orientation in thin films, this is not the case. In repeated experiments, areas with both line and dot structures could be identified for both materials. This observation led to the hypothesis that MH-*b*-PTMSS$_{4.6}$ and XGO-*b*-PTMSS$_{4.6}$, both with oligosaccharide volume fractions of approximately 15%, lie on or close to the BCC sphere/hexagonally packed cylinder phase boundary, which would promote coexistence of these mixed structures, even with their rod–coil block copolymer structure.[26] For such a condition, small perturbations in local film thickness, annealing time, drying, or local solvent vapor concentration during solvent annealing could induce mixed morphologies. Annealing with a mixture of selective solvents could have also changed the $\chi$-parameter of these materials or may have caused a morphology change to occur.

**Figure 3.14** shows an enlarged region of the circular features in the 30 nm thick film that are evident in **Figure 3.13b**, highlighting hexagonal packing and the very small feature size. From the AFM images presented herein, the size of the individual cylinder domains is measured to be approximately 8 nm. It should be noted that many factors, such as AFM tip size (the tip radius used here was reported by the manufacturer to be <10 nm), elastic moduli, instrument resolution, domain boundary definition, and potential domain size change from selective solvent annealing contribute to the discrepancy between the bulk SAXS and AFM measurements and can significantly impact the observed feature sizes.

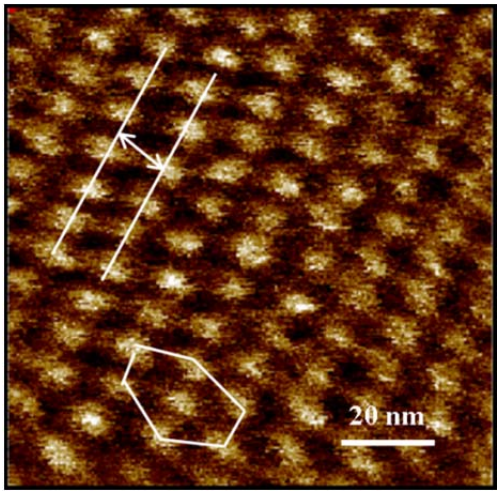


**Figure 3.14:** AFM phase image of MH-*b*-PTMSS$_{4.6}$ after a 50/50 THF/water jar solvent anneal. The row spacing between features shown in this image is 11.4 nm. Reprinted with permission from [2]. Copyright 2012 American Chemical Society.

Unfortunately, it is not possible with a surface sensitive technique, such as AFM, to distinguish between BCC spheres and vertically oriented cylinders within a 30 nm thick film. Supporting evidence for mixed BCC spheres and cylinders can be identified in several regions of **Figure 3.13** with what appears to be epitaxial transformations[27, 28] between crystallographic planes of the BCC lattice and hexagonal packed cylinder lattice providing further evidence for close proximity to a phase boundary. To further investigate the thin film morphology of these materials, a thin film morphology characterization technique such as grazing incidence small angle x-ray scattering (GISAXS) should be used but was not available at the time these experiments were performed.

In contrast to the results shown in **Figure 3.13,** the βCyD-*b*-PTMSS$_{4.6}$ as-cast films exhibited a poorly ordered micelle structure which reproducibly switched to a disordered state after solvent vapor annealing (**Figure 3.15**) consistent with bulk SAXS

data (**Figure 3.12c**). There are several possible reasons why this block copolymer is disordered including the fact that βCyD may be a more rigid block that may distort the phase diagram boundaries through conformational asymmetry effects[29, 30] or the fact that the effective *N* value (proportional to molecular weight) is sufficiently lower than that of MH or XGO to force the BCP into the disordered state after annealing.

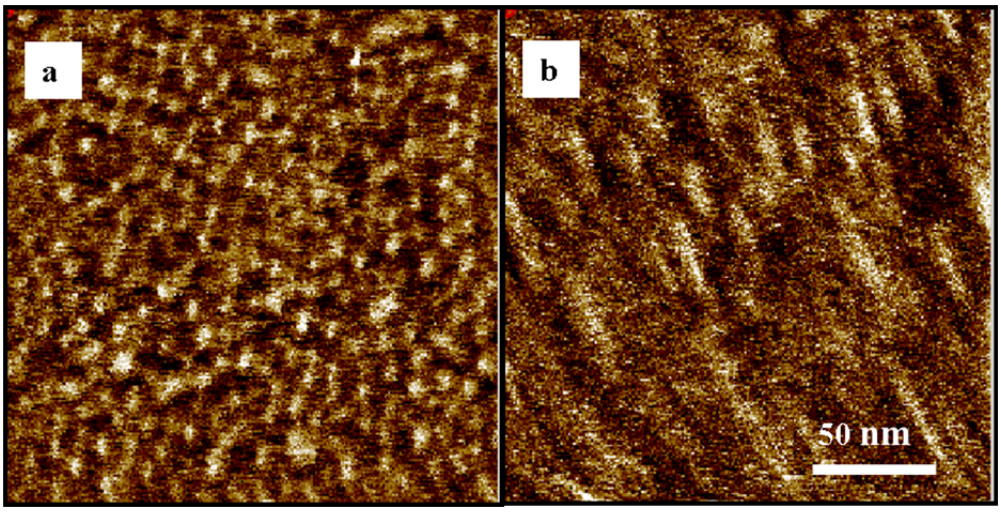


**Figure 3.15:** βCyD-*b*-PTMSS$_{4.6}$ a) as-cast and b) after a 50/50 THF/water jar solvent anneal. Reprinted with permission from [2]. Copyright 2012 American Chemical Society.

A block copolymer that is further from the phase boundary between BCC spheres and hexagonally packed cylinders was also synthesized and examined for comparison to those presented in **Figure 3.13**. This sample, MH-*b*-PTMSS$_{2.7}$, has an oligosaccharide volume fraction of 29.9% and was designed to be more deeply embedded in the cylinder part of the phase diagram. Consistent with the SAXS data from **Figure 3.12d**, this polymer reproducibly exhibits a fingerprint pattern with only some isolated mixed circular features in thin films, likely representing a parallel cylinder orientation (**Figure**

**3.16**). This observation lends some credence to the hypothesis that the samples shown in **Figure 3.13** are near the phase boundary.

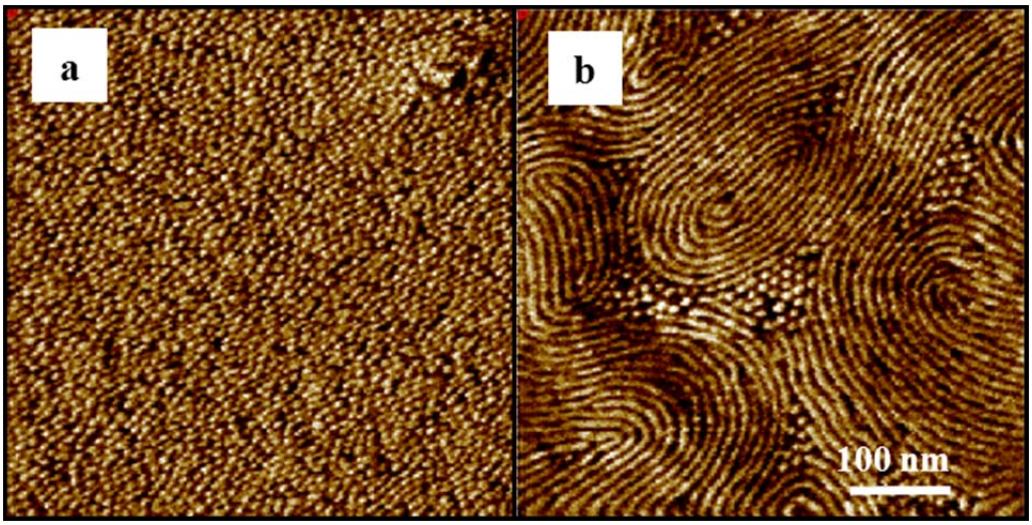


**Figure 3.16:** AFM phase images of (a) as-cast MH-*b*-PTMSS$_{2.7}$, (b) MH-*b*-PTMSS$_{2.7}$ after a 50/50 THF/water jar solvent anneal. Reprinted with permission from [2]. Copyright 2012 American Chemical Society.

### 3.4 Etch Contrast and Pattern Transfer

While the self-assembled features of these block copolymers are much smaller than those that can be made by conventional photolithography, the block copolymer must have high etch contrast in order to be useful for creating high aspect ratio lithographic patterns. Therefore, the etch rates of the oligosaccharide and PTMSS homopolymers were investigated to determine the etch selectivity between the blocks. Polymer solutions for etch studies were filtered with 0.20 μm PTFE filters prior to spin coating. Mica substrates (highest grade V1 mica discs) were purchased from Ted Pella. Prior to ellipsometric measurements, mica substrates were scratched on the back side of the substrate (where no thin film resided) with fine sandpaper to reduce reflections from the

back surface. Oxygen plasma etching was performed with an Oxford Instruments Plasma Lab 80+ operating in inductively coupled plasma mode.

A 15 wt % aqueous solution of a mixture of malto-oligosaccharides (degree of polymerization from 1 to 7) was spin-coated onto a mica substrate. The oligosaccharide mixture was chosen to suppress crystallization, which has been shown to decrease the etch rate of polymeric thin films relative to amorphous polymers.[31] A 4 wt % solution of PTMSS homopolymer was spin-coated onto a silicon wafer with approximately 4 nm native silicon dioxide. The homopolymer films were subjected to a 30 s oxygen etch (90 mTorr chamber pressure, 80 W RF power, 250 W ICP power, 75 sccm $O_2$ flow rate, 5 sccm Ar flow rate), and the film thicknesses were measured to determine etch rates. The results are summarized in **Table 3.3**. The etch selectivity, defined as the oligosaccharide etch rate divided by the PTMSS etch rate, was determined to be 28.3, which represents a considerable improvement over fully petroleum-based block copolymers such as PS-*b*-PMMA, which has an etch selectivity of around 2 depending on the etch conditions.[32]

| Homopolymer Film | Initial Thickness (nm) | Final Thickness (nm) | Etch Rate (nm/sec) |
|---|---|---|---|
| **Oligosaccharide** | 660 ± 20 | 300 ± 7 | 12.1 ± 0.6 |
| **PTMSS** | 135.6 ± 0.3 | 122.8 ± 0.5 | 0.43 ± 0.02 |

**Table 3.3:** Thickness measurements of homopolymer thin films before and after a 30s oxygen plasma etch. The etch selectivity, defined here as the etch rate of the oligosaccharide divided by the etch rate of the PTMSS, is calculated to be 28.3. The error is represented by the standard deviation, taken from 3 different measurements. Reprinted with permission from [2]. Copyright 2012 American Chemical Society.

Block copolymer thin films which were solvent annealed using the aforementioned conditions were subsequently exposed to an oxygen reactive ion etch. Because of the extremely thin nature of the block copolymer film, the sub-10 nm feature

sizes, and a plasma startup transient of our etch tool, the etch rates from **Table 3.3** had to be significantly reduced. Etch conditions were adjusted to 20 mTorr chamber pressure, 10 W RF power, 50 W ICP power, 75 sccm $O_2$ flow rate, 75 sccm Ar flow rate, and 12 s etch time. AFM phase contrast inversion of the etched sample relative to the solvent annealed sample (**Figure 3.17**) is consistent with formation of an oxide layer over the PTMSS matrix domain and suggests at least partial removal of the oligosaccharide block. It is possible that there is a PTMSS wetting layer on top of these films and the oligosaccharide removal in **Figure 3.17b** could be improved by removing this first with a fluorinated etch.

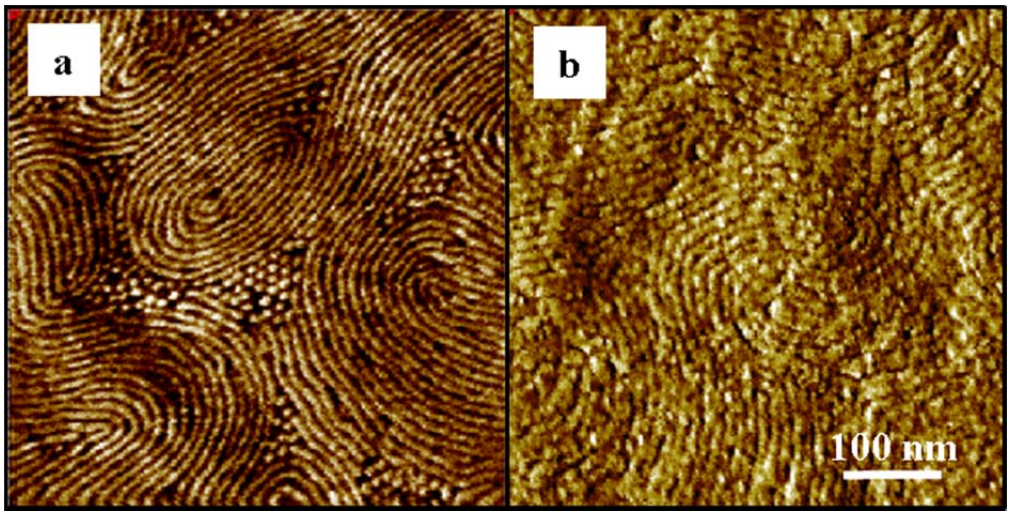


**Figure 3.17:** AFM phase images of MH-*b*-PTMSS$_{2.7}$ (a) after solvent annealing using 50/50 THF/water solvent vapor for 24 h and (b) after solvent annealing and then performing $O_2$ reactive ion etching. Reprinted with permission from [2]. Copyright 2012 American Chemical Society.

### 3.5 CONCLUSIONS

In this chapter, I detailed the synthesis and self-assembly of several PTMSS-*b*-Oligosaccharide materials. Due to their extreme chemical contrast, these materials self-

assemble into some of the smallest reported BCP structures after solvent annealing. While the interaction parameters of these materials cannot be deduced due to the inaccessibility of the glass transition temperature of the oligosaccharide block (interaction parameters must be characterized in the melt state as will be discussed in Chapter 6), they must be large to enable self-assembly of such small features.

While their structures are remarkably small, several features of the synthesis and self-assembly of these materials limit their potential in nanolithography. Without the use of a technique like GISAXS, it is unclear whether the images presented in this chapter are consistent with structures oriented parallel or perpendicular to the plane of the substrate. However, it is unlikely that they are perpendicular since one block of a BCP will typically wet a silicon substrate with native oxide, especially when the surface energies of the blocks are very different. Unfortunately, even with the ability to identify the orientation of the materials, there would not have been enough material left to perform further annealing experiments to find neutral interface conditions. The BCPs were synthesized on very small (several hundred milligram) scales due to the cost of the oligosaccharide starting material (~$600/g) and much of this material is lost in the purification and isolation steps of the functionalization. Therefore by the time bulk studies were performed, very little material was left to perform the thin film experiments presented here. It is also unclear whether the coupling reaction is scalable at high conversions for use in industrial applications like typical living sequential BCP polymerization methods.

A second problem with these materials is the inability to access the $T_g$s of the oligosaccharides since they have low degradation temperatures. While solvent annealing is a potential route to self-assembly and thin film orientation of BCPs, no process in the semiconductor industry currently exists for solvent annealing on a large scale. Solvent

annealing is also much more difficult to control and reproduce from one instrument to another, especially in a jar annealing setup like those used in these experiments. Thermal annealing is more compatible with large-scale manufacturing processes and would be a more desirable method of annealing. Also, without the ability to thermally anneal the samples, the equilibrium bulk properties of the polymers remain unknown. This data would be useful for characterizing the impact of solvent annealing on morphology or domain size that will be explored in Chapter 5 with a different material.

For these reasons, I decided to design another silicon-containing block copolymer with similar chemical contrast to the PTMSS-*b*-Oligosaccharide materials but that is synthesized from inexpensive starting materials, has thermally accessible $T_g$s for both blocks, and has a (likely) scalable synthesis procedure. The material with these design criteria is discussed in Chapter 4 and will be the focus of the rest of this dissertation.

### 3.6 REFERENCES


1. C. M. Bates; J. R. Strahan; L. J. Santos; B. K. Mueller; B. O. Bamgbade; J. A. Lee; J. M. Katzenstein; C. J. Ellison; C. G. Willson, *Langmuir* **2011,** *27*, 2000-2006.
2. J. D. Cushen; I. Otsuka; C. M. Bates; S. Halila; S. Fort; C. Rochas; J. A. Easley; E. L. Rausch; A. Thio; R. Borsali; C. G. Willson; C. J. Ellison, *Acs Nano* **2012,** *6*, 3424-3433.
3. K. A. K. Aissou; I. Otsuka; C. Rochas; S. Fort; S. Halila; R. Borsali, *Langmuir* **2011,** *27*, 4098-4103.
4. A. J. Link; M. K. S. Vink; D. A. Tirrell, *Nat. Protocols* **2007,** *2*, 1884-1887.
5. T. S. Bailey; H. D. Pham; F. S. Bates, *Macromolecules* **2001,** *34*, 6994-7008.
6. J.-S. Wang; K. Matyjaszewski, *Journal of the American Chemical Society* **1995,** *117*, 5614-5615.
7. K. Matyjaszewski; J. Xia, *Chemical Reviews* **2001,** *101*, 2921-2990.
8. A. Goto; T. Fukuda, *Progress in Polymer Science* **2004,** *29*, 329-385.
9. K. Matyjaszewski; K. Davis; T. E. Patten; M. L. Wei, *Tetrahedron* **1997,** *53*, 15321-15329.
10. N. V. Tsarevsky; K. Matyjaszewski, *Chemical Reviews* **2007,** *107*, 2270-2299.
11. A. C. Jones; P. O'Brien, *CVD of compound semiconductors*. Wiley. com: 2008.
12. S. J. Moss; A. Ledwith, *Chemistry of the Semiconductor Industry*. Springer: 1989.

13. W. Jakubowski; K. Matyjaszewski, *Angewandte Chemie International Edition* **2006,** *45*, 4482-4486.
14. W. Jakubowski; K. Min; K. Matyjaszewski, *Macromolecules* **2005,** *39*, 39-45.
15. W. Jakubowski; B. Kirci-Denizli; R. R. Gil; K. Matyjaszewski, *Macromolecular Chemistry and Physics* **2008,** *209*, 32-39.
16. G. D. Fu; L. Q. Xu; F. Yao; K. Zhang; X. F. Wang; M. F. Zhu; S. Z. Nie, *ACS Applied Materials & Interfaces* **2009,** *1*, 239-243.
17. V. Coessens; K. Matyjaszewski, *Journal of Macromolecular Science-Pure and Applied Chemistry* **1999,** *A36*, 667-679.
18. Z. Guo; Y. Jin; T. Liang; Y. Liu; Q. Xu; X. Liang; A. Lei, *Journal of Chromatography A* **2009,** *1216*, 257-263.
19. S. Halila; M. Manguian; S. Fort; S. Cottaz; T. Hamaide; E. Fleury; H. Driguez, *Macromolecular Chemistry and Physics* **2008,** *209*, 1282-1290.
20. I. Otsuka; K. Fuchise; S. Halila; S. b. Fort; K. Aissou; I. Pignot-Paintrand; Y. Chen; A. Narumi; T. Kakuchi; R. Borsali, *Langmuir* **2009,** *26*, 2325-2332.
21. K. A. K. Aissou; I. Otsuka; C. Rochas; S. Fort; S. Halila; R. Borsali, *Langmuir 27*, 4098-4103.
22. M. Harada; T. Suzuki; M. Ohya; D. Kawaguchi; A. Takano; Y. Matsushita; N. Torikai, *Journal of Polymer Science Part B: Polymer Physics* **2005,** *43*, 1486-1494.
23. M. Harada; T. Suzuki; M. Ohya; D. Kawaguchi; A. Takano; Y. Matsushita, *Macromolecules* **2005,** *38*, 1868-1873.
24. Y. Takahashi; T. Kumano; S. Nishikawa, *Macromolecules* **2004,** *37*, 6827-6832.
25. D. J. Kinning; E. L. Thomas, *Macromolecules* **1984,** *17*, 1712-1718.
26. N. Sary; L. Rubatat; C. Brochon; G. Hadziioannou; J. Ruokolainen; R. Mezzenga, *Macromolecules* **2007,** *40*, 6990-6997.
27. K. Kimishima; T. Koga; T. Hashimoto, *Macromolecules* **2000,** *33*, 968-977.
28. M. W. Matsen, *Journal of Chemical Physics* **2001,** *114*, 8165-8173.
29. F. S. Bates; M. F. Schulz; A. K. Khandpur; S. Forster; J. H. Rosedale; K. Almdal; K. Mortensen, *Faraday Discussions* **1994,** *98*, 7-18.
30. M. W. Matsen; F. S. Bates, *Journal of Polymer Science Part B: Polymer Physics* **1997,** *35*, 945-952.
31. E. Wohlfart; J. P. Fernandez-Blazquez; E. Knoche; A. Bello; E. Perez; E. Arzt; A. n. del Campo, *Macromolecules* **2010,** *43*, 9908-9917.
32. R. A. Farrell; N. Petkov; M. T. Shaw; V. Djara; J. D. Holmes; M. A. Morris, *Macromolecules* **2010,** *43*, 8651-8655.

# Chapter 4: Poly(Trimethylsilylstyrene-*block*-*D,L*-Lactide)

While the PTMSS-*b*-Oligosaccharide materials in Chapter 3 self-assemble into some of the smallest reported BCP features, their utility in nanolithography is limited due to the disadvantages in the oligosaccharide block described. For this reason, a new material was investigated to replace the oligosaccharide block as the polar domain while still focusing on the polarity difference between the blocks as a critical design criterion for achieving high $\chi$-parameter materials. Due to its hydrophobicity, relatively easy synthesis, accessible $T_g$, etch resistance, and improvement of $\chi$-parameter over structurally similar PS materials (Chapter 6), PTMSS was used as the nonpolar domain in the studies of this chapter.

In addition to poly(*D,L*-lactide) (PLA), which was ultimately chosen as the hydrophilic block to replace the oligosaccharides, several relatively polar domains such as poly(ethylene oxide) (PEO) and poly(vinyl alcohol) (PVA) were considered. The choice of PLA as the hydrophilic block was ultimately made for two reasons; ease of synthesis and predicted $\chi$-parameter. PEO is synthesized controllably using anionic polymerization.[1] However, ethylene oxide (EO) monomer is hazardous to work with since it is extremely toxic and must be handled as a condensed gas for purification. PVA cannot be directly polymerized and instead requires post-functionalization[2] of synthetically complex[3] poly(vinyl acetate) (PVAc) due to side reactions in polymerization techniques with the acidic OH functional group. PLA, however, can be polymerized easily in one step by an aluminum complex-catalyzed ring-opening polymerization procedure from a hydroxyl-functionalized macroinitiator to form a BCP.[4]

Secondly, the reported $\chi$-parameters of BCPs with these relatively polar domains and a PS domain played a role in material selection. The $\chi$-parameter of PS-*b*-PVA has

not been characterized to the best of my knowledge. Not knowing this value for comparison in addition to being difficult to synthesize made it a less desirable candidate. The χ-parameters of PS-*b*-PLA[5] and PS-*b*-PEO[6] are known and PS-b-PLA's is significantly higher. I believed this made PLA a better choice as the polar domain since adding a TMS group to the PS domain would likely increase the chemical incompatibility of an already relatively high-χ polymer even more. Lactide monomer is also an inexpensive biorenewable resource and PLA has been shown to exhibit biodegradablility,[7] further increasing its attractiveness and sustainability for commercial applications.

Lactide monomer exists as three stereoisomers: *D*-lacide, *L*-lactide, and *meso*-lactide (**Figure 4.1**).[8] Due to their stereoregularity, homopolymers formed using these monomer units are crystalline.[2] I chose to avoid crystalline materials due to the potential for unpredictable self-assembly from crystal breakout[9] and high melting points.[2, 10] Therefore, *D,L*-lactide (a physical mixture of the *D*- and *L*- isomers) was chosen as the lactide monomer since crystallization has been shown to be suppressed in polymers formed from this mixture.[2]

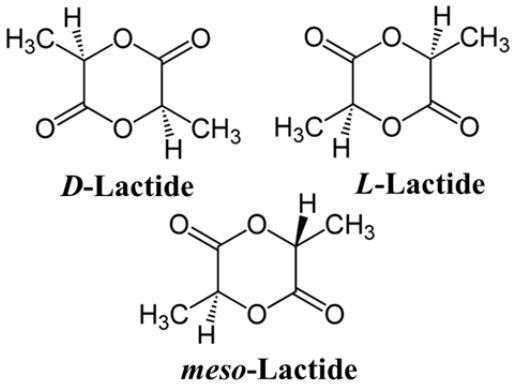


**Figure 4.1**: Stereoisomers of lactide: *D*-lactide, *L*-lactide, and *meso*-lactide. Image is public domain from [8].

## 4.1 Synthesis by Anionic and Ring-Opening Polymerization

PTMSS-*b*-PLA was synthesized through a combination of anionic and ring-opening polymerization (**Scheme 4.1**).[11] The conditions for anionic polymerziation and functionalization of PTMSS were described in Chapter 2. Briefly, An appropriate amount of *sec*-butyllithium was added dropwise to purified cyclohexane under Ar atmosphere and stirred at 40 °C for ten minutes. Several drops of TMSS monomer were added to seed the polymerization and allowed to react for fifteen minutes to initiate all chains without significant propagation. After this time, the remaining TMSS was added dropwise. The solution reacted for 24 hours. The polymer was endcapped with a hydroxyl functionality by adding EO (which had been distilled twice over butyl magnesium chloride) and was allowed to react for 24 hours. In the presence of lithium counter-cations, only one unit of EO will add to the living chain ends. Degassed methanol was added after this time to quench the living anions. The polymer was precipitated in methanol and dried *in vacuo*.

Lactide polymerizations were performed in a drybox using toluene which had been distilled twice over calcium hydride to avoid side reactions with water. *D,L*-lactide was recrystallized from ethyl acetate to remove impurities from the monomer. The reaction procedure was modified and optimized from a previously-reported kinetic study of PLA synthesis.[4] One mole of triethylaluminum ($AlEt_3$) solution (1.1 M) was added dropwise to PTMSSOH in toluene per two moles PTMSSOH to form an aluminum alkoxide macroinitiator. After stirring this solution for 2 hours, *D,L*-lactide was added, the flask was capped, brought out of the drybox, submerged in an oil bath at 90 °C and stirred for 6 hours. After this time, the reaction was quenched with 1 mL 1N HCl and precipitated in a 50:50 methanol:water mixture due to significant solubility of the polymer in pure methanol. The polymer was filtered and dried under vacuum. PLA

homopolymer was synthesized using the same procedure as PTMSS-*b*-PLA, however dry isopropanol was used as the initiator instead of PTMSSOH.

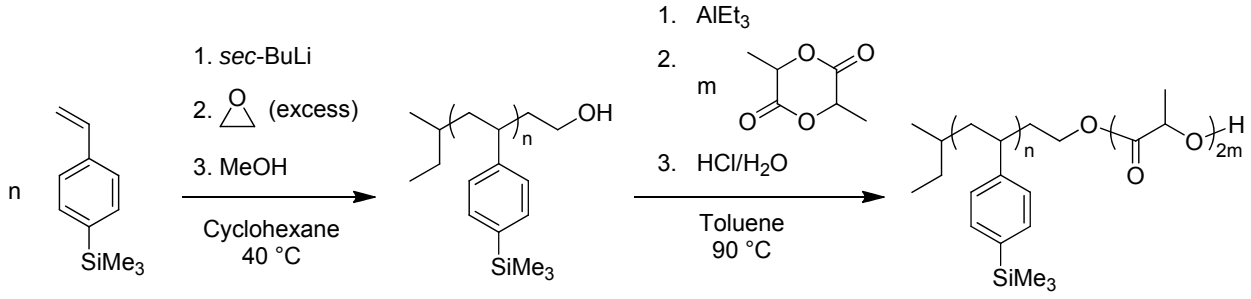


**Scheme 4.1**: Synthesis of PTMSS-b-PLA by a combination of anionic and ring-opening polymerization. Reprinted with permission from [11]. Copyright 2012 American Chemical Society.

The molecular weight and PDI of PTMSSOH and the PDI of the BCP were determined by GPC (representative traces in **Figure 4.2**). Since the PDIs of the first block and BCPs were low and there was a complete peak shift to higher molecular weight in the BCP, it is unlikely that there were coupling or untimely termination events. The molecular weight of the PLA block and volume fractions of the BCP were determined by $^{1}$H NMR using the molecular weight of the PTMSSOH block determined from GPC, the mole fractions from NMR, and the densities of PTMSS and PLA (1.15 g/mL)[12] (**Figure 4.3**).

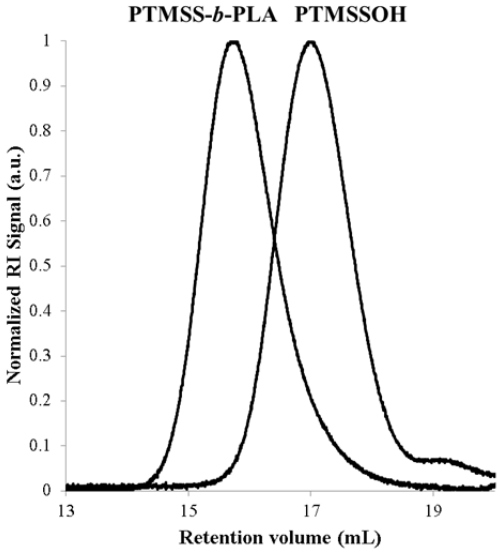


**Figure 4.2**: GPC traces of $PTMSSOH_{5.5}$ and $PTMSS_{5.5}$-*b*-$PLA_{6.6.}$ Reprinted with permission from [11]. Copyright 2012 American Chemical Society.

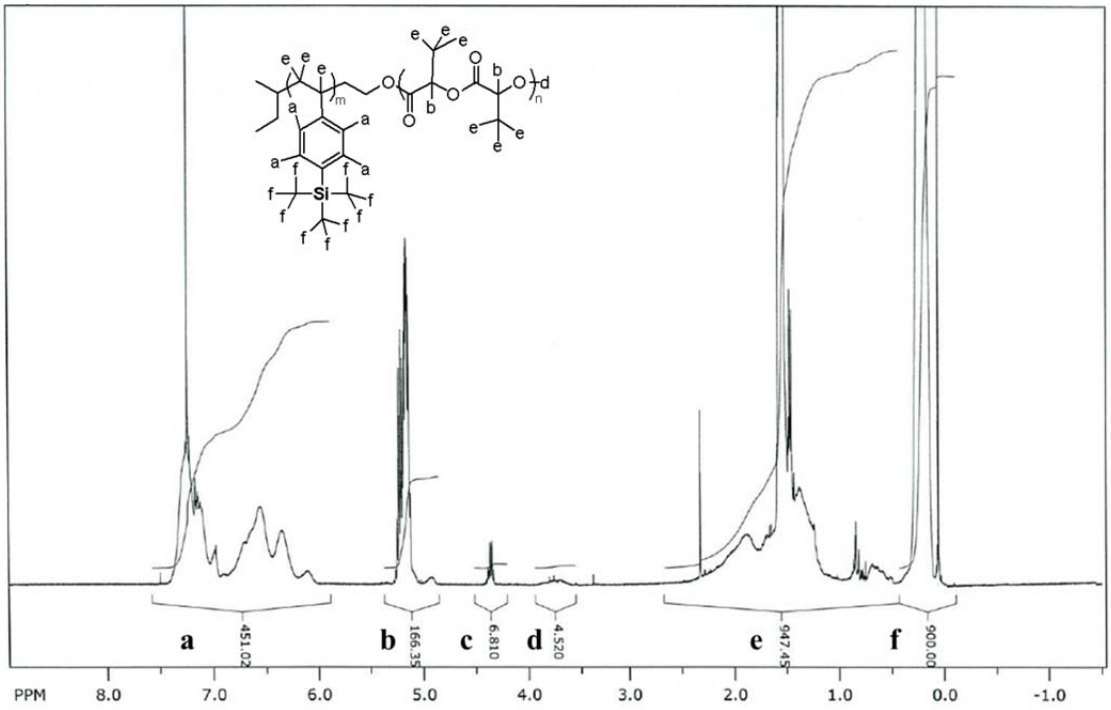


**Figure 4.3**: Representative $^{1}H$ NMR trace from $PTMSS_{5.5}$-*b*-$PLA_{3.7}$. Peaks f and b were used to determine the mole fractions of the material. Peak c is residual THF. Reprinted with permission from [11]. Copyright 2012 American Chemical Society.

The thermal properties of the material were then investigated to determine appropriate annealing conditions for the bulk and thin film samples. The $T_g$s of the blocks were determined from a DSC trace of $PTMSS_{5.5}$-*b*-$PLA_{3.7}$ (**Figure 4.4**). A $T_g$ of ~48 °C was observed for PLA and a $T_g$ of ~100 °C was observed for PTMSS from this analysis. The degradation temperatures of the homopolymers were investgated by TGA (**Figure 4.5**). A $T_d$ of ~250 °C was observed for PLA and ~325 °C for PTMSS.

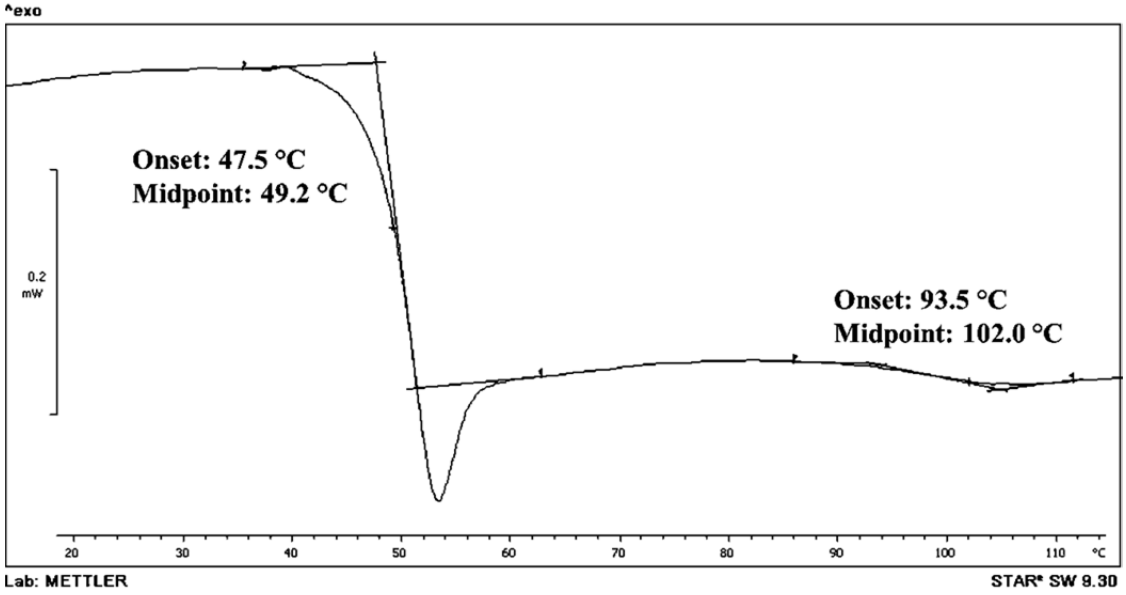


**Figure 4.4**: DSC trace of $PTMSS_{5.5}$-*b*-$PLA_{3.7}$. Reprinted with permission from [11]. Copyright 2012 American Chemical Society.

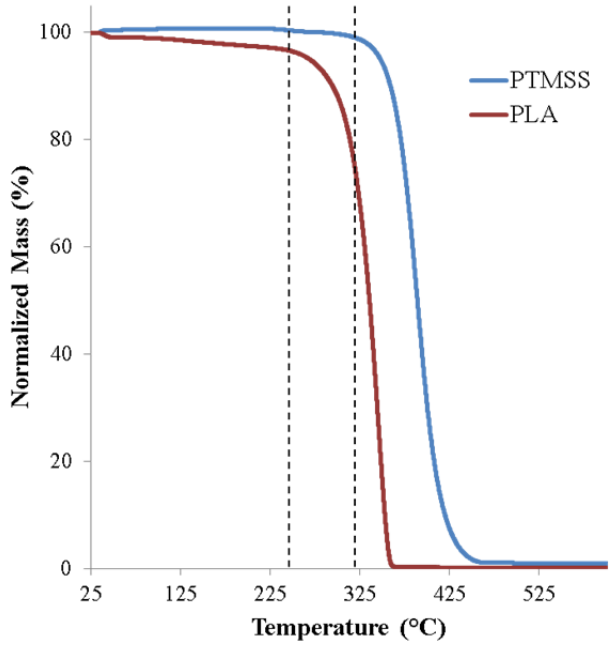


**Figure 4.5**: TGA traces of PTMSSOH and PLA homopolymer. The slight weight loss around 100 °C in the PLA sample is likely due to water loss since PLA is somewhat hygroscopic. The lines are to guide the eye. Reprinted with permission from [11]. Copyright 2012 American Chemical Society.

SAXS was then performed on bulk samples to determine the morphologies and feature dimensions of the PTMSS-*b*-PLA polymers synthesized. Before collecting SAXS patterns, bulk samples were annealed in air at 160 °C for 15 minutes to facilitate self-assembly, a temperature between the $T_g$s and $T_d$s of PTMSS and PLA. The SAXS diffraction pattern from the detector and integrated 2-D pattern of a representative lamellae-forming polymer is shonwn in **Figure 4.6.** Bulk morphologies of samples after thermal annealing were identified by the locations of the peak scattering ratios.

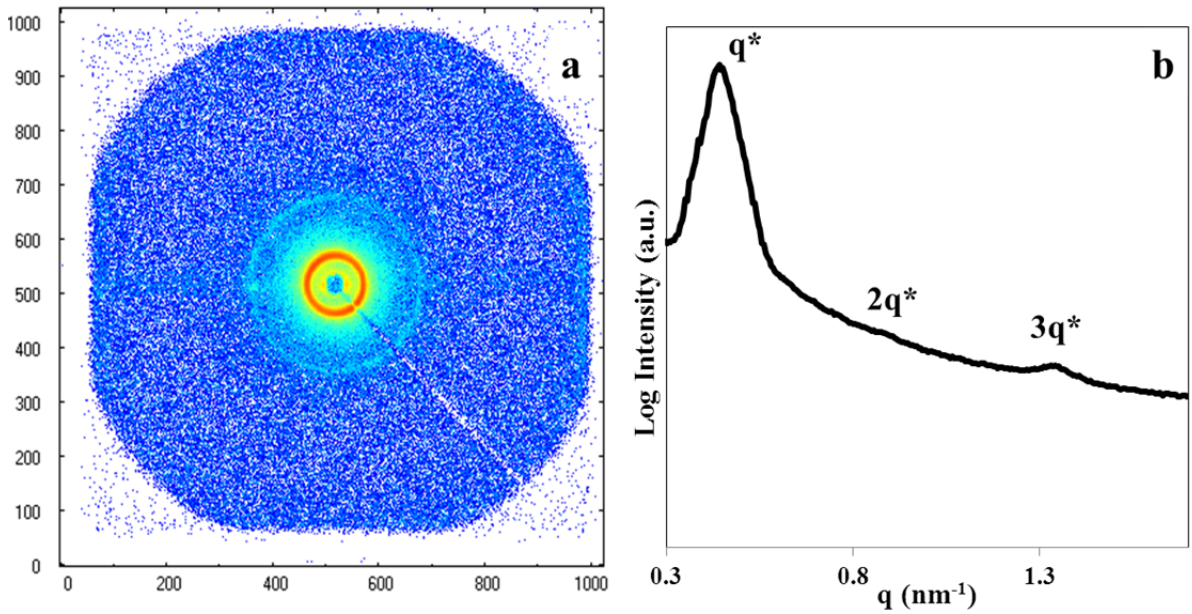


**Figure 4.6**: a) X-ray diffraction pattern obtained for $PTMSS_{5.5}$-*b*-$PLA_{6.6}$ from the SAXS detector. b) Scattering profile obtained after azimuthally integrating the pattern in **Figure 4.6a**.

The characterization data for the PTMSS-*b*-PLA polymers that will be studied in this chapter, Chapter 5, and Chapter 6 are summarized in **Table 4.1**.

| Sample | $M_n$ PTMSSOH | PDI PTMSSOH | $M_n$ PLA | PDI BCP | Vol. % PLA | Morphology | d (nm) |
|---|---|---|---|---|---|---|---|
| **$PTMSS_{5.5}$-*b*-$PLA_{3.7}$** | 5500 | 1.15 | 3700 | 1.08 | 36.2 | Cylindrical | 12.1 |
| **$PTMSS_{5.5}$-*b*-$PLA_{6.5}$** | 5500 | 1.15 | 6500 | 1.07 | 49.7 | Lamellar | 15.3 |
| **$PTMSS_{5.5}$-*b*-$PLA_{6.6}$** | 5500 | 1.15 | 6600 | 1.06 | 50.0 | Lamellar | 14.6 |
| **$PTMSS_{2.3}$-*b*-$PLA_{1.7}$** | 2300 | 1.11 | 1700 | 1.10 | 38.7 | Disordered | - |

**Table 4.1**: Characterization data for the PTMSS-*b*-PLA polymers studied in Chapters 4, 5, and 6.

## 4.2 THIN FILM ORIENTATION CONTROL

The bulk SAXS of the PTMSS-*b*-PLA materials showed that they self-assemble into small structures, indicating strong segregation and thus fulfilling one of the critical criteria for a BCP material in lithographic applications. The $\chi$-parameter was subsequently studied and will be discussed in Chapter 6. After successfully synthesizing and characterizing the materials in the bulk, the next challenge was to control the orientation in thin films.

### 4.2.1 Solvent Annealing with Cyclohexane

Lamellae- and cylinder-forming PTMSS-*b*-PLA were spin coated onto silicon substrates with native oxide layers (without modifying the substrate with a surface treatment). The as-cast films exhibited some kinetically-trapped self-assembly from spin-coating (**Figures 4.7a and d**). After thermal annealing, the domains likely oriented parallel to the plane of the substrate due to the low surface of the PTMSS block as evidenced by a fingerprint pattern for the bulk cylinder-forming sample and a featureless structure for the bulk lamellae-forming sample by top-down imaging (**Figures 4.7b and e**).

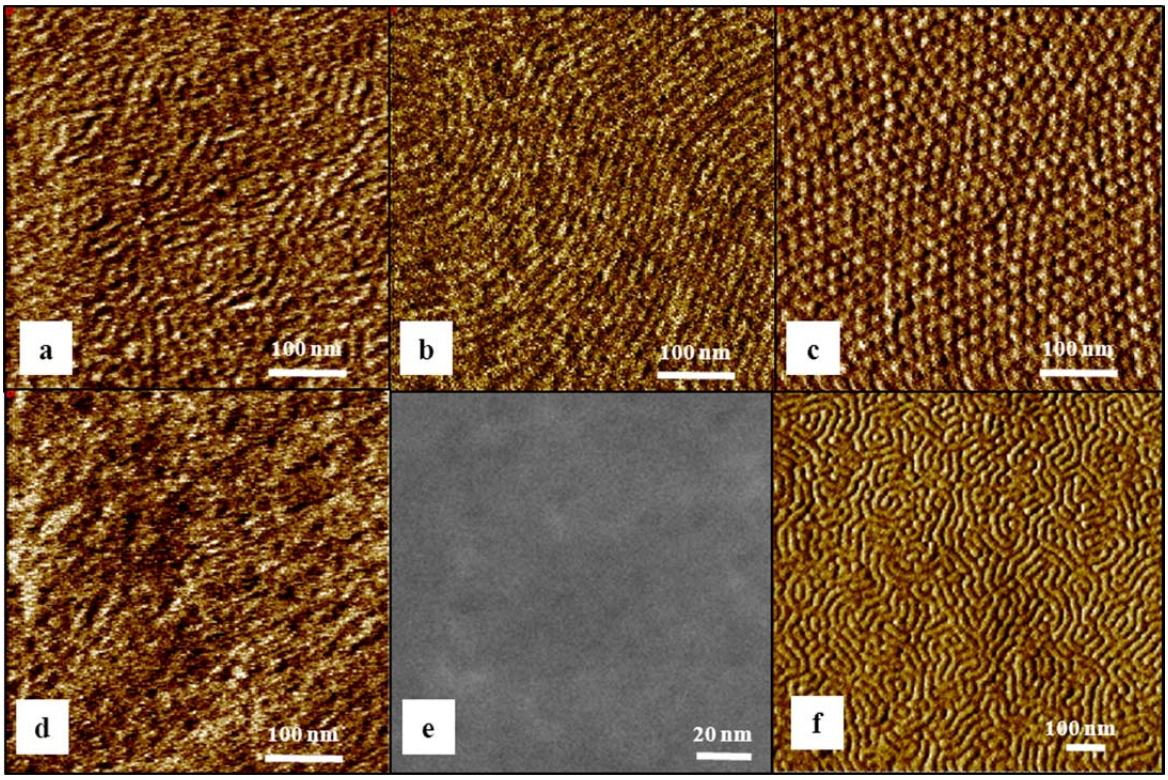


**Figure 4.7**: AFM phase images of a 15 nm thick cylinder-forming $PTMSS_{5.5}$-*b*-$PLA_{3.7}$ film a) as-cast, b) after thermally annealing the sample for four hours at 150 °C, c) after solvent annealing the sample with cyclohexane for four hours, and a 35 nm thick lamellae-forming $PTMSS_{5.5}$-*b*-$PLA_{6.5}$ film d) as-cast, e) SEM image after thermally annealing the sample for fifteen minutes at 160 °C, and f) after solvent annealing the sample with cyclohexane for four hours. Reprinted with permission from [11]. Copyright 2012 American Chemical Society.

Thin films were then solvent annealed in the same jar annealing setup as the PTMSS-*b*-Oligosaccharides using various solvents such as tetrahydrofuran, dimethylformamide, acetone, cyclohexane, mixtures of cyclohexane and acetone, and mixtures of tetrahydrofuran and water. Each of these solvents caused the film to dewet the substrate except the films that were annealed with cyclohexane vapor only, which improved the thin film order. Cylinder-forming $PTMSS_{5.5}$-*b*-$PLA_{3.7}$ was solvent annealed with cyclohexane for various times to investigate the impact of annealing time on thin

film orientation (**Figure 4.8**). A transition from a fingerprint pattern to hexagonally packed dots occured between 2 and 4 hours of annealing time. This transition could represent either a change in the orientation of cylinder domains or the change in morphology from cylinders to BCC spheres.

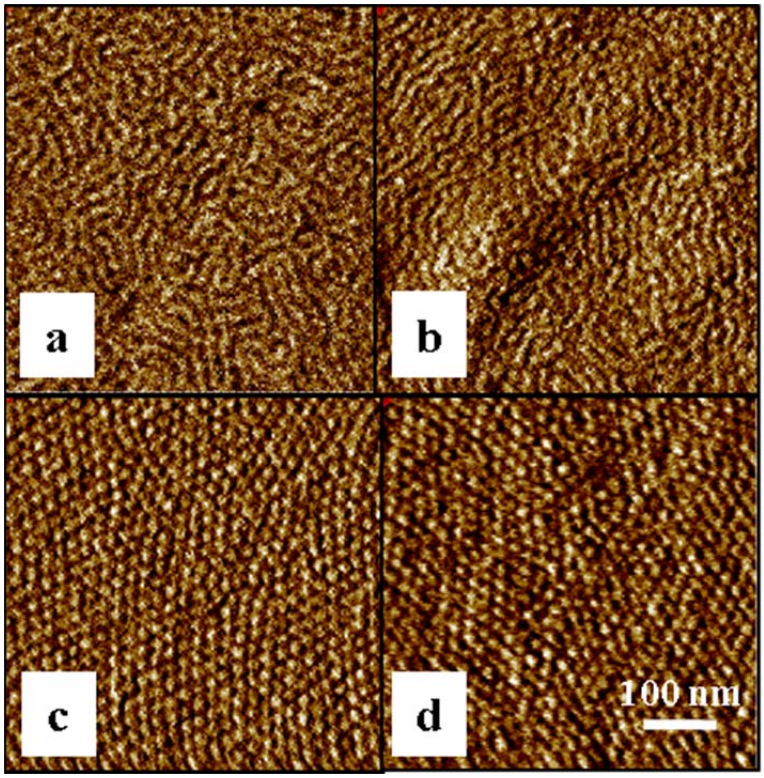


**Figure 4.8**: $PTMSS_{5.5}$-*b*-$PLA_{3.7}$ after annealing with cyclohexane for a) 1h, b) 2h, c) 4h, and d) 24h. Reprinted with permission from [11]. Copyright 2012 American Chemical Society.

After 4 hours of annealing with cyclohexane, the bulk cylinder- and lamellae-forming BCPs produced the structures observed in **Figures 4.7c and f**. It is impossible to distinguish from the top-down imaging alone whether the hexagonally packed dots observed in **Figure 4.7c** are perpendicularly oriented cylinders or BCC spheres. Likewise, it is unclear whether the fingerprint pattern observed in **Figure 4.7f** represents

lamellae oriented perpendicular to the plane of the substrate or parallel cylinders. Grazing incidence small angle x-ray scattering (GISAXS) is a technique commonly used to determine the morphology and through-film strucuture of a BCP film, however at the time these experiments were performed I did not have access to GISAXS. Fortunately, another technique can be used to predict the morphology of a BCP in a thin film.

As described in Chapter 1, if one block preferentially wets one or both interfaces, the BCP will adopt a parallel orientation. If a BCP is spin coated to a film thickness that is incommensurate with the domain periodicity and the domains orient parallel to the substrate upon annealing, it will adopt a frustrated microstructure to maximize the concentration of the low surface energy material at the surface of the film. This causes the structures to terrace, or form micron-scale "islands" or "holes" that are observed in optical and scanning electron microscopy (SEM) images. However, only parallel orientations will terrace since through-film orientations do not form these layers of structure (**Figure 4.9**). So with the combination of the nanostructure (dots or lines) and microstructure, the morphology in the thin film can be predicted. For example, a dot pattern indicates perpendicular cylinders or spheres are present but if terracing is observed the morphology is spherical. Likewise, a fingerprint pattern is representative of parallel cylinders or perpendicular lamellae but terracing indicates that the morphology is cylindrical. A more complete discussion on the implications of terracing will take place in Section 4.2.2.1.

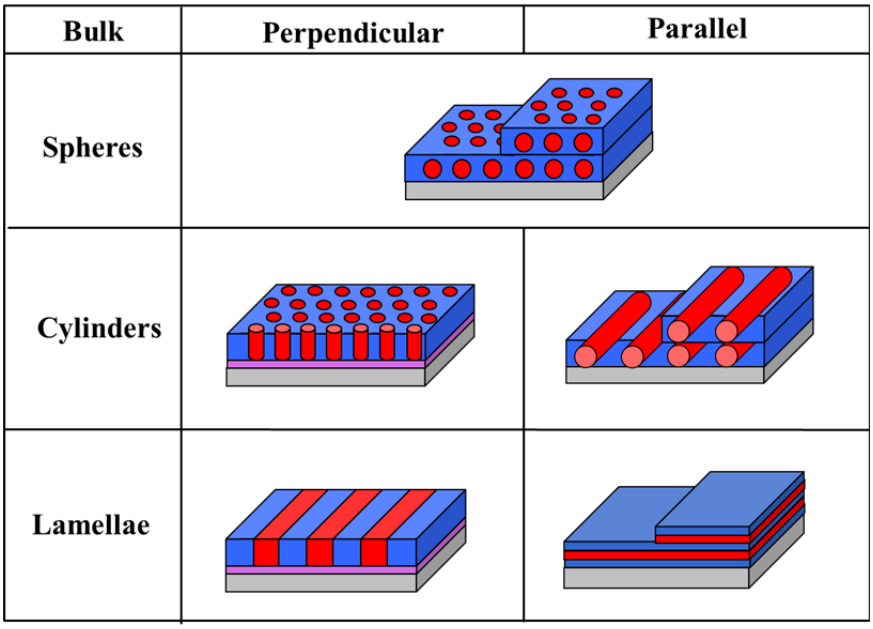


**Figure 4.9**: Terracing with parallel orientations vs. no terracing with perpendicular orientations.

This technique was used to identify the morphologies of the PTMSS-*b*-PLA films annealed with cyclohexane. Low magnification SEM images indicate terracing for both the bulk cylinder (**Figure 4.10a**) and lamellae (**Figure 4.10b**) solvent annealed samples. These SEM images were collected from thin films subjected to the same annealing conditions as samples from **Figures 4.7c and f**, respectively. This means that the dot pattern observed for the bulk cylinder sample and the line pattern observed for the bulk lamellae sample represent a morphology change upon annealing into spherical and parallel cylinder orientation, respectively. SEM images from this point forward were collected on a Zeiss Ultra 55 SEM at HGST.

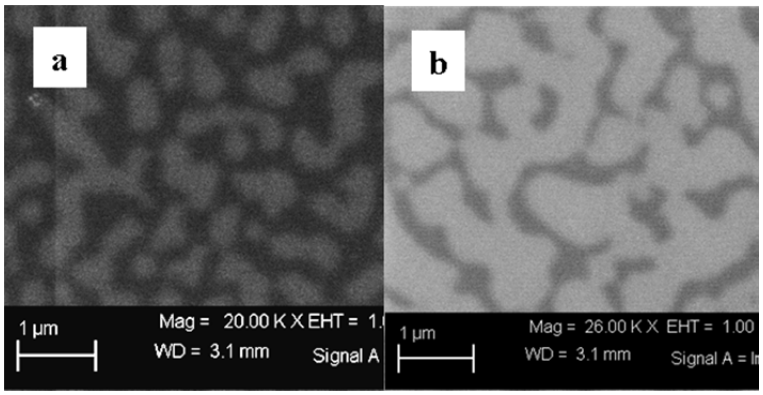


**Figure 4.10**: Low magnification SEM images of a) cylinder-forming $PTMSS_{5.5}$-*b*-$PLA_{3.7}$ and b) lamellae-forming $PTMSS_{5.5}$-*b*-$PLA_{6.5.}$

### 4.2.2 Solvent Annealing with a Mixed Solvent System

It was suspected that a morphology change was taking place upon annealing with cyclohexane due to an effective volume fraction change within the BCP. This could occur if cyclohexane was preferentially segregating into one domain of the PTMSS-*b*-PLA. Morphology changes when solvent annealing with selective solvents have been reported previously.[13-15]

The polymer-solvent interaction parameter $\chi_{P\text{-}S}$ can be used to predict the degree of interaction between a polymer domain and solvent; this parameter can be used as a tool for identifying solvent selectivity. $\chi_{P\text{-}S}$ for a given polymer-solvent pair can be estimated based on solubility parameters of the constituents (**Equation 4.1**) where $V_s$ represents the molar volume of the solvent, R is the ideal gas constant, and $\delta_S$ and $\delta_P$ are the solvent and polymer solubility parameters, respectively.[16]

$$\chi_{P-S} = \frac{V_s}{RT}(\delta_s - \delta_p)^2 \qquad \textbf{Eq. 4.1}$$

The solubility parameters of PLA, cyclohexane, and acetone (another solvent that was of interest in this work) are reported[16] but the solubility parameter of PTMSS is experimentally unknown. In this work, Hildebrand solubility parameters were used instead of the 3-dimensional Hansen solubility parameters since the solubility parameter of PTMSS had to be calculated. The solubility parameter of an unknown material can be estimated using a group contribution method. **Equation 4.2** can be used where $\rho_p$ is the density of the polymer, $F_j$ is the molar attraction constant of each group, and $M_i$ is the molecular weight of the repeat unit. $\rho_p = 0.963 g/cm^3$ for PTMSS, $M_i = 176.35$ for TMSS, and end groups were neglected. In the absence of data for the molar attraction constant of a silicon group with four bonds, the molar attraction constant for a silicon group with two bonds was used. The molar attraction constants and number of groups used in estimating the solubility parameter of PTMSS are reported in **Table 4.2**.

$$\delta_i = \frac{\rho_i \sum F_j}{M_i} \qquad \textbf{Eq. 4.2}$$

| | $F_j$ ($MPa^{1/2}*cm^3/mol$) | Number of groups |
|---|---|---|
| **-Si-** | -77 | 1 |
| **-CH3** | 437 | 3 |
| **-CH2-** | 57 | 1 |
| **=CH-** | 272 | 1 |
| ***p*-phenylene** | 1350 | 1 |
| | **Total F** | **2913 $MPa^{1/2}*cm^3/mol$** |

**Table 4.2**: Data used to calculate the molar attractive constant of PTMSS. Reprinted with permission from [11]. Copyright 2012 American Chemical Society.

The solubility parameter of PTMSS was calculated from **Equation 4.2** and the other known material solubility parameters and relevant material constants are reported in

**Table 4.3**. From these values, the $\chi_{P\text{-}S}$ values were calculated for the various solvent-polymer pairs from **Equation 4.1** and are reported in **Table 4.4**.

| Polymer | $\delta_P$ (MPa$^{1/2}$) | Solvent | $\delta_S$ (MPa$^{1/2}$) | $V_s$ (cm$^3$/mol) |
|---|---|---|---|---|
| **PTMSS** | 17.2 | **Cyclohexane** | 16.8 | 108.0 |
| **PLA** | 20.5 | **Acetone** | 20.3 | 73.4 |

**Table 4.3**: Solubility parameters for the polymers and solvents investigated in this work and the molar volumes of the solvents. Reprinted with permission from [11]. Copyright 2012 American Chemical Society.

| | |
|---|---|
| $\chi_{PTMSS\text{-}cyclohexane}$ | 0.347 |
| $\chi_{PTMSS\text{-}acetone}$ | 0.937 |
| $\chi_{PLA\text{-}cyclohexane}$ | 0.625 |
| $\chi_{PLA\text{-}acetone}$ | 0.341 |

**Table 4.4**: Calculated $\chi_{P\text{-}S}$ values for the polymer-solvent pairs of interest in this work. Reprinted with permission from [11]. Copyright 2012 American Chemical Society.

Based on the $\chi_{P\text{-}S}$ values calculated and reported in **Table 4.4**, cyclohexane is preferential for the PTMSS block. The $\chi_{P\text{-}S}$ values calculated in this study are 0.347 for PTMSS-cyclohexane and 0.937 for PLA-cyclohexane and typically, $\chi_{P\text{-}S}$ values smaller than 0.5 represent a miscible polymer-solvent pair while values greater than 0.5 indicate polymer/solvent immiscibility.

To prevent the morphology change from occurring during solvent annealing, it was hypothesized that adding a second solvent that preferentially swells the PLA domain to the cyclohexane annealing condition would prevent a significant change in relative block volume fraction by swelling both domains equally. Acetone is a selective solvent for PLA as evidenced by $\chi_{P\text{-}S}$ values of 0.625 for PTMSS-acetone and 0.341 for PLA-acetone. When the second solvent was introduced to the annealing protocol, I switched to

annealing in a custom chamber that allowed control over the solvent vapor composition and sample temperatures, and also allowed measurement of the film thickness *in situ*. Solvent vapor was introduced to thin polymer films by bubbling constant flow rates of nitrogen controlled by mass flow controllers through solvent reservoirs and into a chamber containing the thin film samples. The degree of swelling could be adjusted by changing the flow rate of nitrogen through the bubblers, essentially adjusting the mole fraction (or partial pressure) of each solvent within the chamber. The experimental work performed in the rest of this chapter and in Chapter 5 was performed on such a controlled solvent annealing chamber at HGST, as described by **Figure 1.12b**. In each experiment, the thickness of a 55 nm thick film sample of the same material being annealed was monitored by a Filmetrics F20 reflectometer through a glass window in the chamber with the sample of interest. The film thickness of this thicker film was monitored instead of the actual sample to reduce noise in the thickness measurements of the thinner films. It should also be noted that reflectometer measurements of film thickness rely on the refractive index of the polymer remaining constant during the experiment. It is likely that the refractive index of the film changes when swollen with solvent and this could affect the measurement data. Investigation into the role of the change in refractive index with swelling on the film thickness measurements is the subject of further study in this work.

Based on gravimetric analysis of condensed solvents from the outlet stream for a condition of 60 standard cubic centimeters per minute (sccm) nitrogen gas passed through the cyclohexane solvent reservoir, 40 sccm nitrogen gas passed through the acetone reservoir, and 5 sccm nitrogen gas passed through the bypass stream at room temperature, samples in the solvent annealing chamber under these conditions were exposed to vapor with a composition of $x_{Cyclohexane} = 0.049$, $x_{Acetone} = 0.084$, and $x_{N2} = 0.867$, where x is the mole fraction of the component. Assuming the molar ratio of cyclohexane to acetone in

the vapor is identical to the ratio of the mass flow rates of nitrogen through the respective solvent reservoirs, this composition is approximately consistent with an assumption of saturated vapor based on the vapor pressures of the solvents ($p_{cyclohexane}$* = 77 mmHg and $p_{acetone}$ * = 184 mmHg, data from Sigma Aldrich at 20 °C).

Homopolymer film swelling data also supports the conclusion that cyclohexane is PTMSS-preferential and acetone is PLA-preferential. From **Figure 4.11a**, a homopolymer film of PTMSS swells significantly more than a PLA film when 60 sccm of nitrogen is bubbled through cyclohexane into the chamber. Homopolymer film swelling data collected when 40 sccm of nitrogen was bubbled through acetone (**Figure 4.11b**) also supports this conclusion. Unfortunately, the degree of PLA homopolymer swelling cannot be identified for this condition because the film dewets quickly, but dewetting indicates that PLA is likely highly swollen by the acetone and the PTMSS film swells significantly less in acetone than in cyclohexane. When swollen with a mixture of the solvents with the same flow rates through the bubblers indicated previously (60 sccm cyclohexane, 40 sccm acetone), both homopolymer films swelled to similar thicknesses (**Figure 4.11c**). This suggests that a block copolymer of these two components would likely not change significantly in volume fraction from the bulk material when solvent annealed under these conditions. When a $PTMSS_{5.5}$-*b*-$PLA_{6.6}$ film was annealed under these conditions the film swelled approximately 20% (**Figure 4.11d**). For all the mixed solvent annealing experiments and subsequent studies, a lamellae-forming sample was used due to the interest in the lamellar morphology for bit-patterned media,[17] the most likely entry point for application of BCPs in lithography. Since I had used all of the $PTMSS_{5.5}$-*b*-$PLA_{6.5}$ I had made, I synthesized and subsequently used lamellae-forming $PTMSS_{5.5}$-*b*-$PLA_{6.6}$, which was very similar in composition and molecular weight to the sample investigated in the cyclohexane-only annealing studies.

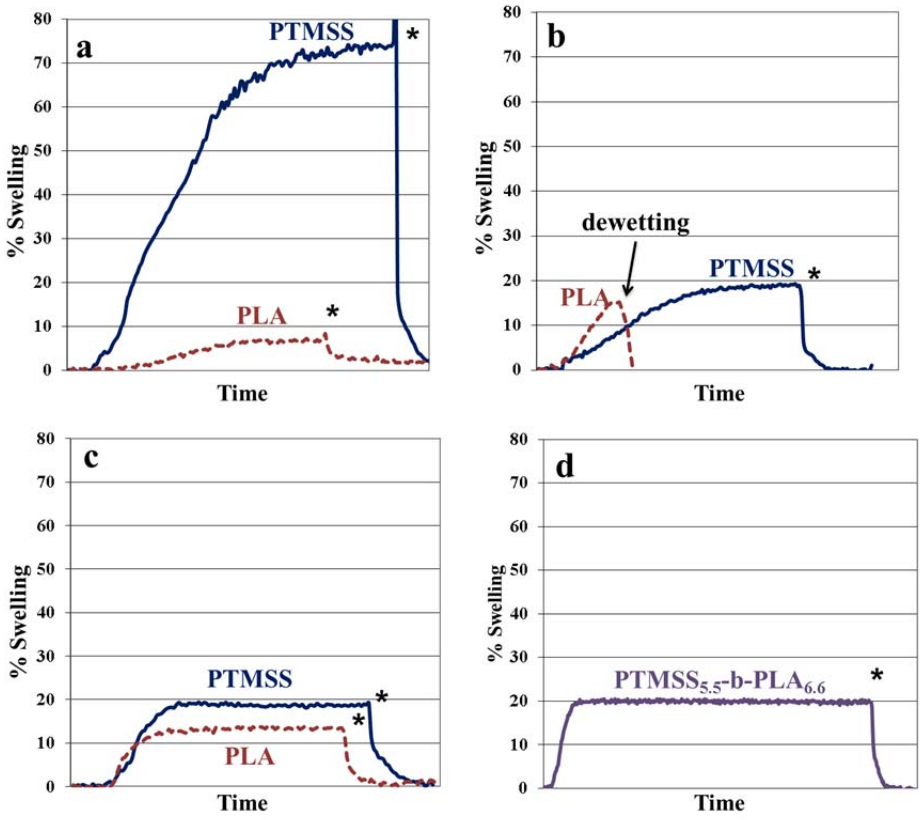


**Figure 4.11**: Swelling of polymer films under different annealing conditions. The * represents the time at which the $N_2$ flow rate through the solvent reservoirs was stopped and the $N_2$ flow rate through the diluting line was set to 500 sccm, enabling rapid removal of solvent from the film and return to the initial film thickness. a) swelling of PTMSS and PLA homopolymer films with a flow rate of 60 sccm $N_2$ through only the cyclohexane reservoir, b) swelling of PTMSS and PLA homopolymer films with a flow rate of 40 sccm $N_2$ through only the acetone reservoir, c) swelling of PTMSS and PLA homopolymer films with a flow rate of 60 sccm $N_2$ through the cyclohexane reservoir and 40 sccm through the acetone reservoir, and d) swelling of lamellae-forming $PTMSS_{5.5}$-*b*-$PLA_{6.6}$ film with a flow rate of 60 sccm $N_2$ through the cyclohexane reservoir and 40 sccm through the acetone reservoir. Reprinted with permission from [11]. Copyright 2012 American Chemical Society.

While adding a second selective solvent with opposite domain selectivity to cyclohexane could prevent a morphology change from occurring, doing so does not mean

that the desired orientation would be present. Recall that orienting a BCP perpendicular to the plane of a substrate requires interface conditions at both the substrate and free surface that neither block preferentially wets. Since optimizing the conditions at both interfaces simultaneously would be incredibly complicated (i.e. determining whether results were from changing the interfacial energy of the substrate or free interface), I focused first on identifying a solvent vapor composition that was nonpreferential for the free surface interface. I changed the surface energy of the free surface by altering the ratio of cyclohexane to acetone and observed the nanostructure at the surface of the film by SEM imaging. I felt that this would be the easiest approach to identifying a neutral annealing condition since phase separation of the BCP at the surface of the film that would likely be observable by top-down imaging even if the substrate was still preferential for one block.

At a low ratio of cyclohexane to acetone (**Figure 4.12a,** 40 sccm nitrogen through the cyclohexane bubbler, 60 sccm through the acetone bubbler), no self-assembly is observed at the surface. The light and dark regions in the SEM correspond to terracing, which will be described in further detail in Section 4.2.2.1. At an intermediate cyclohexane to acetone ratio (**Figure 4.12b**, 50 sccm cyclohexane, 50 sccm acetone), self-assembly is observed in patches in between the terraces. At a higher cyclohexane to acetone ratio (**Figure 4.12c**, 60 sccm cyclohexane, 40 sccm acetone), self-assembly is observed as dots and small lines nearly everywhere at the surface of the film. I was initially concerned that the dot structures observed in **Figure 4.12c** represented a morphology that was no longer lamellar and focused on the 50 sccm cyclohexane, 50 sccm acetone annealing condition for further experiments. Each of these previous experiments were performed on the same PLA-preferential substrate, and at the same film thickness.

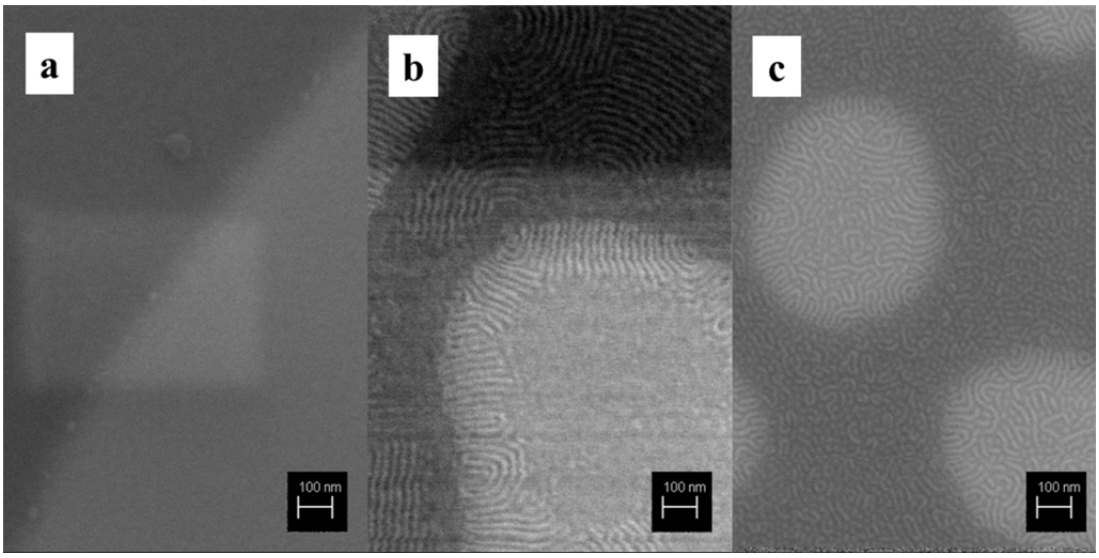


**Figure 4.12**: $PTMSS_{5.5}$-*b*-$PLA_{6.6}$ after annealing for 15 minutes under different conditions: a) 40 sccm $N_2$ through the cyclohexane and 60 sccm $N_2$ through the acetone bubbler, b) 50 sccm $N_2$ through the cyclohexane and 50 sccm $N_2$ through the acetone bubbler, and c) 60 sccm $N_2$ through the cyclohexane and 40 sccm $N_2$ through the acetone bubbler.

For the remainder of the annealing experiments described in this dissertation, unless noted otherwise, the chamber was also subjected to 5 sccm nitrogen that bypassed the solvent reservoirs in addition to the flow through the reservoirs, which from now on will be denoted only by the ratios of the flow rates in sccm (i.e. 50/50 cyclohexane/acetone). All solvent annealing experiments were conducted for 15 minutes and samples were quenched from the swollen state by rapidly stopping the flow through the solvent reservoirs and increasing the $N_2$ flow through the diluting line to 500 sccm, enabling rapid removal of solvent from the film and return to the initial film thickness. This quenching procedure resulted in rapid deswelling (a return to the initial film thickness only took a few seconds) as evidenced by film thickness monitoring in **Figure 4.11**. While several sets of experiments not presented here indicated that the flow rate of the bypass nitrogen and annealing time did not have a significant effect on the self-

assembly of the material (as long as the annealing time was at least 10 minutes), consistency was maintained with the quenching procedure since deviation could have an unpredictable effect on the self-assembly of the material with different solvent removal rates.

#### *4.2.2.1 Choosing a Neutral Surface Treatment*

After choosing a solvent annealing condition that I believed mediated the interfacial energy of the free surface based on the observed top-down self-assembly, I conducted experiments to determine an appropriate substrate surface treatment to neutralize the surface energy of the substrate. Surface treatments, which were described in Chapter 1, are often random copolymers composed of the monomer repeat units in the BCP of interest.[18] Using a random copolymer surface treatment composed of the same repeat units as the BCP allows access to the entire spectrum of surface energies between those of the two block homopolymers by altering the composition of the random copolymer. However, PTMSS-*r*-PLA random copolymers cannot be synthesized due to the ring-opening mechanism required to polymerize lactide. Therefore, surface treatments that do not contain these two components were examined by island/hole screening experiments. Unfortunately, this is a less methodical process than tuning the composition of a random copolymer. However, identifying neutral substrate surface treatments by screening with BCP island/hole experiments and neutral substrate treatments composed of dissimilar chemical moieties than the BCP are established design techniques.[19]

In addition to helping elucidate the morphology of a BCP thin film, terracing of parallel structures can be used as a tool to identify wetting behavior on the substrate when it is known which domain preferentially wets the free surface. This can usually be identified by water contact angle measurements. Due to the low surface energy of a

silicon-containing block, it almost always wets the free surface during thermal annealing. Given the knowledge of which block wets the free surface, if two BCP films with the same thickness (incommensurate with the domain periodicity) are annealed on surface treatments with opposite domain wetting behavior, this will be evident in the terraced microstructure. For example, if a 2.2 $L_o$ thick film of PTMSS-*b*-PLA is annealed on a PLA-preferential substrate (an "asymmetric" wetting condition because PLA prefers the substrate and PTMSS prefers the free surface), most of the film will increase in thickness to 2.5 $L_o$ and a small amount will decrease in thickness to 1.5 $L_o$ to maximize the concentration PTMSS at the surface. This will appear as "holes" in optical microscopy and SEM, with light or dark contrast being determined by the instrument. Likewise, if the same 2.2 $L_o$ thick film is annealed on a PTMSS-preferential substrate (a "symmetric" wetting condition because PTMSS preferentially wets the free surface and substrate), most of the film will increase in thickness to 3 $L_o$ and a small amount will decrease in thickness to 2 $L_o$ and the microstructure will be identified as "islands." This effect is most easily understood in terms of the behavior of individual polymer chains for a lamellar morphology (**Figure 4.13**). The opposite island/hole behavior for the two wetting conditions is observed if the film thickness is decreased to less than 2 $L_o$ or increased to greater than 2.5 $L_o$ so it is important in these experiments that BCPs are the same film thicknesses on all surface treatments to accurately identify the wetting behavior. If neither block preferentially wets the substrate and the free surface is also neutral, island-hole formation/terracing will not be observed since the BCP orients perpendicular to the substrate. If the free surface is in fact neutral and the substrate is strongly preferential, terracing will most likely still occur if the film is thin enough and the BCP feels the effect of the surface strongly (i.e. terracing still exists in **Figure 4.12** even with what we believe is a neutral free surface interface).

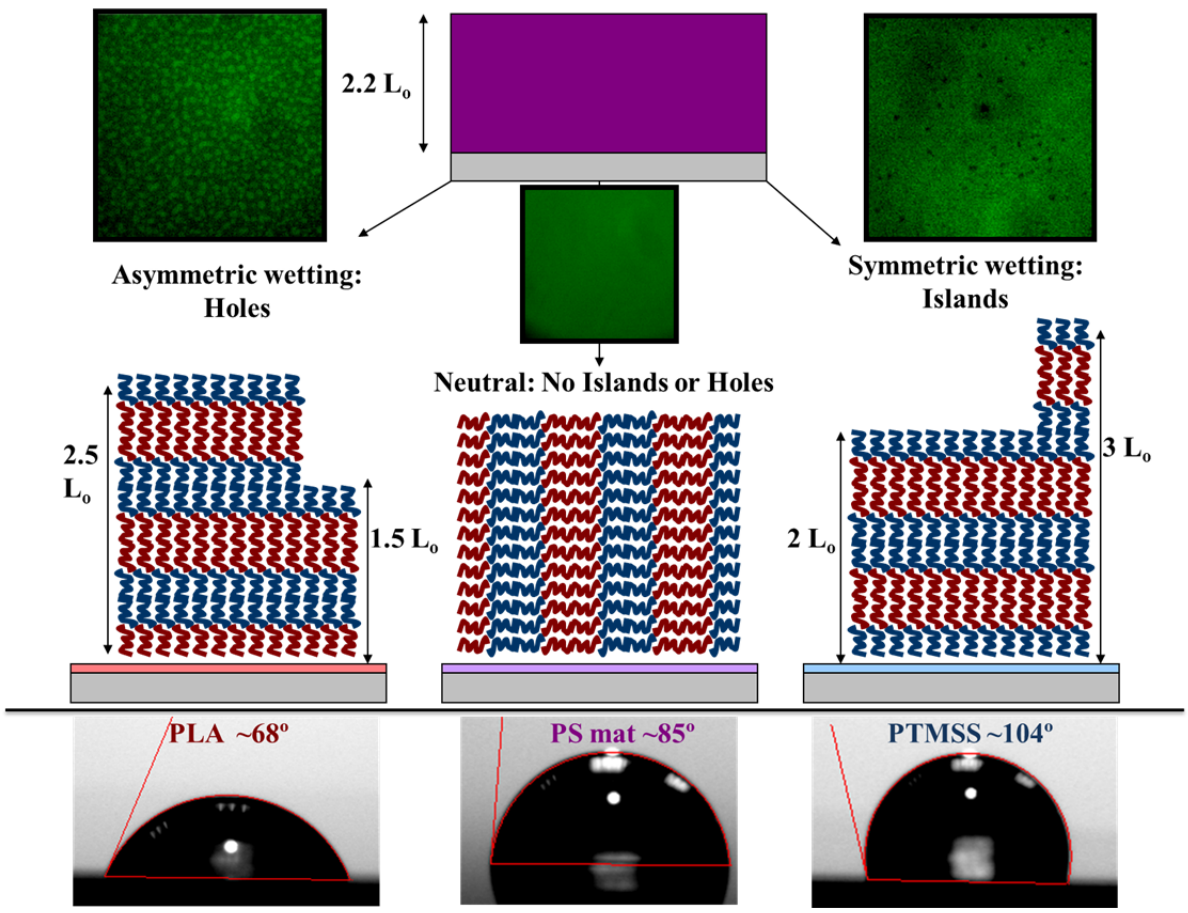


**Figure 4.13**: Diagrams, corresponding representative optical microscope images, and water contact angles for terracing of a lamellae-forming BCP for asymmetric, neutral, and symmetric wetting conditions. Here, PLA is red and PTMSS is blue.

One component in the calculation of a polymer surface energy is the angle a droplet of water forms upon contact with the film. This measurement alone contains inherent inaccuracy since water can significantly swell a polymer, changing its effective surface energy and provide misleading results, but it gives a qualitative idea of the degree of hydrophobicity of the material. Homopolymer films of PLA and PTMSS have water contact angles of 70 ° and 105 °, respectively, so it was predicted that a neutral surface

treatment for the nearly perfectly symmetric BCP would have a water contact angle in the ballpark of halfway between those numbers, 85-90 °. Several surface treatments with water contact angles of 85-90 ° produced BCP films with neither islands nor holes when subjected to the 50/50 cyclohexane/acetone solvent annealing condition. The results of the island/hole and water contact angle experiments are summarized in **Table 4.5**.

| Surface Treatment | Brush Water CA | I/H after anneal |
|---|---|---|
| 5.5 kDa PTMSS Brush | 103° | Islands |
| PTMSS-*r*-PMMA Mat PTMSS>17% | >87° | Islands |
| PS Mat | 85° | None |
| 1.2 kDa PS Brush | 89° | None |
| PS-*r*-PMMA 'A-Brush' | 89° | None |
| PS-*r*-PMMA 'Wisconsin Brush' | 87° | None |
| PTMSS-*r*-PMMA Mat 13-17% PTMSS | 82-87° | None |
| PTMSS-*r*-PMMA Mat PTMSS<13% | <82° | Holes |
| PS-*r*-PMMA 'B-Brush' | 88° | Holes |
| 9.5 kDaPMMA Brush | 72° | Holes |
| 3.0kDa PLA Brush | 68° | Holes |
| P2VP Brush | 68° | Holes |

**Table 4.5**: Water contact angle and island/hole behavior of incommensurate $PTMSS_{5.5}$-*b*-$PLA_{6.6}$ films on different surface treatments after solvent annealing with the 50/50 cyclohexane/acetone condition. The numbers preceding some of the surface treatments indicate the molecular weight of the polymer in kg/mol and some internal names are indicated for brushes with compositions that are proprietary.

Three classes of surface treatments successfully induced perpendicular orientation of a 10 nm thick film of $PTMSS_{5.5}$-*b*-$PLA_{6.6}$ after a 50/50 cyclohexane/acetone anneal. Film thicknesses were determined by scratching the film and measuring the scratch depth by AFM. AFM images were collected on a Veeco Dimension 3100 AFM at HGST. These surface treatments included PS (a mat and brush), two compositions of a PS-*r*-PMMA copolymer brush, and several compositions of an 8 nm thick PTMSS-*r*-PMMA copolymer mat. Representative top-down SEM images of films in these three classes of surface treatments are shown in **Figure 4.14** and the absence of terracing indicates that these structures are perpendicular lamellae. It should be noted from the scale of these images that the pitch increased from bulk SAXS experiments after solvent annealing by approximately 30%. The reasons for this and implications of the domain size increase will be discussed in Chapter 5.

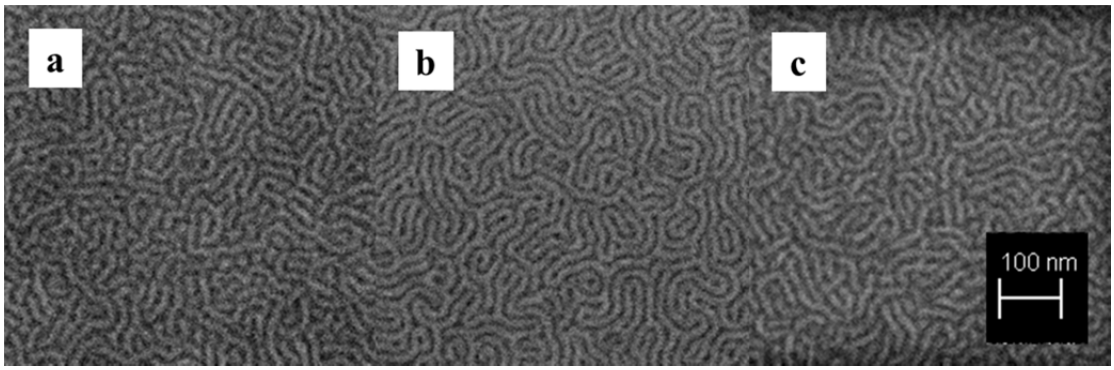


**Figure 4.14**: 10 nm thick films of $PTMSS_{5.5}$-*b*-$PLA_{6.6}$ after annealing with 50/50 cyclohexane/acetone on a) a PS mat, b) PS-*r*-PMMA ('A-brush'), and c) a PTMSS-*r*-PMMA mat.

One additional note should be made about thermally annealing PTMSS-*b*-PLA thin films. It was noticed that thermally annealing the lamellae on all *brush* substrate surface treatments, even those that were PLA-preferential (as predicted by water contact

angle), the island/hole behavior always indicated a PTMSS-preferential substrate surface. This was puzzling until it was considered that the PTMSS-*b*-PLA BCP is essentially a brush itself. After ring-opening PLA, the polymer is end-functionalized with a hydroxyl group that can graft to the substrate upon thermal annealing just as a hydroxyl-functionalized brush does. Even if the surface is treated with a brush, there are still free hydroxyls exposed on the substrate (see **Figure 1.10b**) that the BCP can graft to.[20] Since the hydroxyl functionality is on the PLA block, the low surface energy PTMSS domain is more exposed to the surface after grafting and dominates the wetting behavior of the surface. It was confirmed by contact angle measurements that after thermally annealing the BCP on a brush surface treatment and subsequently removing the BCP by rinsing with toluene, the surface energy of the substrate changes to be PTMSS wetting. It is also hypothesized that after grafting, the BCP chains bend and/or stretch to maximize the areal density of the low surface energy PTMSS at the surface, since a water contact angle was observed that is consistent with a PTMSS homopolymer surface (**Figure 4.15**). To avoid the effect of BCP grafting, any subsequent thermal annealing experiments with the BCP were conducted on mat surface treatments, which mask the free hydroxyls on the substrate. I confirmed by contact angle measurements that thermally annealing the BCP on a mat and then rinsing it off does not change water contact angle of the mat.

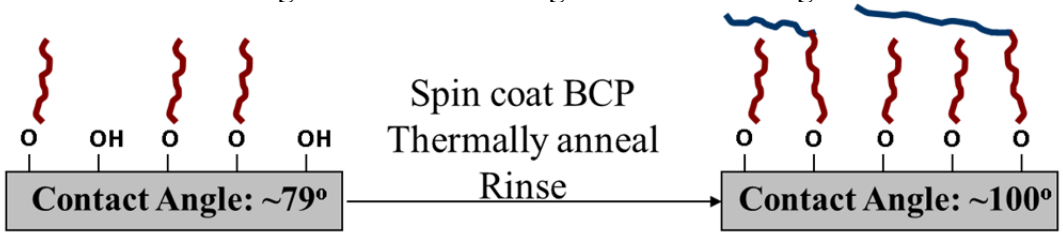


**Figure 4.15**: Change in water contact angle of PLA-preferential brush (PLA is the red domain, PTMSS is blue) after thermal annealing grafts OH-functional PTMSS-*b*-PLA.

#### *4.2.2.2 Film Thickness and Solvent Annealing Condition Optimization*

In the thin film orientation experiments, I observed that thickness played a key role in the self-assembly of the lamellae-forming PTMSS-*b*-PLA. When too thick, films exhibited only patchy areas of perpendicular orientation, and when too thin, self-assembly and correlation length appeared to be compromised. From **Figure 4.16**, it appears that the optimum film thickness of PTMSS-*b*-PLA for perpendicular orientation everywhere without compromising correlation length was 10 nm. This specific set of images was taken for a lamellae-forming $PTMSS_{5.5}$-*b*-$PLA_{6.6}$ film on a PS mat surface treatment after 50/50 cyclohexane/acetone solvent annealing, but the same patchiness trend and optimum film thickness was determined to be the same on the other neutral surface treatments as well.

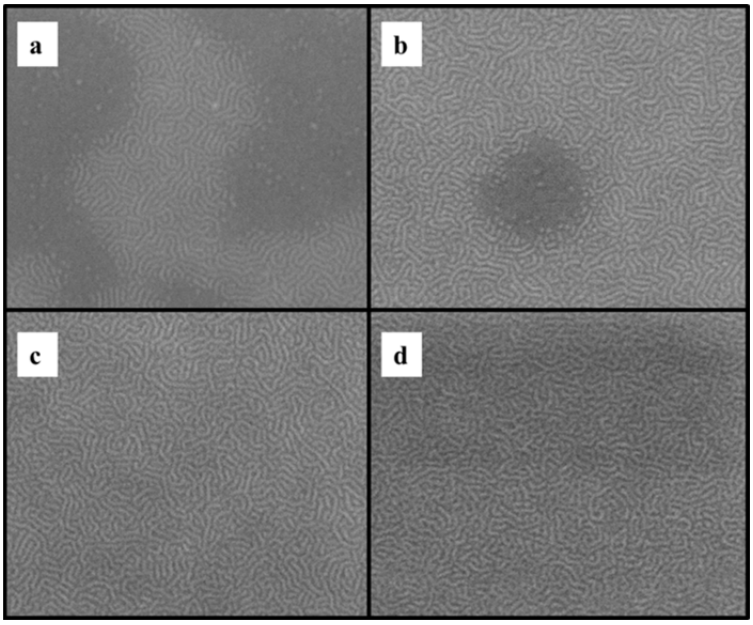


**Figure 4.16**: $PTMSS_{5.5}$-*b*-$PLA_{6.6}$ after annealing with 50/50 cyclohexane/acetone with film thicknesses of a) 15 nm, b) 12 nm, c) 10 nm, and d) 9 nm. Reprinted with permission from [11]. Copyright 2012 American Chemical Society.

The thin film orientation is dependent on the thickness of the film likely because the solvent annealing condition and/or surface treatments chosen do not produce perfectly neutral interfaces for the BCP. An interesting model was proposed by my colleagues while they were investigating the role of top coat neutrality.[21] They assert that if the free surface is not completely nonpreferential for both blocks ($\Delta\gamma \neq 0$), perpendicular orientation will only occur on the entire film within a window of quantized film thicknesses (**Figure 4.17**). This window of film thickness that enables perpendicular orientation is represented by the film thicknesses on the x-axis where portions of any of the curves (which represent different values of $\Delta\gamma$) in **Figure 4.17** lie above zero on the y-axis. While an in-depth discussion of the theory behind the model and a description of the parameters can be found elsewhere,[21] we believe that this is the reason why perpendicular orientation was patchy at film thicknesses greater than 10 nm. We also hypothesize that, since the thickness window for complete perpendicular orientation is small (1-2 nm), this likely means that $\Delta\gamma$ is fairly large and does not have a significant area above zero for the smallest quantized film thickness peak. This would indicate that the free surface interface is still relatively preferential for one block and could be further optimized. It should be noted that we believe the normalized film thickness in **Figure 4.17** is most accurately represented by the swollen film thickness in solvent annealing experiments. In solvent annealing, the equilibrium state is that of the film swollen with solvent (not the dry film) since the structure in the dry film is essentially quenched from the swollen state.

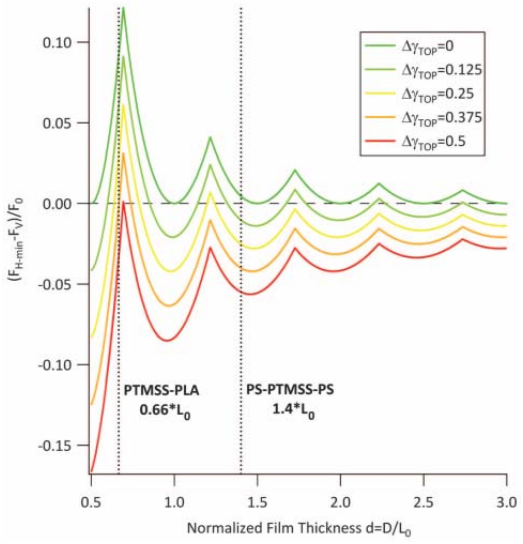


**Figure 4.17**: Differences in BCP thin-film free energies between the horizontal and vertical orientations $(F_{H\text{-}min} - F_V)/F_0$ as a function of reduced film thickness d where D is the actual thickness. For a given d, if the value of $(F_{H\text{-}min} - F_V)/F_0$ is negative, a horizontal orientation is preferred; if it is positive, a vertical orientation is preferred. Different curves represent different values of $\Delta\gamma_{Top}$ measured in mN/m. $\Delta\gamma_{Top} = 0$ mN/m represents a perfectly neutralizing top coat. For $\Delta\gamma_{Top} \geq 0.5$ mN/m, a horizontal orientation is realized for all d. From [21]. Reprinted with permission from AAAS.

Based on the model, if the interface conditions are within an appropriate window of neutrality, perpendicular orientation should also be observed at integer multiples of 10 nm. Therefore, I investigated the self-assembly of the film at 20 nm as well. For a 20 nm thick film of $PTMSS_{5.5}$-*b*-$PLA_{6.6}$, the self-assembly observed with the 50/50 cyclohexane/acetone annealing condition is presented in **Figure 4.18a**. Similarly to the 10 nm film thickness experiments, deviation from 20 nm in film thickness by just a few nanometers significantly decreased the areal density of perpendicular orientation. Since the thin film self-assembly is relatively patchy even at this optimized film thickness, it was hypothesized that perhaps the solvent annealing condition could be improved. I therefore tried optimizing the solvent annealing condition further by slightly changing the

ratios of the solvents. Ultimately, I determined the best orientation control over the 20 nm film was with a 60/40 cyclohexane/acetone annealing condition (**Figure 4.18b**). To support the conclusion that this was a better annealing condition, I applied the same condition to the 10 nm film and observed an improvement in the correlation length (**Figure 4.18d**) over the previous 50/50 cyclohexane/acetone annealing condition (**Figure 4.18c**). While no quantitative measurements were made to calculate correlation length, it is clear by eye that it was improved with annealing condition optimization. My initial concerns about this annealing condition changing the morphology of the polymer in **Figure 4.12c** were likely derived from frustrated self-assembly at the surface and not a morphology change.

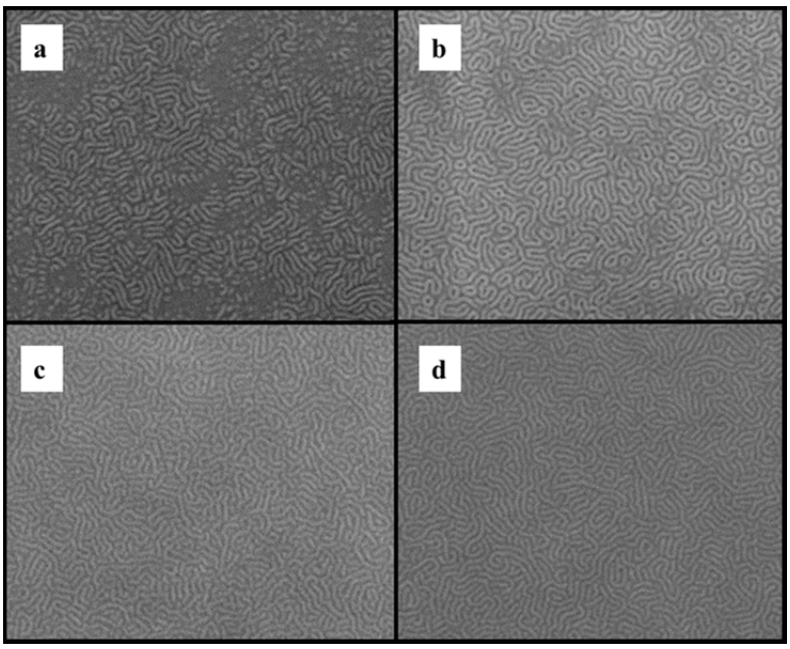


**Figure 4.18**: Lamellae-forming $PTMSS_{5.5}$-*b*-$PLA_{6.6}$ a) 20 nm film after annealing with 50/50 cyclohexane/acetone, b) 20 nm film after annealing with 60/40 cyclohexane/acetone, c) 10 nm film after annealing with 50/50 cyclohexane/acetone, and d) 10 nm film after annealing with 60/40 cyclohexane/acetone. Reprinted with permission from [11]. Copyright 2012 American Chemical Society.

Because of these observations, the 60/40 cyclohexane/acetone annealing condition was used for the remainder of the studies. As an additional note, GISAXS measurements (reported and discussed in Chapter 5) confirmed that the morphology in the thin films of $PTMSS_{5.5}$-*b*-$PLA_{6.6}$ under these solvent annealing conditions was in fact lamellar consistent with the absence of terracing in these films.

### 4.2.3 Thermal Annealing with a Top Coat

At the time the solvent annealing conditions were being optimized for orientation of PTMSS-*b*-PLA, my colleagues were developing a polymeric top coat to induce perpendicular orientation of the material with thermal annealing. The chemical structure of the random copolymer top coat that was used to orient lamellae-forming $PTMSS_{5.5}$-*b*-$PLA_{6.6}$ is shown in **Figure 4.19**.

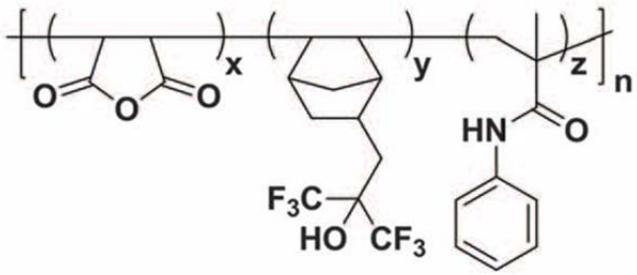


**Figure 4.19**: Structure of the top coat used to achieve perpendicular orientation of $PTMSS_{5.5}$-*b*-$PLA_{6.6}$ where x = 68, y = 21, and z = 11. From [21]. Reprinted with permission from AAAS.

After applying the top coat, the film was annealed at 170 °C for 20 hours. The top coat was then stripped. As shown in **Figure 4.20**, application of the top coat during thermal annealing resulted in perpendicular orientation of the domains while annealing without a top coat yielded no top-down self-assembly. Further details on the top coat and

annealing condition optimization can be found elsewhere.[21] Since the solvent annealing technique was optimized for this system first, I performed the subsequent pattern transfer and DSA studies using solvent annealing as the primary orientation technique.

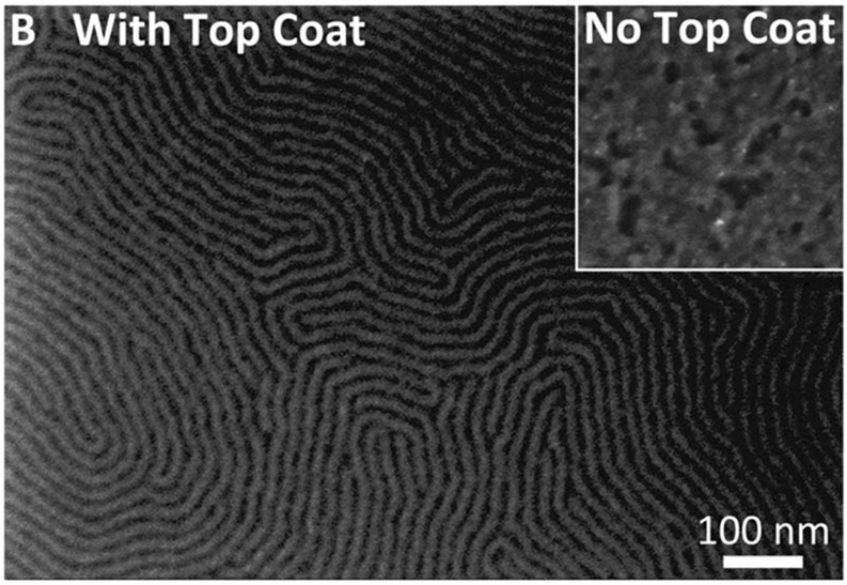


**Figure 4.20**: Perpendicular orientation of $PTMSS_{5.5}$-*b*-$PLA_{6.6}$ after thermal annealing with the top coat in **Figure 4.19**. Inset shows top-down assembly without a top coat. From [21]. Reprinted with permission from AAAS.

### 4.3 PATTERN TRANSFER

After orienting a BCP in thin films, a critical step that determines the BCP's utility in lithography is the ability to transfer the pattern into the underlying substrate. The fingerprint pattern from perpendicularly oriented $PTMSS_{5.5}$-*b*-$PLA_{6.6}$ was transferred to the underlying substrate by reactive ion etching. Two different methods were used to attempt to transfer the pattern: one using the inherent etch contrast from the silicon domain and the other by imparting etch contrast to the PLA domain using atomic layer deposition of an aluminum-containing precursor. PTMSS-*r*-PMMA surface treatments

were avoided for both pattern transfer methods due to potential challenges associated with etching through a silicon-containing surface layer.

### 4.3.1 Oxygen Etch Method

The first method investigated for transferring the $PTMSS_{5.5}$-*b*-$PLA_{6.6}$ fingerprint pattern into the underlying substrate involved using the inherent etch resistance of the silicon-containing block in an $O_2$ etch. Etching was performed on a PlasmaTherm tool at HGST using proprietary etch conditions that will not be reported in this document. The etch rates of PLA and PTMSS homopolymer films in $O_2$ were first examined. For the $O_2$ etch conditions used, PLA was removed at approximately 0.5 nm/sec. The film thickness of PTMSS decreased by approximately 5 nm in the first 30 seconds of etching but thickness changes were negligible after that time (<0.1 nm/sec). The initial decrease in PTMSS thickness is likely due to the relatively low density of silicon in the PTMSS domain. It is likely that the hydrocarbon portion of PTMSS was removed while the silicon oxidizes, and the domain compacts in the z-direction during the first 30 seconds of etching. Further domain removal is likely suppressed by oxidized silicon surrounding the domain. The steps in this etch protocol are detailed in **Figure 4.21**. A diamond-like carbon (DLC) transfer layer was deposited between the surface treatment and BCP to increase the aspect ratio of the structures in pattern transfer. A PS mat was used in these studies as the surface treatment instead of a brush due to the challenges associated with grafting a brush to DLC surfaces.

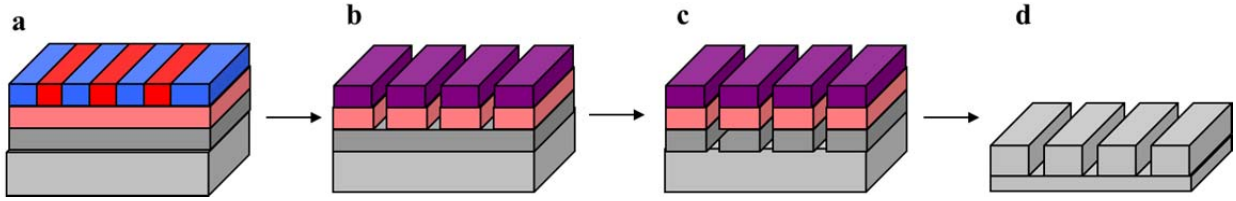


**Figure 4.21**: Steps in $O_2$ etch approach to pattern transfer of $PTMSS_{5.5}$-*b*-$PLA_{6.6}$.a) $PTMSS_{5.5}$-*b*-$PLA_{6.6}$ is spin coated and solvent annealed on a surface treatment above a DLC transfer layer. b) $O_2$ etch removes PLA domain, oxidizes Si in the PTMSS domain, and anisotropically etches surface treatment to the substrate. c) $CO_2$ etch etches through DLC transfer layer. d) Fluorinated etch transfers pattern into underlying silicon substrate and all remaining polymer and DLC is removed.

Recall that $PTMSS_{5.5}$-*b*-$PLA_{6.6}$ lamellae would only orient perpendicular to the substrate everywhere on the film at thicknesses that were integer multiples of 10 nm. Pattern transfer using this etch procedure was attempted for a 10 nm (**Figure 4.22a**) and 20 nm (**Figure 4.22b**) thick films and these images are representative of the top-down and cross-sectional structure after etching into the DLC (no pattern transfer into the substrate). For the 10 nm film, there is significant line breakage in the top-down image and the aspect ratio of the structures in the cross-section is very low. This prevented any reasonable attempts at subsequent transfer of the structure into the substrate. For the 20 nm thick film, while the aspect ratio of the structures was reasonable, polymer removal clearly revealed through film structure that was not perfectly uniform everywhere. This also prevented further successful attempts at pattern transfer.

For these reasons, another approach was taken to transfer the $PTMSS_{5.5}$-*b*-$PLA_{6.6}$ line pattern into the substrate. Reasons why the pattern transfer using this method were likely unsuccessful will be discussed in the next section.

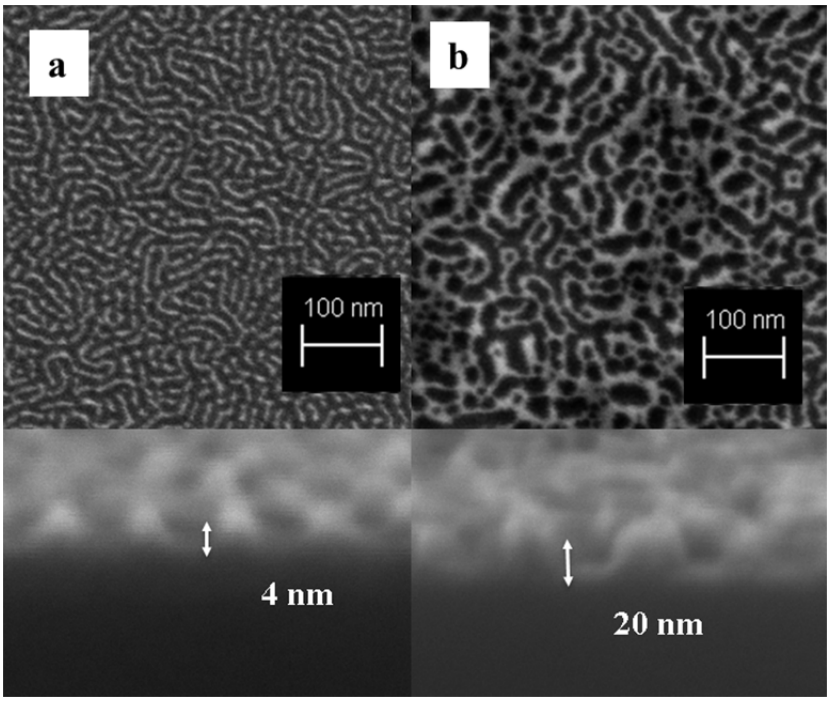


**Figure 4.22**: Top-down and cross section SEM images of $PTMSS_{5.5}$-*b*-$PLA_{6.6}$ etched through the DLC (no pattern transfer step into the substrate) a) for an initial BCP film thickness of 10 nm and b) for an initial BCP film thickness of 20 nm.

### 4.3.2 Atomic Layer Deposition Method

Since pattern transfer into the substrate was not performed with any reasonable success using the $O_2$ etch protocol, another approach was also investigated. Atomic layer deposition (ALD) is a process that chemically incorporates metal oxide into a polymer, making that domain etch resistant. The ALD process involves cycles of creating reactive sites in one of the polymer domains, adding one metal atom to each reactive site, and recreating another reactive site by introducing another molecule. ALD has been shown to impart etch resistance into PMMA thin films through the reaction of a trimethylaluminum (TMA) precursor with the carbonyl groups on PMMA and then recreating the active site by introducing water vapor to the film.[22] This process has also been used previously to impart etch resistance to the PMMA domain of a PS-*b*-PMMA self-assembled BCP.[23]

Since PLA has a fairly similar structure to PMMA, and TMA does not react with PS (and likely would not react with PTMSS either) this seemed like a reasonable technique to try to replicate in the PTMSS-*b*-PLA system.

The process for implementing this procedure with PTMSS-*b*-PLA is shown in **Figure 4.23** and involves imparting etch resistance into the PLA domain and does not use the inherent etch resistance of the silicon-containing domain. First the BCP was self-assembled by solvent annealing on the PS-*r*-PMMA surface treatment. Aluminum was introduced into the PLA domain by ALD. The ALD procedure was optimized with conditions that we believed most likely reacted with carbonyl groups on the polymer through the entire thickness of the film[23] and the procedure that produced the best pattern transfer involved 8 cycles of TMA followed by water. Since $O_2$ etching does not remove PTMSS, a fluorinated etch protocol was used to remove the PTMSS domain. The remaining organic material in the PLA domain and remaining surface treatment was removed by an $O_2$ etch after the PTMSS was removed and then the pattern was transferred into the substrate with an aggressive fluorinated etch. Remaining polymer and aluminum oxide was removed by a NaOH wash.

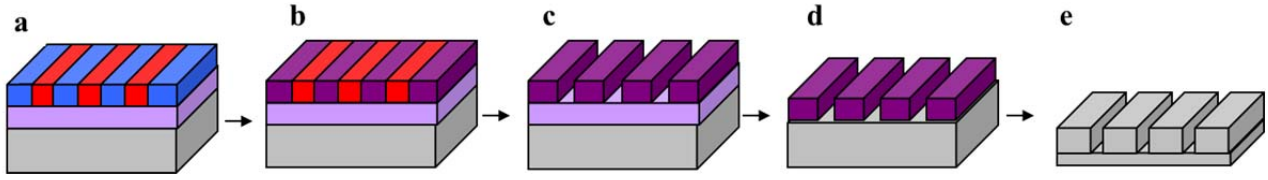


**Figure 4.23**: Steps in the ALD approach to pattern transfer of $PTMSS_{5.5}$-*b*-$PLA_{6.6}$.a) $PTMSS_{5.5}$-*b*-$PLA_{6.6}$ is spin coated and solvent annealed on surface treatment. b) ALD incorporates aluminum into the PLA domain. c) Fluorinated etch removes PTMSS domain while leaving aluminum-containing PLA domain intact. d) $O_2$ trim cleans remaining organic in BCP and surface treatment. e) Aggressive fluorinated etch transfers BCP pattern into the substrate.

Top-down and cross-section images of the $PTMSS_{5.5}$-*b*-$PLA_{6.6}$ fingerprint pattern transferred into the underlying silicon substrate are shown in **Figure 4.24**. As observed in the top-down image, there is significantly less line breakage using this method than in the $O_2$ etch method and there actually appears to be some degree line merging. This is likely due to expansion of the PLA domain with the addition of the aluminum.

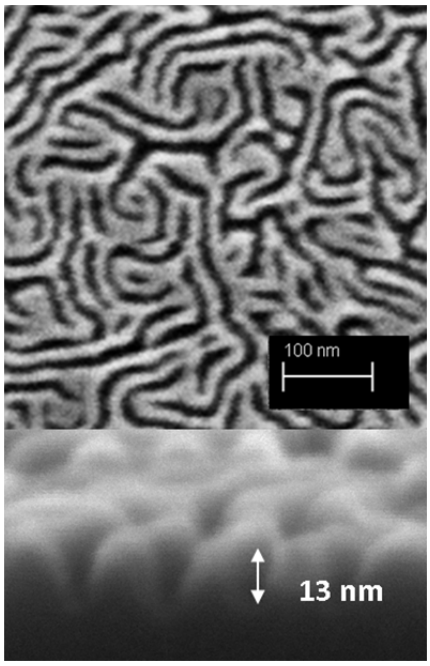


**Figure 4.24**: Top-down and cross section SEM images of $PTMSS_{5.5}$-*b*-$PLA_{6.6}$ transferred into the underlying silicon substrate. All polymer and $AlO_x$ was removed in a cleaning step before the top-down and cross-section images were taken.

While the $PTMSS_{5.5}$-*b*-$PLA_{6.6}$ pattern transferred using the ALD method was clearly better than what was achieved using the $O_2$ method, it was still not optimal. The side walls of the lines are slanted in the cross-section and the tops of the features are fairly rounded as observed in **Figure 4.24**. It could be that the pattern transfer did not work well for reasons that can be explained in **Figure 4.25**. If the substrate and/or the free surface interfaces are not entirely neutral for the BCP, one block may preferentially

wet the surface even if not strongly enough to promote parallel orientation. This preferential condition could exist if the surface treatment or solvent annealing condition were not optimized or could result from slight changes in self-assembly during quenching from the solvent annealed state. Either way, preferential interfaces could cause non-vertical sidewalls in the lamellae domains and with an $O_2$ etch protocol, if the PTMSS slightly preferentially wets the substrate and is subsequently pattern transferred, a breakthrough etch to destroy the wetted SiOx hard mask could destroy the feature uniformity and aspect ratio of the structures. The same effect could be problematic for the opposite wetting condition with the ALD pattern transfer approach.


**Figure 4.25**: Consequences of slightly preferential wetting on subsequent attempts at pattern transfer into the underlying substrate.

### 4.4 DIRECTED SELF-ASSEMBLY

Lithographic applications often require orientational and/or translational order. This is commonly achieved using directed self-assembly (DSA), typically utilizing either chemical or topographic substrate guiding patterns. For $PTMSS_{5.5}$-*b*-$PLA_{6.6}$, chemical contrast patterns were created by patterning sparse lines of cross-linked polystyrene using electron beam lithography. The bare silicon substrate between the crosslinked polystyrene was then backfilled with a polymer brush. The critical parameters of a chemical contrast pattern include the pitch of the lines (which should be commensurate with an integer multiple of the pitch of the BCP), the width of the lines (must be commensurate with the half-pitch of the BCP) and the chemical contrast, which is

defined by the choice of mat and backfill materials. The solvent annealing conditions used to orient the BCP were the same conditions as were used for the unaligned sample.

Two different patterns were optimized for DSA of the lamellae-forming $PTMSS_{5.5}$-*b*-$PLA_{6.6}$; one to multiply the density of the underlying pattern by a factor of two and one by a factor of three. The chemical contrast patterns were prepared by Lei Wan at HGST. The pitch of the mat lines were designed to be integer multiples of the pitch (determined by image analysis to be ~19 nm) and the width of the pre-patterned line was designed to be commensurate with the half-pitch of the solvent annealed BCP (~9 nm). Many different backfill brushes were investigated (not shown here) and most caused patchy self-assembly and/or island/hole formation. The best backfill material investigated was a PS-*r*-PMMA random copolymer. The best conditions were optimized and images and conditions are shown for 2x (**Figure 4.26a**) and 3x density multiplication (**Figure 4.26b**).

Clearly, there are still a significant number of defects in both the 2x and 3x density multiplications of the BCP material. Since the pitch and mat width were optimized, it is likely that the chemical contrast needs to be further optimized to decrease the defectivity of the aligned patterns.

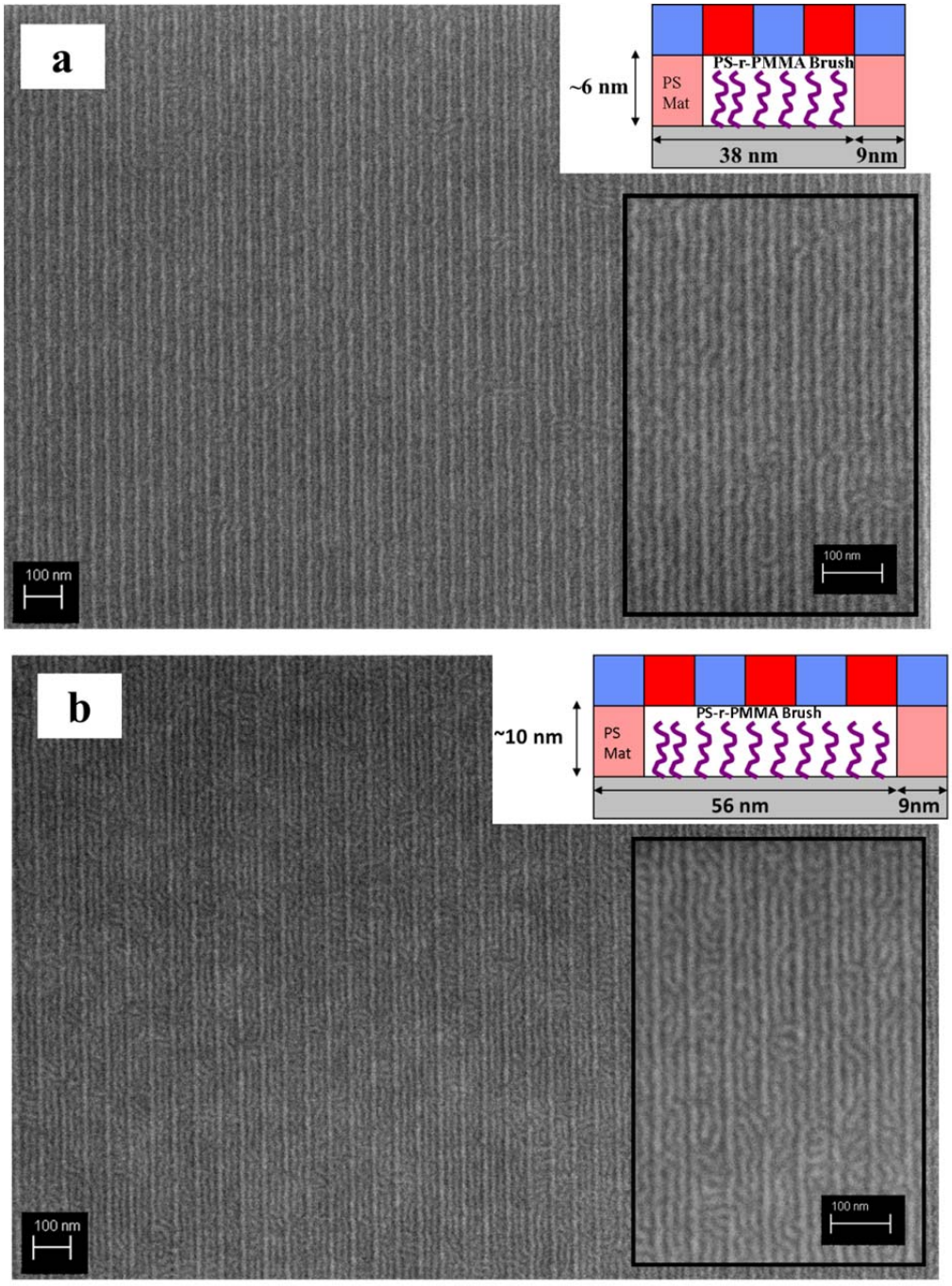


**Figure 4.26**: DSA of solvent annealed 10 nm thick $PTMSS_{5.5}$-*b*-$PLA_{6.6}$ with a density multiplication of a) 2x and b) 3x. Insets show prepattern dimensions.

## 4.5 CONCLUSIONS

In this chapter, the synthesis, self-assembly, pattern transfer, and DSA of PTMSS-*b*-PLA was investigated. Of all the BCPs explored, this polymer exhibited the highest $\chi$-parameter and the most success in thin film processing. However, significant challenges still would need to be overcome for this polymer to be useful in lithography. To achieve better pattern transfer, by either the $O_2$ or ALD approach, better self-assembly must be achieved. Since controlling the thin film self-assembly with this level of precision is likely nearly impossible with solvent annealing optimization, the best approach would probably be to transfer the pattern after thermal annealing with a top coat after fine-tuning interface neutrality. Also, while nice first demonstrations of DSA using a chemical contrast pattern were shown, the defectivity is very high and should be further reduced. While solvent annealing the PTMSS-*b*-PLA, some interesting thermodynamics of self-assembly were observed. The details of these observations are the subject of discussion in Chapter 5.

## 4.6 REFERENCES


1. M. A. Hillmyer; F. S. Bates, *Macromolecules* **1996,** *29*, 6994-7002.
2. O. Dechy-Cabaret; B. Martin-Vaca; D. Bourissou, *Chemical Reviews* **2004,** *104*, 6147-6176.
3. A. Debuigne; J.-R. Caille; N. Willet; R. Jérôme, *Macromolecules* **2005,** *38*, 9488-9496.
4. Y. B. Wang; M. A. Hillmyer, *Macromolecules* **2000,** *33*, 7395-7403.
5. A. S. Zalusky; R. Olayo-Valles; J. H. Wolf; M. A. Hillmyer, *Journal of the American Chemical Society* **2002,** *124*, 12761-12773.
6. E. W. Cochran; D. C. Morse; F. S. Bates, *Macromolecules* **2003,** *36*, 782-792.
7. M. Vert; G. Schwach; R. Engel; J. Coudane, *Journal of Controlled Release* **1998,** *53*, 85-92.
8. Lactide Stereoisomers Structural Formulae. Wikimedia Commons. (2009)
9. Y. L. Loo; R. A. Register; A. J. Ryan, *Macromolecules* **2002,** *35*, 2365-2374.

10. J. D. Cushen; I. Otsuka; C. M. Bates; S. Halila; S. Fort; C. Rochas; J. A. Easley; E. L. Rausch; A. Thio; R. Borsali; C. G. Willson; C. J. Ellison, *Acs Nano* **2012,** *6*, 3424-3433.
11. J. D. Cushen; C. M. Bates; E. L. Rausch; L. M. Dean; S. X. Zhou; C. G. Willson; C. J. Ellison, *Macromolecules* **2012,** *45*, 8722-8728.
12. S. C. Schmidt; M. A. Hillmyer, *Macromolecules* **1999,** *32*, 4794-4801.
13. J. W. Jeong; W. I. Park; M.-J. Kim; C. A. Ross; Y. S. Jung, *Nano Letters* **2011,** *11*, 4095-4101.
14. Y. S. Jung; C. A. Ross, *Advanced Materials* **2009,** *21*, 2540-2545.
15. T.-Y. Lo; C.-C. Chao; R.-M. Ho; P. Georgopanos; A. Avgeropoulos; E. L. Thomas, *Macromolecules* **2013**.
16. J. Brandrup; E. H. Immergut; E. A. Grulke; A. Abe; D. R. Bloch, John Wiley & Sons.
17. R. Ruiz; E. Dobisz; T. R. Albrecht, *Acs Nano* **2010,** *5*, 79-84.
18. P. Mansky; Y. Liu; E. Huang; T. P. Russell; C. J. Hawker, *Science* **1997,** *275*, 1458-1460.
19. R. D. Peters; X. M. Yang; T. K. Kim; P. F. Nealey, *Langmuir* **2000,** *16*, 9620-9626.
20. G. L. Liu; S. X. Ji; K. O. Stuen; G. S. W. Craig; P. F. Nealey; F. J. Himpsel, *Journal of Vacuum Science & Technology B* **2009,** *27*, 3038-3042.
21. C. M. Bates; T. Seshimo; M. J. Maher; W. J. Durand; J. D. Cushen; L. M. Dean; G. Blachut; C. J. Ellison; C. G. Willson, *Science* **2012,** *338*, 775-779.
22. C. A. Wilson; R. K. Grubbs; S. M. George, *Chemistry of Materials* **2005,** *17*, 5625-5634.
23. Q. Peng; Y.-C. Tseng; S. B. Darling; J. W. Elam, *Acs Nano* **2011,** *5*, 4600-4606.

# Chapter 5: Domain Size Increase and Inducing Order in PTMSS-*b*-PLA by Solvent Annealing

In Chapter 4, a mixture of domain-selective solvents was used to successfully mobilize and orient lamellae-forming $PTMSS_{5.5}$-*b*-$PLA_{6.6}$ perpendicular to the substrate. However, a discrepancy between the domain periodicity of the bulk sample after thermal annealing and the thin film after solvent annealing was apparent. An observed ~30% increase in the pitch of $PTMSS_{5.5}$-*b*-$PLA_{6.6}$ in a thin film after solvent annealing was initially attributed to error in the image analysis. However, the best chemical contrast patterns for 2x and 3x density multiplication of the lamellae-forming polymer also had a preferred PS mat line pitch that was an integer multiple of a ~30% greater domain periodicity than the thermally annealed polymer. This discrepancy was investigated further by characterizing the top-down and through film structure after solvent annealing and a simulations study was carried out.[1] As described in this chapter, the discrepancy was ultimately attributed to the thermodynamics of self-assembly during solvent annealing using a mixture of domain-selective solvents.

Simulation studies were performed by Gunja Pandav and Venkat Ganesan at the Univeristy of Texas. For the simulations sections that follow in this chapter, they used self-consistent field theory (SCFT) methodology to study the bulk phase behavior of PTMSS-*b*-PLA with two selective solvents, $S_1$ (cyclohexane) and $S_2$ (acetone). SCFT has been used as a successful tool for predicting, with quantitative accuracy, phase behavior of block copolymer systems in both the presence and absence of solvents[2-13] with details of the calculations reported elsewhere.[1] The model system was described by a symmetric diblock copolymer (volume fraction, $f = 0.5$) and degree of polymerization, $N = 100$. A parameterization was adopted wherein the selectivity of solvent $S_1$ to the A block and selectivity of solvent $S_2$ to the B block was chosen such that $-\chi_{AS1} = \chi_{BS1} = \chi_{AS2} = -\chi_{BS2} = \chi$,

where $\chi_{ij}$ is the Flory-Huggins interaction parameter between the components *i* and *j*, and $\chi>0$ ($\chi \neq \chi_{AB}$). The above parameterization accounts for the selectivity of A (B) blocks to the solvent $S_1$ ($S_2$) and the (relative) incompatibility between A (B) blocks and the solvent $S_2$ ($S_1$) (a negative $\chi$ parameter models favorable interactions between the components). Moreover, to limit the number of parameters to as few as possible, it was assumed that the solvents do not interact with each other ($\chi_{S1\text{-}S2} = 0$). The selectivity of solvents for the diblock copolymer was varied in the range $\chi = 0.2 - 1.0$ (corresponding to an increasing affinity of the solvents to the preferential block). We note that these $\chi$ values differ from the experimentally deduced $\chi$s between the segments and the solvents, and hence we only offer qualitative comparisons between our model results and experiments.

For the remainder of the chapter, the solvent annealing conditions that were optimized in Chapter 4 were used: 60 sccm $N_2$ through the cyclohexane bubbler, 40 sccm $N_2$ through the acetone bubbler, 5 sccm $N_2$ through the diluting line for 15 minutes.

## 5.1 Pitch Increase in Bulk Lamellae-Forming PTMSS-*b*-PLA

In previous work, it has been shown that domain periodicity of a block copolymer decreases in the presence of a nonselective solvent. This is due to an increase in the miscibility of the solvent-modified blocks since the solvent molecules can travel across domains (**Figure 5.1**), thus decreasing the effective $\chi$–parameter, $\chi_{eff,}$ of the BCP with solvent.[15] $\chi$ is proportional to domain periodicity (d) in the strongly segregated regime by the relationship $d \sim N^{2/3}\chi^{1/6}$, where N is the degree of polymerization.[16] In the case of constant N, a decrease in $\chi_{eff}$ will result in a decrease in domain periodicity. It has also been observed that the domain size of a BCP can increase when annealed with a single domain-selective solvent.[15] A solvent selective for one domain will partition primarily

into that domain since the solvent wants to minimize contact with the opposite domain (**Figure 5.1**), decreasing the miscibility of the two block domains and increasing $\chi_{eff}$. Morphological transformations due to changes in the effective relative volume fractions can also occur, provided that all block copolymer domains are in their liquid state.[17-19]

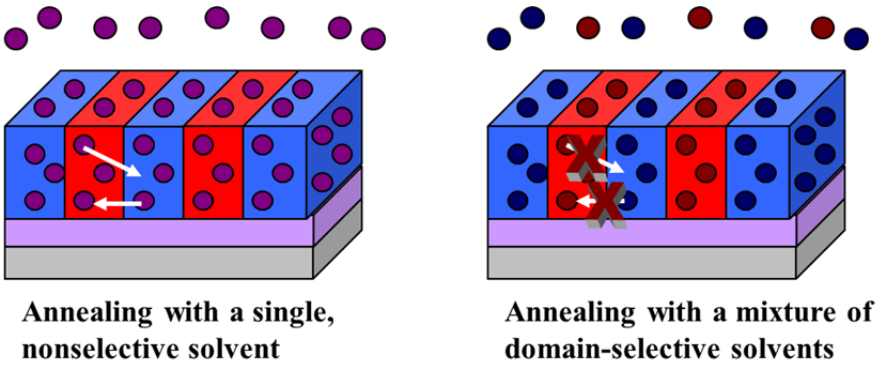


**Figure 5.1**: Annealing with a single, nonselective solvent vs. a mixture of domain-selective solvents.

This is also supported by simulations data[1] describing the partitioning of two domain-selective solvents into the different domains under these conditions. **Figure 5.2** displays the density profiles for copolymer and solvent at a fixed copolymer volume fraction, $\varphi = 0.8$ for two values of $\chi$. At low $\chi$ the solvents are almost equally distributed among the copolymer domains. Upon increasing $\chi$, the solvents preferentially segregate in the respective domains causing both domains to swell. In order to minimize unfavorable contacts (B-$S_1$ and A-$S_2$), the copolymer chains stretch, which leads to an increase in the domain spacing.

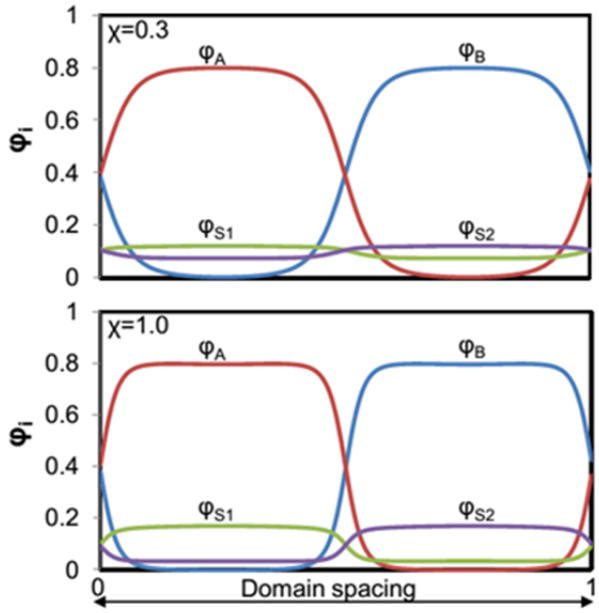


**Figure 5.2**: Solvent and polymer segment profiles for $\chi = 0.3$ and $\chi = 1.0$ at fixed copolymer volume fraction, $\varphi = 0.8$ *and* $\chi_{AB}N = 30$. Reproduced with permission from [1].

In Section 5.1.1, experimental evidence from several techniques demonstrates that the $PMSS_{5.5}$-*b*-$PLA_{6.6}$ exhibits a perpendicular lamellae structure in thin films and that the domain periodicity increases with solvent annealing. My colleagues' simulations data for a selective solvent annealing condition in Section 5.1.2 supports this observation.

### 5.1.1 Experimental Evidence for a Change Domain Periodicity

A 10 nm film of $PTMSS_{5.5}$-*b*-$PLA_{6.6}$ on a PS-*r*-PMMA brush was solvent annealed as described in Chapter 4, resulting in a top-down fingerprint pattern (**Figure 5.3a**). The domain periodicity of the structures in this SEM image was determined by performing a standard fast Fourier transform on the image as detailed elsewhere.[20] The power spectral density was circularly averaged and $L_o$ was determined from the relationship $L_o = 2\pi/k_o$, where $k_o$ is the location of the primary peak. From this analysis, the domain periodicity of the BCP structures in **Figure 5.3a** is 18.7 nm (**Figure 5.3b**).

Upon thermally annealing a thin film of $PTMSS_{5.5}$-*b*-$PLA_{6.6}$ at 160 °C for 15 minutes, featureless terraces were observed by AFM (**Figure 5.3c**), indicating a parallel lamellar morphology. All AFM data in this chapter was collected on a Veeco Dimension 3100 AFM at HGST. The terrace height was measured by AFM to be 14-15 nm (**Figure 5.3b,** inset). As described in Chapter 4, terrace heights are commensurate with the $L_o$ value of the BCP, so this value is consistent with the domain periodicity of bulk $PTMSS_{5.5}$-*b*-$PLA_{6.6}$ after thermal annealing under the same conditions.

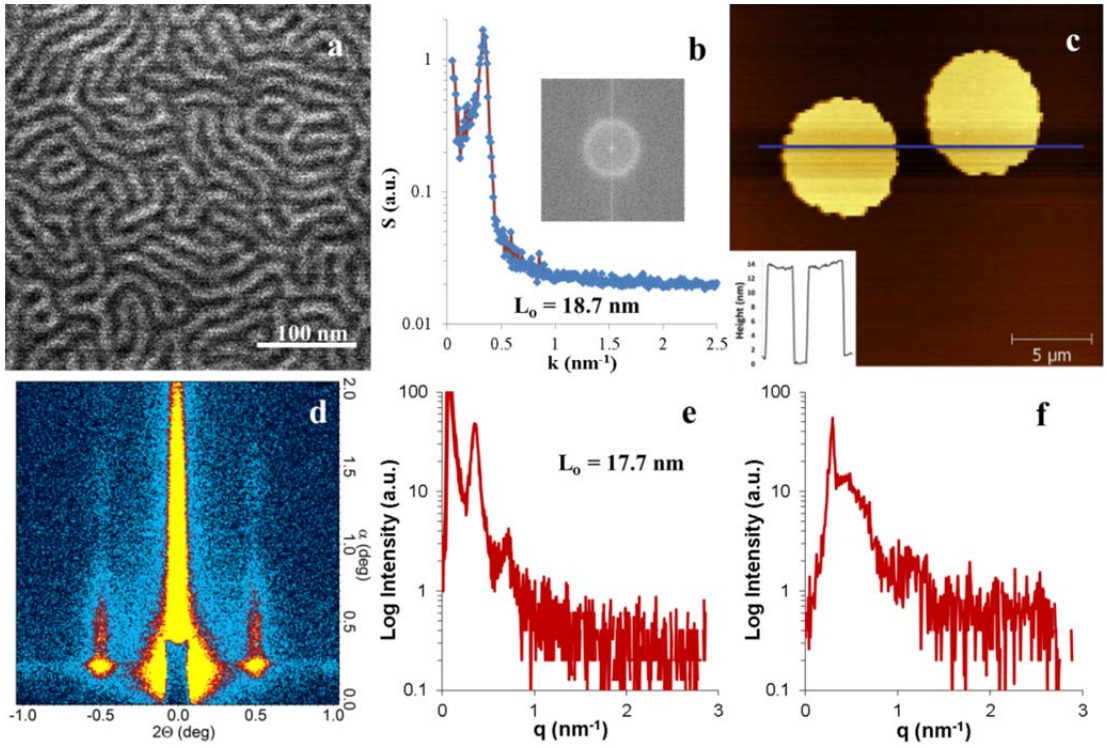


**Figure 5.3**: a) SEM image of $PTMSS_{5.5}$-*b*-$PLA_{6.6}$ on a PS-*r*-PMMA brush after solvent annealing. b) Circularly averaged PSD and resulting $L_o$ value of 18.7 nm for **Figure 5.3a**. c) AFM image of terracing in $PTMSS_{5.5}$-*b*-$PLA_{6.6}$ after thermally annealing at 160°C for 15 minutes. Terrace height (inset) was measured to be 14-15 nm. d) GISAXS pattern of the film in **Figure 5.3a**. e) In-plane I(q) from **Figure 5.3d** shows a domain periodicity of 17.7 nm, with peak ratios 1:2. f) Out-of-plane I(q) from **Figure 5.3d** is consistent with a domain height of 8-10 nm. Reproduced with permission from [1].

Investigation of the through-film structure of the same film imaged in **Figure 5.3a** by GISAXS was made possible by collaboration with the University of Houston. GISAXS measurements were performed by Indranil Mitra and Gila Stein using a RIGAKU-GISAXS S-MAX3000 with x-ray energy irradiated from a Cu target with an energy of 8.04 keV ($\lambda$ = 0.154 nm). The incident angle was adjusted to be above the critical angle of the polymer film and the diffracted intensity was recorded using a 2-D single photon counting detector. The exposure times ranged from 10-15 minutes and the data set is a map of intensity, $I(2\theta, \alpha_f)$ where $2\theta$ is the in-plane diffraction angle and $\alpha_f$ is the out of plane diffraction angle. The sample to detector distance was calibrated using a silver behenate standard.

By GISAXS (**Figure 5.3d** and integrated I(q) in **Figures 5.3e and 5.3f**), the in-plane structure of the film in **Figure 5.3a** has peaks in a ratio of 1:2, which could be interpreted as perpendicular lamellae or parallel cylinders, and the out-of-plane structure has fringes that indicate a feature height 8-10 nm tall. Together, this is most likely consistent with a perpendicular orientation of lamellae since it is unlikely that parallel cylinders with a domain periodicity of 17.7 nm identified in the GISAXS pattern would propagate nearly the entire thickness of a 10 nm thick film. Additionally, parallel cylinders with this domain periodicity would be expected to terrace at this film thickness but this film was completely smooth after solvent annealing.

It has been previously established that $\chi$ varies inversely with temperature for PTMSS-*b*-PLA.[21] To rule out the possibility that the increase in $\chi$ observed when solvent annealing with a mixture of selective solvents is due to the difference in temperature between thermal annealing (performed at 160°C) and solvent annealing, which is done at room temperature, SAXS data was analyzed for $PTMSS_{5.5}$-*b*-$PLA_{6.6}$ between 120 °C and 180 °C. As seen in **Figures 5.4a** and **5.4b**, it was observed that domain spacing of this

polymer does not change significantly with temperature. When extrapolated to room temperature and assuming a (1/6) power law relationship between domain size and annealing temperature, temperature effects could only account for about a 1 nm increase in the domain spacing from 160 °C to room temperature.

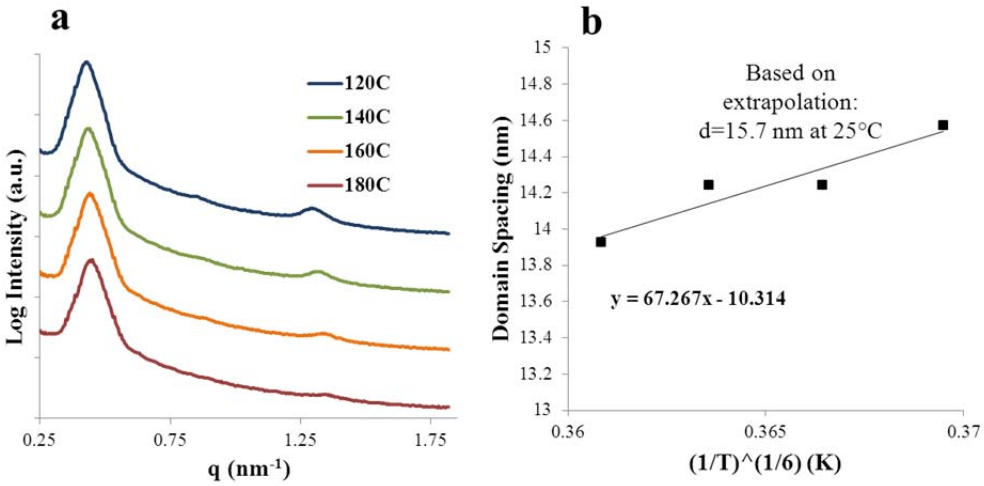


**Figure 5.4**: a) SAXS patterns of $PTMSS_{5.5}$-*b*-$PLA_{6.6}$ collected at temperatures ranging from 120-180°C b) Plot of domain spacing vs. temperature for $PTMSS_{5.5}$-*b*-$PLA_{6.6}$ with d-spacing data obtained from the SAXS data in **Figure 5.4a**. Reproduced with permission from [1].

### 5.1.2 Simulations Evidence for a Change in χ

**Figure 5.5** displays the variation in domain spacing (normalized by radius of gyration, $R_g$ of the copolymer) with copolymer volume fraction for varying monomer-solvent interaction parameters ($\chi$) at fixed $\chi_{AB}N = 30$ (the lines are guides to the eye). For low to moderate values of solvent selectivity ($\chi$), the domain spacing decreases with increasing solvent volume fraction. In contrast, for moderate-high solvent selectivity, the domain spacing can increase with increasing solvent fractions. Moreover, in support of experimental evidence, domain spacing increases of ~30 % can indeed be achieved for appropriate parameters.

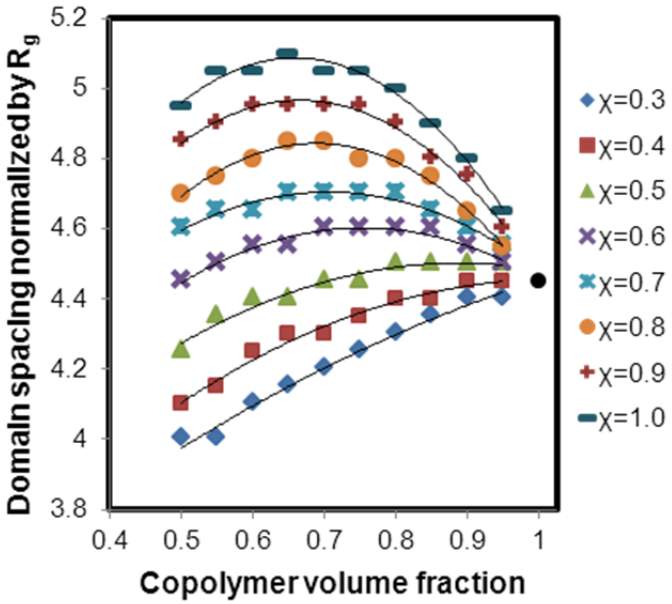


**Figure 5.5**: Variation in domain spacing (normalized by $R_g$) with copolymer volume fraction for varying monomer-solvent interaction parameters ($\chi$) at fixed $\chi_{AB}N=30$. The black circle indicates the domain spacing for pure diblock system (copolymer volume fraction =1). The lines are a guide to the eye. Reproduced with permission from [1].

### 5.2 Inducing Order in Bulk Disordered PTMSS-*b*-PLA

To fully explore the implications of increased $\chi_{eff}$ during solvent annealing, a polymer disordered in the bulk ($\chi N<10.5$) was solvent annealed using the same conditions described previously. Disordered $PTMSS_{2.3}$-*b*-$PLA_{1.7}$ was solvent annealed in a thin film on an 8.8 nm thick cross-linked polystyrene substrate surface treatment. Cross-linked PS was used as a surface treatment to prevent the hydroxyl end group on the BCP from grafting to hydroxyls on the substrate surface during subsequent thermal annealing experiments.

A BCP sample that is disordered (with a $\chi N$ just below the ODT on the phase diagram upon thermal annealing) could be pushed into the ordered state if a large enough increase in $\chi_{eff}$ is induced during solvent annealing. This can be visualized as moving

upward on the phase diagram across the ODT (**Figure 5.6**) when annealing under certain conditions. Section 5.2.1 presents evidence that this order can be induced experimentally and Section 5.2.2 presents simulation evidence for a lowering of the critical χN when solvent annealing using a mixture of domain-selective solvents.

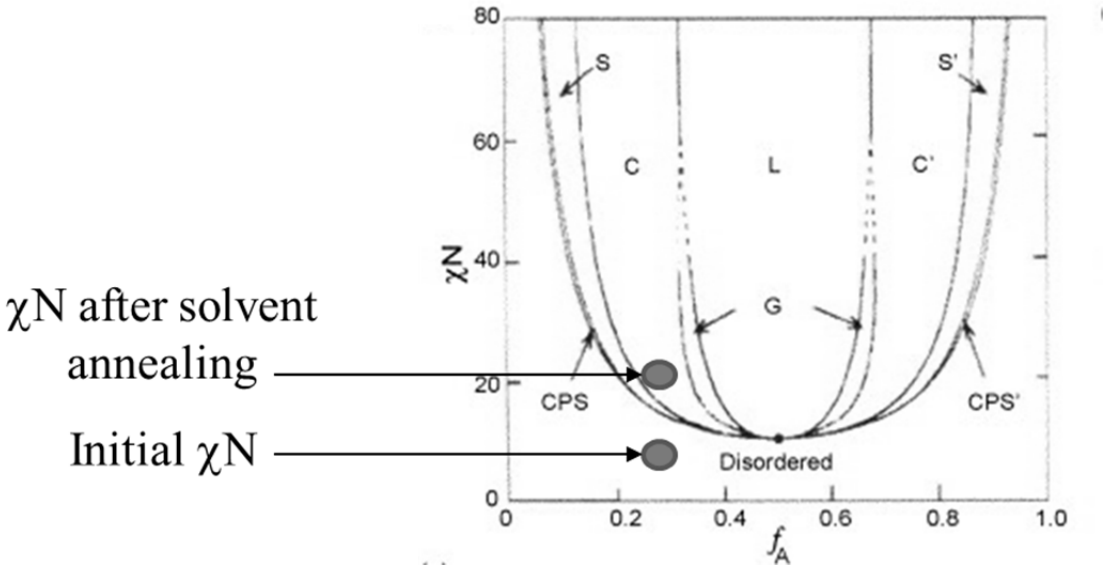


**Figure 5.6**: Proposed ordering pathway of an otherwise disordered sample due to an increase in χ (or lowering of χN at the ODT) with domain-selective solvent annealing. Reprinted with permission.[22] Copyright 1999, American Institute of Physics.

### 5.2.1 Experimental Evidence for Order Induced by Solvent Annealing

After solvent annealing bulk disordered $PTMSS_{2.3}$-*b*-$PLA_{1.7}$, in a thin film, order was observed by top-down imaging (**Figure 5.7a**). From the circularly averaged PSD, the domain periodicity of the fingerprint pattern was determined to be 13.5 nm (**Figure 5.7b**). An AFM height trace shows terracing in the film, indicating a parallel cylinder morphology (**Figure 5.7c**). Note that a dry terrace height of 10 nm (inset of **Figure 5.7c**) corresponds to a swollen terrace height of approximately 12 nm with 20% film thickness

swelling during solvent annealing. A domain periodicity of 12 nm determined from the terrace height is consistent with the periodicity of the polymer by image analysis. The Bragg peaks in the GISAXS pattern of the film (**Figure 5.7d** and integrated I(q) in **Figure 5.7e**) correspond to a cylindrical morphology with a 12.6 nm pitch, which is also consistent with the previous methods of analysis.

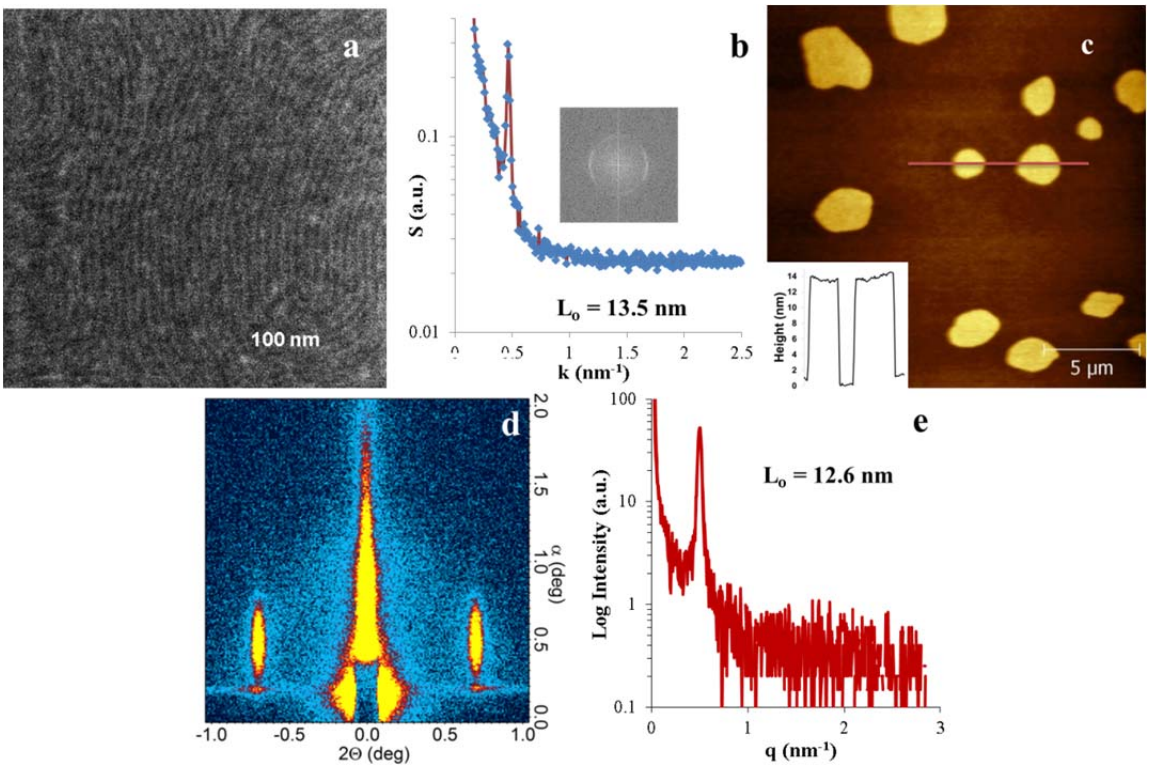


**Figure 5.7**: a) Top-down SEM image of $PTMSS_{2.3}$-*b*-$PLA_{1.7}$ after solvent annealing. b) Circularly averaged PSD of **Figure 5.7a** with a $L_o$ value of 13.5 nm. c) AFM trace of **Figure 5.7a** showing terracing of the cylinder domains. Inset shows the height profile across two terraces. d) GISAXS pattern of the film in **Figure 5.7a**. e) In-plane I(q) from **Figure 5.7d** with a $L_o$ value of 12.6 nm. Reproduced with permission from [1].

$PTMSS_{2.3}$-*b*-$PLA_{1.7}$ disorders after a subsequent thermal anneal under vacuum at 160°C for 15 minutes as observed in the top-down SEM image in **Figure 5.8a**. The

corresponding GISAXS pattern also indicates disorder (**Figure 5.8b** and integrated I(q) in **Figure 5.8c**) evidenced by a broad, low intensity halo scattering pattern. The sample orders into a cylindrical morphology again after a second solvent annealing step as indicated by top-down SEM imaging and GISAXS (not shown).

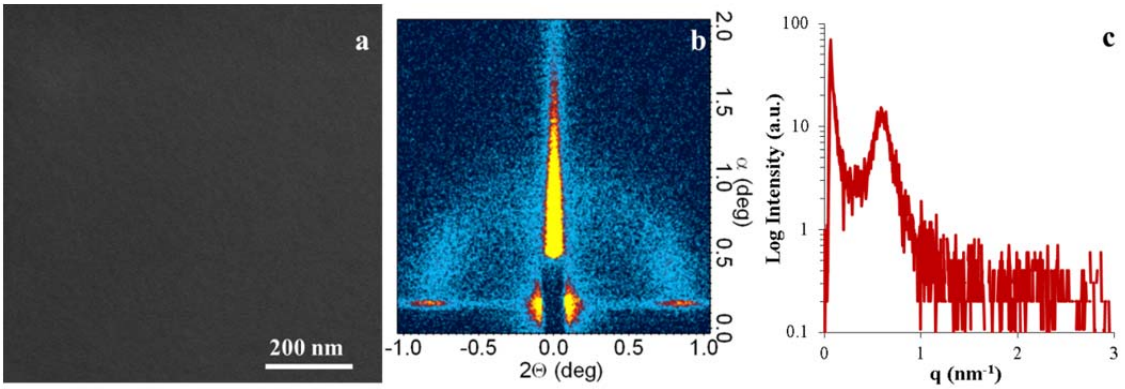


**Figure 5.8**: a) SEM image after thermally annealing the film in **Figure 5.7** for 15 minutes at 160°C in vacuum. b) GISAXS pattern of the film in **Figure 5.8a**. c) In-plane integrated GISAXS pattern in **Figure 5.8b.** Reproduced with permission from [1].

Bulk $PTMSS_{2.3}$-*b*-$PLA_{1.7}$ exposed to identical solvent annealing conditions also orders into a cylindrical morphology, disorders after a subsequent thermal anneal, and orders again after a second solvent anneal as evidenced by bulk SAXS (**Figure 5.9**). The measured pitch of the bulk and thin film solvent annealed samples are nearly identical at 13.4 nm and 13.5 nm, respectively.

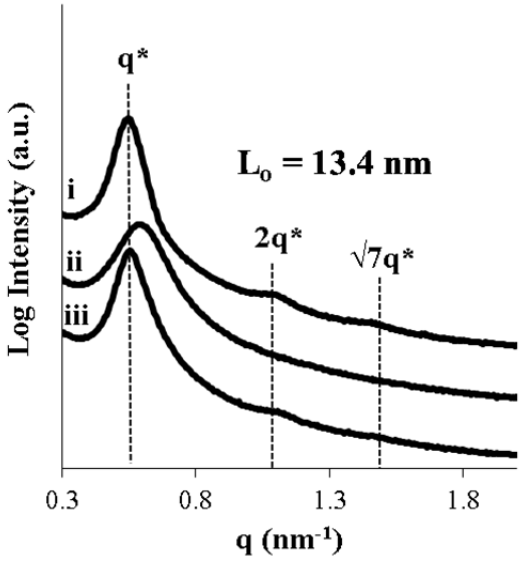


**Figure 5.9**: SAXS patterns of a bulk sample of $PTMSS_{2.3}$-*b*-$PLA_{1.7}$ after the i) first solvent anneal, ii) subsequent thermal anneal at 160°C for 15 minutes, and iii) second solvent anneal after the thermal anneal. Reproduced with permission from [1].

Since $\chi$ is temperature-dependent, ordering of a BCP can also be temperature-dependent, i.e. at a low temperature a polymer may be ordered while it is disordered at a higher temperature. To rule out the possibility that the ordering observed is due to the difference in temperature between thermal and solvent annealing, SAXS and rheological data were analyzed for $PTMSS_{2.3}$-*b*-$PLA_{1.7}$ samples over a range of temperatures. SAXS data was collected for $PTMSS_{2.3}$-*b*-$PLA_{1.7}$ over a temperature range of 120-180 °C and it was observed that the sample remains in the disordered state over the entire range (**Figure 5.10a**). Rheology data in **Figure 5.10b** for $PTMSS_{2.3}$-*b*-$PLA_{1.7}$ also indicates that it remains disordered for all temperatures above 105 °C as evidenced by an order of magnitude difference in G' and G" over all temperatures. Rheology data were collected on a TA Instruments AR-2000ex in strain controlled mode at 1 rad/s frequency in the linear viscoelastic regime. This data suggests that the domain selectivity of the solvent

annealing process likely contributes more significantly to the ordering of the BCP than the lower temperature at which the solvent annealing process takes place.

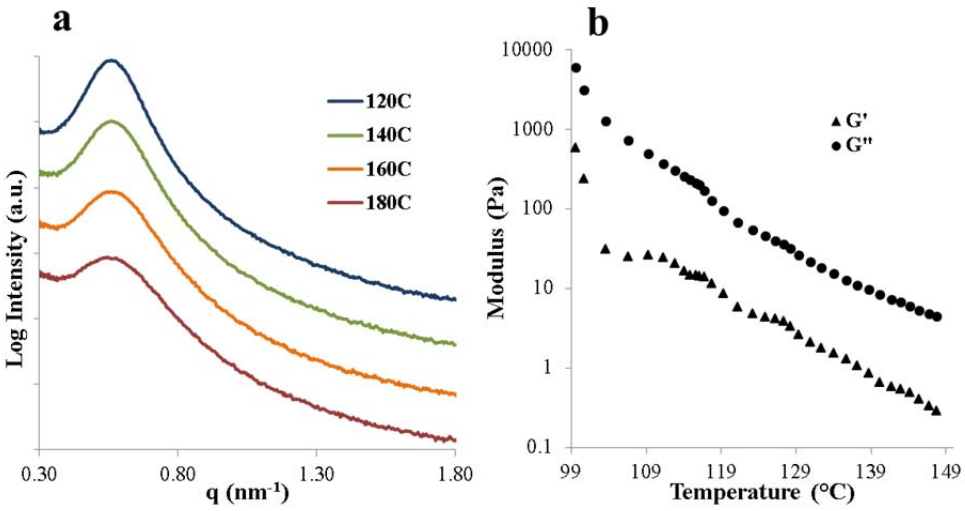


**Figure 5.10**: a) SAXS patterns of $PTMSS_{2.3}$-*b*-$PLA_{1.7}$ at temperatures ranging from 120-180 °C. b) Rheology data for $PTMSS_{2.3}$-*b*-$PLA_{1.7}$ at temperatures ranging from 100-150 °C. Reproduced with permission from [1].

### 5.2.3 Simulations Evidence for a decrease in ODT

Simulations data supports the experimental data in Section 5.2.1 by suggesting that $\chi N$ at the ODT decreases with domain-selective solvent annealing. **Figure 5.11** displays ODT $\chi$s, denoted as $(\chi_{AB}N)_s$, for the diblock copolymer system with various solvent volume fractions. For small $\chi$, corresponding to a pair of almost neutral solvents, we observe that the ODT $(\chi_{AB}N)_s$ increases with increasing solvent fraction. Such a trend is consistent with earlier studies in the context of neutral solvents.[12, 13] However, beyond a critical $\chi$ (for our parameters, the critical $\chi$ = 0.3) the $\chi_{AB}N$ corresponding to the ODT decreases with increasing solvent fraction. Moreover, the system can form ordered phases at $\chi_{AB}N$ even lower than the critical value for a pure melt which corresponds to $\chi_{AB}N$ = 10.495. Such results indicate that a pair of highly preferential solvents can serve to

promote the ordering of block copolymers even at $\chi_{AB}N$ well below that required for the pure block copolymer system and is consistent with the experimentally observed formation of the ordered phase by solvent annealing of the disordered sample in **Figure 5.7**. An interesting outcome of our theoretical model is the prediction that only solvents with sufficiently strong preferential interactions can facilitate such a behavior.

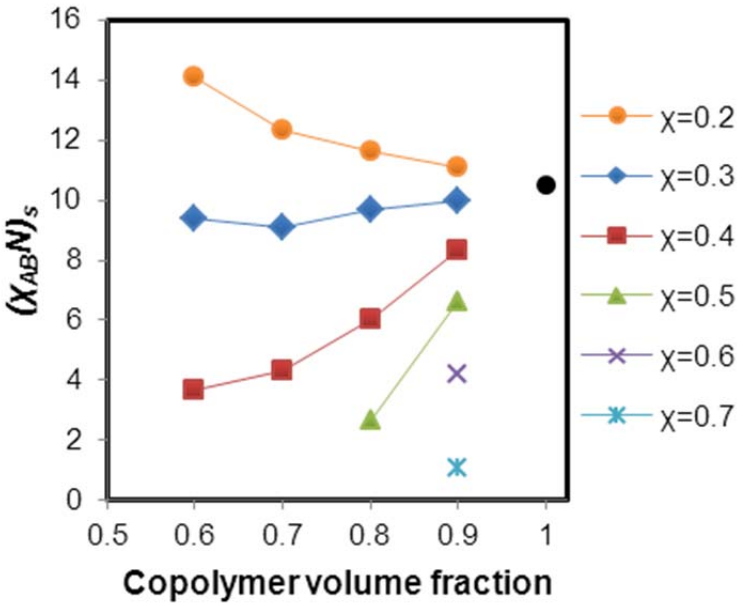


**Figure 5.11**: $(\chi_{AB}N)_s$ predicted by SCFT as a function of copolymer volume fraction for varying monomer-solvent interaction parameters ($\chi$). The black circle indicates the ODT for pure diblock system (copolymer volume fraction =1). The lines are a guide to the eye. Reproduced with permission from [1].

The increase in domain periodicity and induced order in a disordered sample presented here has several applications in BCP self-assembly. BCPs have an equilibrium domain periodicity after thermal annealing that is governed by the synthesis, i.e. volume fraction and molecular weight of the synthesized sample. For applications where fine-tuning of the domain periodicity is desirable or hitting target molecular weights and

compositions is difficult, solvent annealing with the conditions presented in this chapter may be an attractive means of reaching desired volume fractions and domain periodicities. Altering the thermodynamics of self-assembly with a condition that results in stretching of the polymer chains may also make one or both domains less dense in polymer and have implications in etch rates and pattern transfer that could be useful in lithography. For polymers where the molecular weight of one or more domains cannot be altered (i.e. non-polymerized molecules, like oligosaccharides), solvent annealing with domain-selective solvents may be an effective method of inducing order in the system if the polymer is otherwise disordered.

### 5.2.2 DSA of 13 nm Pitch Lines

For $PTMSS_{2.3}$-*b*-$PLA_{1.7}$, a topographic pattern was created by Lei Wan at HGST, who patterned sparse lines of cross-linked polystyrene using electron beam lithography. The pitch of the DSA pattern was designed to be three times the ~13 nm pitch of the solvent annealed polymer to multiply the density of the underlying pattern by a factor of three. The width of the pre-patterned line was designed to be commensurate with the ~6 nm half-pitch of the solvent annealed cylinder-forming BCP. The bare silicon substrate between the cross-linked polystyrene was filled with a 1.2 kDa polystyrene brush. Block copolymer cylinders assembled on the pre-pattern aligned after solvent annealing with the same conditions as the unaligned sample. Since there is little chemical contrast between the cross-linked polystyrene and the polystyrene brush, a small difference in height between the cross-linked polystyrene and the PS brush contributes most significantly to the alignment of the domains.

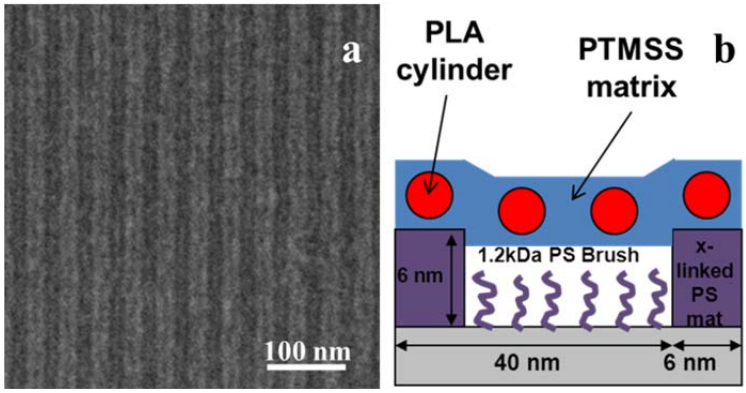


**Figure 5.12**: a) Directed self-assembly of $PTMSS_{2.3}$-*b*-$PLA_{1.7}$ after solvent annealing on a topographical pattern and b) the dimensions of the underlying pattern and assembled block copolymer. Reproduced with permission from [1].

Several high-$\chi$ materials such as poly(styrene-*block*-dimethylsiloxane), PS-*b*-PDMS,[23] and a polyhedral oligomeric silesquioxane-containing polymer, poly(methyl methacrylate-*block*-PMAPOSS), PMMA-*b*-PMAPOSS[24] have been similarly aligned by DSA techniques and solvent annealing. However, the alignment of PTMSS-*b*-PLA described here enables the formation of a line pattern with a domain periodicity similar to 12 nm PMMA-*b*-PMAPOSS hexagonally-packed dot patterns formed from a spherical morphology and is smaller than the 17.5 nm pitch line pattern formed from PS-*b*-PDMS cylinders. Order in our $PTMSS_{2.3}$-*b*-$PLA_{1.7}$ sample is directed into 13 nm pitch line patterns, the highest density line patterns reported to be directed by topographical patterns.

### 5.3 REFERENCES

1. J. Cushen; L. Wan; G. Pandav; I. Mitra; G. Stein; V. Ganesan; R. Ruiz; C. G. Willson; C. J. Ellison, *Journal of Polymer Science Part b* **2013,** *in press*.
2. K. J. Hanley; T. P. Lodge; C.-I. Huang, *Macromolecules* **2000,** *33*, 5918-5931.
3. G. Fredrickson, *Equilibrium Theory of Inhomogeneous Polymers, The. International Series of Monographs on Physics*. Oxford Scholarship Online: 2006.
4. G. H. Fredrickson; V. Ganesan; F. Drolet, *Macromolecules* **2002,** *35*, 16-39.
5. M. W. Matsen, *Macromolecules* **2003,** *36*, 9647-9657.
6. M. W. Matsen; M. D. Whitmore, *Journal of Chemical Physics* **1996,** *105*, 9698-9701.

7. J. D. Vavasour; M. D. Whitmore, *Macromolecules* **1992,** *25*, 5477-5486.
8. Z. Wu; B. Li; Q. Jin; D. Ding; A.-C. Shi, *The Journal of Physical Chemistry B* **2010,** *114*, 15789-15798.
9. M. Banaszak; M. D. Whitmore, *Macromolecules* **1992,** *25*, 3406-3412.
10. M. D. Whitmore; J. D. Vavasour, *Macromolecules* **1992,** *25*, 2041-2045.
11. J. R. Naughton; M. W. Matsen, *Macromolecules* **2002,** *35*, 5688-5696.
12. C. I. Huang; T. P. Lodge, *Macromolecules* **1998,** *31*, 3556-3565.
13. T. P. Lodge; K. J. Hanley; B. Pudil; V. Alahapperuma, *Macromolecules* **2003,** *36*, 816-822.
14. K. Mori; H. Hasegawa; T. Hashimoto, *Polymer* **2001,** *42*, 3009-3021.
15. K. Mori; H. Hasegawa; T. Hashimoto, *Polymer* **2001,** *42*, 3009-3021.
16. F. S. Bates; G. H. Fredrickson, *Annual Review of Physical Chemistry* **1990,** *41*, 525-557.
17. J. W. Jeong; W. I. Park; M.-J. Kim; C. A. Ross; Y. S. Jung, *Nano Letters* **2011,** *11*, 4095-4101.
18. Y. S. Jung; C. A. Ross, *Advanced Materials* **2009,** *21*, 2540-2545.
19. T.-Y. Lo; C.-C. Chao; R.-M. Ho; P. Georgopanos; A. Avgeropoulos; E. L. Thomas, *Macromolecules* **2013**.
20. R. Ruiz; R. L. Sandstrom; C. T. Black, *Advanced Materials* **2007,** *19*, 587-+.
21. C. M. Bates; T. Seshimo; M. J. Maher; W. J. Durand; J. D. Cushen; L. M. Dean; G. Blachut; C. J. Ellison; C. G. Willson, *Science* **2012,** *338*, 775-779.
22. F. S. Bates; G. H. Fredrickson, *Physics Today* **1999,** *52*, 32-38.
23. Y. S. Jung; J. B. Chang; E. Verploegen; K. K. Berggren; C. A. Ross, *Nano Letters* **2010,** *10*, 1000-1005.
24. Y. Tada; H. Yoshida; Y. Ishida; T. Hirai; J. K. Bosworth; E. Dobisz; R. Ruiz; M. Takenaka; T. Hayakawa; H. Hasegawa, *Macromolecules* **2011,** *45*, 292-304.

# Chapter 6: Measuring the χ-Parameters of Block Copolymers

The interaction (χ) parameter of a BCP describes how chemically incompatible the blocks are and is directly related to the minimum attainable feature sizes the BCP can form.[1] Knowing the values and temperature dependence of χ for different BCP systems allows a comparison of their minimum attainable feature sizes that can be made and is thus useful in selecting a block copolymer for high resolution lithography applications. Determining the values and temperature dependence of χ is not trivial, and the two methods used in the literature to extract this relationship are described in this chapter. These methods were used to determine the temperature dependence of the χ-parameters of most of the BCP systems described in the previous chapters and then comparisons were made between these new BCP systems and other BCPs that are being considered for lithography. Unfortunately, the χ-parameters of the PTMSS-*b*-Oligosaccharide systems could not be determined since both methods require analysis of the BCP in the melt state and $T_g$s of the oligosaccharide blocks are not accessible.

## 6.1 Determining χ by the $T_{ODT}$ Method

The first method of characterizing χ leverages the fact that the value of χN at the order-disorder transition is predicted from mean field theory for perfectly symmetric (50:50 by volume) diblock ($\chi N_{ODT}=10.5$)[2, 3] or ABA triblock ($\chi N_{ODT}=17.9$)[2, 4] copolymers. The relationship between χ and 1/T in the strong segregation limit has been established as approximately linear with a temperature-dependent enthalpic and excess entropic component[5] adopting the form in **Equation 6.1** where T is in K.

$$\chi = A/T + B \qquad \textbf{Eq. 6.1}$$

These two known relationships can be combined and rearranged into the form in **Equation 6.2** for diblock copolymers.

$$10.5/N = A/T_{ODT} + B \quad \textbf{Eq. 6.2}$$

A polymer sample can be synthesized and characterized by common polymer characterization techniques to determine its N (degree of polymerization) and order-disorder transition temperature ($T_{ODT}$) if it is accessible in the melt. For a set of samples with different N values (and different corresponding $T_{ODT}$s), 10.5/N can be plotted vs. $T_{ODT}$ and the A and B parameters can be extracted from linear regression of the data. These parameters can then be inserted into **Equation 6.1** to establish a relationship between $\chi$ and T. This method has been used to determine the $\chi$-parameter for a number of polymers in the literature.[6, 7]

**Equations 6.1** and **6.2** originate from Leibler's mean field theory,[3] which assumes segmental symmetry (A and B repeat units have the same segment length) in a perfectly symmetric (by volume) BCP. However, there is almost always some degree of segmental asymmetry between the A and B monomer units. Therefore, some considerations must be made since degree of polymerization is not an accurate definition of N with segmental asymmetry. When determining $\chi$ using this method, the degree of polymerization is usually normalized by an arbitrary reference volume (often the segment volume of a 4-carbon repeat unit, 118 $Å^3$), to remove the effects of segmental asymmetry. **Equation 6.3** is used to normalize the repeat unit molecular weight where $M_{norm}$ is the normalized repeat unit molecular weight for calculation of N, $V_{sp}$ is the reference volume, $\rho$ is the monomer density, and $N_a$ is Avogadro's number.[8] For example, for a polymer density of 1 g/mL, $M_{norm}$ is 71 g/mol so the measured polymer $M_n$ would be divided by 71 to get the normalized N.

$$M_{norm} = V_{sp}*\rho*N_a \quad \textbf{Eq. 6.3}$$

However, this analysis does not result in an "absolute" or "universal" $\chi$ since its calculated value is highly dependent on the choice of an arbitrarily chosen reference

volume for normalization (several different reference volumes have been used in characterization of $\chi$ in the literature). The size of the repeat unit of interest proves to be important; for the polymers investigated in this work, the segment volumes of the repeat units (TMSS, MTMSMA, S, LA) are significantly larger than the reference volume. Large repeat units result in a significantly larger N after normalization and a significantly smaller calculated $\chi$-parameter than what is calculated without normalization. For this reason, it is better to describe the segregation strength of a polymer by $\chi N$ instead of $\chi$, since regardless of reference volume used in the calculation, $\chi N$ will be the same for a given polymer at a specific temperature.

When making comparisons between the $\chi$-parameters determined using the absolute intensity SAXS method (described in Section 6.2), we observed similar $\chi$ values to those calculated using the $T_{ODT}$ method without the normalization, but very different results when N was normalized to the reference volume. Discrepancy between the two methods has been observed in the literature and was attributed to isotope effects from deuteration for neutron scattering[9, 10] and chain stretching near the ODT.[10] In this study we were not investigating any deuterated polymers, however the chain stretching effect or the large change in $\chi$ from reference volume normalization could be reasons for the discrepancy. While the calculated $\chi$-parameters provide a ballpark comparison of the segregation of the materials, a more thorough investigation into comparison between the two methods could be the subject of future work and $\chi$-parameter comparisons should only be made between polymers whose $\chi$-parameters were determined using the same method.

### 6.1.1 PS-*b*-PMTMSMA

To determine $\chi$ by the $T_{ODT}$ method, ten approximately symmetric (by volume) PS-*b*-PMTMSMA samples were synthesized at various molecular weights. The characterization data for these samples is summarized in **Table 6.1.** The characterization data (except the $T_{ODT}$) was obtained using the methods described in Chapter 2.

| Sample | PS $M_n$ (kDa) | PS PDI | PMTMSMA $M_n$ (kDa) | BCP PDI | Vol. % PMTMSMA | $T_{odt}$ |
|---|---|---|---|---|---|---|
| $PS_{10.2}$-*b*-$PMTMSMA_{11.5}$ | 10.2 | 1.06 | 11.5 | 1.07 | 53.0 | 180°C |
| $PS_{10.2}$-*b*-$PMTMSMA_{12.2}$ | 10.2 | 1.07 | 12.2 | 1.07 | 54.5 | 184°C |
| $PS_{10.4}$-*b*-$PMTMSMA_{12.4}$ | 10.4 | 1.10 | 12.4 | 1.06 | 54.4 | 187°C |
| $PS_{10.5}$-*b*-$PMTMSMA_{12.0}$ | 10.5 | 1.07 | 12.0 | 1.07 | 53.2 | 213°C |
| $PS_{11.0}$-*b*-$PMTMSMA_{12.2}$ | 11.0 | 1.07 | 12.2 | 1.07 | 52.6 | 224°C |
| $PS_{10.9}$-*b*-$PMTMSMA_{12.3}$ | 10.9 | 1.08 | 12.3 | 1.07 | 53.0 | 236°C |
| $PS_{11.2}$-*b*-$PMTMSMA_{12.9}$ | 11.2 | 1.06 | 12.9 | 1.07 | 53.5 | 250°C |
| $PS_{11.1}$-*b*-$PMTMSMA_{12.7}$ | 11.1 | 1.08 | 12.7 | 1.07 | 53.3 | 253°C |
| $PS_{11.2}$-*b*-$PMTMSMA_{12.9}$ | 11.2 | 1.06 | 12.9 | 1.09 | 53.4 | 269°C |
| $PS_{11.6}$-*b*-$PMTMSMA_{13.5}$ | 11.6 | 1.08 | 13.5 | 1.06 | 53.8 | 275°C |

**Table 6.1:** Materials used to calculate $\chi$ for PS-*b*-PMTMSMA using the $T_{ODT}$ method.

The $T_{ODT}$s of the samples in **Table 6.1** were determined by rheology. The data were obtained at low strains, determined to be in the linear viscoelsastic regime by performing a strain sweep first, to minimize nonlinear effects.[12] The strain sweep for $PS_{10.2}$-*b*-$PMTMSMA_{11.5}$ (**Figure 6.1**), performed at 160 °C, is representative of all BCP samples of this polymer. Based on this scan, a strain of 2% was chosen for subsequent

experiments since this is in the linear regime. The frequency for the temperature scan experiments was chosen such that it was below the crossover frequency for the polymer separating domain and single-chain dynamics.[12] Therefore a frequency of 1 rad/s was used for all temperature scans.

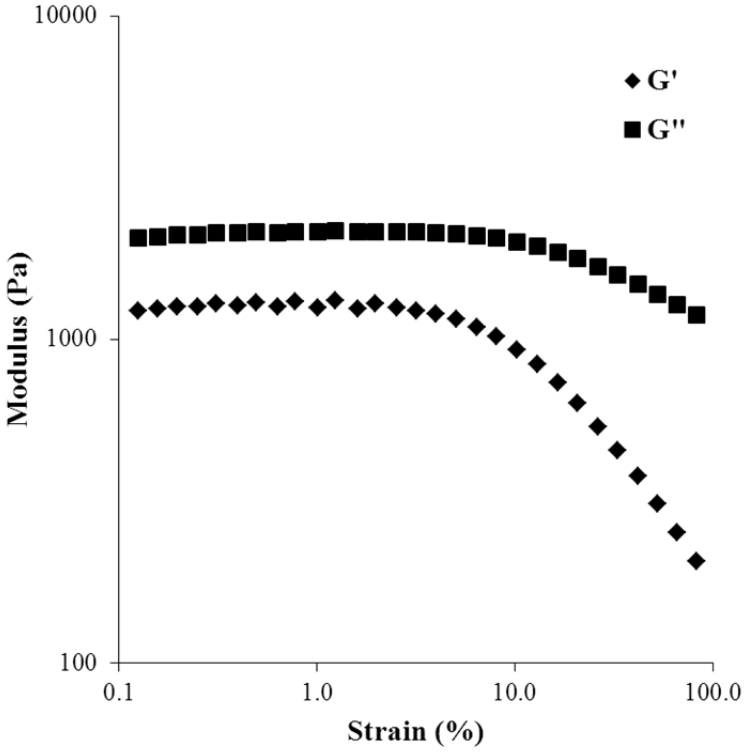


**Figure 6.1:** Strain sweep for $PS_{10.2}$-*b*-$PMTMSMA_{11.5,}$ representative of all PTMSS-*b*-PMTMSMA samples.

The $T_{ODT}$ was determined by monitoring the change in the dynamic elastic (G') and loss (G") moduli as a function of temperature. The presence of a $T_{ODT}$ is indicated by a precipitous drop in G' and G" during a temperature scan at a constant frequency and strain (experimental conditions determined *a priori*) during the measurement.[12] A typical temperature sweep for a block copolymer with an accessible $T_{ODT}$ is shown in **Figure**

**6.2**. The value of the $T_{ODT}$ used in determination of the $\chi$-parameter was the approximate onset temperature of disordering, determined at the intersection of the extrapolated ordered and transition state elastic modulus.

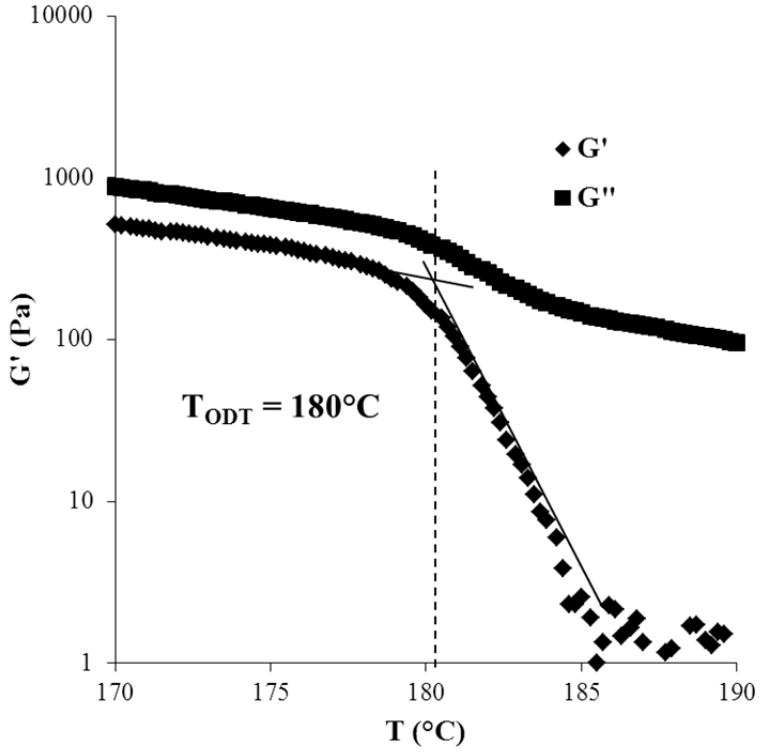


**Figure 6.2:** G' and G" over a temperature range of 170°C-190°C for $PS_{10.2}$-*b*-$PMTMSMA_{11.5,}$ indicating the presence of a $T_{ODT}$ around 180°C.

As a side note, the response of G' and G" to temperature could also be used to determine whether a block copolymer of interest was in the ordered or disordered state, even if a $T_{ODT}$ was not accessible for the sample. Temperature scans of a typical ordered (**Figure 6.3a**) and disordered (**Figure 6.3b**) BCP have very different rheological behavior. In the ordered sample, the difference in G' and G" is less than an order of magnitude and in a disordered sample the difference is an order of magnitude or greater.

These measurements were used to supplement SAXS data when determining if a sample was in the ordered or disordered state at a given temperature.

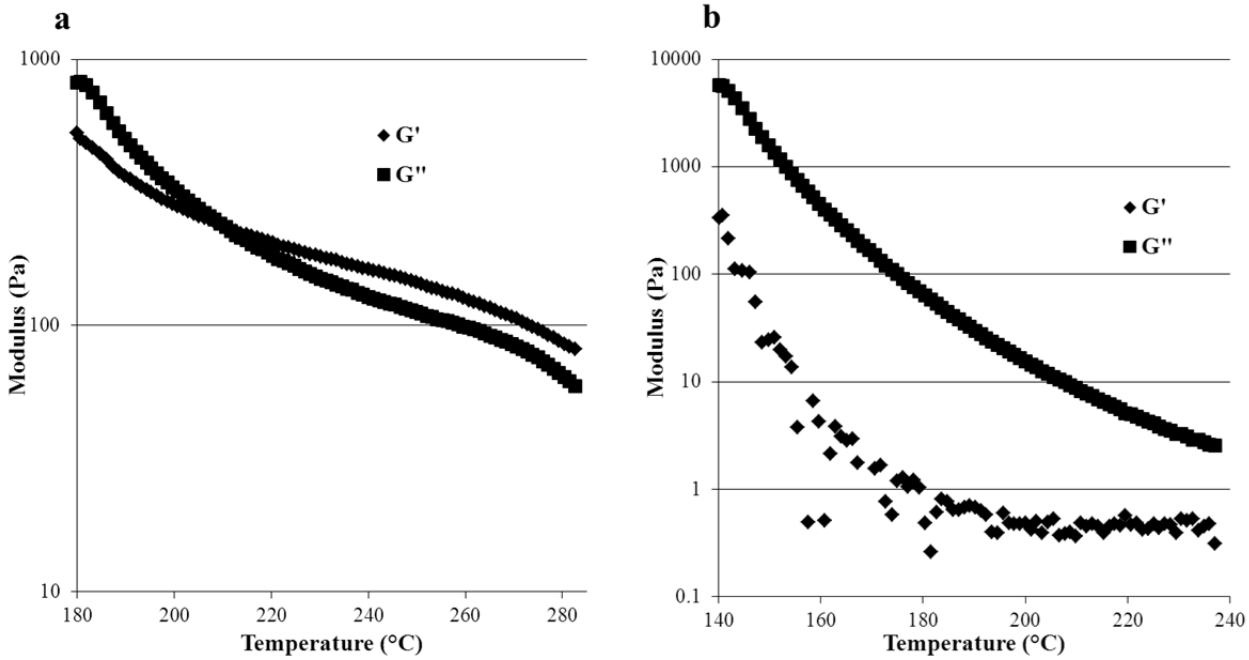


**Figure 6.3:** Representative rheology data for a PS-*b*-PMTMSMA sample that is a) ordered and b) disordered throughout the entire temperature range investigated.

After determining the $T_{ODT}$ of each sample in **Table 6.1**, 10.5/N was plotted vs. $1/T_{ODT}$ with and without reference volume normalization. A linear relationship was established between these parameters and the values of A and B in **Equation 6.1** were extracted. The plot of 10.5/N vs. $1/T_{ODT}$ and linear fit of the data with and without reference volume normalization with regression is shown in **Figure 6.4**.

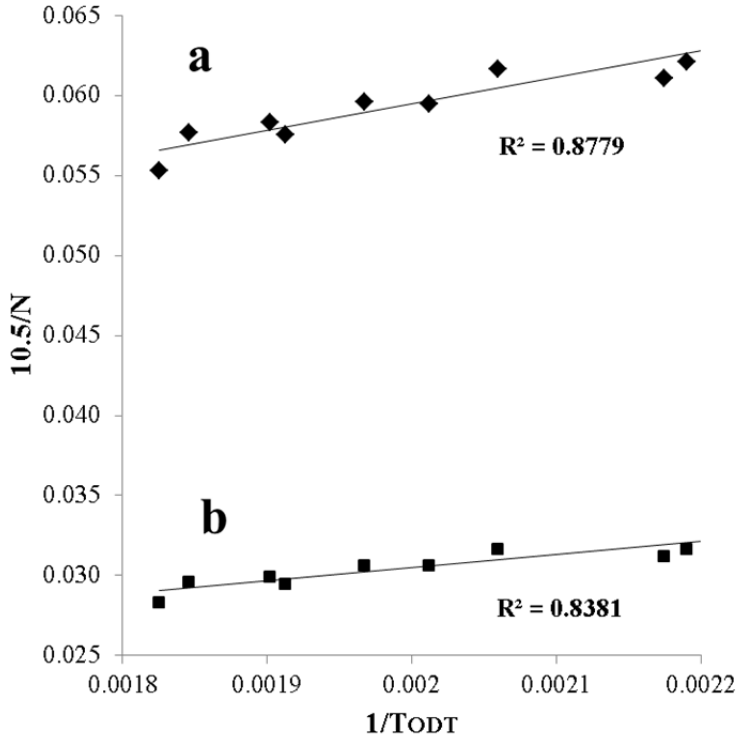


**Figure 6.4:** Plot of 10.5/N vs. $1/T_{ODT}$ for the samples in **Table 6.1** and linear regression of the data a) without reference volume normalization and b) with reference volume normalization.

Linear regression of the data in Figure 6.4 results in the relationship between $\chi$ and T in **Equation 6.3** without reference volume normalization and **Equation 6.4** with reference volume normalization.

$$\chi = 16.55/T + 0.0264 \qquad \textbf{Eq. 6.3}$$

$$\chi = 8.28/T + 0.0139 \qquad \textbf{Eq. 6.4}$$

The range of $\chi$ values for PS-*b*-PMTMSMA for a temperature range of 100-200°C calculated using this method is 0.06-0.07 without reference volume normalization and 0.02-0.03 with normalization.

### 6.1.2 PS-*b*-PTMSS-*b*-PS

The χ-parameter of PS-*b*-PTMSS-*b*-PS was also determined by using the $T_{ODT}$ method. Two approximately symmetric (by volume) ABA triblock copolymer samples were synthesized at various molecular weights. The characterization data for these samples is summarized in **Table 6.2.** The characterization data (except the $T_{ODT}$) was obtained using the methods described in Chapter 2.

| Sample | PTMSS $M_n$ (kDa) | PTMSS PDI | PS $M_n$ (kDa) | BCP PDI | Vol. % PTMSS | $T_{odt}$ |
|---|---|---|---|---|---|---|
| $PS_{16.0}$-*b*-$PTMSS_{33.1}$-*b*-$PS_{16.0}$ | 33.1 | 1.09 | 32.0 | 1.09 | 51.0 | 241°C |
| $PS_{18.5}$-*b*-$PTMSS_{33.3}$-*b*-$PS_{18.5}$ | 33.9 | 1.12 | 36.9 | 1.13 | 47.6 | 246°C |

**Table 6.2:** Materials used to calculate χ for PS-*b*-PTMSS-*b*-PS using the $T_{ODT}$ method.

Since only two samples were synthesized with accessible $T_{ODT}$s, a relationship between χ and temperature was not determined for this polymer using this method due to the likelihood of significant error in fitting only two data points. However, χ was extracted at these $T_{ODT}$s using the relationship $\chi N = 17.9$ for a symmetric ABA triblock copolymer. The χ values extracted for this polymer with and without reference volume normalization at the two $T_{ODT}$s are reported in **Table 6.3**.

| T (°C) | T (K) | χ | $\chi_{Norm}$ |
|---|---|---|---|
| 241 | 514 | 0.0361 | 0.0183 |
| 246 | 519 | 0.0330 | 0.0173 |

**Table 6.3:** χ values extracted for PS-*b*-PTMSS-*b*-PS at two $T_{ODT}$s.

For $PS_{16.0}$-*b*-$PTMSS_{33.1}$-*b*-$PS_{16.0}$, the evolution of the primary SAXS peak across the $T_{ODT}$ was investigated to supplement measurement of the $T_{ODT}$ by rheology. **Figure 6.5** shows a 3-D plot of scattering intensity as a function of q for the primary scattering peak at various temperatures above and below the $T_{ODT}$. As will be described in Section 6.2, the primary scattering peak of a BCP decreases in peak intensity and broadens as the polymer goes from ordered to disordered with increasing temperature. From the plot in **Figure 6.5**, the primary scattering peak broadens and decreases in peak intensity in the temperature range of 244-250°C, indicating the presence of a $T_{ODT}$ with a value that is consistent with rheology measurements.

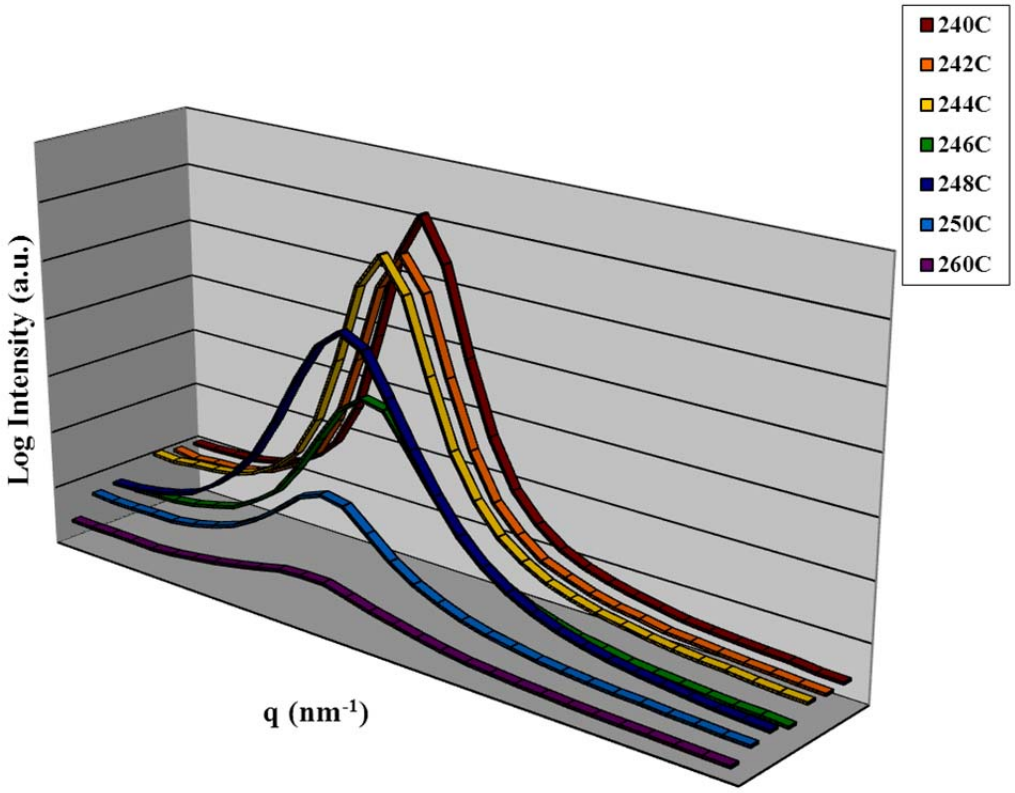


**Figure 6.5:** SAXS profiles of $PS_{16.0}$-*b*-$PTMSS_{33.1}$-*b*-$PS_{16.0}$ across the order-disorder transition temperature.

### 6.1.3 Challenges and Limitations

In practice, synthesizing these sample sets is quite difficult and labor intensive. Synthesizing a statistically significant set of BCP samples with different N values, all with low PDIs and perfectly symmetric blocks (requirements to assume a constant value of $\chi N$ of 10.5 from mean field theory) is a formidable challenge even for a skilled polymer chemist. For polymers that are difficult to synthesize or require multiple isolation steps, it can be even more time consuming. The difficulty is compounded by the fact that a $T_{ODT}$ must be accessible for it to be measured; it must exist between the glass transition temperatures of the blocks in the sample and must be below its degradation temperature. Since many polymers have a $\chi$-parameter that is weakly a function of temperature (small changes in molecular weight lead to large changes in $T_{ODT}$) and this may dictate a sample MW synthesis window of only a few kDa for samples to have accessible $T_{ODT}$s.

## 6.2 Determining $\chi$ by Absolute Intensity SAXS

A second method enables the determination of $\chi$ by fitting a neutron or x-ray scattering intensity curve predicted by mean field theory to experimental data on an absolute scale from a disordered sample at a specific temperature above its $T_g$. In the disordered state, a sample exhibits intensity in a SAXS pattern due to density fluctuations of the segments within the material. The density fluctuations in the bulk state and the effect on the intensity and shape of the primary scattering peak can be visualized as a function of temperature by **Figure 6.6.** SAXS patterns corresponding to the schematics were taken from the $PS_{16.0}$-*b*-$PTMSS_{33.1}$-*b*-$PS_{16.0}$ SAXS data in **Figure 6.5** at various temperatures where intensities are plotted on the same arbitrary intensity scale.

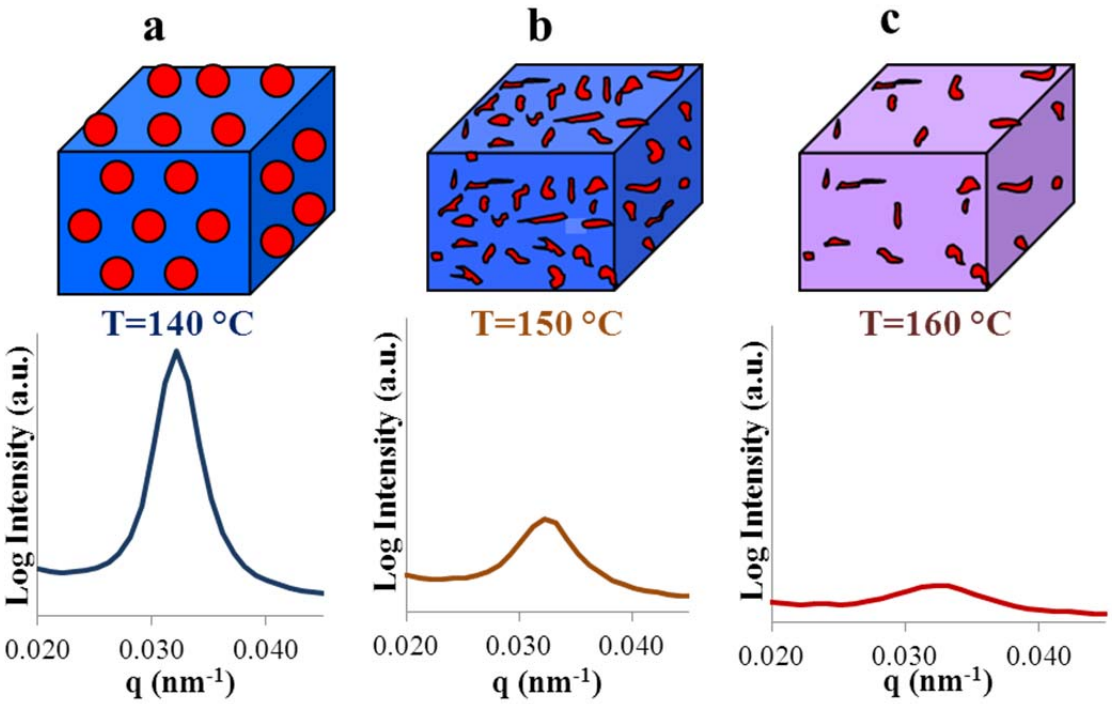


**Figure 6.6:** BCP structure in the bulk at various temperatures surrounding the $T_{ODT}$ and corresponding SAXS patterns of the primary scattering peak for $PS_{16.0}$-*b*-$PTMSS_{33.1}$-*b*-$PS_{16.0}$ from **Figure 6.5**. a) At temperatures below the $T_{ODT}$, the BCP is in the ordered state as evidenced by a high intensity, narrow primary scattering peak. b) At temperatures just above the $T_{ODT}$, the BCP is no longer phase-separated into an ordered morphology, however density fluctuations occur within the disordered material, giving rise to a broad, low intensity scattering peak. c) At temperatures higher than those that produce the bulk structure in **Figure 6.6b**, the disordered material is more homogeneous, giving rise to a SAXS pattern that is even lower intensity and broader than the pattern produced by **Figure 6.6b**.

The degree of inhomogeneity in the disordered state is dependent on a variety of physical and thermodynamic properties of the polymer and affects the intensity and shape of the disordered scattering peak. A correlation between these properties and the shape of the disordered scattering peak has been modeled previously. Leibler's mean field theory provided the framework for this analysis,[3] and was later modified for polydispersity and segmental asymmetry.[11] Since all of the parameters in the theory can be measured or

calculated directly except $\chi$, one can determine $\chi$ by fitting theoretical data with $\chi$ as an adjustable parameter to experimental data. While an in-depth discussion of the theoretical model they originate from will not be detailed here, the equations used to determine the $\chi$-parameter are summarized by **Equations 6.5a-6.5k**.[11]

In the following, X represents either block A or B. I(q) is the theoretical absolute intensity. $f_X$ is the volume fraction of X and is determined by NMR, $v_X$ is the molar volume of the X monomer and is determined from the molecular weight and density of the monomer. $N_{X,n}$ and $N_{X,w}$ are the number- and weight-average degree of polymerization, respectively and are determined by GPC. $b_X$ is the segment length of X and is either reported in the literature or used as a fitted parameter in the $\chi$ characterization. $\lambda_X$ is the PDI of the X block and is either characterized by GPC for the first block polymerized or by **Equation 6.5k** from the PDI of the block copolymer and the known PDI of the first block. $w_x$ is the weight fraction of the x block.

$$I(q) = K[S(q)/W(q)-2\chi]^{-1} \quad \textbf{Eq. 6.5a}$$

$$S(q) = \langle S_{A,A}\rangle + 2\langle S_{A,B}\rangle + \langle S_{B,B}\rangle \quad \textbf{Eq. 6.5b}$$

$$W(q) = \langle S_{A,A}\rangle * \langle S_{A,B}\rangle - \langle S_{B,B}\rangle^2 \quad \textbf{Eq. 6.5c}$$

$$\langle S_{X,X}(q)\rangle = r_{c,n} f^2_{X,n} g^{(2)}_{X,n}(q) \quad \textbf{Eq. 6.5d}$$

$$\langle S_{A,B}(q)\rangle = r_{c,n} f_A f_B g^{(1)}_{A,n}(q)\, g^{(1)}_{B,n}(q) \quad \textbf{Eq. 6.5e}$$

$$r_{c,n} = (v_A N_{A,n} + v_B N_{B,n})/(v_A * v_B)^{1/2} \quad \textbf{Eq. 6.5f}$$

$$g^{(1)}_{X,n}(q) = 1/x_{X,n}\{1 - [x_{X,n}(\lambda_X-1) + 1]^{-(\lambda_x^{-1})\hat{}-1}\} \quad \textbf{Eq. 6.5g}$$

$$g^{(2)}_{X,n}(q) = 2/x_{X,n}^2\{-1 + [x_{X,n}(\lambda_X-1) + 1]^{-(\lambda_x^{-1})\hat{}-1}\} \quad \textbf{Eq. 6.5h}$$

$$x_{X,n} = (N_{X,n} b_X^2/6)q^2 \quad \textbf{Eq. 6.5i}$$

$$\lambda_A = N_{X,w}/N_{X,n} \quad \textbf{Eq. 6.5j}$$

$$\lambda_B = ((\lambda_{BCP} -1-(\lambda_A - 1)*w_A^2)/(1-w_A)^2+1 \quad \textbf{Eq. 6.5k}$$

The experimental SAXS data is first converted to an absolute scale (i.e. absolute number of scattered x-rays that reach the detector) before theoretical data fitting to maintain consistency between the experimental data and theoretical origins. In practice this conversion is not trivial and requires running several calibration standards since SAXS detectors do not count the number of x-rays collected but are rather on an arbitrary intensity scale. The experimental data is transformed from an arbitrary to absolute scale by three corrections: 1) a correction based on the x-ray transmission of the sample to account for the number of x-rays that make it through the sample vs. those that are absorbed, 2) a correction by subtracting the background from the blank to correct for baseline air in the chamber and scattering from the kapton tape that surrounds the sample, and 3) a scaling factor correction from a precalibrated standard that transforms the data to an absolute scale. The standards that must be run before collecting data for a sample include AgBe to calibrate the q-scale, a blank, and an absolute intensity calibration standard, typically low density polyethylene (LDPE). The absolute intensity SAXS pattern of the absolute intensity calibration standard is typically determined using a synchrotron source against a sample with a known scattering intensity that is independent of q, such as water.[13] All three calibration standards are run for the exact same amount of time (one hour in this work) and immediately before the BCP sample to reduce error from day-to-day fluctuations in x-ray source intensity.

The x-ray transmission of a block copolymer sample can be calculated from the relationship in **Equation 6.6**, where T is the transmission, $\mu$ is the average attenuation coefficient for the BCP in $cm^{-1}$, and t is the thickness in cm.[14] The x-ray transmission denotes the fraction of x-rays that make it through a specific material with a given thickness vs. those that are absorbed.

$$T = e^{-\mu t} \qquad \textbf{Eq. 6.6}$$

After measuring the thickness of the sample, the only other unknown in **Equation 6.6** is the average attenuation coefficient. The average attenuation coefficient for a material composed of multiple elements, such as a block copolymer, is calculated from the mass attenuation coefficients of the elements within the sample that are weighted by elemental composition on a mass basis. This relationship is shown in **Equation 6.7**, and the material is assumed to be homogeneous. Homopolymer attenuation coefficients ($\mu_x$) were determined first and then weighted based on their mass fraction in the BCP to determine the total attenuation coefficient. In **Equation 6.7**, $(\mu/\rho)_j$ represents the mass attenuation coefficient of element j, $w_j$ is the weight fraction of the element within the polymer, and $\rho_P$ is the overall mass density of the polymer.[14]

$$\mu_x = \rho_P \sum_j \left(\frac{\mu}{\rho}\right)_j w_j \qquad \textbf{Eq. 6.7}$$

The mass attenuation coefficients for the elements that comprise the polymers in this work for CuKα radiation are summarized in **Table 6.4**.[14]

| **Element** | **C** | **H** | **O** | **Si** |
|---|---|---|---|---|
| **$\mu/\rho$ ($cm^2/g$)** | 4.51 | 0.391 | 11.5 | 63.7 |

**Table 6.4:** Mass attenuation coefficients for the elements in the polymers in this work for a CuKα radiation source.

Based on the values listed in **Table 6.4** and their elemental composition, the attenuation coefficients of the homopolymer components in this work were calculated and are listed in **Table 6.5**.

| Polymer | wt. % C | wt. % H | wt. % O | wt. % Si | $\mu_x$ ($cm^2/g$) |
|---|---|---|---|---|---|
| **PS** | 92.24 | 7.76 | - | - | 4.19 |
| **PMTMSMA** | 55.75 | 9.38 | 18.57 | 16.30 | 15.07 |
| **PTMSS** | 74.91 | 9.16 | - | 15.93 | 13.56 |
| **PLA** | 50.00 | 5.60 | 44.40 | - | 7.38 |

**Table 6.5:** Attenuation coefficients for the homopolymer components of the BCPs synthesized in this work.

The equation used to correct the arbitrary intensity to an absolute scale is represented in **Equation 6.8**, where $I_{abs}$ is the absolute intensity, K is the scaling factor from the calibration standard, I(q) is the arbitrary intensity, T is the transmission, $I_B$ is the background, and t is the thickness in mm. This equation encompasses the three of the corrections necessary for absolute intensity calibration described previously.

$$I_{abs}(q) = K*[(I(q)/T-I_B)/t] \quad \textbf{Eq. 6.8}$$

I(q) and $I_B$ were collected and T, t, and $I_{abs}(q)$ were previously calculated and measured for a precalibrated LDPE calibration standard. The standard and pre-determined parameters for it were kindly supplied by Dr. Richard Register at Princeton University. K, the scaling factor which is needed from the calibration standard for adjusting the BCP scattering data to absolute intensity on a specific instrument, was extracted by minimizing the sum of the errors between the experimental and the known calibration standard intensity at each q by changing K. A plot typical of the fitted arbitrary intensity data after corrections and optimization of the K value is shown in **Figure 6.7.**

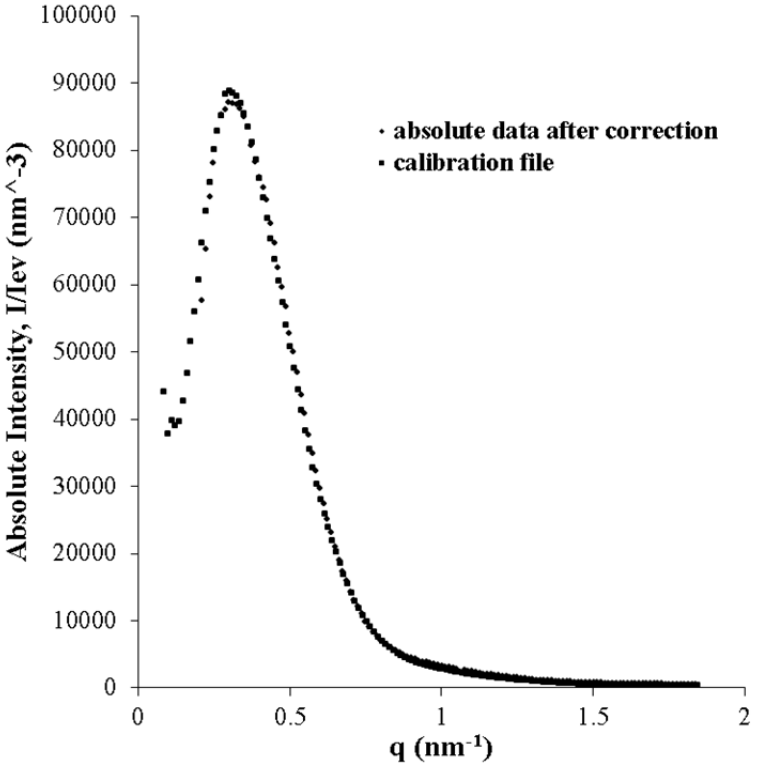


**Figure 6.7:** Fitting of corrected relative intensity data for LDPE calibration standard to the absolute intensity standard calibration file.

After extracting K from this analysis, all parameters in **Equation 6.8** were either collected or calculated for the BCP sample and K was used as a scaling factor to plot the experimental data on an absolute scale. In addition to the corrections mentioned previously, a thermal baseline intensity subtraction was also applied to the scattering data for the BCP samples. The following sections will now detail the experimental parameters for the BCPs investigated using this method.

### 6.2.1 PS-*b*-PMTMSMA

The $\chi$-parameter of PS-*b*-PMTMSMA was determined using the absolute intensity SAXS method to compare the values determined to those using the $T_{ODT}$ method. The parameters used to extract $\chi$ from **Equations 6.5a-k** for PS-*b*-PMTMSMA

are summarized in **Table 6.6.** In addition to $\chi$, $b_{MTMSMA}$ was also used as an adjustable parameter in the fitting of the theoretical intensity curve since the value is not available from literature. Since changing only one unknown segment length moves the curve on the x-axis and changing $\chi$ does not, there is only one value of the unknown segment length that satisfies the fitting of the experimental curve so we are confident in using this parameter as an adjustable parameter.

| **Block** | **w** | **f** | **N** | **b** | ***v*** | **λ** |
|---|---|---|---|---|---|---|
| **S** | 0.478 | 0.470 | 97.94 | 0.68 | 114.5 | 1.06 |
| **MTMSMA** | 0.522 | 0.530 | 66.8 | 1.02 | 195.1 | 1.21 |

**Table 6.6:** Parameters used in **Equations 6.5a-k** to determine $\chi$ for PS-*b*-PMTMSMA.

The fitting of the theoretical absolute intensity profile to the experimental data corrected to an absolute scale is shown in **Figure 6.8**. $\chi$ was fitted by minimizing the sum of the error between the theoretical fit and absolute experimental data.

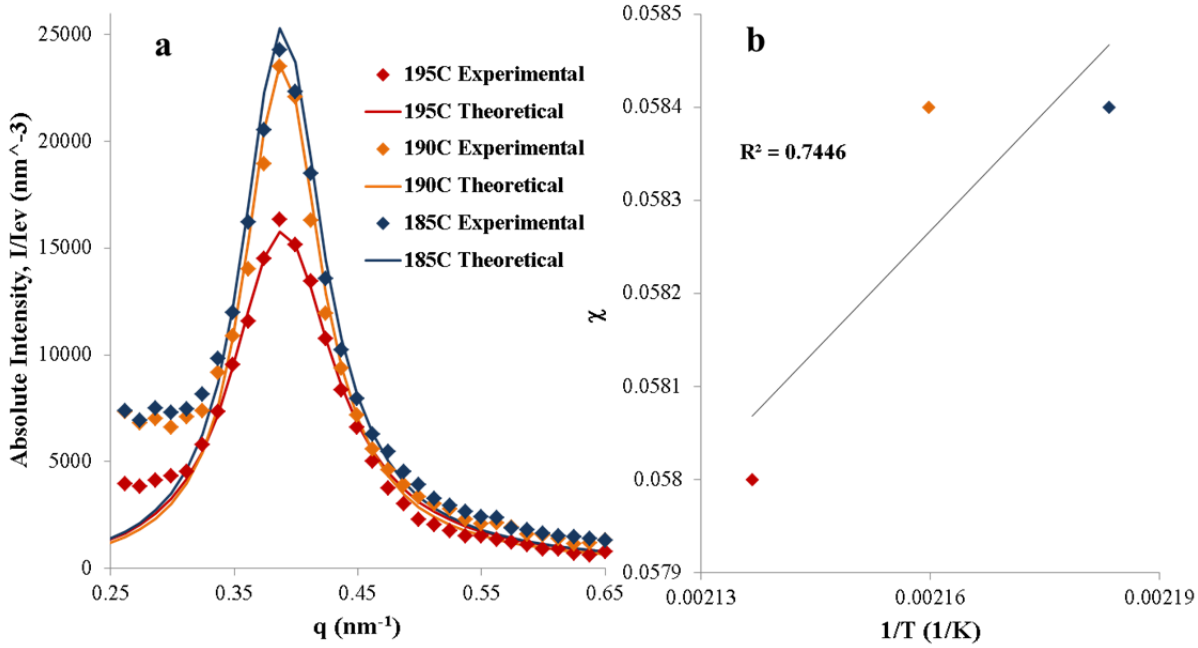


**Figure 6.8:** a) Experimental (markers) and theoretical fitting (corresponding lines) of absolute intensity SAXS data for PS-*b*-PMTMSMA at three temperatures and b) linear fitting of χ vs. 1/T to extract temperature dependence on χ.

For clarity, **Table 6.7** lists the values of χ extracted from this analysis for the absolute intensity SAXS profiles collected for disordered PS-*b*-PMTMSMA at three different temperatures.

| T (°C) | T (K) | χ |
|---|---|---|
| 185 | 458 | 0.0584 |
| 190 | 463 | 0.0584 |
| 195 | 468 | 0.0580 |

**Table 6.7:** χ values extracted at three temperatures for PS-*b*-PMTMSMA.

Linear regression of these values results in the relationship between $\chi$ and T in **Equation 6.9**. The range of $\chi$ values for PS-*b*-PMTMSMA for a temperature range of 100-200°C calculated using this method is 0.058-0.061.

$$\chi = 8.54/T + 0.040 \qquad \textbf{Eq. 6.9}$$

### 6.2.2 PS-*b*-PTMSS-*b*-PS

The $\chi$-parameter of PS-*b*-PTMSS-*b*-PS was also determined using the absolute intensity SAXS method. For a symmetric triblock copolymer, the equations used to perform this analysis differ slightly from a diblock copolymer.[15] These equations are summarized in **Equations 6.10a-d**.

$$\langle S_{A,A}(q)\rangle = 2r_{c,n}f^2_{A,n}\{g^{(2)}_{A,n}(q) + g^{(1)}_{A,n}(q)^2 * [1/(x_{B,n}(\lambda_B-1)+1)]\text{^}[1/(\lambda_B-1)]\} \qquad \textbf{Eq. 6.10a}$$

$$\langle S_{B,B}(q)\rangle = r_{c,n}f^2_{B,n}g^{(2)}_{B,n}(q) \qquad \textbf{Eq. 6.10b}$$

$$\langle S_{A,B}(q)\rangle = 2r_{c,n}f_Af_Bg^{(1)}_{A,n}(q)\, g^{(1)}_{B,n}(q) \qquad \textbf{Eq. 6.10c}$$

$$\lambda_{BCP}-1 = 2(\lambda_B-1)w^2_A + (\lambda_B-1)w^2_B \qquad \textbf{Eq. 6.10d}$$

The characterization data for the disordered sample used to perform the absolute intensity SAXS measurements of PS-*b*-PTMSS-*b*-PS is summarized in **Table 6.8.**

| Block | w | f | N | b | *v* | $\lambda$ |
|---|---|---|---|---|---|---|
| **S** | 0.673 | 0.674 | 182 | 0.68 | 114.6 | 1.21 |
| **TMSS** | 0.327 | 0.326 | 104 | 0.75 | 194 | 1.10 |

**Table 6.8:** Parameters used in **Equations 6.5a-k** and **6.10a-d** to determine $\chi$ for PS-*b*-PTMSS-*b*-PS. Note that the way **Equations 6.10a-d** are defined, the N value for styrene (the A block of the ABA triblock copolymer) is defined as ½ the total degree of polymerization of the A block.

The fitting of the theoretical absolute intensity profile to the experimental data corrected to an absolute scale is shown in **Figure 6.9**. χ was fitted by minimizing the sum of the error between the theoretical fit and absolute experimental data.

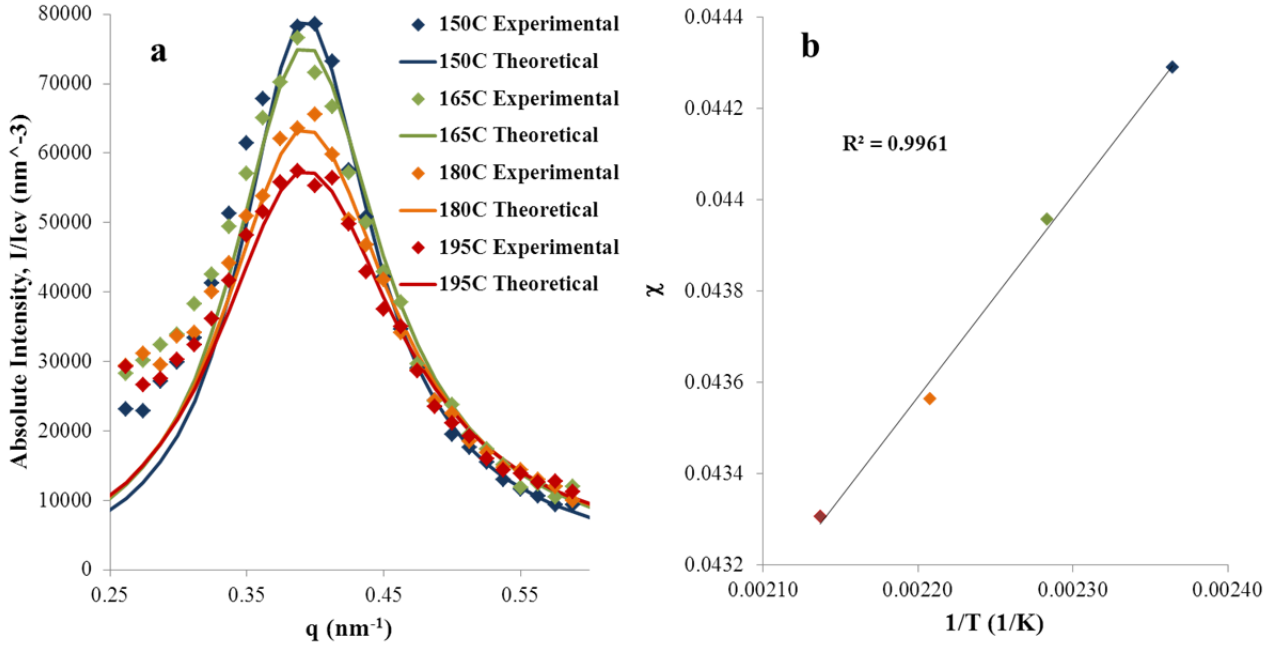


**Figure 6.9:** a) Experimental (markers) and theoretical fitting (corresponding lines) of absolute intensity SAXS data for PS-*b*-PTMSS-*b*-PS at four temperatures and b) linear fitting of χ vs. 1/T to extract temperature dependence on χ.

For clarity, **Table 6.9** lists the values of χ extracted from this analysis for absolute intensity SAXS profiles collected for disordered PS-*b*-PTMSS-*b*-PS at each temperature investigated. **Equation 6.11** reports the relationship between χ and temperature based on this analysis.

| T (°C) | T (K) | χ |
|---|---|---|
| 150 | 423 | 0.0443 |
| 165 | 438 | 0.0440 |
| 180 | 453 | 0.0436 |
| 195 | 468 | 0.0433 |

**Table 6.9:** χ values extracted at four temperatures for PS-*b*-PTMSS-*b*-PS.

$$\chi = 4.42/T + 0.034 \qquad \textbf{Eq. 6.11}$$

### 6.2.3 PTMSS-*b*-PLA

The χ-parameter of PTMSS-*b*-PLA was also determined using the absolute intensity SAXS method. The characterization data for the disordered sample used to perform the absolute intensity SAXS measurements is summarized in **Table 6.10.**

| Block | w | f | N | b | *v* | λ |
|---|---|---|---|---|---|---|
| **TMSS** | 0.589 | 0.615 | 13.04 | 0.75 | 194 | 1.11 |
| **LA** | 0.411 | 0.385 | 12.07 | 1.39 | 121.5 | 1.37 |

**Table 6.10:** Parameters used in **Equations 6.5a-k** to determine χ for PTMSS-*b*-PLA.

The fitting of the theoretical absolute intensity profile to the experimental data corrected to an absolute scale is shown in **Figure 6.10**. χ was fitted by minimizing the sum of the error between the theoretical fit and absolute experimental data.

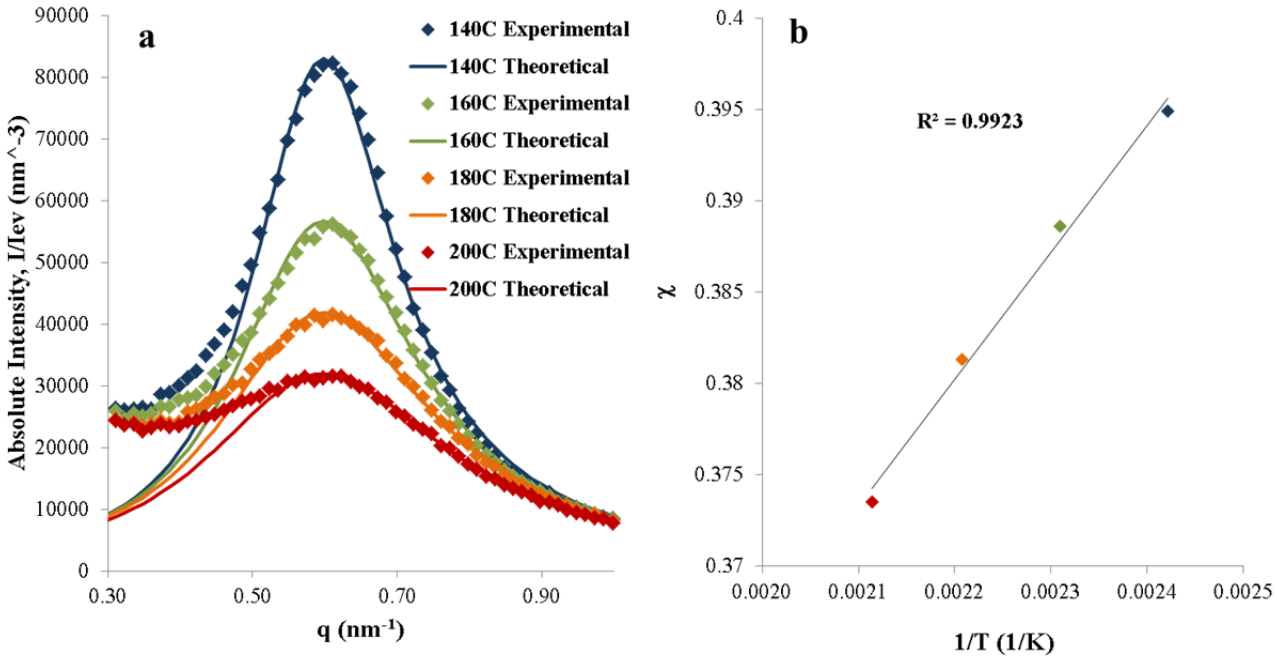


**Figure 6.10:** a) Experimental (markers) and theoretical fitting (corresponding lines) of absolute intensity SAXS data for PTMSS-*b*-PLA at four temperatures and b) linear fitting of χ vs. 1/T to extract temperature dependence on χ.

For clarity, **Table 6.11** lists the values of χ extracted from this analysis for absolute intensity SAXS profiles collected for disordered PTMSS-*b*-PLA at each temperature investigated. **Equation 6.12** reports the relationship between χ and temperature for PTMSS-*b*-PLA based on this analysis.

| T (°C) | T (K) | χ |
|---|---|---|
| 140 | 413 | 0.395 |
| 160 | 433 | 0.389 |
| 180 | 453 | 0.381 |
| 200 | 473 | 0.374 |

**Table 6.11:** χ values extracted at four temperatures for PTMSS-*b*-PLA.

$$\chi = 69.58/T + 0.227 \qquad \textbf{Eq. 6.12}$$

### 6.2.4 Challenges and Limitations

Compared to the first method described, the absolute intensity SAXS method of determining $\chi$ requires only synthesizing one disordered sample that does not have to satisfy the symmetric condition criterion. However, to transform experimental SAXS data onto an absolute scale, it must be normalized by the intensity curve of a pre-calibrated sample with a known absolute intensity scattering profile, which is experimentally difficult to obtain. Fortunately, Dr. Register was kind enough to supply us with a calibration standard, otherwise there are only a few people in the world who know how to calibrate such a standard and without it we would not have been able to perform this analysis. The statistical segment length of the polymer must also be known for the calculations, and can be experimentally difficult to determine for new polymers. We used it as an adjustable parameter in these calculations instead of determining it experimentally.

## 6.3 Comparison of Calculated $\chi$-parameters to Literature

The $\chi$-parameters of various BCPs in the literature and those calculated from this work are plotted as a function of temperature in **Figure 6.11**. Those calculated from this work are denoted by a *, those calculated using the absolute intensity SAXS method are denoted by a solid line, values from literature with reference volume normalization and PS-*b*-PMTMSMA calculated using the $T_{ODT}$ method without reference volume normalization are dashed (PS-*b*-PTMSS-*b*-PS unfilled diamond), and PS-*b*-PMTMSMA with reference volume normalization is dotted (PS-*b*-PTMSS-*b*-PS filled diamond).

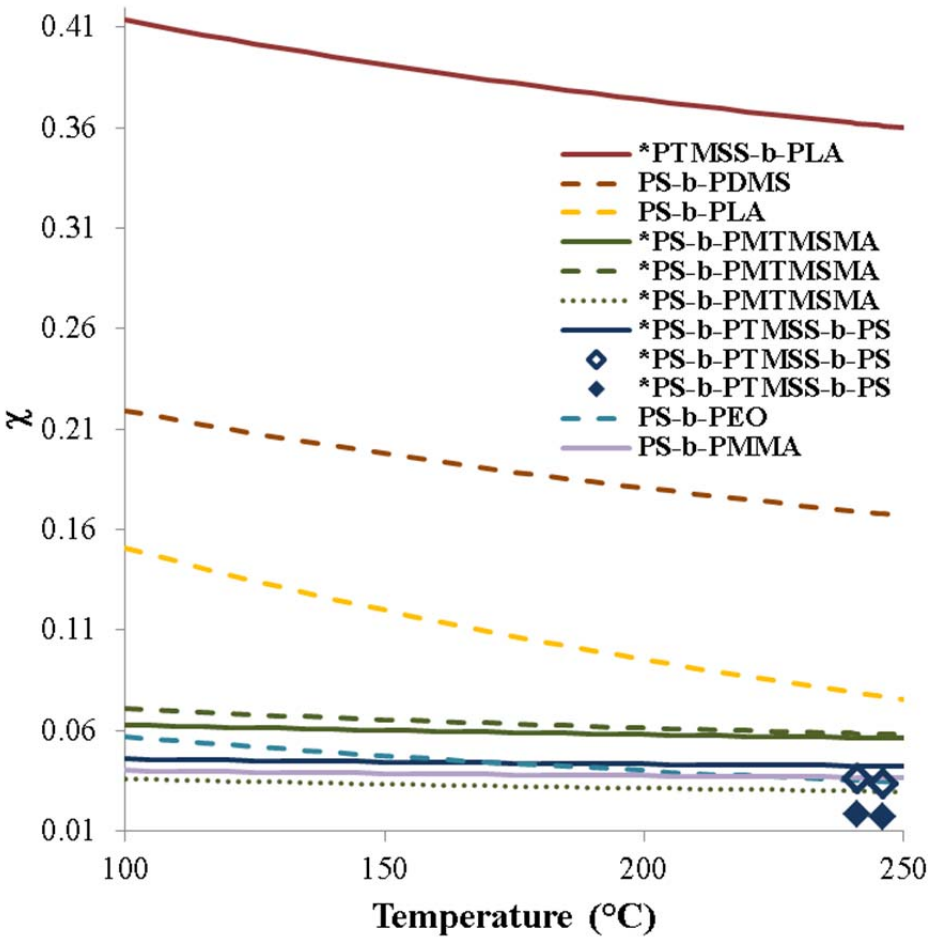


**Figure 6.11:** χ as a function of temperature for the polymers in this work (denoted by a *) as well as several reported in the literature: PS-*b*-PDMS,[6] PS-*b*-PLA,[7] PS-*b*-PEO,[6] PS-*b*-PMMA.[9] Solid lines were calculated using absolute intensity SAXS, dashed lines were calculated using the $T_{ODT}$ method.

The χ-parameter of PLA-*b*-PDMS-*b*-PLA will be discussed in the following paragraphs but is not plotted in **Figure 6.12** since it is so large (~1.1)[16] that it would be difficult to resolve the lower χ-parameter materials on the same plot if it was included. The χ-parameters of PS-*b*-PMTMSMA and PS-*b*-PTMSS-*b*-PS were calculated by both methods (with and without reference volume normalization) but the χ-parameter of

PTMSS-*b*-PLA was only calculated by the absolute intensity SAXS method due to the synthetic difficulty of this polymer with the $T_{ODT}$ method.

When the χ-parameters of PS-*b*-PMTMSMA and PS-*b*-PTMSS-*b*-PS were calculated without reference volume normalization, they were more consistent with the absolute intensity SAXS method; PS-*b*-PMTMSMA and PS-*b*-PTMSS-*b*-PS had calculated χ-parameters within about 10% by the two methods. With normalization, however, the calculated χ-parameters were approximately 50% lower. This is likely due to the reasons noted earlier in this chapter, notably the large change in χ with reference volume normalization of large repeat units. Therefore, we should only consider these χ-parameter calculations ballpark figures and should only compare them to those calculated using the same method.

Comparing the interaction parameters of known materials offered some insight into what makes a χ-parameter large and thus helped in choosing blocks for a high-χ material, which was discussed briefly in Chapter 4. In general, the χ-parameter of a material is related to the degree of chemical incompatibility between the two blocks, i.e. the different blocks can be thought of as being on a scale of polarity. The further apart they are on that scale, the greater the χ-parameter between the domains. This is represented by **Figure 6.12**, where the lengths of the lines between domains are proportional to the χ-parameter between them. This assumption that polarity is the only influence in χ-parameter is not always accurate, for example note the discrepancy between the calculated χ in **Figure 6.11** and the scale in **Figure 6.12** for PS-*b*-PMTMSMA and PS-*b*-PTMSS-*b*-PS. However, this "scale" represents the general polarity difference I considered when designing the materials presented in the previous chapters.

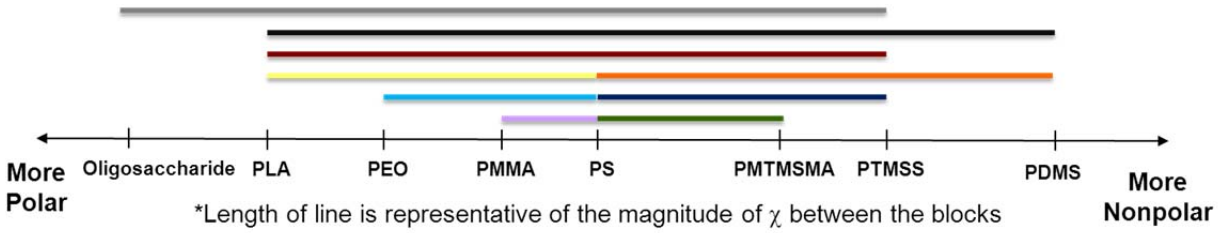


**Figure 6.12:** Generalized polarity scale considered in the investigation of new high-χ materials. The lengths of the lines between domains represent proportionality to the χ-parameter between the domains.

It is clear from **Figures 6.11** and **6.12** that the χ-parameter of PTMSS-*b*-PLA is significantly higher than the other BCPs investigated in this study except for PLA-*b*-PDMS-*b*-PLA. This is the reason so much work was performed with this polymer and why it remains an attractive candidate for lithography applications. We hope to be able to overcome the challenges associated with the processing conditions discussed in Chapter 4 for this reason and facing these challenges remains the subject of future study. It is also possible that with the knowledge we now have from these studies, BCPs with even higher χs can be synthesized and studied in future work.

### 6.4 REFERENCES

1. F. S. Bates; G. H. Fredrickson, *Annual Review of Physical Chemistry* **1990,** *41*, 525-557.
2. M. D. Gehlsen; K. Almdal; F. S. Bates, *Macromolecules* **1992,** *25*, 939-943.
3. L. Leibler, *Macromolecules* **1980,** *13*, 1602-1617.
4. M. W. Matsen; R. B. Thompson, *The Journal of Chemical Physics* **1999,** *111*, 7139-7146.
5. T. P. Russell; R. P. Hjelm; P. A. Seeger, *Macromolecules* **1990,** *23*, 890-893.
6. E. W. Cochran; D. C. Morse; F. S. Bates, *Macromolecules* **2003,** *36*, 782-792.
7. A. S. Zalusky; R. Olayo-Valles; J. H. Wolf; M. A. Hillmyer, *Journal of the American Chemical Society* **2002,** *124*, 12761-12773.
8. L. J. Fetters; D. J. Lohse; D. Richter; T. A. Witten; A. Zirkel, *Macromolecules* **1994,** *27*, 4639-4647.
9. Y. Zhao; E. Sivaniah; T. Hashimoto, *Macromolecules* **2008,** *41*, 9948-9951.

10. W. W. Maurer; F. S. Bates; T. P. Lodge; K. Almdal; K. Mortensen; G. H. Fredrickson, *The Journal of Chemical Physics* **1998,** *108*, 2989-3000.
11. N. Sakamoto; T. Hashimoto, *Macromolecules* **1995,** *28*, 6825-6834.
12. J. H. Rosedale; F. S. Bates, *Macromolecules* **1990,** *23*, 2329-2338.
13. O. Kratky; I. Pilz; P. J. Schmitz, *Journal of Colloid and Interface Science* **1966,** *21*, 24-&.
14. R.-J. Roe, *Methods of X-Ray and Neutron Scattering in Polymer Science*. Oxford University Press: 2000.
15. S. Sakurai; K. Mori; A. Okawara; K. Kimishima; T. Hashimoto, *Macromolecules* **1992,** *25*, 2679-2691.
16. M. D. Rodwogin; C. S. Spanjers; C. Leighton; M. A. Hillmyer, *ACS Nano* **2010,** *4*, 725-732.
17. J.-B. Chang; J. G. Son; A. F. Hannon; A. Alexander-Katz; C. A. Ross; K. K. Berggren, *ACS Nano* **2012,** *6*, 2071-2077.
18. S. Park; D. H. Lee; J. Xu; B. Kim; S. W. Hong; U. Jeong; T. Xu; T. P. Russell, *Science* **2009,** *323*, 1030-1033.

# Chapter 7: Naturally-Derived Oligosaccharide-Wax Amphiphilic BCPs

The preceding chapters described the synthesis and self-assembly of silicon-containing BCPs for lithographic applications. As described in Chapter 6, the motivation behind synthesizing the BCPs presented in this dissertation was to maximize the polarity difference between the two blocks to create high $\chi$-parameter materials that self-assemble into small domains. During the process of designing BCPs for lithography, we considered a material that consisted of the most hydrophobic component bound to the most hydrophilic component we could conceive, both at low molecular weights to facilitate self-assembly into small domains. The BCP material that came to mind and that will be detailed in this chapter consists of the extremely hydrophilic oligosaccharide described in Chapter 3 bound to a hydrophobic straight chain saturated alkane. **Figure 7.1** shows the structures of the blocks we chose for the BCP materials that will be described in this chapter. They consist of two different oligosaccharide geometries and various chain lengths of a straight chain saturated alkane.

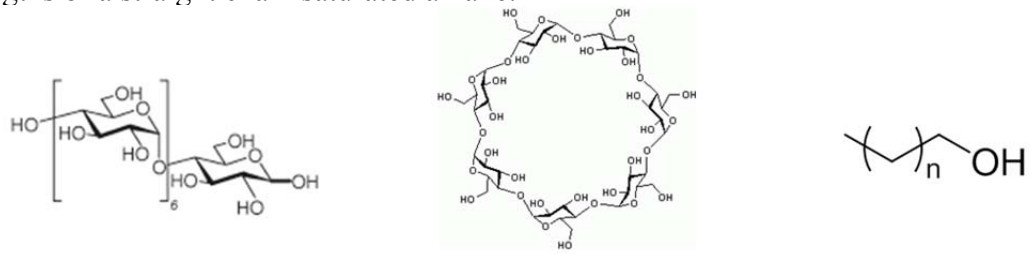


**Figure 7.1**: Structures of the oligosaccharide and wax precursors chosen for the BCP materials described in this chapter.

While initially chosen for lithography applications, we also realized that the oligosaccharide-wax BCPs are derived from naturally-occurring materials. **Table 7.1** reports some of the common uses of the specific block precursor materials that will be

described in this work. As shown in this table, the materials have some common uses in the drug, supplement, and cosmetics industries. This makes them attractive for biological applications since they are already determined to be nontoxic and safe for human consumption.

| Block | Precursor | # of Carbons | Source | Uses |
|---|---|---|---|---|
| Wax | Octacosanol | 28 | Plants and wheat germ[1] | Cholesterol-lowering supplement, treatment of Parkinson's disease[2] |
| | Policosanol | 22-30 | Plant extract and beeswax[3] | Nutritional supplement to lower cholesterol[4] |
| | Docosanol | 22 | | Cosmetics, nutritional supplements, constituent of Abreva[5] |
| | Octadecanol | 18 | From stearic acid (animal and vegetable fat)[6] | Lubricants, cosmetics, ointments, shampoos, conditioners[6] |
| **Block** | **Precursor** | **Geometry** | **Source** | **Uses** |
| Sugar | Maltoheptaose | Linear | Enzymatically ring-opened βCyD | |
| | Betacyclodextrin | Cyclic | Enzymatically-modified starch[7] | Various uses in the food, pharmaceutical, and agriculture industries[7] |

**Table 7.1**: Common uses of the oligosaccharide and wax precursor materials described in this chapter. Policosanol consists of a mixture of chain lengths of fatty alcohols but consists primarily of octacosanol.

We expected that the oligosaccharide-wax materials would be amphiphilic since they are composed of a very polar and a very nonpolar component. Amphiphilic BCPs are particularly useful for drug delivery since they can form micelles or vesicles that can encapsulate a drug and release it with changes in pH or upon degradation in the body.[8]

Therefore, the focuses of this chapter will be on the synthesis of these BCPs and experiments to evaluate their ability to encapsulate molecules for drug delivery applications.

## 7.1 Synthesis of Sugar-Wax BCPs

The oligosaccharide and wax components that make up the BCPs in this chapter were chosen from the oligosaccharides described in Chapter 3 and several waxes that were chosen specifically to have a hydroxyl group to enable azide functionalization. The two materials were alkyne and azide functionalized, respectively, and then coupled by azide-alkyne cycloaddition similarly to the BCPs described in Chapter 3.

### 7.1.1 Sugar Functionalization

Maltoheptaose was kindly supplied by the Nissan Chemical Company. Maltoheptaose[9] and β-cyclodextrin[10] were functionalized with an alkyne group using established procedures. Since I functionalized the oligosaccharides used in this chapter (the oligosaccharides used in Chapter 3 were functionalized at CERMAV) I will briefly describe the procedure here.

Maltoheptaose functionalization is described in **Scheme 7.1**. Propargylamine (12 mL) was added to maltoheptaose (3.0 g) and stirred at room temperature for 72 hours. The success of the reaction was checked by TLC using butanol:ethanol:water in a ratio of 1:2:1 as the eluent and the TLC plate was stained with iodine. After confirming the success of the reaction, 30 mL methanol was added to the solution to dilute it and the functionalized MH was precipitated in 90 mL of dichloromethane (DCM). The white solid was washed with 60 mL DCM and dried *in vacuo*. 2.5 g of this product was dissolved in 200 mL methanol. Acetic anhydride (10 mL) was added and stirred for 12 hours. The success of the reaction was checked by TLC with an eluent of

acetonitrile:water in a ratio of 13:7. The solvent was then removed by rotary evaporation and the functionalized maltoheptaose product was freeze dried from water.

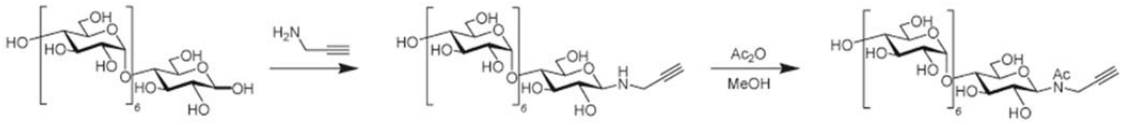

**Scheme 7.1**: Alkyne functionalization of maltoheptaose. Adapted with permission from [9]. Copyright 2009 American Chemical Society.

Betacyclodextrin functionalization is described in **Scheme 7.2.** Sodium hydroxide (2.5 g) was stirred for 10 minutes in 300 mL water. The solution was cooled to 0 °C and 15 g betacyclodextrin was added to the solution. 6 g tosyl chloride was added to the solution and stirred. After two hours another 9 g tosyl chloride was added. Unreacted tosyl chloride was filtered out and the reaction was quenched with 90 mL 10% HCl. The reaction was cooled in the refrigerator for 72 hours. The resulting tosylated betacyclodextrin was filtered and dried. In a second step, propargylamine (4.5 mL) was added to 1.24 g tosylated betacyclodextrin. The solution was heated to 65 °C, sparged with argon, and stirred for 12 hours. The resulting solid was precipitated in acetonitrile and dried *in vacuo*.

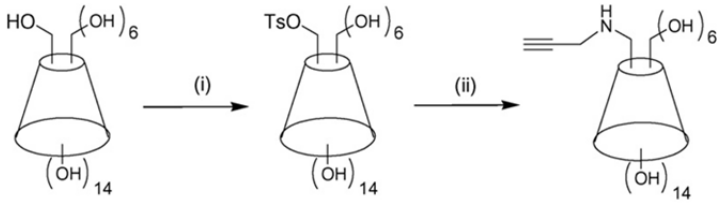

**Scheme 7.2**: Functionalization of β-cyclodextrin by (i) tosylation and (ii) alkyne functionalization. Reprinted from [10] Copyright 2009, with permission from Elsevier.

### 7.1.2 Wax Functionalization

The hydroxyl-functionalized waxes were tosylated and then functionalized with azide using a procedure adapted from literature (**Scheme 7.3**).[11] A representative procedure for docosanol functionalization follows: docosanol (~5 g, 15.3 mmol) was dissolved in triethyl amine (100 mL) and a 10 molar excess of tosyl chloride (15 g, 76.5 mmol) was added to the solution. The cloudy solution was heated to 70 °C and reacted for 18 h. The resulting cloudy brown solution was diluted with dichloromethane and extracted 3 times with water and one time with dichloromethane to remove excess tosyl chloride. The resulting solution was concentrated and precipitated in methanol and dried *in vacuo*. Tosylated docosane (5 g, 10.4 mmol) was then dissolved in DMF (150 mL). The solution was heated to 65 °C to enable complete dissolution of the wax in DMF. A 6 molar excess of sodium azide (4.06 g, 62.4 mmol) was added to the solution and allowed to react for 18 h. The resulting product was precipitated in water.

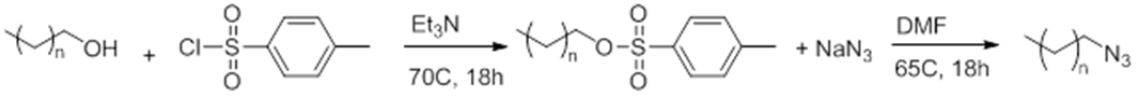


**Scheme 7.3**: General procedure for azide-functionalizing the waxes.

The success of the wax functionalization was monitored by IR (shown in Section 7.1.3) and NMR. **Figure 7.2** shows the progression of the NMR of the policosane (representative of all the waxes) through each functionalization step. From this figure, it can be seen that the peak from the hydrogens on the carbon next to the hydroxyl completely disappears with tosylation indicating complete functionalization in addition to new peaks from the tosyl group. Upon adding the azide, the tosyl peaks completely

disappear and a peak from the hydrogens on the carbon next to the azide appears. This indicates nearly complete azide functionalization of the wax.

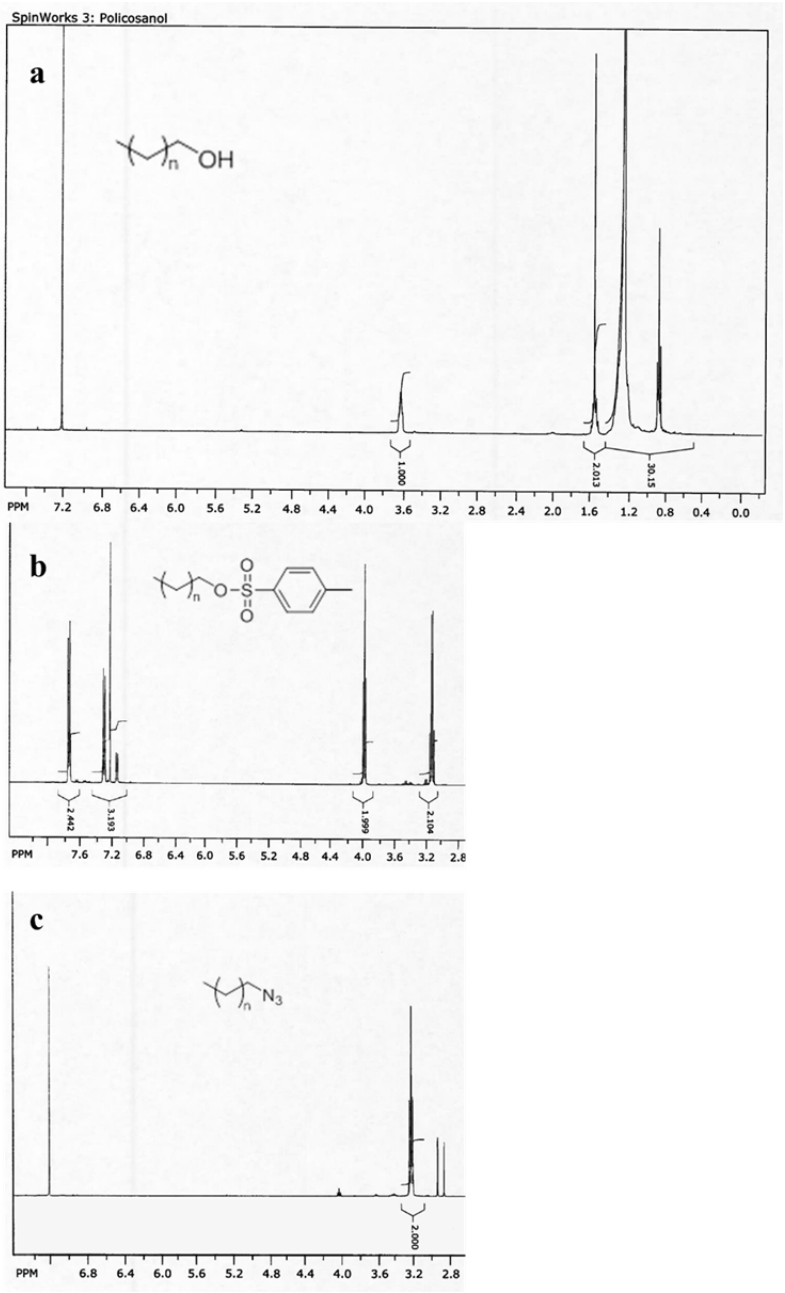


**Figure 7.2**: NMR of a) policosanol b) after tosylation and c) after azide functionalization. Only 2.8-7 ppm shown after functionalization for clarity.

### 7.1.3 Sugar-Wax coupling by "Click" Chemistry

The azide-functionalized waxes were coupled to the alkyne-functionalized oligosaccharides on approximately a 1 g scale (**Scheme 7.4**). A representative procedure for coupling docosane-Az and ethynyl-Maltoheptaose follows: docosane-Az (0.12g, 0.00034 mmol) was dissolved in DMF (30 mL) and heated to 70 °C to promote dissolution. A 0.75 molar excess of ethynyl-MH (0.74 g, 0.00059 mmol) was dissolved in DMF (30 mL) at room temperature in a separate flask and a 0.5 molar excess of PMDETA (0.11 mL, 0.00051 mmol) ligand was added to the flask. Both flasks were sparged with pure Ar for 15 minutes. The contents of the flasks were then cannulated into a third flask charged with a 0.5 molar excess of CuBr (73.4 mg, 0.00051 mmol) and immediately submerged in a 70 °C oil bath. The brown solution reacted for 72h and was then diluted with THF, which immediately caused the solution to turn blue. The solution was filtered through alumina to remove the copper, however the filtrate still contained a significant amount of copper as evidenced by its blue color. The solution was concentrated and precipitated in a 1:1 water::methanol mixture and the nearly white precipitate was vacuum filtered.

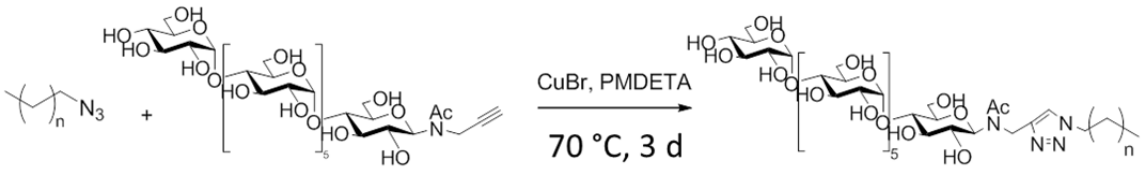


**Scheme 7.4**: General procedure for sugar-wax coupling by azide-alkyne cycloaddition.

The success of the coupling reactions was confirmed by IR. **Figures 7.3** and **7.4** show the IR traces of maltoheptaose coupled to octacosane and betacyclodextrin and maltoheptaose coupled to policosane. MH-*b*-docosane and MH-*b*-octadecane were also

successfully synthesized but will not be described further to reduce the overwhelming quantity of results presented in this chapter. The complete disappearance of the hydroxyl peak after tosylation and appearance of the azide peak in both the IR and NMR confirm that these reactions went to nearly 100% completion. The complete disappearance of the azide peak in IR indicates that the coupling of the wax went to nearly 100% completion. Since the polymer was precipitated in water/methanol and free oligosaccharide is very soluble in water and methanol, excess oligosaccharide was likely removed during precipitation but there is no way to characterize this definitively.

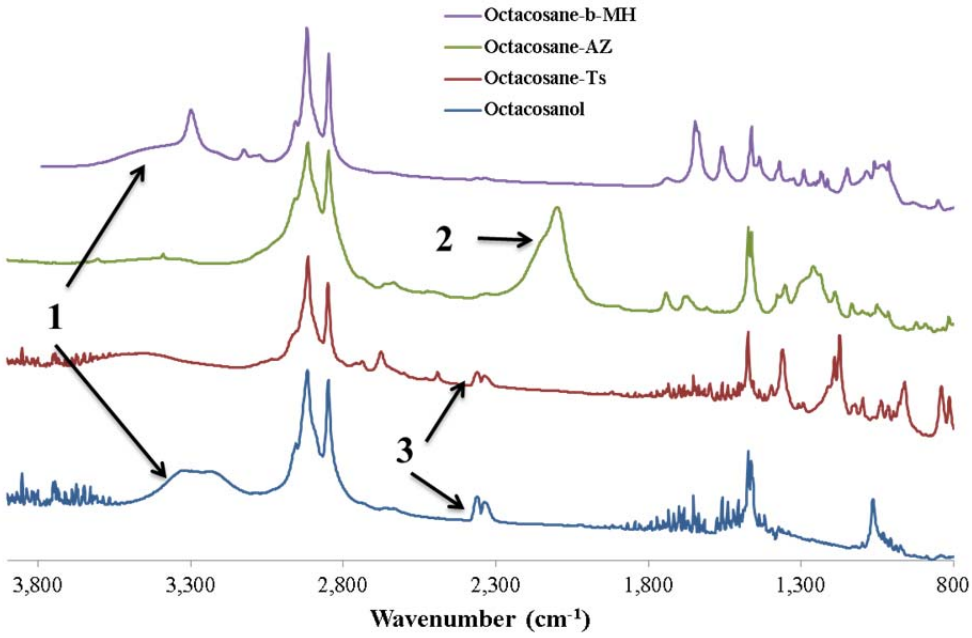


**Figure 7.3**: IR spectra of octacosanol functionalization and coupling to maltoheptaose. The disappearance of hydroxyls (peak 1) indicates the tosylation of octacosanol and the reappearance in the peak after coupling indicates coupling to maltoheptaose. The appearance of azide (peak 2) indicates azide functionalization and its complete disappearance indicates complete coupling of the material. Peak 3 is $CO_2$ contamination. Spectra are shifted for clarity.

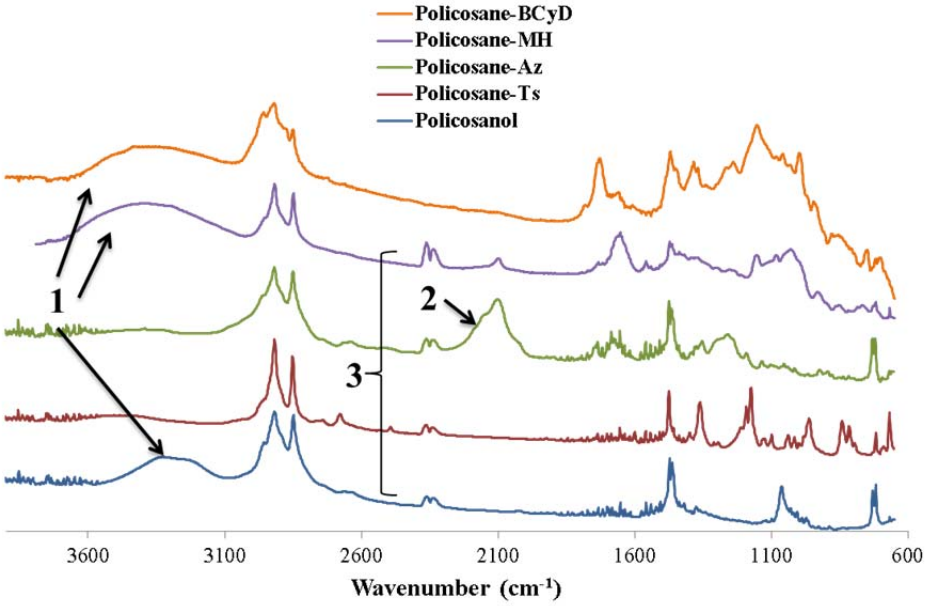


**Figure 7.4**: IR spectra of policosanol functionalization and coupling to maltoheptaose. The disappearance of hydroxyls (peak 1) indicates the tosylation of policosanol and the reappearance in the peak after coupling indicates coupling to maltoheptaose and betacyclodextrin. The appearance of azide (peak 2) indicates azide functionalization and its disappearance indicates complete coupling of the material. A small azide peak is observed in MH-*b*-Policosane, which indicates there may be some policosane-Az that did not react. Peak 3 is $CO_2$ contamination. Spectra are shifted for clarity.

The molecular weights of the polymers descruibed in this chapter are summarized in **Table 7.2**. As evidenced by their very small molecular weights, these BCPs are practically oligomeric.

| | **Sugar MW (g/mol)** | **Wax MW (g/mol)** | **Total MW (g/mol)** |
|---|---|---|---|
| **MH-*b*-Octacosane** | 1232 | 410 | 1642 |
| **MH-*b*-Policosane** | 1232 | ~410 | ~1642 |
| **βCyD-*b*-Policosane** | 1072 | ~410 | ~1482 |

**Table 7.2**: Molecular weights of the materials investigated in this study

## 7.2 Bulk Self-Assembly by Solvent Annealing

We initially intended to use the oligosaccharide-wax BCPs (designed to have high $\chi$s) for lithography applications. However, these materials suffer from the same annealing challenges as the PTMSS-*b*-Oligosaccharide materials described in Chapter 3 due to the low degradation temperatures of the oligosaccharides. Since we also initially had difficulty finding a solvent that would dissolve the BCPs to enable spin coating, solvent annealing a bulk sample was performed to investigate its self-assembly.

As precipitated, a SAXS pattern was observed for MH-*b*-Octacosane that was similar to the as-precipitated samples of the PTMSS-*b*-Oligosaccharides, characteristic of poorly ordered micelles (**Figure 7.5d**). After solvent annealing in a jar with a 50:50 by volume mixture of THF and water, no improvement in order was observed after 24 or 48 hours (**Figure 7.5c** and **b,** respectively). However, when the sample was heated to 160 °C for 30 minutes after solvent annealing, higher-order scattering peaks consistent with a cylindrical morphology appeared (**Figure 7.5a**). The q* peak is consistent with an $L_o$ value of 8.4 nm. The heating step was likely necessary to remove solvent that may have been trapped in the polymer, preventing self-assembly.

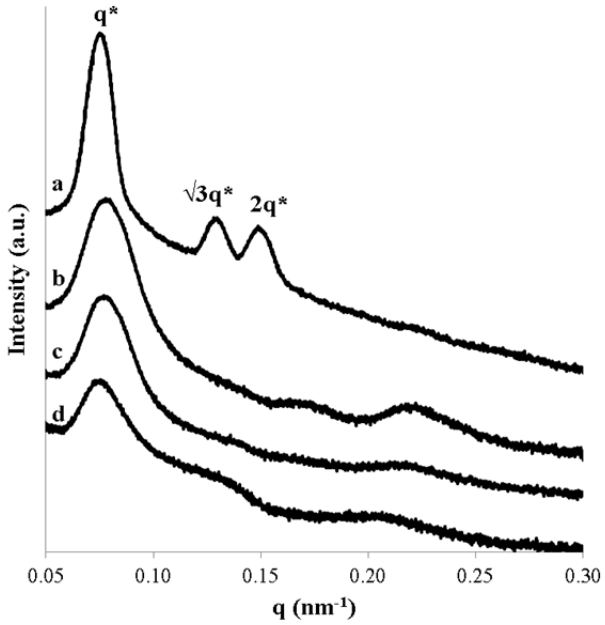


**Figure 7.5**: Evolution of SAXS patterns after solvent annealing/heating MH-*b*-Octacosane. a) After solvent annealing for 48 h and heating to 160 °C for 30 minutes, b) after solvent annealing for 48 h c) after solvent annealing for 24 h, and d) as-precipitated. Curves are shifted vertically for clarity.

Since a solvent that would dissolve the polymer could not be found initially to enable spin coating, we shifted the focus for application of this material away from lithography since it would not be useful without the ability to spin coat it. We later found that THF would dissolve the sugar-wax BCPs and investigation into solvent annealing thin films of these materials is the subject of future work.

### 7.3 Solution Studies

As mentioned in the introduction to this chapter, nontoxic, naturally occurring polymeric materials are attractive in the medical industry for applications such as medical devices and drug delivery. Amphiphilic BCPs, such as those described in this chapter, are particularly attractive for drug delivery if they can form micelles or vesicles in aqueous solution and can encapsulate and release a drug in the body either over time or in a

specific location in the body.[12] Therefore, we performed some basic studies to evaluate the ability of the sugar-wax materials to form vesicles, encapsulate hydrophobic molecules, and encapsulate an actual cancer therapeutic drug, doxorubicin (DOX).

### 7.3.1 Micelle Formation

For biological applications, water is the most attractive solvent in which to prepare BCP vesicles since the body is an aqueous system. Unfortunately, we discovered that the sugar-wax BCPs are only slightly soluble in water. In fact, trying to dissolve 1 mg BCP in 10 mL water even with heating to improve solubility resulted in very little of the polymer going into solution. To improve the dispersion of the polymer in solution, a nanoprecipitation method was employed to prepare the micelle solutions; this method has been used in the literature previously to prepare similar solutions.[13]

The nanoprecipitation method of forming micelles is described by the schematic in **Figure 7.6**. First, 1 mg of BCP was dissolved in 2 mL of solvent. We found that THF fully dissolved the sugar-wax materials, although many of the solutions had to be gently heated to fully dissolve the polymer. Next, the THF solution was added dropwise to 10 mL water. The THF was removed by heating the solution to 90 °C for 15 minutes (above the boiling point of THF) and pulling vacuum on the solution for about 15 minutes to remove any remaining THF. After removing the THF, some of the polymer had precipitated from the water solution due to the low solubility of the BCPs in water. These large particle aggregates were removed by filtering the solution through a 1 μm pore size filter. Compared to trying to directly dissolve the BCPs in water, the nanoprecipitation method resulted in better dispersion of the BCP in water, likely due to reduced aggregation of the material.

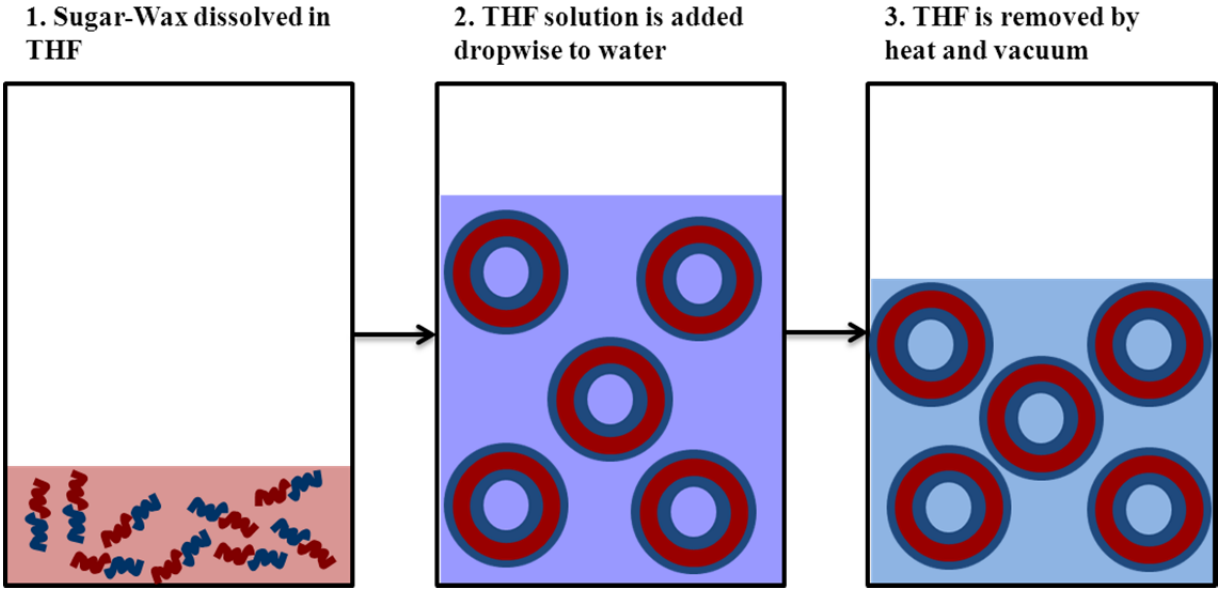


**Figure 7.6**: Method used to prepare oligosaccharide-wax vesicles in water. 1) 1 mg oligosaccharide-wax BCP is dissolved in 2 mL THF. 2) THF solution is added dropwise to 10 mL water. 3) THF is removed by heat and vacuum and solution is filtered through 1 μm filter.

After creating the vesicles by nanoprecipitation, their size was characterized by dynamic light scattering (DLS). DLS experiments were carried out on a Zetasizer nano instrument. The DLS trace of MH-*b*-Octacosane prepared by the nanoprecipitation method described in the previous paragraph is shown in **Figure 7.7a**. The particle size curve is approximately Gaussian and the cumulants fit of the correlation function (**Figure 7.7b**) is typical of a good fit of the data. We found that filtering through a 5 um filter resulted in poor DLS data likely due to large particle aggregates that the DLS had difficulty analyzing. The z-average particle diameter of this material was approximately 71 nm. Since this would be an unreasonably large diameter for micelles of a BCP of this molecular weight, these are likely vesicle (bilayer) structures, not micelles. Further experiments are necessary to determine this with certainty.

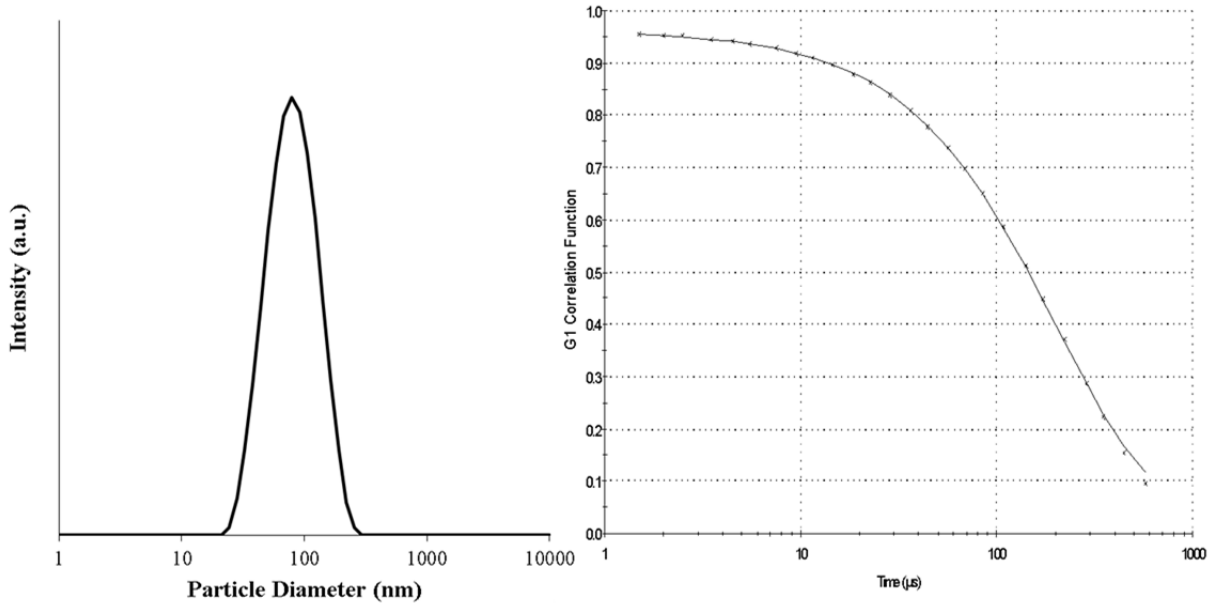


**Figure 7.7**: a) DLS trace for MH-*b*-Octacosane with a z-average particle diameter of 71 nm and b) cumulants fit data of the correlation function.

DLS was also performed on MH-*b*-Policosane (**Figure 7.8**) and βCyD-*b*-Policosane. Since policosanol consists primarily of octacosanol, it is unsurprising that the z-average particle diameter of MH-*b*-Policosane is similar to that of MH-*b*-Octacosane. However, it is interesting that two peaks are present in the DLS curve for MH-*b*-Policosane. Due to the polydispersity of the policosanol precursor, it is possible that the smaller peak represents micelles of the material from the shorter chain wax coupled to MH and the larger peak represents vesicles similarly to the MH-*b*-Octacosane. The correlation function for this DLS experiment was also good, indicating good fitting of the particle size. For the βCyD-*b*-Policosane, no peak was observed, indicating that self-assembled structure is not present solution. This could be because the bulky geometry of the betacyclodextrin that prohibits micelle/vesicle formation.

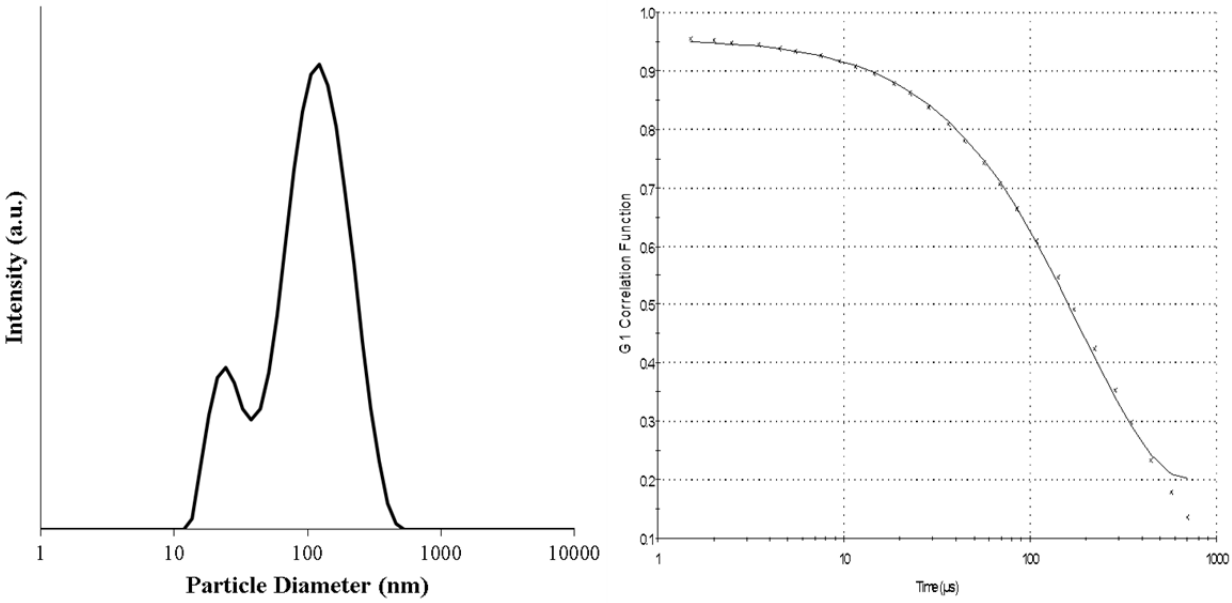


**Figure 7.8**: a) DLS trace for MH-*b*-Policosane with a z-average particle diameter of 75 nm and b) cumulants fit data of the correlation function.

DLS provides information about the relative size of structures in solution (based on the assumption that the particles are spherical) but does not give information about the shape of the structures. The solutions were imaged by transmission electron microscopy (TEM) by drop-casting (i.e. depositing a drop of solution and then allowing the solvent to evaporate, leaving the vesicles behind) on a TEM grid. The process of sample preparation had to be carefully optimized due to the low solubility of the polymer in water. If too large of a drop of solution was deposited on the grid, only large areas of aggregation were observed. As the water from the drop cast sample evaporated, this likely caused the polymer solution to concentrate and eventually the polymer crashed out of solution. By keeping the drop size small (5 μL), the solution could not concentrate as much and the individual structures were able to be imaged. I did observe some aggregation in the 5 μL samples but imaging was much improved with the smaller drop size.

With the MH-*b*-Octacosane vesicles, two main classes of structures were observed from imaging. Most of the area of the TEM grid looked like the structures shown in **Figure 7.9**. The size of these structures is approximately consistent with the range of particle sizes in the solution characterized by DLS. However, a few regions on the TEM grid had the structures shown in **Figure 7.10**. Both TEM and SEM images of the grid were collected to characterize the through and surface structure of the features. These larger vesicles appear to be faceted, a phenomenon that has been observed for crystalline amphiphilic materials in the literature, however a third component usually must be added to the material to cause the faceting to occur.[14] We believe that the highly crystalline nature of both blocks contributes to the faceting of these structures in the larger particles.

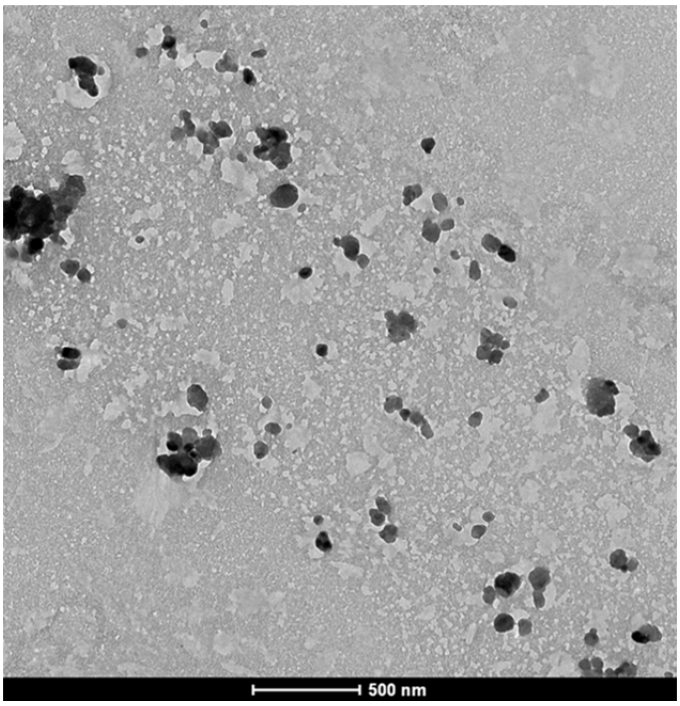


**Figure 7.9**: Small structures observed by TEM after drop casting.

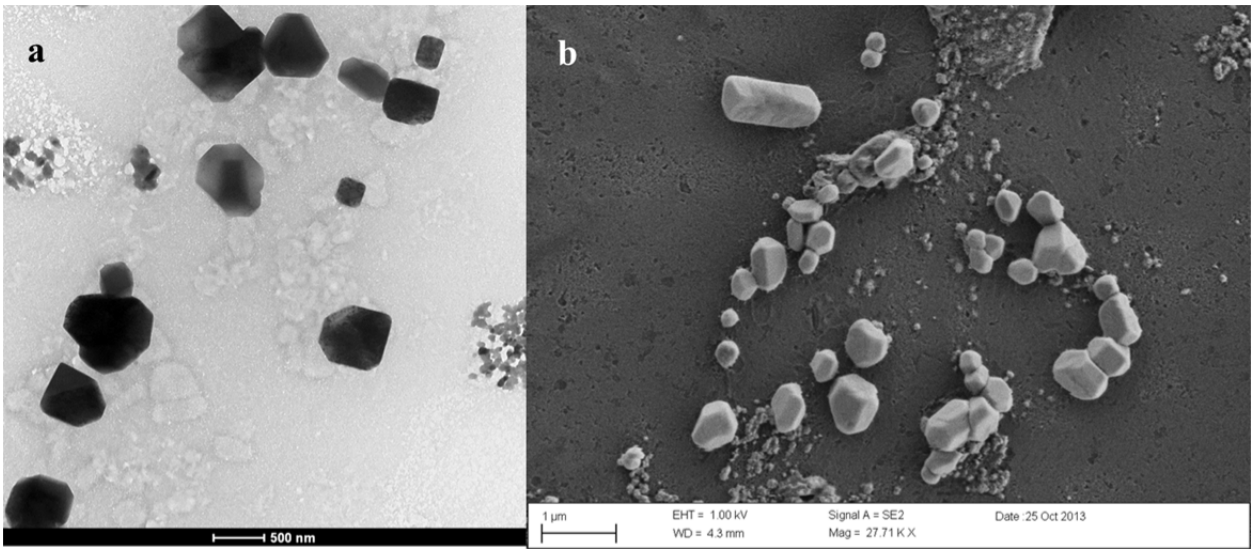


**Figure 7.10**: Larger, faceted structures observed by a) TEM and b) SEM after drop casting.

We considered that the faceted structures could be crystals of the sugar or wax precursor material (since both precursors are crystalline compounds) if incomplete functionalization or coupling took place in the synthesis. However, we established in Section 7.1 that complete tosylation and subsequent azide functionalization of the wax took place (by NMR) and that complete coupling of the completely azide-functionalized wax also occurred (by IR). This means that there is likely no free wax left in the material and even if there was, it would be insoluble and filtered out anyway in a water solution. Since an excess of oligosaccharide was used in the synthesis, it is more likely that the faceted structures could be crystals of free unreacted oligosaccharide. However, the BCPs were precipitated and washed with water/methanol, in which free oligosaccharide is highly soluble. To support the claim that the crystals are not free sugar or wax, control solutions of the wax in THF and maltoheptaose in water were prepared at similar concentrations to the BCP sample and drop cast onto a TEM grid. The faceted structures were not observed by TEM for either of the control samples.

### 7.3.2 Hydrophobic Component Encapsulation

Next, the ability of the MH-*b*-Octacosane to encapsulate hydrophobic components was investigated. We first tried to encapsulate a relatively short chain hydrocarbon; short enough that it would be soluble in THF but long enough that it would be relatively insoluble in water. I chose dotriacontane as the hydrophobic component and characterized encapsulation of the material by monitoring the diameter of the vesicles before and after encapsulation by DLS. The method of preparing the micelles to encapsulate the hydrophobic material is shown in **Figure 7.11**. The preparation method was identical to preparing the micelles, except 2 mg dotriacontane was added to the THF solution and excess material was expected to precipitate out upon addition to water.

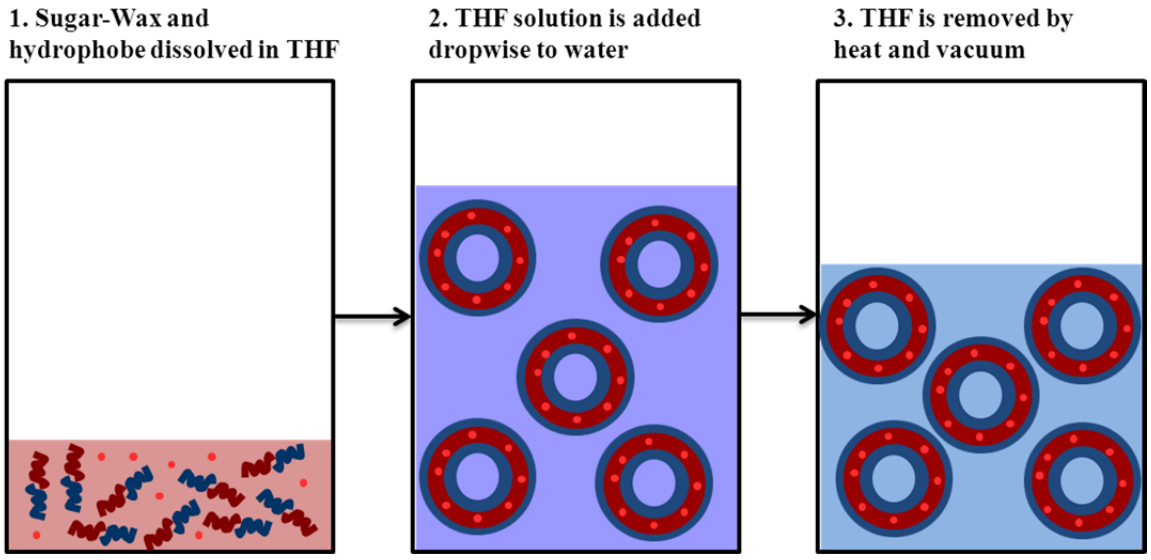


**Figure 7.11**: Method of preparing dotriacontane or dye-encapsulated micelles. 1) 1 mg Oligosaccharide-wax and 2 mg hydrophobic component are dissolved in 2 mL THF. 2) THF solution is added dropwise to 10 mL water. 3) THF is removed by heat and vacuum and solution is filtered through a 1 μm filter to removed BCP and excess hydrophobic component aggregates.

The particle diameter of the vesicles was then measured by DLS. The peak shift in **Figure 7.12** shows the shift to a larger particle diameter after encapsulation of the dotriacontane. The z-average particle size shifted from 71 nm for just the vesicles to 120 nm with encapsulated dotriacontane, a notable increase and suggesting successful encapsulation of the dotriacontane.

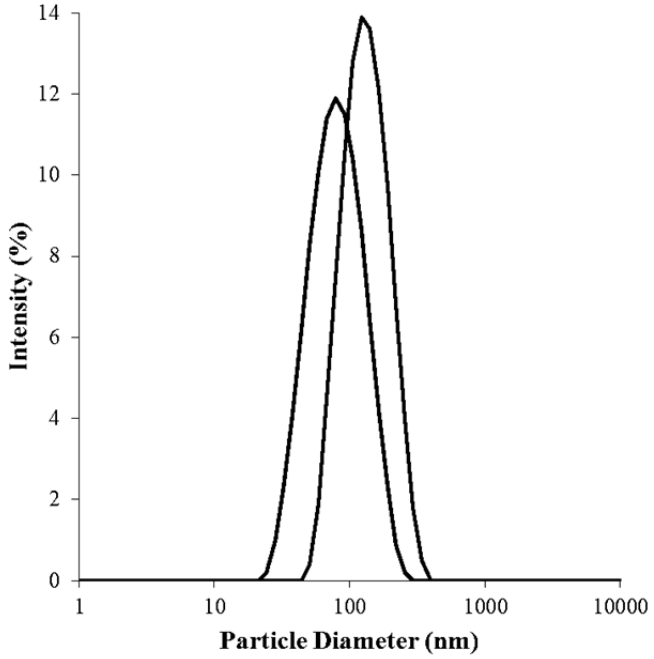


**Figure 7.12**: Peak shift from MH-*b*-Octacosane vesicles (with a z-average particle diameter of 71 nm) to a larger particle diameter with encapsulated dotriacontane (with a z-average particle diameter of 120 nm).

A similar increase in particle diameter was observed after encapsulating dotriacontane with MH-*b*-Policosane (**Figure 7.13**). The z-average particle diameter increased from 75 nm for just the vesicles to 190 nm when encapsulated dotriacontane was present. Interestingly, the smaller particle diameter peak disappeared after encapsulation of dotriacontane. This could be due to different self-assembly

characteristics with addition of dotriacontane that could prevent micelles from forming. Further experiments are necessary to determine whether or not this is happening.

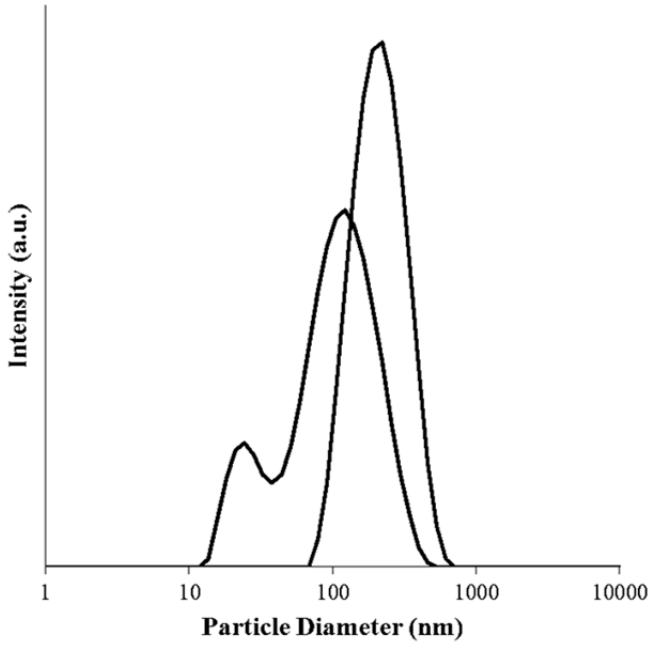


**Figure 7.13**: Peak shift from MH-*b*-Policosane vesicles (black curve, z-average particle diameter of 75 nm) to a larger particle diameter with encapsulated dotriacontane (red curve, z-average particle diameter of 190 nm).

After adding dotriacontane to the vesicles, I imaged drop cast samples of MH-*b*-Octacosane by TEM again. I observed some of the structures like those observed for just the vesicles in **Figure 7.9** but also more faceted structures shown in **Figure 7.14**. None of the large vesicles were observed in this case; the vesicles observed with the encapsulated dotriacontane were smaller than the faceted vesicles in **Figure 7.10**. It is possible that the addition of a crystalline hydrophobic component alters the self-assembly of the vesicles in solution and enables faceting of smaller vesicles. It is also possible that the crystals are excess dotriacontane that did not get filtered out or that was dissolved in water, but this is unlikely since a wax control did not show faceted structures in TEM imaging.

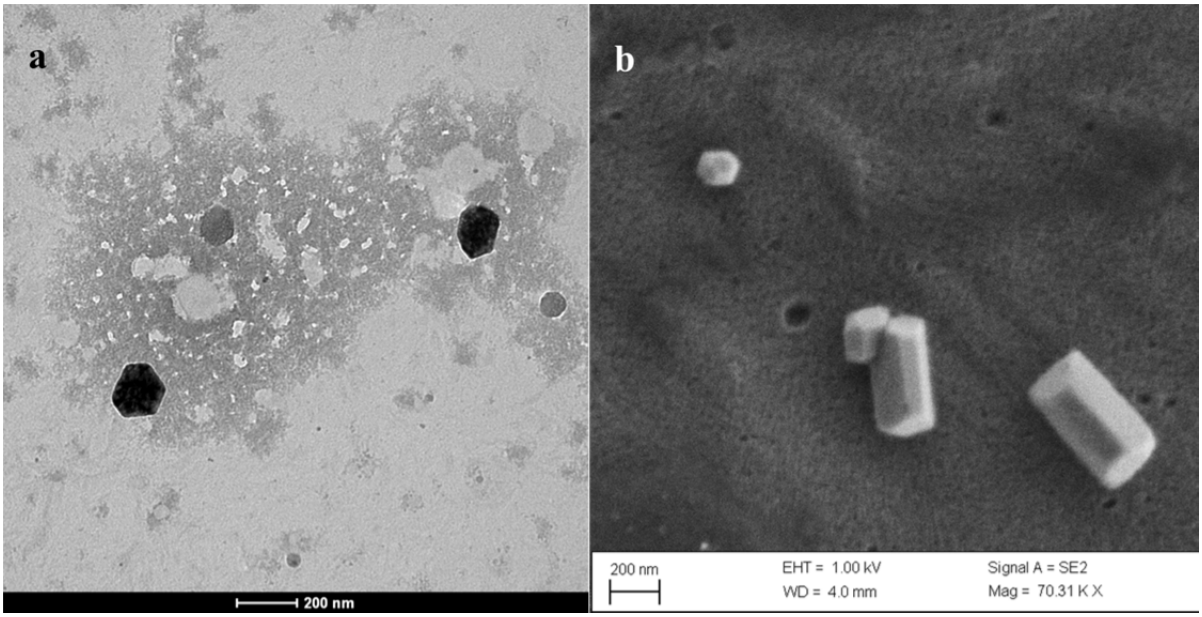


**Figure 7.14**: Faceted structures observed by a) TEM and b) SEM after drop casting a solution of MH-*b*-Octacosane vesicles with encapsulated dotriacontane.

### 7.3.3 Dye Encapsulation

To support the evidence from DLS that a hydrophobic component could be encapsulated by the MH-*b*-Octacosane micelles, another method of characterizing encapsulation was investigated. UV-vis and fluorescence spectroscopy can be used to characterize the encapsulation of anthracene and pyrene, respectively. Solutions of the vesicles with the respective dyes were prepared in an identical manner to the solutions prepared with dotriacontane, just with anthracene or pyrene as the hydrophobic component.

The UV vis spectrum of anthracene is well characterized; there is one major peak at 251 nm and three small peaks at 339, 356, and 375 nm in the spectrum. The UV-vis spectra of the MH-*b*-Octacosane micelles with encapsulated anthracene and several

controls are shown in **Figure 7.15a** and an enlarged region to highlight the detail of the smaller peaks is shown in **Figure 7.15b**. A relatively featureless spectrum is observed for anthracene in water (i.e. prepared identically to the micelles with the hydrophobic component but with no BCP). This is unsurprising since anthracene is insoluble in water and therefore we would not expect to see it in a water solution in UV-vis. Deionized water was used as the background (i.e. as the reference cell solution) for this sample. Just the vesicles in water exhibit a small shoulder of intensity around 275 nm and increasing intensity below 250 nm. Deionized water was also used as the background for this sample. When anthracene was encapsulated by the micelles and using water as the background for the measurement, shoulders of intensity were observed around 250 nm and 275 nm, and small peaks were observed around 339, 356, and 75 nm, consistent with the UV-vis spectrum of anthracene with a shoulder of intensity at 275 nm from the polymer vesicles. To increase the resolution of low intensity peaks in the spectrum, a solution of just the vesicles in water was used as the background and the anthracene peaks became more apparent. The absence of peak intensity in the anthracene control sample suggests that very little if any anthracene is dissolved in the water so the intensity observed in the UV-vis spectrum of the micelles with anthracene must be encapsulated anthracene.

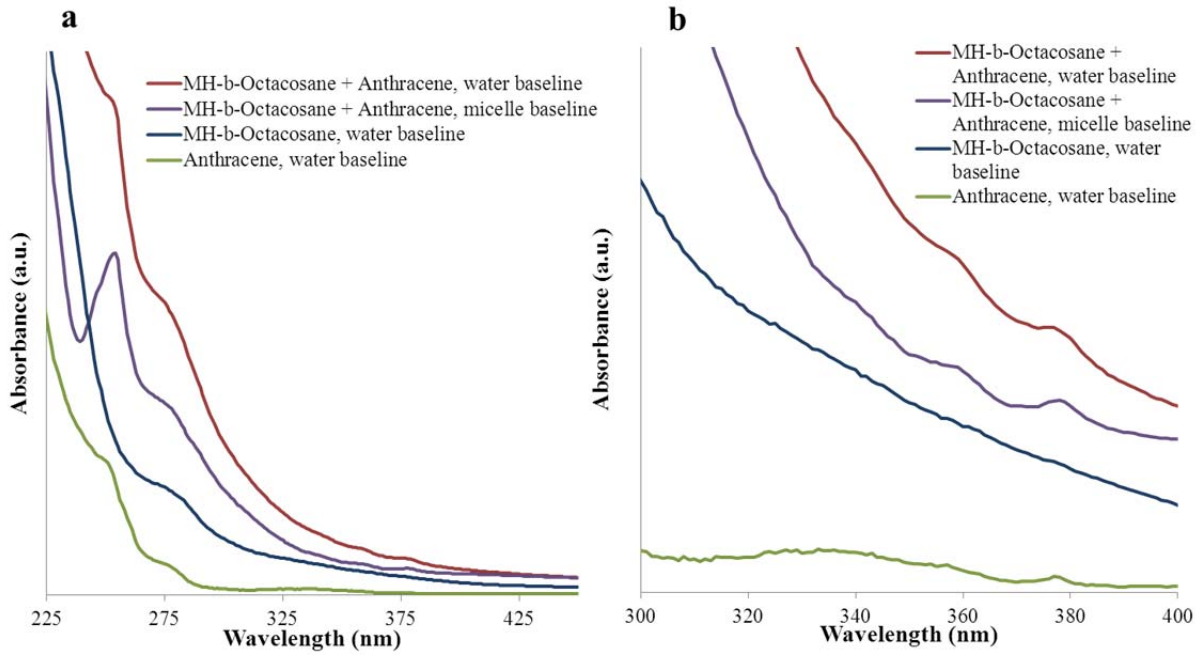


**Figure 7.15**: UV-vis spectra for MH-*b*-Octacosane micelles with and without encapsulated anthracene a) over a range of 225-450 nm and b) and enlarged region to highlight the low intensity peaks.

A second method of dye encapsulation characterization involved encapsulating pyrene. Pyrene has been used in previous experiments to characterize whether it is in a hydrophobic or hydrophilic environment, based on the 373 and 393 nm peak ratios in fluorescence spectroscopy.[15] If the ratio of the 373 nm to 393 nm peak is high, this often means that the pyrene is in a hydrophilic environment and if it is low, it is surrounded by a hydrophobic environment. **Figure 7.16** shows the fluorescence spectra of pyrene in water and encapsulated in the vesicles, both normalized to the 373 nm peak. In a water solution made identically to the micelle solutions prepared by nanoprecipitation, the 373 nm peak is higher than the 393 nm peak, indicating it is in a hydrophilic environment. Pyrene has some limited solubility in water so it is unsurprising that these peaks were observed. In the micelle solution, the 373 nm peak is lower than the 393 nm peak,

indicating that it is in a hydrophobic environment (i.e. encapsulated within the vesicle bilayer). This difference would likely be even more pronounced if pyrene was removed from the water by dialysis before measurement.

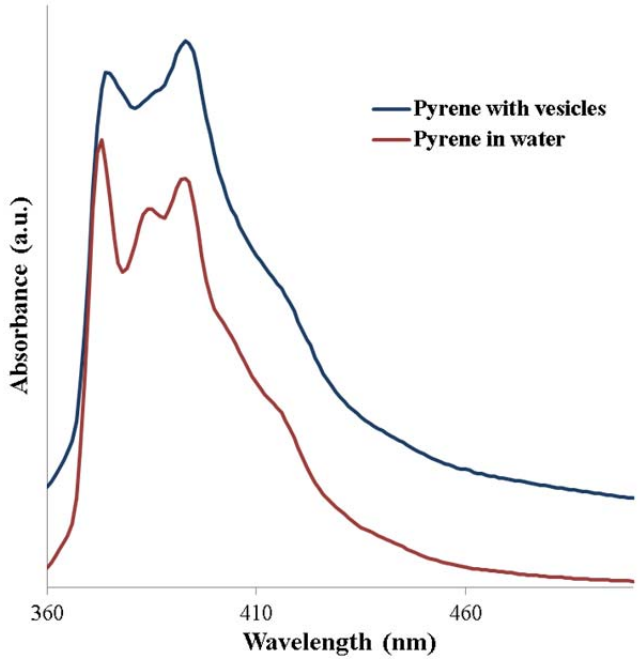


**Figure 7.16**: Fluorescence spectra for pyrene in water and pyrene encapsulated within the vesicles. Spectra are shifted vertically for clarity.

TEM and SEM images of the pyrene-loaded vesicles were also collected after drop casting the solution on a TEM grid. The entire grid looked like the images in **Figure 7.17** and I did not observe any faceted structures after loading the vesicles with pyrene. It is possible that encapsulation of the pyrene disrupts the faceting of the vesicles due to changes in crystallinity of the blocks in the vesicle.

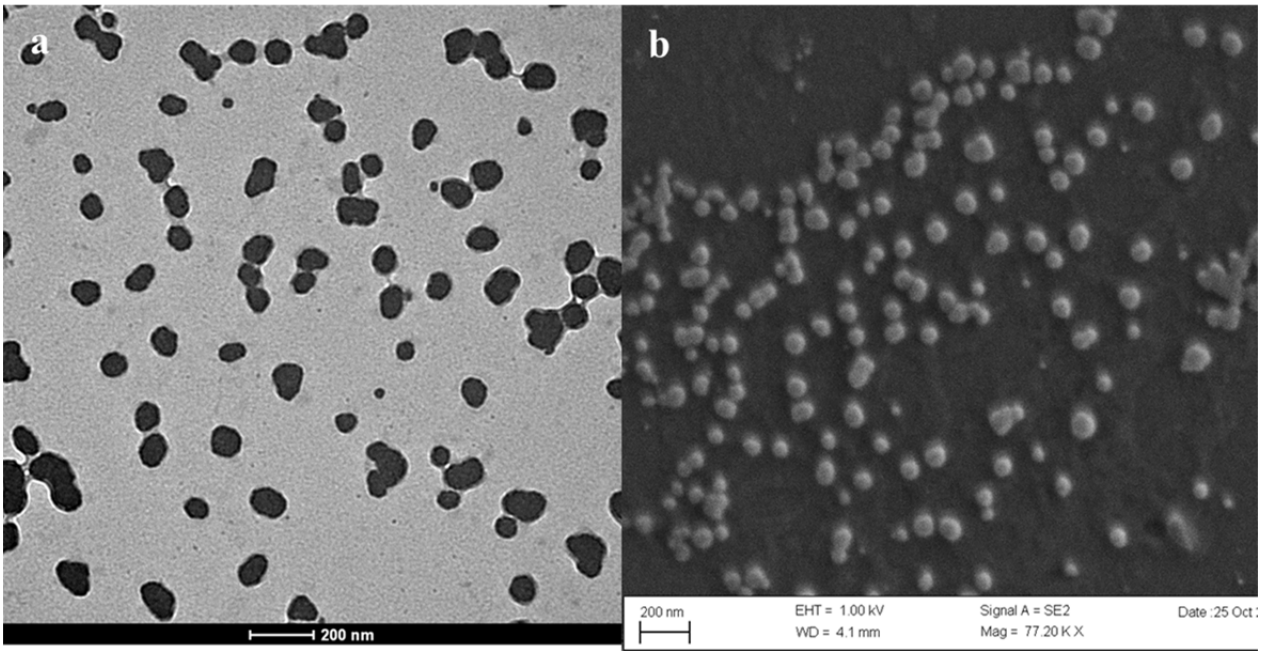


**Figure 7.17**: Structures observed by a) TEM and b) SEM after drop casting a solution of MH-*b*-Octacosane vesicles with encapsulated pyrene.

### 7.3.4 Doxorubicin Encapsulation

While I demonstrated successful encapsulation of a hydrophobic material in the previous section, it would be ideal to show encapsulation of a drug such as DOX to demonstrate the use of these BCPs in biomedical applications. To prepare solutions to encapsulate DOX, I used two procedures slightly different than those used to encapsulate the hydrophobic components since DOX is water soluble (**Figure 7.18**). For the first procedure, I directly dissolved 2 mg MH-*b*-Octacosane and 2 mg DOX in 10 mL water. The solution was heated to 70 °C for 15 minutes. A dialysis step was then performed to remove the free DOX. A 3.5-5.0 kDa molecular weight cut off (MWCO) cellulose ester (CE) dialysis membrane was used for dialysis. The solution was dialyzed for approximately 36 hours, and the dialysis water was refreshed twice, approximately every 12 hours and then the solution was filtered through a 5 μm filter. For the second

procedure, 1 mg MH-*b*-Octacosane was dissolved in 2 mL THF and 2 mg DOX was dissolved in water. The THF solution was then added dropwise to the DOX/water solution. The solution was heated to 90 °C for 15 minutes to remove the THF, dialyzed for 36 hours, and filtered through a 1 μm filter.

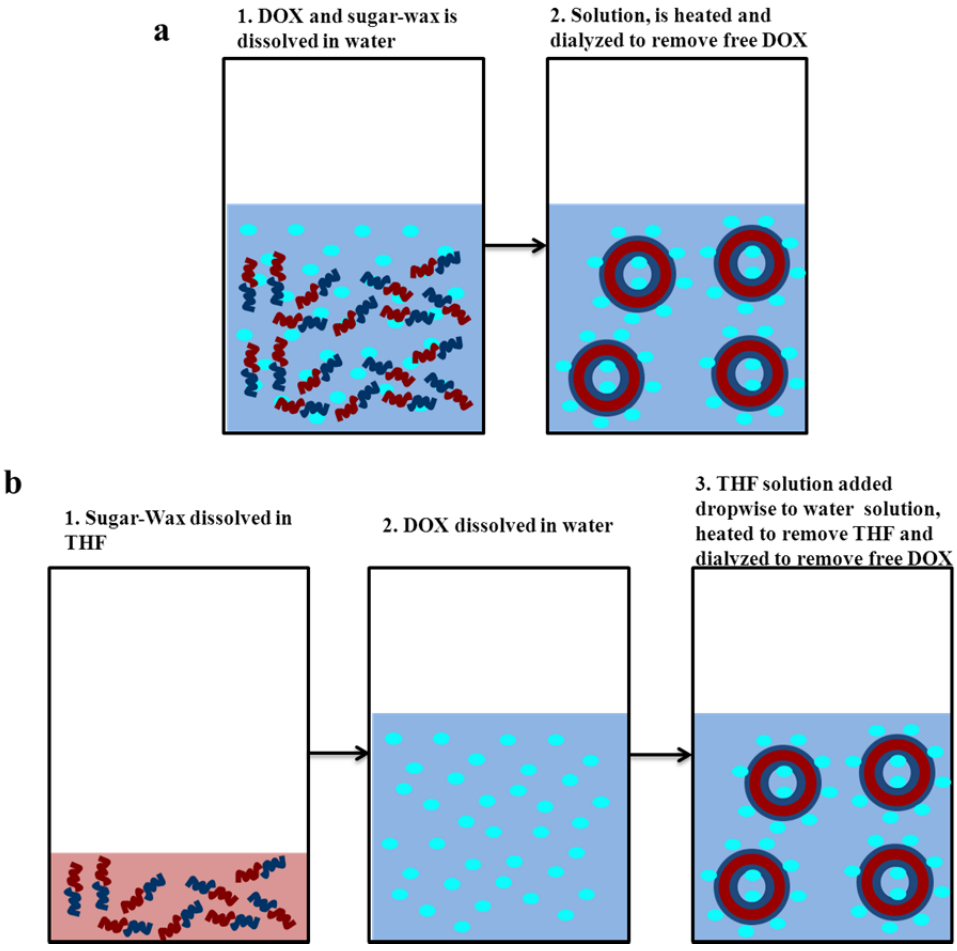


**Figure 7.18**: Two procedures for complexing DOX with the MH-*b*-Octacosane. a) Direct dissolution method: 1) 2 mg MH-*b*-Octacosane and 2 mg DOX are dissolved in 10 mL water. 2) The solution is heated to 90 °C for 15 minutes and dialyzed for 36 hours to remove free DOX. b) Nanoprecipitation method: 1) 1 mg MH-*b*-Octacosane is dissolved in 2 mL THF. 2) 2 mg DOX is dissolved in 10 mL water. 3) The THF solution is added dropwise to the water solution, heated to 90 °C for 15 minutes to remove THF and dialyzed for 36 hours to remove free DOX.

I used UV vis spectroscopy to characterize the amount of DOX encapsulated by the vesicles. The calibration curve in **Figure 7.19** plots the absorbance of a series of solutions with a known DOX concentration at 485 nm. The DOX concentration in the vesicles was then determined by measuring the absorbance of the vesicles with DOX at 485 nm and making several corrections based on control samples. Three controls were run. 2 mg DOX was added to water and dialyzed for 36 hours to establish a baseline amount of free DOX in solution after dialysis. Two samples of vesicles prepared without DOX using both preparation methods described previously were also made to subtract a background absorbance from the MH-*b*-Octacosane polymer. The raw measured absorbance, absorbance corrected for the DOX baseline and background MH-*b*-Octacosane absorbance, and concentration calculated from the calibration curve in **Figure 7.19** are shown in **Table 7.2**.

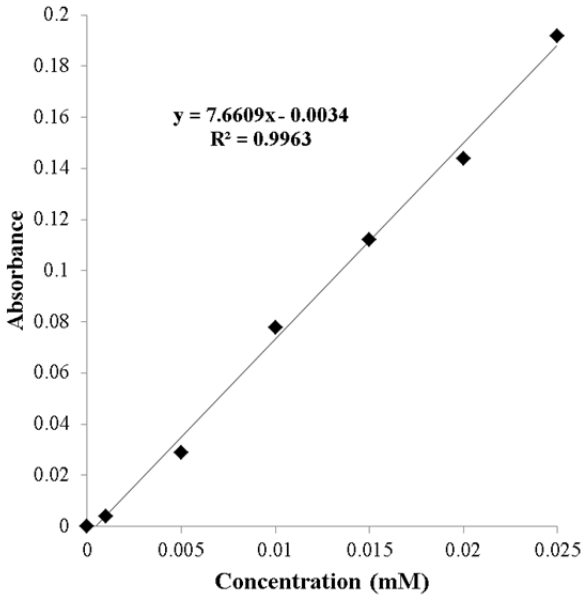


**Figure 7.19**: Calibration curve created for absorbance at 485 nm as a function of concentration for DOX.

| Sample | Raw Absorbance | Corrected Absorbance | Corrected DOX Concentration |
|---|---|---|---|
| DOX Control | 0.00533 | 0 | - |
| MH-*b*-Octacosane | 0.06478 | - | - |
| MH-*b*-Octacosane + DOX | 0.15674 | 0.08662 | 0.012 mM |
| MH-*b*-Octacosane nanoprecipitated | 0.00026 | - | - |
| MH-*b*-Octacosane nanoprecipitated + DOX | 0.00957 | 0.00397 | 0.001 mM |

**Table 7.3**: Measured absorbance, corrected absorbance, and calculated DOX concentrations for the vesicle/DOX and control samples.

From the data in **Table 7.3**, it appears DOX is being encapsulated by the MH-*b*-Octacosane vesicles prepared by direct dissolution but maybe not those prepared by nanoprecipitation. This conclusion is drawn since the raw absorbance of the vesicles with DOX is over a magnitude greater than the DOX background when prepared by direct dissolution but only about double the background absorbance when prepared by nanoprecipitation. This suggests that the addition of THF may hinder the complexation/encapsulation of DOX with the vesicles. There were also several experimental details that were slightly different between the two methods (temperature, amount of BCP dissolved, filter pore size) that should be made consistent in another experiment to determine whether they affect the DOX encapsulation.

As drawn in **Figure 7.18**, we believed that DOX was complexing with the oligosaccharide instead of being encapsulated by the vesicle. We believe this largely because DOX, a red material, heavily stained both regenerated cellulose and cellulose ester dialysis tubing (**Figure 7.20**). The dialysis tubing (made of cellulose) has a similar repeat unit structure to the oligosaccharides. This led us to believe that DOX interacts

with the repeat unit structures in these types of materials. To investigate this, a control experiment was performed where DOX and maltoheptaose were dissolved in water, dialysis was performed, and the DOX concentration was measured by UV vis. My hypothesis was that if the DOX was complexing with the oligosaccharide in the vesicle it should be complexing with the free oligosaccharide as well. From this control experiment however, no absorbance above DOX baseline was observed. Unfortunately, it was difficult to find dialysis tubing to perform this experiment since DOX (543 g/mol) and maltoheptaose (1232 g/mol) have similar molecular weights. I used 1 kDa MWCO regenerated cellulose (RC) dialysis tubing, which could have caused free DOX and the oligosaccharide (potentially with DOX complexed to it) to be removed from the solution. Determining the mechanism of DOX encapsulation/complexation is a matter of future work on this project.

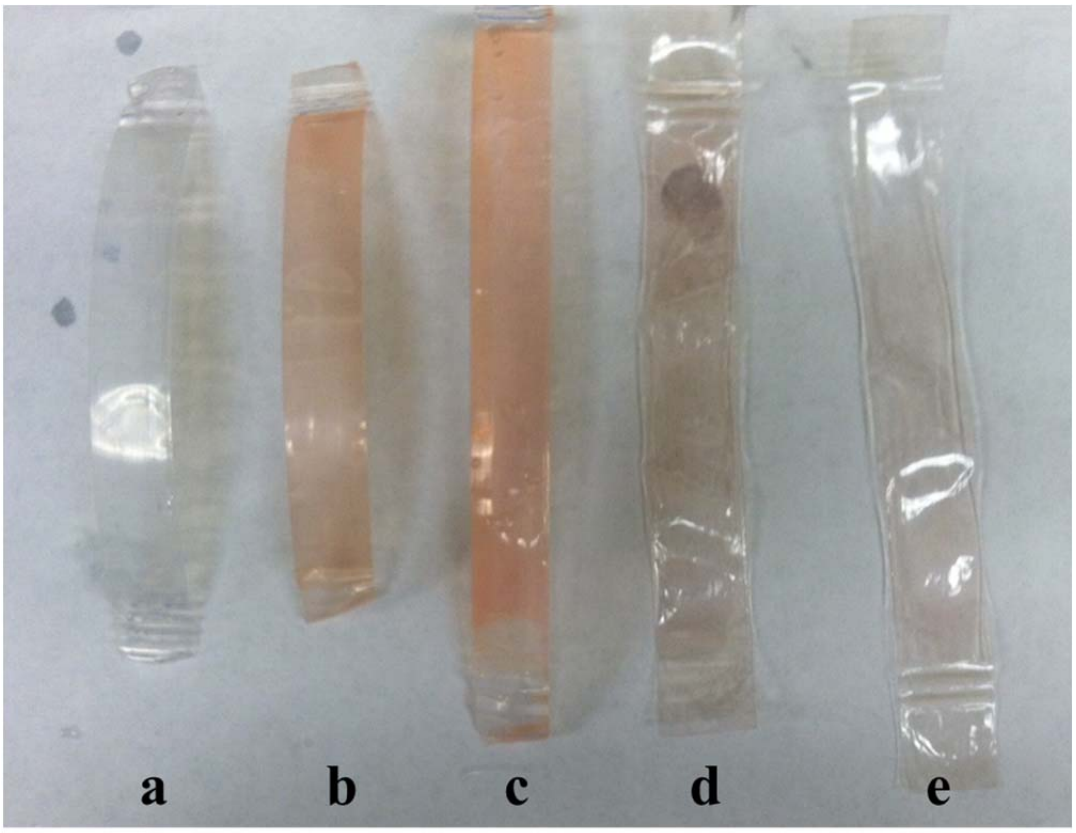


**Figure 7.20**: Photograph of dialysis tubing after dialysis experiments. a) After dialyzing just micelles in water, no staining is evident. b) After dialyzing micelles with DOX, the CE dialysis tubing is stained red. c) After dialyzing just DOX in water, the CE dialysis tubing is stained red. d) After dialyzing maltoheptaose and DOX the RC tubing is stained red. e) After dialyzing just DOX the RC dialysis tubing is stained red.

### 7.4 CRYOGENIC TEM

As a final note, drop casting is not an ideal method for imaging self-assembled structures in solution since changes can take place in the self-assembly of the material as the solvent evaporates. Cryogenic TEM is a method that can be used to image the exact structures of vesicles in solution. Briefly, cryo TEM involves freezing a thin film of the solution on TEM grid and imaging it while it is frozen. The sample preparation is very complicated and time consuming, and very few facilities in the world exist to perform

this imaging technique. Fortunately, I had the opportunity to travel to the University of Minnesota and work with Joe Lott, a post-doc in Timothy Lodge's group to learn the cryo TEM techniques and look at some of my samples.

We soon realized that we had two unfortunate problems when attempting to image the oligosaccharide-wax solutions by cryo TEM. The first was related to imaging faceted structures. Due to the complexity of the sample preparation process, it is difficult (maybe impossible) to freeze a sample on a TEM grid without having any water from the atmosphere condense and freeze on the TEM grid. Unfortunately, these water crystals look almost identical to the faceted structures we were trying to image. **Figure 7.21** was taken from a water control sample with no vesicles in solution. Since these structures were observed on both the water control and samples with vesicles, it was impossible to distinguish between ice crystals and faceted vesicles when there was polymer in solution.

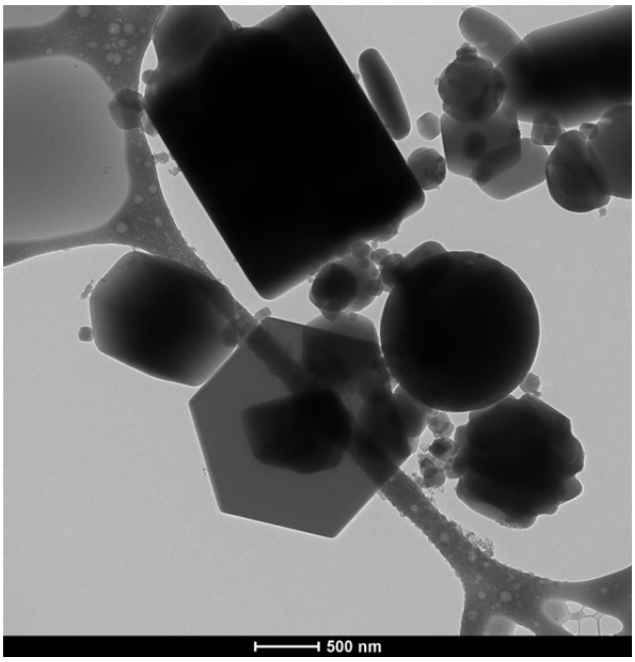


**Figure 7.21**: Cryo TEM image of ice crystals on a TEM grid from a water control sample.

The second issue with cryo TEM is that only a thin film of the sample can be deposited on the TEM grid, otherwise the electrons cannot penetrate a thick film and imaging is not possible. If the solution is dilute, which was the case with the MH-*b*-Octacosane solutions because of the BCP's low solubility in water, it may be difficult or impossible to observe any structure in cryo TEM with very little structure there. When drop casting, a large amount of solution (several orders of magnitude more than cryo TEM) is used. This means that a dilute solution can be imaged since a large amount of dilute solution concentrates down to a density of structures that can be imaged. We believe that this may have been one of the reasons why we were unable to image these samples by cryo TEM.

## 7.5 CONCLUSIONS

While initially designed as high $\chi$ materials for lithography applications, in this chapter, I described new amphiphilic BCP materials that show promise in biomedical applications. These new BCPs are attractive for biomedical applications since they are derived from natural materials that are already known to be nontoxic and safe for human consumption. I demonstrated that these oligosaccharide-wax materials can form vesicles in solution which encapsulate hydrophobic molecules and show potential in delivery of doxorubicin. While more studies need to be pursued to answer some outstanding questions and probe the release mechanism of the encapsulated materials, the studies performed in this chapter show that these materials show promise in biomedical applications.

## 7.6 REFERENCEES

1. E. Baker, *Chemistry and morphology of plant epicuticular waxes*. Academic Press: London, 1982.

2. S. R. Snider, *Annals of Neurology* **1984,** *16*, 723-723.
3. C. P. F. Marinangeli; A. N. Kassis; D. Jain; N. Ebine; S. C. Cunnane; P. J. H. Jones, *British Journal of Nutrition* **2007,** *97*, 381-388.
4. H. K. Berthold; S. Unverdorben; R. Degenhardt; M. Bulitta; I. Gouni-Berthold, *JAMA* **2006,** *295*, 2262-2269.
5. D. H. Katz; J. F. Marcelletti; M. H. Khalil; L. E. Pope; L. R. Katz, *Proceedings of the National Academy of Sciences* **1991,** *88*, 10825-10829.
6. 1-Octadecanol. (accessed October 28). Wikipedia.
7. Betacyclodextrin. (accessed October 28). Wikipedia.
8. M. L. Adams; A. Lavasanifar; G. S. Kwon, *Journal of Pharmaceutical Sciences* **2003,** *92*, 1343-1355.
9. I. Otsuka; K. Fuchise; S. Halila; S. b. Fort; K. Aissou; I. Pignot-Paintrand; Y. Chen; A. Narumi; T. Kakuchi; R. Borsali, *Langmuir* **2009,** *26*, 2325-2332.
10. Z. Guo; Y. Jin; T. Liang; Y. Liu; Q. Xu; X. Liang; A. Lei, *Journal of Chromatography A* **2009,** *1216*, 257-263.
11. A. J. Link; M. K. S. Vink; D. A. Tirrell, *Nat. Protocols* **2007,** *2*, 1884-1887.
12. J. Yan; Z. Ye; M. Chen; Z. Liu; Y. Xiao; Y. Zhang; Y. Zhou; W. Tan; M. Lang, *Biomacromolecules* **2011,** *12*, 2562-2572.
13. L. G. Yin; M. C. Dalsin; A. Sizovs; T. M. Reineke; M. A. Hillmyer, *Macromolecules* **2012,** *45*, 4322-4332.
14. M. A. Greenfield; L. C. Palmer; G. Vernizzi; M. O. de la Cruz; S. I. Stupp, *Journal of the American Chemical Society* **2009,** *131*, 12030-+.
15. G. B. Ray; I. Chakraborty; S. P. Moulik, *Journal of Colloid and Interface Science* **2006,** *294*, 248-254.

# Chapter 8: Future Work

The previous chapters in this dissertation detailed the work I completed during my graduate study involving the synthesis, self-assembly, and processing of BCPs for lithography. In this chapter, I will provide a brief outlook on the future of BCPs in lithography as it relates to the specific work I completed during my graduate study. I will also present a short section on future work related to the oligosaccharide-wax materials.

Few will disagree that the lithography industry is at a very interesting point in its history. Since the introduction of photolithography, the industry has relied on improvements to the photolithographic process as the sole method of pursuing smaller feature dimensions. However, due to the physical limitations described in Chapter 1, this method of improvement is no longer possible. While e-beam, EUV, and BCP lithography present several solutions to these physical limitations, it still remains a matter of debate as to which one will ultimately be adopted by the lithography industry. BCPs represent one possible alternative to the "top down" photolithography approach (i.e. sending all the information about the structure through an etch mask), by a very different "bottom up" approach (i.e. all the structural information is contained in the material in contact with the substrate). Three main factors will influence the patterning technique that is ultimately adopted by the industry: cost, patterning capability (throughput and resolution), and timing. Incorporating BCPs into a lithography process using currently available tools is also a concern for their application.

BCPs are particularly attractive to the lithography industry because they are inexpensive compared to new equipment (such as rotary e-beam and EUV tools) that will be required for other alternatives to photolithography tools. Even for specialty BCPs, which are expensive when compared to commodity polymers for example, their cost is

incremental compared to the expensive tools that are currently used in manufacturing. They are required in small amounts as dilute solutions and for the most part, current equipment is compatible with their processing.

However, a big issue with BCPs is their limitations in pattern geometry. Using diblock copolymers, dot and line patterns are the only features that can be patterned into a substrate, and that's after overcoming the extremely difficult orientational and alignment challenges described in the previous chapters. Research is ongoing to attain different pattern geometries through the use of DSA patterns and multiblock copolymers. These may overcome some of the feature geometry limitations, however it is unlikely that BCP lithography will ever be able to pattern all the feature geometries necessary for complex circuit design that photolithography can currently produce. The other alternatives, being "top-down" approaches similar to photolithography do not have such constraints since all the feature geometry information is contained in the lithography mask.

Finally, timing is perhaps the most critical consideration in the next-generation lithography challenge. The industry is heavily tied to the cost of the process, but will likely adopt the first solution that overcomes photolithography's feature size limitations if it is economically feasible. Even if BCPs present the most cost-effective solution but are unable to be implemented in manufacturing before another solution proves feasible, the other process may be implemented. If this happens, it is unlikely that BCPs will be adopted once the capital costs for implementing the more expensive solution have been expelled.

One final consideration is that BCPs meet some resistance from the lithography industry simply due to the radical change in the manufacturing process that would occur upon their implementation. BCP lithography requires a number of different processing steps and fundamental changes in the way manufacturing works that the lithography

industry is not familiar with. This may also have some influence on which technique is ultimately adopted.

### 8.1 THE FUTURE OF BCP MATERIALS IN LITHOGRAPHY

Perhaps the most important question in considering the future of BCPs in lithography is "which BCP would be used?" Heavily studied materials, such as PS-*b*-PMMA, show promise in pattern transfer[1] but are limited in minimum feature size resolution by their low $\chi$-parameters.[2] The focus of this dissertation has therefore been on the design and processing of BCPs that self-assemble into small features for high pattern densities. Small features are surely critical to make the implementation of such a different patterning process economical and impactful in the industry. However, I have presented far inferior pattern transfer and orientational order in the BCP systems explored than what is necessary for industry standards. This is not unlike many high-$\chi$ BCP systems in the literature which are notoriously difficult to orient in thin films. These challenges are likely due to the large difference in surface energy between the domains, which is directly related to the $\chi$-parameter of the material we are trying to maximize in the first place. However, if the final pattern transfer and orientational issues cannot be optimized, it does not matter how small of features can be formed with the material, it is useless for lithographic applications.

Despite these challenges, I believe high-$\chi$ BCP materials have a lot of potential. Whether the materials presented in this dissertation are evaluated further or new materials are created, in the past several years our group and others have a significantly improved understanding and control of orientation of BCPs in thin films. If orientation can be universally controlled to a reasonable degree, I believe high-$\chi$ BCPs could be the solution to high density patterning.

As described in the introduction to this chapter, multiblock copolymers are another class of materials that could make a significant impact in BCP lithography. Multiblock copolymers show promise in accessing more complex feature geometries such as ring and square dot arrays[3-5] that cannot be achieved by diblocks and are necessary for more complex device patterns. Unfortunately, due to the complexity of these BCPs and the relatively incomplete understanding of them,[6] the timing of their maturity as a patterning technique may be a big issue. Significantly more fundamental research may be required before enough is known about them for use in lithography to the extent that diblocks are currently used.

## 8.2 ORIENTATION STRATEGIES

A method for creating consistent through-film structure is necessary for pattern transfer of domains as shown in Chapter 4, and discovering a universal method for orienting different BCP systems would be a critical step forward for BCP lithography. Currently, relatively few methods exist for inducing perpendicular orientation of BCP materials. The most common is solvent annealing, which, as shown in the previous chapters has significant disadvantages due to the uncertain changes that occur such as volume fraction, self-assembly thermodynamics, and surface energy within the blocks and at each interface during annealing. The process of finding a solvent annealing condition is largely trial and error and can be difficult to reproduce on different solvent annealing tools that results in unpredictable through-film structure and pattern transfer. Also, no industrial-scale equipment currently exists to implement solvent annealing in a manufacturing process.

The top coat materials developed in our group are a promising route to overcoming these disadvantages, relying on surface neutralizing coatings on both

interfaces that are stable and predictable during thermal annealing.[7] However, we have only demonstrated the ability to induce perpendicular orientation in a few block copolymer systems. An ongoing area of research in our group is designing top coat materials that can be methodically fine-tuned and ideally, could be modified for any BCP system to achieve perpendicular orientation.

### 8.3 PATTERN TRANSFER

As described Chapter 1, one of the advantages of silicon-containing polymers is the incorporation of inherent etch resistance in the silicon-containing domain to facilitate pattern transfer. Besides their high $\chi$-parameters, this is the main reason we chose to work with silicon-containing materials in our group. However, since the time we began working with these materials, significant advances have been made in the pattern transfer of wholly organic BCPs with relatively low inherent etch contrast. Atomic layer deposition has been used with great success to impart etch resistance into BCP domains with reactive groups and has demonstrated success in subsequent pattern transfer.[8] Improved understanding of etching characteristics of BCPs has contributed to huge improvements in the etch contrast of materials like PS-*b*-PMMA. While it is currently uncertain which material will be used in BCP lithography, it is almost equally uncertain which etch protocol will be necessary to transfer the pattern. For this reason, much work is being directed toward each method of improving etch contrast and it is possible that the improved inherent etch contrast in inorganic-containing materials will not be necessary for successful pattern transfer. It is also currently under investigation how the chemical makeup of inorganic-containing block copolymers (density and structure of the inorganic components) makes the inorganic-containing domain a good etch mask.

## 8.4 Directed Self-Assembly

Directed self-assembly has been used many times in the literature to successfully align BCP domains in the in-plane direction so they are useful for electronics applications.[9] However, fine-tuning DSA patterns to produce low defectivity over large areas can be somewhat reliant on trial and error. The more that is understood about DSA patterns and defect reduction, the more effectively they can be implemented with BCPs.[10] It is also the subject of ongoing research to minimize the e-beam write time with low density prepatterns that are density multiplied by the BCP since e-beam write time is the most expensive step of the DSA process.[11]

As mentioned in the introduction, DSA will likely play a key role in accessing feature geometries that diblock copolymers will not adopt spontaneously. Since the use of multiblock copolymers is likely a long way off, the use of DSA in attaining these non-conventional feature geometries is the subject of ongoing research in many BCP groups[12-14] and will likely be necessary for BCP lithography to succeed in even simple applications.

## 8.5 The Future of Sugar-Wax Materials for Biological Applications

In Chapter 7, I presented the synthesis, vesicle formation, and encapsulation of hydrophobic components and doxorubicin with highly amphiphilic BCPs. However, there is still much work to be done in understanding more about these materials. I would like to pursue thin film studies of the materials (now that we have a solvent that shows promise for spin coating them) with solvent annealing. These studies would allow us to evaluate the materials for lithography applications since they self-assemble into remarkably small features.

There are also several unanswered questions related to the vesicle application that need to be addressed. First, a better understanding of what the faceted structures are and

why they form is necessary. Some of these faceted structures are 500 nm – 1μm in diameter, which is larger than the particle sizes in solution measured by DLS. This could be because there are many more of the smaller structures that dominate the DLS measurement than the larger faceted structures but it could also be for another reason, such as the presence of free oligosaccharide contaminant which would not show up as structure in the DLS since it is soluble in water. I would like to understand with certainty whether these structures are BCP vesicles or precursor contaminant, and if they are vesicles, what the mechanism of the faceting is.

While the hydrophobic molecule encapsulation was demonstrated with relative certainty, I would also like to pursue more experiments to understand the mechanism of DOX encapsulation/complexation. Since the major application of these materials is in drug delivery, it would be ideal to be able to demonstrate how the vesicles are encapsulating (or complexing with) a drug. I also did not pursue any release studies with this material, which are critical to understand for drug delivery applications. Finally, a big drawback of these materials is that they are very expensive to make. An area of ongoing research in this field could include designing similarly naturally occurring materials that are not as expensive to synthesize.

### 8.6 REFERENCES


1. L. Oria; A. Ruiz de Luzuriaga; J. A. Alduncin; F. Perez-Murano, *Microelectronic Engineering* **2013,** *110*, 234-240.
2. Y. Zhao; E. Sivaniah; T. Hashimoto, *Macromolecules* **2008,** *41*, 9948-9951.
3. V. P. Chuang; C. A. Ross; J. Gwyther; I. Manners, *Advanced Materials* **2009,** *21*, 3789-3793.
4. J. Bang; S. H. Kim; E. Drockenmuller; M. J. Misner; T. P. Russell; C. J. Hawker, *Journal of the American Chemical Society* **2006,** *128*, 7622-7629.
5. V. P. Chuang; J. Gwyther; R. A. Mickiewicz; I. Manners; C. A. Ross, *Nano Letters* **2009,** *9*, 4364-4369.

6. F. S. Bates; M. A. Hillmyer; T. P. Lodge; C. M. Bates; K. T. Delaney; G. H. Fredrickson, *Science* **2012,** *336*, 434-440.
7. C. M. Bates; T. Seshimo; M. J. Maher; W. J. Durand; J. D. Cushen; L. M. Dean; G. Blachut; C. J. Ellison; C. G. Willson, *Science* **2012,** *338*, 775-779.
8. S.-J. Jeong; G. Xia; B. H. Kim; D. O. Shin; S.-H. Kwon; S.-W. Kang; S. O. Kim, *Advanced Materials* **2008,** *20*, 1898-1904.
9. S. O. Kim; H. H. Solak; M. P. Stoykovich; N. J. Ferrier; J. J. de Pablo; P. F. Nealey, *Nature* **2003,** *424*, 411-414.
10. C.-C. Liu; A. Ramírez-Hernández; E. Han; G. S. W. Craig; Y. Tada; H. Yoshida; H. Kang; S. Ji; P. Gopalan; J. J. de Pablo; P. F. Nealey, *Macromolecules* **2013,** *46*, 1415-1424.
11. H. Kang; G. S. W. Craig; E. Han; P. Gopalan; P. F. Nealey, *Macromolecules* **2011,** *45*, 159-164.
12. J. K. W. Yang; Y. S. Jung; J.-B. Chang; R. A. Mickiewicz; A. Alexander Katz; C. A. Ross; K. K. Berggren, *Nat Nano* **2010,** *5*, 256-260.
13. M. P. Stoykovich; H. Kang; K. C. Daoulas; G. Liu; C.-C. Liu; J. J. de Pablo; M. Müller; P. F. Nealey, *ACS Nano* **2007,** *1*, 168-175.
14. J. Chai; J. M. Buriak, *ACS Nano* **2008,** *2*, 489-501.

## References


1. DynaTAC8000X. Wikimedia Commons. (2008)
2. Z. Vega. IPhone 5. Wikimedia Commons. (2012)
3. R. de Rijcke. IBM PC 5150. Wikimedia Commons. (2010)
4. T. Malabuyo. MacBook Air black. Wikimedia Commons. (2008)
5. Transistor Count and Moore's Law. Wikimedia Commons. (2011)
6. G. E. Moore, Solid-State Circuits Society Newsletter, IEEE 2006, 11, 33-35.
7. C. Walter, Scientific American 2005, 32-33.
8. G. Robinson, EE Times 2000, 26.
9. R. A. Athale; G. W. Euliss; J. N. Mait, Proceedings of SPIE 2008, 6978, H1-H5.
10. R. Jaeger, Introduction to Microelectronic Fabrication. 2nd ed.; Prentice Hall: 2002.
11. Photolithography etching process. Wikimedia Commons.
12. B. J. Lin, Journal of Microlithography Microfabrication and Microsystems 2004, 3, 377-395.
13. B. l. Fontaine, SPIE Professional 2010, 20.
14. C. W. Gwyn; R. Stulen; D. Sweeney; D. Attwood, Journal of Vacuum Science & Technology B 1998, 16, 3142-3149.
15. M. M. Greve; B. Holst, Journal of Vacuum Science & Technology B: Microelectronics and Nanometer Structures 2013, 31, 043202-043208.
16. R. Ruiz; H. M. Kang; F. A. Detcheverry; E. Dobisz; D. S. Kercher; T. R. Albrecht; J. J. de Pablo; P. F. Nealey, Science 2008, 321, 936-939.
17. F. Hua; Y. G. Sun; A. Gaur; M. A. Meitl; L. Bilhaut; L. Rotkina; J. F. Wang; P. Geil; M. Shim; J. A. Rogers; A. Shim, Nano Letters 2004, 4, 2467-2471.
18. H.-C. Kim; S.-M. Park; W. D. Hinsberg, Chemical Reviews 2010, 110, 146-177.
19. F. S. Bates; G. H. Fredrickson, Annual Review of Physical Chemistry 1990, 41, 525-557.
20. F. S. Bates; G. H. Fredrickson, Physics Today 1999, 52, 32-38.
21. R. A. Segalman, Materials Science and Engineering: R: Reports 2005, 48, 191-226.
22. M. Park; C. Harrison; P. M. Chaikin; R. A. Register; D. H. Adamson, Science 1997, 276, 1401-1404.
23. M. A. Hillmyer, Nanoporous materials from block copolymer precursors. In Block Copolymers II, Abetz, V., Ed. 2005; Vol. 190, pp 137-181.
24. G. J. Liu; J. F. Ding; T. Hashimoto; K. Kimishima; F. M. Winnik; S. Nigam, Chemistry of Materials 1999, 11, 2233-2240.
25. R. Ruiz; E. Dobisz; T. R. Albrecht, ACS Nano 2011, 5, 79-84.
26. W. K. Li; S. Yang, Journal of Vacuum Science & Technology B 2007, 25, 1982-1984.
27. W. Zheng; Z.-G. Wang, Macromolecules 1995, 28, 7215-7223.
28. V. P. Chuang; J. Gwyther; R. A. Mickiewicz; I. Manners; C. A. Ross, Nano Letters 2009, 9, 4364-4369.
29. J. G. Son; J. Gwyther; J.-B. Chang; K. K. Berggren; I. Manners; C. A. Ross, Nano Letters 2011, 11, 2849-2855.

30. K. Asakawa; T. Hiraoka; H. Hieda; M. Sakurai; Y. Kamata, Journal of Photopolymer Science and Technology 2002, 15, 465-470.
31. S. P. Delcambre; R. A. Riggleman; J. J. de Pablo; P. F. Nealey, Soft Matter 2010, 6, 2475-2483.
32. S. Park; J.-Y. Wang; B. Kim; J. Xu; T. P. Russell, ACS Nano 2008, 2, 766-772.
33. G. Kim; M. Libera, Macromolecules 1998, 31, 2569-2577.
34. J. N. L. Albert; T. H. Epps III, Materials Today 2010, 13, 24-33.
35. E. W. Edwards; M. P. Stoykovich; H. H. Solak; P. F. Nealey, Macromolecules 2006, 39, 3598-3607.
36. D. Y. Ryu; K. Shin; E. Drockenmuller; C. J. Hawker; T. P. Russell, Science 2005, 308, 236-239.
37. C. M. Bates; J. R. Strahan; L. J. Santos; B. K. Mueller; B. O. Bamgbade; J. A. Lee; J. M. Katzenstein; C. J. Ellison; C. G. Willson, Langmuir 2011, 27, 2000-2006.
38. P. Mansky; Y. Liu; E. Huang; T. P. Russell; C. J. Hawker, Science 1997, 275, 1458-1460.
39. R. Guo; E. Kim; J. Gong; S. Choi; S. Ham; D. Y. Ryu, Soft Matter 2011, 7, 6920-6925.
40. E. Huang; T. P. Russell; C. Harrison; P. M. Chaikin; R. A. Register; C. J. Hawker; J. Mays, Macromolecules 1998, 31, 7641-7650.
41. C. M. Bates; T. Seshimo; M. J. Maher; W. J. Durand; J. D. Cushen; L. M. Dean; G. Blachut; C. J. Ellison; C. G. Willson, Science 2012, 338, 775-779.
42. T. P. Lodge; B. Pudil; K. J. Hanley, Macromolecules 2002, 35, 4707-4717.
43. M. Y. Paik; J. K. Bosworth; D. M. Smilges; E. L. Schwartz; X. Andre; C. K. Ober, Macromolecules 2010, 43, 4253-4260.
44. J. N. L. Albert; T. D. Bogart; R. L. Lewis; K. L. Beers; M. J. Fasolka; J. B. Hutchison; B. D. Vogt; T. H. Epps, Nano Letters 2011, 11, 1351-1357.
45. Y. S. Jung; C. A. Ross, Advanced Materials 2009, 21, 2540-2545.
46. M. Vayer; M. A. Hillmyer; M. Dirany; G. Thevenin; R. Erre; C. Sinturel, Thin Solid Films 2010, 518, 3710-3715.
47. J. Cushen; L. Wan; G. Pandav; I. Mitra; G. Stein; V. Ganesan; R. Ruiz; C. G. Willson; C. J. Ellison, Journal of Polymer Science Part b 2013, in press.
48. I. Koren; Z. Koren, Proceedings of the IEEE 1998, 86, 1819-1838.
49. T. Thurn-Albrecht; J. Schotter; G. A. Kästle; N. Emley; T. Shibauchi; L. Krusin-Elbaum; K. Guarini; C. T. Black; M. T. Tuominen; T. P. Russell, Science 2000, 290, 2126-2129.
50. S. H. Kim; M. J. Misner; L. Yang; O. Gang; B. M. Ocko; T. P. Russell, Macromolecules 2006, 39, 8473-8479.
51. S. Park; D. H. Lee; J. Xu; B. Kim; S. W. Hong; U. Jeong; T. Xu; T. P. Russell, Science 2009, 323, 1030-1033.
52. B. C. Berry; A. W. Bosse; J. F. Douglas; R. L. Jones; A. Karim, Nano Letters 2007, 7, 2789-2794.
53. S. M. Park; M. P. Stoykovich; R. Ruiz; Y. Zhang; C. T. Black; P. E. Nealey, Advanced Materials 2007, 19, 607-611.

54. I. Bita; J. K. W. Yang; Y. S. Jung; C. A. Ross; E. L. Thomas; K. K. Berggren, Science 2008, 321, 939-943.
55. J. Y. Cheng; C. T. Rettner; D. P. Sanders; H.-C. Kim; W. D. Hinsberg, Advanced Materials 2008, 20, 3155-3158.
56. S. O. Kim; H. H. Solak; M. P. Stoykovich; N. J. Ferrier; J. J. de Pablo; P. F. Nealey, Nature 2003, 424, 411-414.
57. D. Zschech; D. H. Kim; A. P. Milenin; R. Scholz; R. Hillebrand; C. J. Hawker; T. P. Russell; M. Steinhart; U. Gosele, Nano Letters 2007, 7, 1516-1520.
58. S. J. Jeong; G. D. Xia; B. H. Kim; D. O. Shin; S. H. Kwon; S. W. Kang; S. O. Kim, Advanced Materials 2008, 20, 1898-1904.
59. S. J. Ku; G. C. Jo; C. H. Bak; S. M. Kim; Y. R. Shin; K. H. Kim; S. H. Kwon; J.-B. Kim, Nanotechnology 2013, 24, 085301.
60. M. Colburn; A. Grot; M. Amistoso; B. J. Choi; T. Bailey; J. Ekerdt; S. V. Sreenivasan; S. Hollenhorst; C. G. Willson, Step and flash imprint lithography for sub-100nm patterning. In Emerging Lithographic Technologies IV, Dobisz, E. A., Ed. Spie-Int Soc Optical Engineering: Bellingham, 2000; Vol. 3997, pp 453-457.
61. M. D. Rodwogin; C. S. Spanjers; C. Leighton; M. A. Hillmyer, ACS Nano 2010, 4, 725-732.
62. Y. S. Jung; C. A. Ross, Nano Letters 2007, 7, 2046-2050.
63. V. P. Chuang; C. A. Ross; J. Gwyther; I. Manners, Advanced Materials 2009, 21, 3789-3793.
64. T. Hirai; M. Leolukman; C. C. Liu; E. Han; Y. J. Kim; Y. Ishida; T. Hayakawa; M.-a. Kakimoto; P. F. Nealey; P. Gopalan, Advanced Materials 2009, 21, 4334-4338.
65. E. W. Cochran; D. C. Morse; F. S. Bates, Macromolecules 2003, 36, 782-792.
66. C. A. Ross; Y. S. Jung; V. P. Chuang; F. Ilievski; J. K. W. Yang; I. Bita; E. L. Thomas; H. I. Smith; K. K. Berggren; G. J. Vancso; J. Y. Cheng In Si-containing block copolymers for self-assembled nanolithography, AVS: 2008; pp 2489-2494.
67. R. D. Peters; X. M. Yang; T. K. Kim; B. H. Sohn; P. F. Nealey, Langmuir 2000, 16, 4625-4631.
68. Y. Xuan; J. Peng; L. Cui; H. Wang; B. Li; Y. Han, Macromolecules 2004, 37, 7301-7307.
69. T. P. Russell; R. P. Hjelm; P. A. Seeger, Macromolecules 1990, 23, 890-893.
70. V. Khanna; E. W. Cochran; A. Hexemer; G. E. Stein; G. H. Fredrickson; E. J. Kramer; X. Li; J. Wang; S. F. Hahn, Macromolecules 2006, 39, 9346-9356.
71. T. Vu; N. Mahadevapuram; G. M. Perera; G. E. Stein, Macromolecules 2011, 44, 6121-6127.
72. M. W. Matsen, Macromolecules 2009, 43, 1671-1674.
73. M. Harada; T. Suzuki; M. Ohya; A. Takano; Y. Matsushita, Polymer Journal 2004, 36, 538-541.
74. P. Chaumont; G. Beinert; J. E. Herz; P. Rempp, Makromolekulare Chemie-Macromolecular Chemistry and Physics 1982, 183, 1181-1190.
75. D. Uhrig; J. W. Mays, Journal of Polymer Science Part a-Polymer Chemistry 2005, 43, 6179-6222.

76. H. Hsieh; R. Quirk, Anionic Polymerization 1996.
77. T. S. Bailey; H. D. Pham; F. S. Bates, Macromolecules 2001, 34, 6994-7008.
78. S. K. Varshney; Z. S. Gao; X. F. Zhong; A. Eisenberg, Macromolecules 1994, 27, 1076-1082.
79. P. Hiemenz; T. Lodge, Polymer Chemistry. 2 ed.; 2007.
80. L. A. Wall; S. Straus; R. E. Florin; L. J. Fetters, Journal of Research of the National Bureau of Standards Section a-Physics and Chemistry 1973, A 77, 157-170.
81. T. Kashiwagi; A. Inaba; J. E. Brown; K. Hatada; T. Kitayama; E. Masuda, Macromolecules 1986, 19, 2160-2168.
82. I. W. Hamley; V. Castelletto, Progress in Polymer Science 2004, 29, 909-948.
83. M. Harada; T. Suzuki; M. Ohya; D. Kawaguchi; A. Takano; Y. Matsushita; N. Torikai, Journal of Polymer Science Part B: Polymer Physics 2005, 43, 1486-1494.
84. M. Harada; T. Suzuki; M. Ohya; D. Kawaguchi; A. Takano; Y. Matsushita, Macromolecules 2005, 38, 1868-1873.
85. Hashimot.T; Nagatosh.K; A. Todo; H. Hasegawa; H. Kawai, Macromolecules 1974, 7, 364-373.
86. C. M. Bates; J. R. Strahan; L. J. Santos; B. K. Mueller; B. O. Bamgbade; J. A. Lee; J. M. Katzenstein; C. J. Ellison; C. G. Willson, Langmuir 2011, 27, 2000-2006.
87. J. D. Cushen; I. Otsuka; C. M. Bates; S. Halila; S. Fort; C. Rochas; J. A. Easley; E. L. Rausch; A. Thio; R. Borsali; C. G. Willson; C. J. Ellison, Acs Nano 2012, 6, 3424-3433.
88. K. A. K. Aissou; I. Otsuka; C. Rochas; S. Fort; S. Halila; R. Borsali, Langmuir 2011, 27, 4098-4103.
89. A. J. Link; M. K. S. Vink; D. A. Tirrell, Nat. Protocols 2007, 2, 1884-1887.
90. J.-S. Wang; K. Matyjaszewski, Journal of the American Chemical Society 1995, 117, 5614-5615.
91. K. Matyjaszewski; J. Xia, Chemical Reviews 2001, 101, 2921-2990.
92. A. Goto; T. Fukuda, Progress in Polymer Science 2004, 29, 329-385.
93. K. Matyjaszewski; K. Davis; T. E. Patten; M. L. Wei, Tetrahedron 1997, 53, 15321-15329.
94. N. V. Tsarevsky; K. Matyjaszewski, Chemical Reviews 2007, 107, 2270-2299.
95. A. C. Jones; P. O'Brien, CVD of compound semiconductors. Wiley. com: 2008.
96. S. J. Moss; A. Ledwith, Chemistry of the Semiconductor Industry. Springer: 1989.
97. W. Jakubowski; K. Matyjaszewski, Angewandte Chemie International Edition 2006, 45, 4482-4486.
98. W. Jakubowski; K. Min; K. Matyjaszewski, Macromolecules 2005, 39, 39-45.
99. W. Jakubowski; B. Kirci-Denizli; R. R. Gil; K. Matyjaszewski, Macromolecular Chemistry and Physics 2008, 209, 32-39.
100. G. D. Fu; L. Q. Xu; F. Yao; K. Zhang; X. F. Wang; M. F. Zhu; S. Z. Nie, ACS Applied Materials & Interfaces 2009, 1, 239-243.
101. V. Coessens; K. Matyjaszewski, Journal of Macromolecular Science-Pure and Applied Chemistry 1999, A36, 667-679.
102. Z. Guo; Y. Jin; T. Liang; Y. Liu; Q. Xu; X. Liang; A. Lei, Journal of Chromatography A 2009, 1216, 257-263.

103. S. Halila; M. Manguian; S. Fort; S. Cottaz; T. Hamaide; E. Fleury; H. Driguez, Macromolecular Chemistry and Physics 2008, 209, 1282-1290.
104. I. Otsuka; K. Fuchise; S. Halila; S. b. Fort; K. Aissou; I. Pignot-Paintrand; Y. Chen; A. Narumi; T. Kakuchi; R. Borsali, Langmuir 2009, 26, 2325-2332.
105. K. A. K. Aissou; I. Otsuka; C. Rochas; S. Fort; S. Halila; R. Borsali, Langmuir 27, 4098-4103.
106. Y. Takahashi; T. Kumano; S. Nishikawa, Macromolecules 2004, 37, 6827-6832.
107. D. J. Kinning; E. L. Thomas, Macromolecules 1984, 17, 1712-1718.
108. N. Sary; L. Rubatat; C. Brochon; G. Hadziioannou; J. Ruokolainen; R. Mezzenga, Macromolecules 2007, 40, 6990-6997.
109. K. Kimishima; T. Koga; T. Hashimoto, Macromolecules 2000, 33, 968-977.
110. M. W. Matsen, Journal of Chemical Physics 2001, 114, 8165-8173.
111. F. S. Bates; M. F. Schulz; A. K. Khandpur; S. Forster; J. H. Rosedale; K. Almdal; K. Mortensen, Faraday Discussions 1994, 98, 7-18.
112. M. W. Matsen; F. S. Bates, Journal of Polymer Science Part B: Polymer Physics 1997, 35, 945-952.
113. E. Wohlfart; J. P. Fernandez-Blazquez; E. Knoche; A. Bello; E. Perez; E. Arzt; A. n. del Campo, Macromolecules 2010, 43, 9908-9917.
114. R. A. Farrell; N. Petkov; M. T. Shaw; V. Djara; J. D. Holmes; M. A. Morris, Macromolecules 2010, 43, 8651-8655.
115. M. A. Hillmyer; F. S. Bates, Macromolecules 1996, 29, 6994-7002.
116. O. Dechy-Cabaret; B. Martin-Vaca; D. Bourissou, Chemical Reviews 2004, 104, 6147-6176.
117. A. Debuigne; J.-R. Caille; N. Willet; R. Jérôme, Macromolecules 2005, 38, 9488-9496.
118. Y. B. Wang; M. A. Hillmyer, Macromolecules 2000, 33, 7395-7403.
119. A. S. Zalusky; R. Olayo-Valles; J. H. Wolf; M. A. Hillmyer, Journal of the American Chemical Society 2002, 124, 12761-12773.
120. M. Vert; G. Schwach; R. Engel; J. Coudane, Journal of Controlled Release 1998, 53, 85-92.
121. Lactide Stereoisomers Structural Formulae. Wikimedia Commons. (2009)
122. Y. L. Loo; R. A. Register; A. J. Ryan, Macromolecules 2002, 35, 2365-2374.
123. J. D. Cushen; C. M. Bates; E. L. Rausch; L. M. Dean; S. X. Zhou; C. G. Willson; C. J. Ellison, Macromolecules 2012, 45, 8722-8728.
124. S. C. Schmidt; M. A. Hillmyer, Macromolecules 1999, 32, 4794-4801.
125. J. W. Jeong; W. I. Park; M.-J. Kim; C. A. Ross; Y. S. Jung, Nano Letters 2011, 11, 4095-4101.
126. T.-Y. Lo; C.-C. Chao; R.-M. Ho; P. Georgopanos; A. Avgeropoulos; E. L. Thomas, Macromolecules 2013.
127. J. Brandrup; E. H. Immergut; E. A. Grulke; A. Abe; D. R. Bloch, John Wiley & Sons.
128. R. Ruiz; E. Dobisz; T. R. Albrecht, Acs Nano 2010, 5, 79-84.
129. R. D. Peters; X. M. Yang; T. K. Kim; P. F. Nealey, Langmuir 2000, 16, 9620-9626.

130. G. L. Liu; S. X. Ji; K. O. Stuen; G. S. W. Craig; P. F. Nealey; F. J. Himpsel, Journal of Vacuum Science & Technology B 2009, 27, 3038-3042.
131. C. A. Wilson; R. K. Grubbs; S. M. George, Chemistry of Materials 2005, 17, 5625-5634.
132. Q. Peng; Y.-C. Tseng; S. B. Darling; J. W. Elam, Acs Nano 2011, 5, 4600-4606.
133. K. J. Hanley; T. P. Lodge; C.-I. Huang, Macromolecules 2000, 33, 5918-5931.
134. G. Fredrickson, Equilibrium Theory of Inhomogeneous Polymers, The. International Series of Monographs on Physics. Oxford Scholarship Online: 2006.
135. G. H. Fredrickson; V. Ganesan; F. Drolet, Macromolecules 2002, 35, 16-39.
136. M. W. Matsen, Macromolecules 2003, 36, 9647-9657.
137. M. W. Matsen; M. D. Whitmore, Journal of Chemical Physics 1996, 105, 9698-9701.
138. J. D. Vavasour; M. D. Whitmore, Macromolecules 1992, 25, 5477-5486.
139. Z. Wu; B. Li; Q. Jin; D. Ding; A.-C. Shi, The Journal of Physical Chemistry B 2010, 114, 15789-15798.
140. M. Banaszak; M. D. Whitmore, Macromolecules 1992, 25, 3406-3412.
141. M. D. Whitmore; J. D. Vavasour, Macromolecules 1992, 25, 2041-2045.
142. J. R. Naughton; M. W. Matsen, Macromolecules 2002, 35, 5688-5696.
143. C. I. Huang; T. P. Lodge, Macromolecules 1998, 31, 3556-3565.
144. T. P. Lodge; K. J. Hanley; B. Pudil; V. Alahapperuma, Macromolecules 2003, 36, 816-822.
145. K. Mori; H. Hasegawa; T. Hashimoto, Polymer 2001, 42, 3009-3021.
146. R. Ruiz; R. L. Sandstrom; C. T. Black, Advanced Materials 2007, 19, 587-+.
147. Y. S. Jung; J. B. Chang; E. Verploegen; K. K. Berggren; C. A. Ross, Nano Letters 2010, 10, 1000-1005.
148. Y. Tada; H. Yoshida; Y. Ishida; T. Hirai; J. K. Bosworth; E. Dobisz; R. Ruiz; M. Takenaka; T. Hayakawa; H. Hasegawa, Macromolecules 2011, 45, 292-304.
149. M. D. Gehlsen; K. Almdal; F. S. Bates, Macromolecules 1992, 25, 939-943.
150. L. Leibler, Macromolecules 1980, 13, 1602-1617.
151. M. W. Matsen; R. B. Thompson, The Journal of Chemical Physics 1999, 111, 7139-7146.
152. L. J. Fetters; D. J. Lohse; D. Richter; T. A. Witten; A. Zirkel, Macromolecules 1994, 27, 4639-4647.
153. Y. Zhao; E. Sivaniah; T. Hashimoto, Macromolecules 2008, 41, 9948-9951.
154. W. W. Maurer; F. S. Bates; T. P. Lodge; K. Almdal; K. Mortensen; G. H. Fredrickson, The Journal of Chemical Physics 1998, 108, 2989-3000.
155. N. Sakamoto; T. Hashimoto, Macromolecules 1995, 28, 6825-6834.
156. J. H. Rosedale; F. S. Bates, Macromolecules 1990, 23, 2329-2338.
157. O. Kratky; I. Pilz; P. J. Schmitz, Journal of Colloid and Interface Science 1966, 21, 24-&.
158. R.-J. Roe, Methods of X-Ray and Neutron Scattering in Polymer Science. Oxford University Press: 2000.

159. S. Sakurai; K. Mori; A. Okawara; K. Kimishima; T. Hashimoto, Macromolecules 1992, 25, 2679-2691.
160. J.-B. Chang; J. G. Son; A. F. Hannon; A. Alexander-Katz; C. A. Ross; K. K. Berggren, ACS Nano 2012, 6, 2071-2077.
161. E. Baker, Chemistry and morphology of plant epicuticular waxes. Academic Press: London, 1982.
162. S. R. Snider, Annals of Neurology 1984, 16, 723-723.
163. C. P. F. Marinangeli; A. N. Kassis; D. Jain; N. Ebine; S. C. Cunnane; P. J. H. Jones, British Journal of Nutrition 2007, 97, 381-388.
164. H. K. Berthold; S. Unverdorben; R. Degenhardt; M. Bulitta; I. Gouni-Berthold, JAMA 2006, 295, 2262-2269.
165. D. H. Katz; J. F. Marcelletti; M. H. Khalil; L. E. Pope; L. R. Katz, Proceedings of the National Academy of Sciences 1991, 88, 10825-10829.
166. 1-Octadecanol. (accessed October 28). Wikipedia.
167. Betacyclodextrin. (accessed October 28). Wikipedia.
168. M. L. Adams; A. Lavasanifar; G. S. Kwon, Journal of Pharmaceutical Sciences 2003, 92, 1343-1355.
169. J. Yan; Z. Ye; M. Chen; Z. Liu; Y. Xiao; Y. Zhang; Y. Zhou; W. Tan; M. Lang, Biomacromolecules 2011, 12, 2562-2572.
170. L. G. Yin; M. C. Dalsin; A. Sizovs; T. M. Reineke; M. A. Hillmyer, Macromolecules 2012, 45, 4322-4332.
171. M. A. Greenfield; L. C. Palmer; G. Vernizzi; M. O. de la Cruz; S. I. Stupp, Journal of the American Chemical Society 2009, 131, 12030-+.
172. G. B. Ray; I. Chakraborty; S. P. Moulik, Journal of Colloid and Interface Science 2006, 294, 248-254.
173. L. Oria; A. Ruiz de Luzuriaga; J. A. Alduncin; F. Perez-Murano, Microelectronic Engineering 2013, 110, 234-240.
174. J. Bang; S. H. Kim; E. Drockenmuller; M. J. Misner; T. P. Russell; C. J. Hawker, Journal of the American Chemical Society 2006, 128, 7622-7629.
175. F. S. Bates; M. A. Hillmyer; T. P. Lodge; C. M. Bates; K. T. Delaney; G. H. Fredrickson, Science 2012, 336, 434-440.
176. S.-J. Jeong; G. Xia; B. H. Kim; D. O. Shin; S.-H. Kwon; S.-W. Kang; S. O. Kim, Advanced Materials 2008, 20, 1898-1904.
177. C.-C. Liu; A. Ramírez-Hernández; E. Han; G. S. W. Craig; Y. Tada; H. Yoshida; H. Kang; S. Ji; P. Gopalan; J. J. de Pablo; P. F. Nealey, Macromolecules 2013, 46, 1415-1424.
178. H. Kang; G. S. W. Craig; E. Han; P. Gopalan; P. F. Nealey, Macromolecules 2011, 45, 159-164.
179. J. K. W. Yang; Y. S. Jung; J.-B. Chang; R. A. Mickiewicz; A. Alexander Katz; C. A. Ross; K. K. Berggren, Nat Nano 2010, 5, 256-260.
180. M. P. Stoykovich; H. Kang; K. C. Daoulas; G. Liu; C.-C. Liu; J. J. de Pablo; M. Müller; P. F. Nealey, ACS Nano 2007, 1, 168-175.
14. J. Chai; J. M. Buriak, ACS Nano 2008, 2, 489-501.